論文 / 著書情報
Article / Book Information

題目(和文)	
Title(English)	A study on low threshold GaInAsP/InP surface emitting lasers grown by chemical beam epitaxy
著者(和文)	宮本智之
Author(English)	Tomoyuki Miyamoto
出典(和文)	学位:博士（工学）, 学位授与機関:東京工業大学, 報告番号:甲第3256号, 授与年月日:1996年3月26日, 学位の種別:課程博士, 審査員:
Citation(English)	Degree:Doctor (Engineering), Conferring organization: Tokyo Institute of Technology, Report number:甲第3256号, Conferred date:1996/3/26, Degree Type:Course doctor, Examiner:
学位種別(和文)	博士論文
Type(English)	Doctoral Thesis

DOCTORAL DISSERTATION

A Study on Low Threshold GaInAsP/InP Surface Emitting Lasers Grown by Chemical Beam Epitaxy

by

Tomoyuki MIYAMOTO

1996

Adviser: Professor Kenichi IGA, Dr. Eng.

Department of Information Processing
Interdisciplinary Graduate School of Science and Engineering
Tokyo Institute of Technology
4259 Nagatsuta, Midori-ku, Yokohama 226, JAPAN

A Study on Low Threshold GaInAsP/InP Surface Emitting Lasers Grown by Chemical Beam Epitaxy

(CBE法によるGaInAsP/InP面発光レーザの低しきい値化に関する研究)

論文概要

二次元アレイ化可能な光通信用光源である1.55μm帯GaInAsP/InP面発光レーザの実現を目指し，いくつかの新しい構造を提案して低しきい値化の可能性を示した．まず，化学ビーム成長(CBE)技術を確立し，面発光レーザウェハのための優れた結晶成長を実現した．また，量子井戸構造の特性の構造依存性を指摘した．次に，メサキャップ構造面発光レーザを製作してCBE法で初めての発振を得るとともに，高性能複合反射鏡により11°Cでのパルス発振と電流狭窄構造で77K連続動作における0.3mAの世界最低しきい値電流を達成した．また，高性能化のために電流注入に関する問題と歪量子井戸活性層の適用の検討を行なった．本研究により，長波長帯面発光レーザの飛躍的特性向上の可能性を見出した．

Table of Contents

Chapter 1

Introduction

In this chapter, the background of optical communications is reviewed, and then the advantage and progress of surface emitting lasers are described. The problems for obtaining low threshold long wavelength surface emitting lasers are pointed out. Lastly, the objective of this study is presented.

1.1 Background of Optical Communications

1.1.1 Optical Communications

In recent years, the information communication is greatly paid attentions. The reason is development and possibility of new information services, such as computer networking, data base services (e.g., banking, shopping, library), video-conferencing, entertainment services (e.g., video on demand, transmission KARAOKE) and so on. These services require high performance transmission systems such as wide service area, high speed, large capacity, low cost, etc. To realize such information services, wired transmission systems have been played a very important role because of its stable transmission channels.

There are two types of wired transmission systems. One uses "electrical" signals with coaxial cables and another uses optical signals via optical fibers. Table 1.1 shows characteristics of these transmission channels [1]. The optical fiber system has great advantages against "electrical" cable system at the point of not only transmission capacity but also easy system construction. Hence, almost trunk lines have exchanged to the optical fiber lines and the transmission capacities have been improved as shown in Fig. 1.1. The maximum capacities of coaxial cable systems are 10800ch (C60M: analog) and 5760ch (DC400M: 400Mbps : bit per second). On the other hand, the optical fiber system of F-10G with bit rate of 10Gbps (129000ch) will be soon introduced and the relative cost is estimated to be less than 1/100 of DC400M. Further improvement of optical transmissions is expected by

wavelength division multiplexing (WDM) systems and optical soliton transmission systems.

From such advantages of optical fiber system, the importance will increase more in trunk lines. Furthermore, the optical communication system has been also planned to introduce subscriber networks as the system of fiber to the home (FTTH) to transmit new information services. In recent years, the other new field of optical transmission systems has been considered as the optical interconnection system between system-system, circuit board-board and LSI chip-chip. Up to this time, almost of all interconnect systems have been constructed by electrically wired systems. However, the transmission speed, delay time and cross section area of cables is considered to be not sufficient for near future computer systems.

Table 1.1 Comparison of coaxial cables and optical fibers for trunk lines. (The band width of optical fiber indicates the range of optical frequency for λ=1.5-1.6μm)

	Loss (dB/km)	Band Width (GHz)	Line No.	Diameter (mm)
Coaxial Cable	33	0.2	18	65
Optical Fiber	< 0.2	12500	600	34

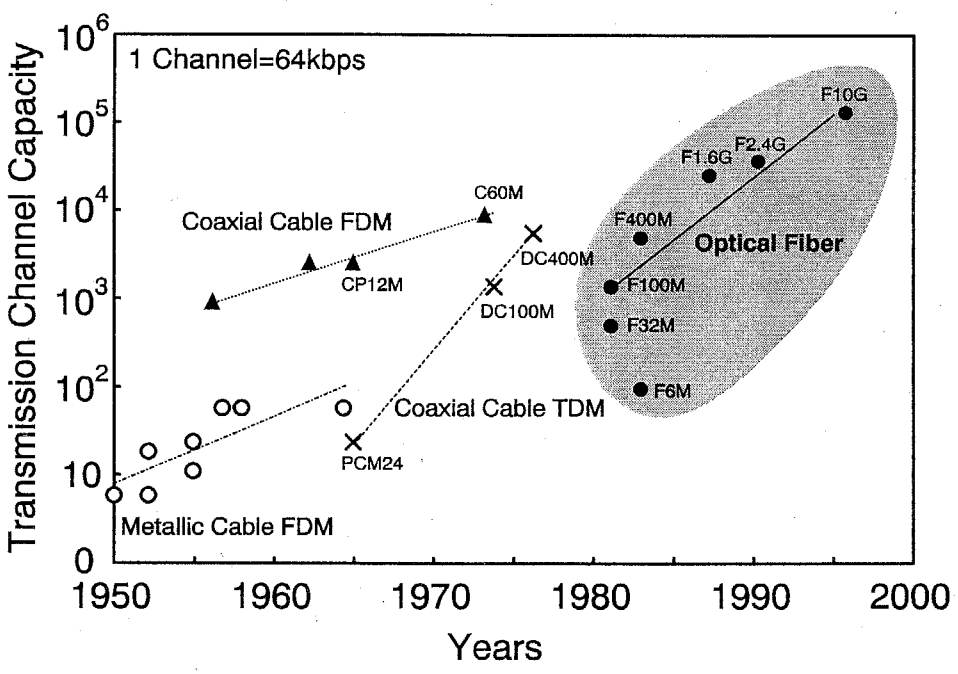

Fig. 1.1 Trend in transmission capacity for wired transmission systems. The plotted data are commercial systems introduced in Japan [1].

For example, the clock speed of recent CPU is reached to over 200MHz with the data bus width of 64bit, which equals to the transmission speed of 13Gbps, but the interface bus clock is suppressed to less than 100MHz because of the difficulty of design of high speed electrical board and large delay time of signals. Hence, the optical interconnect is attractive system for future computer systems such as extremely fast data transfer, parallel computing and so on. These optical interconnect systems are expected to become an important field of optical systems as well as previous optical communication systems. In this way, the applicability of optical transmission systems has been increased to wide fields.

1.1.2 Progress of Long Wavelength Semiconductor Lasers

As described above, the optical transmission system has been developed and used in various systems. It would be said that the real start of optical communication systems was started after the suggestion of extremely low loss optical fiber [2] and achievement of room temperature operation of semiconductor lasers [3, 4] in 1970. The low loss window of silica fiber was developed at long wavelength range (>1μm) [5, 6] and ultimately low loss of 0.2dB/km was achieved at the wavelength of 1.55μm [7] which was supported by theoretical limit [8, 9]. Furthermore, the zero index dispersion was predicted in 1.3μm wavelength [10] which is another important parameter for long distance transmission. Hence, the development of semiconductor laser for optical communications has been progressed on the InGaAsP/InP system with 1.3μm and 1.55μm wavelength, because the GaInAsP material system has possibility of emitting at this wavelength range. The historical perspective and recent progress of semiconductor lasers in long wavelength region are summarized as follows [11].

The first lasing operation in semiconductor injection lasers was achieved in 1962 [12, 13, 14]. These lasers operated at around 0.85μm wavelength with GaAs p-n homojunction under 77K condition. The limited utility of homojunction laser diodes was immediately recognized and it was suggested to use of the heterostructure for improving laser characteristics [15]. Then, the room temperature CW operation of semiconductor lasers was achieved by GaAlAs/GaAs lasers in 1970 [3, 4]. After a while, the wavelength beyond 1μm for optical fiber communication was demonstrated in 1976 [16, 17, 18, 19]. In the late 1970's, variety of index guided structures known as buried heterostructures (BH) was introduced to GaInAsP/InP systems for transverse modal stability. Then, high performance single frequency lasers were realized by distributed feed back (DFB) lasers in early 1980's [20, 21]. These lasers were developed with double heterostructure (DH) bulk active layers. On the other hand, a quantum well (QW) laser was achieved the first lasing in 1975 [22]. The QW laser characteristics were improved rapidly in GaAs based lasers in early 1980's [23, 24]. The real development of long wavelength QW lasers have been started slightly later in late 1980's because of the difficulty of low threshold current due to large inter-valence band absorption

and large Auger non-radiative recombination. However, after the suggestion of strained QW structures in 1986 [25, 26], lasing characteristics of long wavelength QW lasers were much improved [27]. The development of strained QW structure and buried techniques lowered the threshold current and less than 1mA threshold currents was reported in 1.55μm wavelength region [28, 29, 30, 31] as well as GaAs based lasers [32]. The other laser characteristic of long wavelength region has been also improved, such as low temperature dependence, high temperature operation, high speed modulation and so on.

To realize next generation optical transmission systems such as high performance trunk lines, low cost subscriber systems and parallel optical interconnection systems, improvements of performances in light sources have been required still now. A surface emitting laser is expected as one of representative of such new generation lasers.

1.2 Surface Emitting Lasers for Optical Communications

1.2.1 Advantages of Surface Emitting Lasers

A surface emitting laser is very attractive optical device [33, 34]. A fundamental characteristic of surface emitting lasers is light output direction which is normal to the substrate surface and different from conventional edge emitting lasers. Though the surface emitting lasers are classified to some structures by the surface emitting methods [35], a vertical-cavity type is most interesting structure because of possibility of extremely micro structure. The schematic structure of vertical-cavity surface emitting laser is shown in Fig. 1.2. According to the vertical emitting with small cavity, the surface emitting laser has following advantages;

1) Densely packed two-dimensional laser array,
2) Dynamic single mode operation due to large mode spacing,
3) High efficiency fiber coupling due to sharp circular beam,
4) Ultra-low power consumption with micro structure,
5) Fabricated by a fully monolithic process,
6) Vertical integration with the other planar devices,
7) Initial probe test without device separation.

These features are satisfy the required characteristics for the next generation light sources in not only optical communication systems but also optical memory systems, optical integrated circuits and so on.

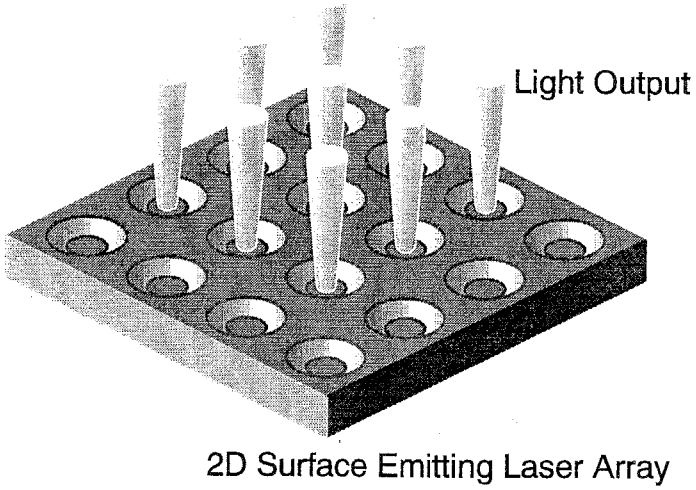

Fig. 1.2 Schematic view of two-dimensional arrayed surface emitting lasers.

1.2.2 Progress of Surface Emitting Lasers

In 1977, the surface emitting injection laser was proposed first by Iga of Tokyo Institute of Technology and adviser of this study. The first achievement of current injection surface emitting lasers were reported by Soda et al. with GaInAsP/InP system in 1979 [36]. The lasing was observed under 77K pulsed condition and the threshold current was 860mA (11kA/cm^2). The mirrors were formed by epitaxial surface and polished substrate surface, and current confinement was realized by a circular electrode. Then, the buried heterostructure (BH) was reported to confine current in 1981 [37] and the short cavity structure formed by removing substrate was proposed for reducing absorption loss in 1982 [38]. In 1984, the first GaAlAs/GaAs surface emitting laser was demonstrated and achieved the first room temperature pulsed operation of surface emitting lasers by Ibaraki et al. [39]. To realize high reflectivity mirrors, the applicability of semiconductor distributed Bragg reflector (DBR) was examined for GaInAsP/InP system in 1985 [40] and a dielectric multilayer mirror was applied to GaAs system in 1986 [41]. The first room temperature continuous wave (CW) operation was achieved in GaAlAs/GaAs system by Koyama et al. in 1988 [42]. From these days, research about the surface emitting laser had been increased.

In 1989, a multi-quantum well (MQW) structure was introduced into a GaAlAs/GaAs surface emitting laser for the first time [43] and InGaAs/GaAs strained QW with AlAs/GaAs DBR was reported with a very low threshold by Jewell et al. [44]. Soon, the threshold reduction was rapidly realized in InGaAs/GaAs system and less than 1mA has been reported by many groups [45, 46]. These threshold currents were equal or less then the minimum threshold current of conventional edge emitting lasers. Especially, native oxide current

definition was effectively lowered threshold current [47], and in recent time, threshold current less than 100μA was reported by Hayashi et al. (70μA) [48] and Yang et al. (8μA) [49] in 1995. The threshold current is the lowest in semiconductor lasers. Furthermore, the wavelength range of surface emitting lasers have been extended to red visible region with AlGaInP/GaAs system [50] and a ZnSe based blue-green surface emitting laser was also reported at 77K [51]. In this way, the surface emitting laser has been progressed rapidly. In recent years, the InGaAs/GaAs surface emitting laser arrays have been commercially available.

1.2.3 Requirements for Long Wavelength Surface Emitting Lasers

As described in background of optical communications, the long wavelength region of 1.3μm and 1.55μm is important for realizing high performance optical transmission systems. Therefore, the GaInAsP/InP surface emitting laser is suitable as well as conventional lasers.

Though the research of surface emitting lasers were started in a GaInAsP/InP system, the progress of surface emitting lasers has been rapidly in short wavelength systems as described above. Even though the lasing characteristics were also improved for long wavelength surface emitting lasers, the lasing characteristics were worse than that of short wavelength surface emitting lasers. The lasing characteristics in 1990, the start time of this study, were follows. The target wavelength had been only at 1.3μm and 1.55μm-wavelength device was not reported. The operating temperature of long wavelength surface emitting lasers were not reached to room temperature even at pulsed condition. The maximum operating temperature was -10°C and the threshold current was extremely large (>400mA) though the minimum threshold current of 0.98μm wavelength of InGaAs/GaAs systems was 1.3mA at room temperature.

Such poor lasing characteristics are due to some substantial difficulties for making long wavelength surface emitting lasers. The difficulties of long wavelength surface emitting lasers are considered to be due to the following reasons.

i) The Auger nonradiative recombination is noticeable and this makes the threshold current density abnormally high at near room temperature.
ii) There is a large absorption known as inter-valence band absorption (IVBA) for long wavelength light. This IVBA increases the cavity losses and consequently the carrier density for lasing.
iii) Difficulty of high reflectivity semiconductor multilayer reflectors due to small index difference between GaInAsP and InP.

These difficulties increase the threshold current density and hence threshold current. The increase of current density and current raises the device temperature, and unfortunately, it

effectively increases Auger recombination and inter-valence band absorption. Due to such negative feedback, the low threshold current and high operation temperature of long wavelength surface emitting lasers are difficult.

The improvements of lasing characteristics for long wavelength surface emitting lasers are difficult due to above problems, however many researches have conquered these problems. The recent progress of long wavelength surface emitting lasers are follows.

The first room temperature operation in long wavelength region was realized by photopumped operation in 1990 [52]. Immediately, the first room temperature injection laser was reported using an n-side GaInAsP/InP DBR under pulsed condition [53] and near room temperature pulsed operation was also obtained applying Si/SiO_2 multilayer mirrors [54]. Then, a lasing above room temperature of 66°C was realized under pulsed condition and threshold current was lowered to 1.5mA at 77K [55]. In these days, the threshold current density at 77K was reduced to around 500A/cm^2 [55, 56]. Room temperature pulsed operation of 1.58μm surface emitting lasers with GaInAsP/InP DBR was reported with low threshold of 21kA/cm^2 in 1992 [57]. In late 1992, the operating temperature was up to 144°C under optically pumped condition by a fused GaAs/AlAs DBR device [58]. In early 1993, the first room temperature CW operation was achieved by Baba et al. by LPE grown 1.3μm device which consisted good thermal conductivity mirror of MgO/Si multilayers [59]. Its threshold current was 22mA (19kA/cm^2) at 14°C. In 1994, a low threshold of 9mA (pulsed) device was reported by injection type GaAs/AlAs fused structure [60]. The first QW long wavelength surface emitting laser was realized by Uomi et al. [61] and a strained QW surface emitting laser operated up to 150°C under photopumped condition [62]. In 1995, a double fused GaAs/AlAs mirror device with bulk active layer was reported with threshold current density of 3kA/cm^2 [63], and then the room temperature operation was achieved at 2.3mA threshold current with strained QW and double fused mirror structure by Babic et al. [64]. On the other hand, applying dielectric mirror of Si/Al_2O_3 and MOCVD regrowth of buried heterostructure, 12mA threshold current was also achieved under room temperature CW condition [65]. Figure 1.3 shows the progress of threshold current and maximum operating temperature of GaInAsP/InP long wavelength surface emitting lasers.

Even though the lasing characteristics have been much improved as described above, the applicability of long wavelength surface emitting lasers is not sufficient for practical use comparable with short wavelength devices. The most effective method to realize practical use level devices is considered to be reduction of threshold current and its current density.

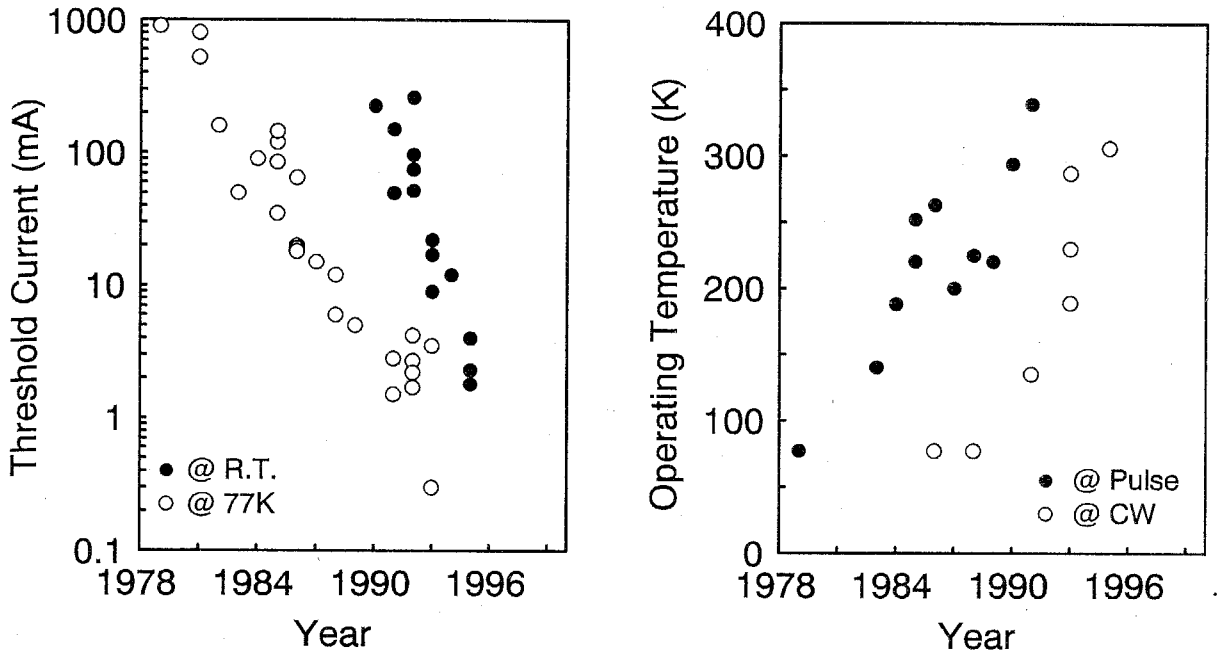

Fig. 1.3 Progress of GaInAsP/InP long wavelength surface emitting lasers. Plotted data are for current injection surface emitting lasers.

1.3 Objectives of This Study

1.3.1 Objectives of This Study

The purpose of this study is, therefore, the realization of long wavelength (especially 1.55μm range) surface emitting lasers and improvement of its lasing performances. In this study, the GaInAsP/InP material is selected and the relatively new epitaxial technique of chemical beam epitaxy (CBE) is used to grow the laser structures.

The purpose of this study is summarized as follows;

1) Design optimization of 1.55μm GaInAsP/InP surface emitting lasers for lowering threshold current.
2) Establishment of CBE technique for applying to surface emitting lasers.
3) Realization of 1.55μm surface emitting lasers and investigation of laser characteristics.

1.3.2 Outline of This Thesis

In chapter 2, GaInAsP/InP surface emitting laser structures are designed for lowering threshold current density by optimizing structure. Then, high reflectivity mirrors are also designed.

In chapter 3, the background of chemical beam epitaxy (CBE) and CBE system is described first. Then, the CBE growth of InP and GaInAsP are discussed. Lastly, the laser material of bulk active layer is characterized for applying to surface emitting lasers.

In chapter 4, the quantum well structures are grown by CBE and evaluated by photoluminescence characterization. Then, the laser characteristics of QW edge emitting lasers are discussed.

In chapter 5, bulk active laser wafers grown by CBE are fabricated to surface emitting lasers. Then, the lasing operations are demonstrated and the lasing characteristics are discussed.

In chapter 6, the lasing characteristics of surface emitting lasers with hybrid mirrors are fabricated. Then, a small active size device was demonstrated. Lastly, the quantum well surface emitting lasers are considered.

In chapter 7, electrical characteristics of p-type multilayer mirrors are considered for applying to surface emitting lasers. Furthermore, the current injection uniformity is discussed. Then, future prospects of high performance long wavelength lasers are described.

Lastly, the conclusions of this thesis are summarized in chapter 8.

References

[1] S. Shimada, "Technological evolution in transmission systems : from millimeter-wave to lightwave," *The Journal of IEICE*, vol. 78, pp. 1098-1106, 1995.

[2] F. P. Kapron, D. B. Keck, and R. D. Mauer, "Radiation losses in glass optical waveguides," *Appl. Phys. Lett.*, vol. 17, p. 423, 1970.

[3] I. Hayashi, M. B. Panish, P. W. Foy, and A. Sumski, "Junction lasers which operate continuously at room temperature," *Appl. Phys. Lett.*, vol. 17, p. 109, 1970.

[4] Zh. I. Alferov, V. M. Andreev, D. Z. Garbuzov, Yu. V. Zhilyaev, E. P. Morozov, E. L. Portnoi, and V. G. Trofim, "Investigation of the laser threshold current and the realization of continuos emission at room temperature," *Sov. Phys. Semicond.*, vol. 4, p. 1573, 1971 (translated from *Fiz. Tekh. Poluprovodn.*, vol. 4, p. 1826, 1970).

[5] Y. Terunuma, T. Hosaka, and T. Miyashita, "An ultimately low-loss single-mode fiber at 1.55μm," *Electron. Lett.*, vol. 1, p. 106, 1979.

[6] M. Horiguchi, "Spectral losses of low-OH-content optical fibers," *Electron. Lett.*, vol. 12, pp. 310-312, 1976.

[7] T. Miya, Y. Terunuma, T. Hosaka, and T. Miyashita, "Ultimate low-loss single-mode fiber at 1.55μm," *Electron. Lett.*, vol. 15, pp. 106-108, 1979.

[8] D. B. Keck, R. D. Maurer, and P. C. Schulta, "On the ultimate lower limit of attenuation in glass optical waveguides," *Appl. Phys. Lett.*, vol. 22, p. 307, 1973.

[9] T. Izawa, N. Shibata, and A. Takeda, "Optical attenuation in pure and doped fused silica in the ir wavelength region," *Appl. Phys. Lett.*, vol. 31, pp. 33-35, 1977.

[10] D. N. Payne and W. A. Gambling, "Zero material dispersion in optical fibers," *Electron. Lett.*, vol. 17, p. 176, 1975.

[11] T. P. Lee, "Recent advantages in long-wavelength semiconductor lasers for optical fiber communication," *Proc. IEEE*, vol. 79, pp. 253-276, 1991.

[12] R. N. Hall, G. E. Fenner, J. D. Kinsley, T. J. Soltys, and R. O. Carson, "Coherent light emission from GaAs junction," *Phys. Rev. Lett.*, vol. 9, p. 366, 1962.

[13] M. I. Nathan, W. P. Dumke, G. Burns, F. H. Dill, Jr., and G. Lasher, "Stimulated emission of radiation from GaAs p-n junctions," *Appl. Phys. Lett.*, vol. 1, p. 62, 1962.

[14] T, M, Quist, R. H. Radiker, R. J. Keyes, W. E. Krag, B. Lax, A. L. McWhorter, and H. J. Zeigler, "Semiconductor maser of GaAs," *Appl. Phys. Lett.*, vol. 1, p. 91, 1962.

[15] H. Kroemer, "A proposed class of heterojunction injection lasers," *Proc. IEEE*, vol. 51, p. 1782, 1963.

[16] R. E. Nahory and M. A. Pollack, "Low-threshold room-temperature double-heterostructure $GaAs_{1-x}Sb_x/Al_yGa_{1-y}As_{1-x}Sb_x$ injection lasers at 1-μm wavelengths," *Appl. Phys. Lett.*, vol. 27, pp. 562-564, 1975.

[17] R. E. Nahory, M. A. Pollack, E. D. Beebe, J. C. DeWinter, and R. W. Dixon, "Continuous operation of 1.0-μm-wavelength $GaAs_{1-x}Sb_x/Al_yGa_{1-y}As_{1-x}Sb_x$ double-heterostructure injection lasers at room temperature," *Appl. Phys. Lett.*, vol. 28, pp. 19-21, 1976.

[18] J. J. Hsieh, J. A. Rossi, and J. P. Donnelly, "Room-temperature cw operation of GaInAsP/InP double-heterostructure diode lasers emitting at 1.1μm," *Appl. Phys. Lett.*, vol. 28, pp. 709-710, 1976.

[19] C. J. Nuese, G. H. Olsen, M. Ettenberg, J. J. Gannon, and T. J. Zamerowski, "cw room-temperature $In_xGa_{1-x}As/In_yGa_{1-y}P$ 1.06-μm lasers," *Appl. Phys. Lett.*, vol. 29, pp. 807-809, 1976.

[20] K. Utaka, K. Kobayashi, and Y. Suematsu, "Lasing characteristics of 1.5-1.6μm GaInAsP/InP integrated twin-guide lasers with first-order distributed Bragg reflectors," *IEEE J. Quantum Electron.*, vol. QE-17, p. 651, 1981.

[21] F. Koyama, S. Arai, Y. Suematsu, and K. Kishino, "Dynamic spectral width of rapidly modulated 1.58μm GaInAsP/InP buried heterostructure distributed-Bragg-reflector integrated-twin-guide lasers," *Electron. Lett.*, vol. 17, pp. 938-940, 1981.

[22] J. P. van der Ziel, R. Dingle, R. C. Miller, W. Wiegmann, and W. A. Nordland Jr., "Laser oscillation from quantum states in very thin GaAs-$Al_{0.2}Ga_{0.8}As$ multilayer structures," *Appl. Phys. Lett.*, vol. 26, pp. 463-465, 1975.

[23] N. Holonyak et al., IEEE J. Quantum Electron., QE-16, p.170, 1980.

[24] W. T. Tsang, "Extremely low threshold (AlGa)As modified multiquantum well heterostructure lasers grown by molecular-beam epitaxy," *Appl. Phys. Lett.*, vol. 39, pp. 786-788, 1981.

[25] A. R. Adams, "Band-structure engineering for low-threshold high-efficiency semiconductor lasers," *Electron. Lett.*, vol. 22, pp. 249-250, 1986.

[26] E. Yablonovitch and E. O. Kane, "Reduction of lasing threshold current density by the lowering of valence band effective mass," *J. Lightwave Technol.*, vol. LT-4, pp. 504-506, 1986.

[27] P. J. A. Thijs and T. van Dongen, "High quantum efficiency, high power, modulation doped GaInAs strained-layer quantum well laser diodes emitting at 1.5μm," *Electron. Lett.*, vol. 25, pp. 1735-1737, 1989.

[28] H. Temkin, N. K. Dutta, T. Tanbun-Ek, R. A. Logan, and A. M. Sergent, "InGaAs/InP quantum well lasers with sub-mA threshold current," *Appl. Phys. Lett.*, vol. 57, pp. 1610-1612, 1990.

[29] C. E. Zah, F. J. Favire, R. Bhat, S. G. Menocal, N. C. Andreadakis, D. M. Hwang, M. Koza, and T. P. Lee, "Submilliampere-threshold 1.5μm strained-layer multiple quantum well lasers," *IEEE Photon. Technol. Lett.*, vol. 2, pp. 852-853, 1990.

[30] P. J. A. Thijs, J. J. M. Binsma, L. F. Tiemeijer, and T. van Dongen, "Submilliamp threshold current (0.62mA at 0°C) and high output power (220mW) 1.5μm tensile strained InGaAs single quantum well lasers," *Electron. Lett.*, vol. 28, pp. 829-830, 1992.

[31] J. S. Osinski, P. Grodzinski, Y. Zou, P. D. Dapkus, Z. Karim, and A. R. Tanguay, Jr., "Low threshold current 1.5μm buried heterostructure lasers using strained quaternary quantum wells," *IEEE Photon. Technol. Lett.*, vol. 4, pp. 1313-1315, 1992.

[32] P. L. Derry, A. Yariv, K. Y. Lau, N. Bar-Chaim, K. Lee, and J. Rosenberg, "Ultralow-threshold graded-index separate-confinement single quantum well buried heterostructure (Al,Ga)As lasers with high reflectivity coatings," *Appl. Phys. Lett.*, vol. 50, pp. 1773-1775, 1987.

[33] K. Iga, "Surface emitting lasers," *Optoelectronics*, vol. 9, pp.167-176, 1994.

[34] K. Iga, "Surface emitting lasers and parallel operating devices - fundamentals and prospects -," *IEICE Trans.*, vol. E75-A, pp. 12-19, 1992.

[35] K. Iga, "Surface emitting semiconductor lasers and surface operating functional devices," *IEICE Jpn.*, vol. J75-C-I, pp. 245-256, 1992.

[36] H. Soda, K. Iga, C. Kitahara, and Y. Suematsu, "GaInAsP/InP surface emitting injection lasers," *Jpn. J. Appl. Phys.*, vol. 18, pp. 2329-2330, 1979.

[37] H. Okuda, H. Soda, K. Moriki, Y. Motegi, and K. Iga, "GaInAsP/InP surface emitting injection laser with buried heterostructures," *Jpn. J. Appl. Phys.*, vol. 20, pp. L563-566, 1981.

[38] Y. Motegi, H. Soda, and K. Iga, "Surface-emitting GaInAsP/InP injection laser with short cavity length," *Electron. Lett.*, vol. 18, pp. 461-463, 1982.

[39] A. Ibaraki, S. Ishikawa, S. Ohkouchi, and K. Iga, "Pulsed oscillation of GaAlAs/GaAs surface emitting laser," *Electron. Lett.*, vol. 20, pp. 420-422, 1984.

[40] A. Chailertvanitkul, K. Iga, and K. Moriki, "GaInAsP/InP surface emitting laser (λ=1.4 μm, 77K) with heteromultilayer Bragg reflector," *Electron. Lett.*, vol. 21, pp. 303-304, 1985.

[41] S. Kinoshita, T. Kobayashi, T. Sakaguchi, T. Odagawa, and K. Iga, "Room temperature pulse operation of GaAs surface emitting laser by using TiO_2/SiO_2 dielectric multilayer reflector," *Trans. IECE of Jpn.*, vol. J69-C, pp. 412-420, 1986.

[42] F. Koyama, S. Kinoshita, and K. Iga, "Room temperature CW operation of GaAs vertical cavity surface emitting laser," *Trans. IEICE*, vol. E71, pp. 1089-1090, 1988.

[43] H. Uenohara, F. Koyama, and K. Iga, "Application of the multiquantum well (MQW) to a surface emitting laser," *Jpn. J. Appl. Phys.*, vol. 28, pp. 740-741, 1989.

[44] J. L. Jewell, A. Scherer, S. L. McCall, Y. H. Lee, S. Walker, J. P. Harbison, and L. T. Florez, "Low-threshold electrically pumped vertical-cavity surface-emitting microlasers," *Electron. Lett.*, vol. 25, pp. 1123-1124, 1989.

[45] R. S. Geels and L. A. Coldren, "Submilliamp threshold vertical-cavity laser diodes," *Appl. Phys. Lett.*, vol. 57, pp. 1605-1607, 1991.

[46] T. Numai, T. Kawakami, T. Yoshikawa, M. Sugimoto, Y. Sugimoto, H. Yokoyama, K. Kasahara, and K. Asakawa, "Record low threshold in microcavity surface-emitting laser," *Jpn. J. Appl. Phys.*, vol. 32, pp. L1533-L1534, 1993.

[47] D. L. Huffaker, D. G. Deppe, K. Kumar, and T. J. Rogers, "Native-oxide defined ring contact for low threshold vertical-cavity lasers," *Appl. Phys. Lett.*, vol. 65, pp. 97-99, 1994.

[48] Y. Hayashi, T. Mukaihara, N. Hatori, N. Ohnoki, A. Matsutani, F. Koyama, and K. Iga, "Record low-threshold index-guided InGaAs/GaAlAs vertical-cavity surface-emitting laser with a native oxide confinement structure," *Electron. Lett.*, vol. 31, pp. 560-562, 1995.

[49] G. M. Yang, M. H. MacDougal, and P. D. Dapkus, "Ultralow threshold VCSELs fabricated by selective oxidation from all epitaxial structure," *CLEO'95*, Baltimore, Maryland, May 21-25, paper CPD4-1, 1995.

[50] J. A. Lott, R. P. Schneider, K. D. Choquette, S. P. Kilcoyne, and J. J. Figiel, "Room temperature continuous wave operation of red vertical cavity surface emitting laser diodes," *Electron. Lett.*, vol. 29, pp. 1693-1694, 1993.

[51] T. Yokogawa, S. Yoshii, A. Tsujiyama, Y. Sasai, and J. Mertz, "Electrically pumped CdZnSe/ZnSe blue-green vertical-cavity surface-emitting lasers," *Jpn. J. Appl. Phys.*, vol. 34, pp. L751-L753, 1995.

[52] D. G. Deppe, S. Shingh, R. D. Dupuis, N. D. Gerrard, G. J. Zydzik, J. P. van der Ziel, C. A. Green, and C. J. Pinzone, "Room-temperature photopumped operation of an InGaAs-InP vertical cavity surface-emitting laser," *Appl. Phys. Lett.*, vol. 56, pp. 2172-2174, 1990.

[53] Y. Imajo, A. Kasukawa, S. Kashiwa, and H. Okamoto, "GaInAsP/InP semiconductor multilayer reflector grown by metalorganic chemical vapor deposition and its application to surface emitting laser diode," *Jpn. J. Appl. Phys.*, vol. 29, pp. L1130-L1132, 1990.

[54] M. Oshikiri, F. Koyama, and K. Iga, "Flat surface circular buried heterostructure surface emitting laser with highly reflective Si/SiO_2 mirrors," *Electron. Lett.*, vol. 27, pp. 2038-2039, 1991.

[55] H. Wada, D. I. Babic, D. L. Crawford, T. E. Reynolds, J. J. Dudley, J. E. Bowers, E. L. Hu, J. L. Merz, B. I. Miller, U. Koren, and M. G. Young, "Low-threshold, high-temperature pulsed operation of InGaAsP/InP vertical cavity surface emitting lasers," *IEEE Photon. Technol. Lett.*, vol. 3, pp. 977-979, 1991.

[56] S. Kubota, F. Koyama, and K. Iga, "Low-threshold GaInAsP/InP transmission-type surface emitting laser," *Appl. Phys. Lett.*, vol. 31, pp. L175-L176, 1992.

[57] T. Tadokoro, H. Okamoto, Y. Kohama, T. Kawakami, and T. Kurokawa, "Room temperature pulsed operation of 1.5μm GaInAsP/InP vertical-cavity surface-emitting laser," *IEEE Photon. Technol. Lett.*, vol. 4, pp. 409-411, 1992.

[58] J. J. Dudley, M. Ishikawa, D. I. Babic, B. I. Miller, R. Mirin, W. B. Jiang, J. E. Bowers, and E. L. Hu, "144°C operation of 1.3μm InGaAsP vertical cavity lasers on GaAs substrate," *Appl. Phys. Lett.*, vol. 61, pp. 3095-3097, 1992.

[59] T. Baba, Y. Yogo, K. Suzuki, F. Koyama, and K. Iga, "Near room temperature continuous wave lasing characteristics of GaInAsP/InP surface emitting laser," *Electron. Lett.*, vol. 29, pp. 913-914, 1993.

[60] J. J. Dudley, D. I. Babic, R. Mirin, L. Yang, B. I. Miller, R. J. Ram, T. Reynolds, E. L. Hu, and J. E. Bowers, "Low threshold, wafer fused long wavelength vertical cavity lasers," *Appl. Phys. Lett.*, vol. 64, pp. 1463-1465, 1994.

[61] K. Uomi, S. J. B. Yoo, A. Scherer, R. Bhat, N. C. Andreadakis, C. E. Zah, M. A. Koza, and T. P. Lee, "Low threshold, room temperature pulsed operation of 1.5μm vertical-cavity surface emitting lasers with an optimized multi-quantum well active layer," *IEEE Photon. Technol. Lett.*, vol. 6, pp. 317-319, 1994.

[62] C. H. Lin, C. L. Chua, Z. H. Zhu, F. E. Ejeckam, T. C. Wu, and Y. H. Lo, "Photopumped long wavelength vertical-cavity surface-emitting lasers using strain-compensated multiple quantum wells," *Appl. Phys. Lett.*, vol. 64, pp. 3395-3397, 1994.

[63] D. I. Babic, J. J. Dudley, K. Streubel, R. P. Mirin, J. E. Bowers, and E. L. Hu, "Double-fused 1.52μm vertical-cavity lasers," *Appl. Phys. Lett.*, vol. 66, pp. 1030-1032, 1995.

[64] D. I. Babic, K. Streubel, R. P. Mirin, N. M. Margalit, J. E. Bowers, E. L. Hu, D. E. Mars, L. Yang, and K. Carey, "Room-temperature continuous-wave operation of 1.54-μm vertical-cavity lasers," *IEEE Photon. Technol. Lett.*, vol. 7, pp. 1225-1227, 1995.

[65] S. Uchiyama, and S. Kashiwa, "GaInAsP/InP SBH surface emitting laser with Si/Al_2O_3 mirror," *Electron. Lett.*, vol. 31, pp. 1449-1451, 1995.

Chapter 2

Design of Low Threshold GaInAsP/InP Surface Emitting Lasers

In this chapter, it is considered how to reduce the threshold current density of 1.55μm GaInAsP surface emitting lasers. To realize high performance lasers, the optimum design of active layer structure, effect of reducing optical absorption in cladding layer and design of high reflectivity mirrors are discussed.

2.1 Threshold Condition of Surface Emitting Lasers

To design surface emitting laser structures, general expressions of lasing threshold conditions are represented first. The basic structure of surface emitting lasers and conventional edge emitting lasers is composed of two mirrors and an active layer as shown in Fig. 2.1 (a) and (b). The expression of threshold gain for surface emitting lasers is shown as follows;

$$g_{th} = \alpha_{ac} + \left(\frac{1}{\xi} - 1\right) \cdot \alpha_{ex} + \frac{1}{\xi \cdot L} \ln\left(\frac{1}{R}\right) \qquad (2.1)$$

where g_{th} is threshold gain. L is cavity length and R is mirror reflectivity. α_{ac} and α_{ex} is absorption coefficient in active layer and cladding layer, respectively. As the confinement factor ξ is determined as the ratio of optical power in the active layer and overall optical power, the confinement factor ξ is written as follows;

$$\xi = \xi_t \cdot \xi_l \qquad (2.2)$$

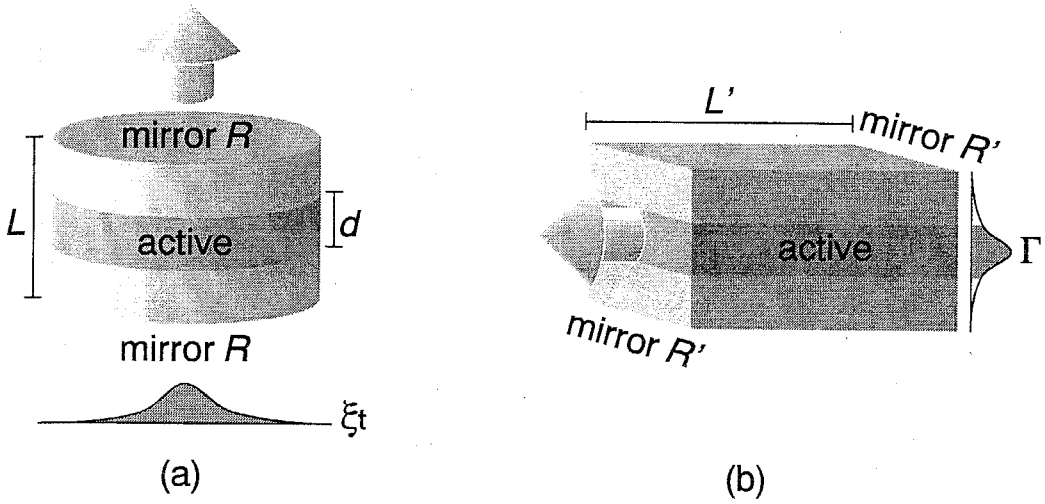

Fig. 2.1 Schematic structure of surface emitting laser (a) and edge emitting laser (b) for considering threshold conditions.

where ξ_t and ξ_l represents the confinement factor for the transverse direction and the longitudinal direction, respectively. ξ_t is calculated by the transverse modal field of optical waveguide and the diffraction loss, and hence ξ_t is considered to be almost unity if the device size is much larger than the lasing wavelength. On the other hand, the longitudinal optical field is optical standing wave and ξ_l is represented as;

$$\xi_l = \frac{d}{L}\left[1+\frac{\sin\left(\frac{2\pi nd}{\lambda}\right)}{\frac{2\pi nd}{\lambda}}\right] \qquad (2.3)$$

where λ is lasing wavelength and n is refractive index in the active layer. Figure 2.2 shows the matching factor represented as later term of Eq. (2.3). The order of active layer thickness is usually about or less than lasing wavelength, and hence ξ_l is enhanced if the active layer is placed at the peak of the optical standing wave in the cavity [1]. The matching factor is increased and approaches to 2 for very thin active layer ($d<0.1\mu m$). For the case of thick active layer, the confinement factor ξ is represented approximately as $\xi = d/L$.

The threshold condition of edge emitting lasers is also represented as follow;

$$g_{th} = \alpha_{ac} + \left(\frac{1}{\Gamma}-1\right)\cdot\alpha_{ex} + \frac{1}{\Gamma\cdot L'}\ln\left(\frac{1}{R'}\right) \qquad (2.4)$$

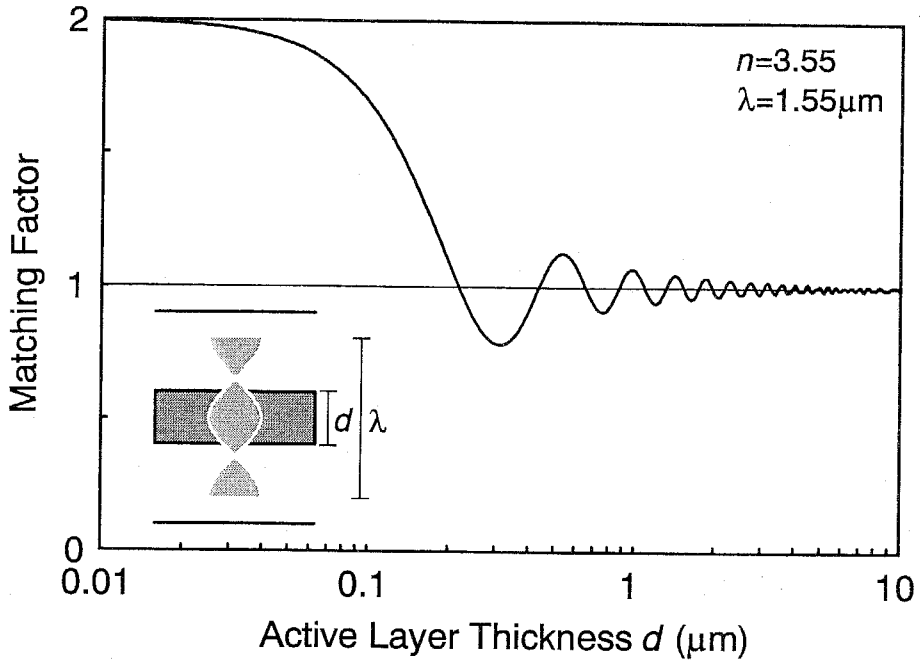

Fig. 2.2 Matching factor vs. active layer thickness. The wavelength is assumed 1.55μm and index is assumed 3.55 which corresponds to index of GaInAsP (λg=1.55μm) for 1.55μm wavelength light.

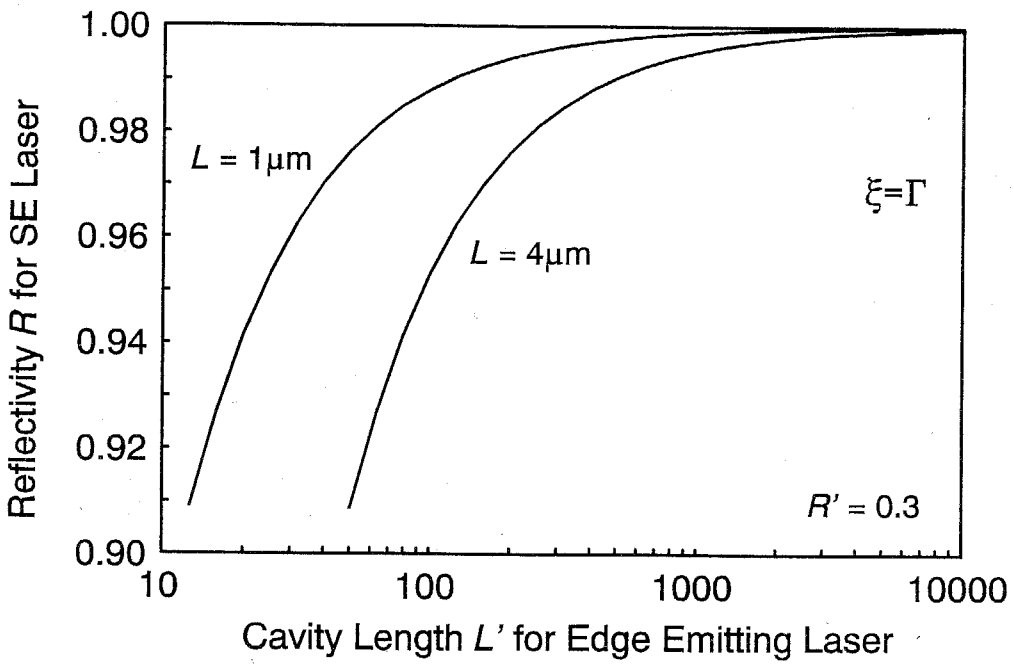

Fig. 2.3 Relation between surface emitting laser reflectivity and edge emitting laser cavity length for the same threshold gain. The confinement factor is assumed to be the same.

where Γ is the optical confinement factor which is calculated by modal field of the optical waveguide. The difference between Eq. (2.1) and (2.4) is only notation of confinement factor, cavity length and reflectivity. If the confinement factor is assumed to be the same for both structures (which is possible condition), the surface emitting laser reflectivity R is represented as $R = R'^{(L/L')}$ for the same threshold gain condition. Assuming the reflectivity R' of 0.3 for edge emitting lasers and the cavity length L of 1~4μm for surface emitting lasers, the reflectivity R of surface emitting laser is calculated as shown in Fig. 2.3 as a function of edge emitting laser cavity length L'. Thus very high reflectivity (>90%) is usually required for surface emitting lasers due to short gain length.

Next, the relations between gain and current density are represented. The gain in active layer is increased by current injection. Assuming the constant differential gain A_0, the relation between gain g and carrier density N is represented as;

$$g = A_0 \cdot (N - N_{tr}) = A_0 \cdot N - \alpha_{in} \qquad (2.5)$$

where N_{tr} is transparency carrier density and $\alpha_{in} = A_0 \cdot N_{tr}$ is residual absorption loss. The threshold carrier density is calculated by Eq. (2.1) and (2.5). The threshold current density J_{th} is related with threshold carrier density N_{th} as follows;

$$J_{th} = ed \cdot \frac{N_{th}}{\tau_s} \approx ed\left(B \cdot N_{th}^2 + C \cdot N_{th}^3\right) \qquad (2.6)$$

where e is electron charge and carrier lifetime τ_s is approximated as;

$$\frac{1}{\tau_s} = B_r \cdot N + \left(A + B_{nr} \cdot N + C \cdot N^2\right) \approx B_{eff} \cdot N \qquad (2.7)$$

where A, B and C are recombination coefficients. A is recombination coefficient disproportion to the carrier density and possible to negligible. B_r is called radiative recombination coefficient and C is related to Auger nonradiative recombination [2, 3]. $B = B_r + B_{nr}$ is used in Eq. (2.6). B_{eff} is effective recombination coefficient, however it does not approximate if Auger recombination effect is large.

From the above expressions, it is considered how to reduce the threshold current density. A_0 and N_{tr} in Eq. (2.5) is varied by active materials such as bulk, quantum well (QW) and strained materials. To reduce the threshold gain of Eq. (2.1), reduction of the absorption loss (α_{ac} and α_{ex}) and increase of the reflectivity R is effective. In following sections, I design the laser structures concerning these points to realize low threshold surface emitting lasers.

2.2 Optimization of Surface Emitting Laser Structure

2.2.1 Active Layer Materials for Surface Emitting Lasers

As mentioned above section, the gain characteristics are one of the most important factor for lowering threshold current density. In this section, the active layer material for surface emitting laser is considered first.

The bulk material with double heterostructures has been used as an active layer since the first continuous wave (CW) operation by Panish and Hayashi of AT&T bell laboratory in 1970 [4]. The bulk active layer is usually thick (more than several 100Å) single crystal as shown in Fig. 2.4. The material properties of bulk crystals have been enough studied and established, and therefore bulk material is one of the useful active layers.

Superlattice structures were suggested to realize new material properties by Esaki and Tsu of IBM Thomas J. Watson Laboratory in 1970 [5]. This idea has been realized as the quantum well (QW) structure in semiconductor lasers [6]. The carriers are confined in the potential well which is formed by a ultra-thin layer sandwiched by wide bandgap materials as shown in Fig. 2.4. As the result of carrier confinement effect, the density of states is changed to step-like, and furthermore the dipole moment parallel to the well becomes large [7]. Such change of density of states and dipole moment increases A_0 in Eq. (2.6) and therefore the threshold current density of semiconductor lasers is expected to be reduced [8, 9]. The other advantages of QWs are less temperature dependence [10], narrow gain spectrum, high modulation response, emission wavelength control by well width, etc. [11, 12].

It has been known that material properties are also changed by stress in the crystal. As

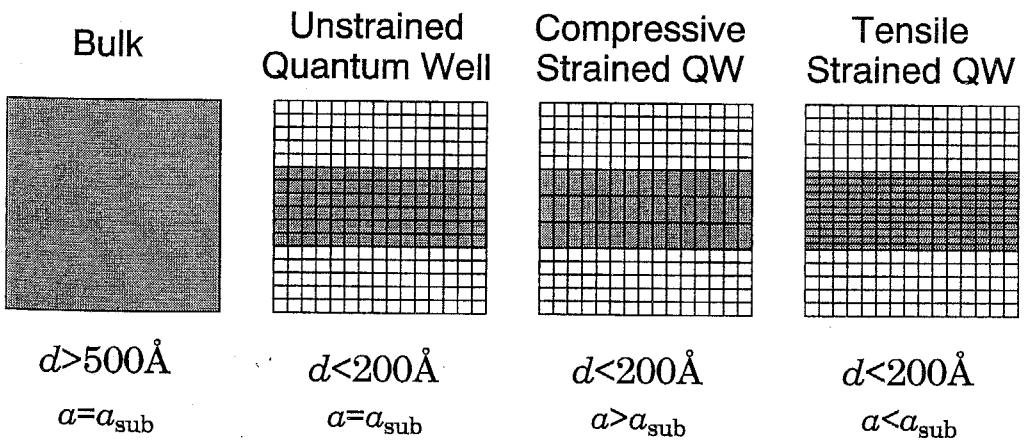

Fig. 2.4 Active materials are shown. d is thickness of active layer and a is lattice constant of free standing active layer material. a_{sub} is lattice constant of substrate material.

the result of stress, the band structure is changed [13] and the lasing characteristic is also modified [14, 15, 16]. We can give stress in the crystal by growing the lattice mismatch material. Though the relatively thick lattice mismatched material has the crystal defects [17, 18], sufficiently thin films such as QWs can be grown without defect and the stress is introduced successively in the crystals. Such QW structures are called strained QW. The advantages of strained materials on the optical device are suggested by Adams of University of Surrey, UK, and Yablonovitch and Kane of Bell Communications Research in 1986 [19, 20]. The strained materials are classified to two types by stress direction, compressive strain and tensile strain. As the result of band structure change, the laser threshold current is expected to be reduced, and Auger recombination and inter-valence band absorption (IVBA) is also expected to be effectively eliminated by band structure change. In short, coefficients of A_0, N_{tr} α_{ac}, and C are expected to be improved by strained QWs.

As the other high potential active materials, quantum wire and quantum box structures were suggested and have been studied [8], however these structures have disadvantages of difficulty on fabrication in this time.

2.2.2 Design of Bulk Active Layer Surface Emitting Lasers

In this section, the threshold current density of surface emitting lasers with bulk active layer is considered. The QW structure is known as superior gain characteristic material compared with bulk active layer. However, the active layer thickness of QWs is not so thick compared with bulk active layer even if we apply the multiple-QW (MQW) structures. Hence the bulk active layer structure is also candidacy of active layers for the surface emitting laser.

First, the gain characteristic of bulk material is considered. To calculate the linear gain coefficient against injection carrier density, the density matrix theory taking into account the intra-band relaxation is most effective [21]. As the target wavelength is 1.55μm, the active layer is assumed to be GaInAsP (λg=1.55μm) lattice matched to InP. From the result of the gain calculation, the peak gain of the bulk active layer is increased linearly against injected carrier as described in Eq. (2.5), and parameters are estimated to be $A_0 = 2.5 \times 10^{-16} cm^2$ and $N_{tr} = 1.2 \times 10^{18} cm^{-3}$ $\left(\alpha_{in} = 300 cm^{-1}\right)$ at room temperature [22].

The injected carrier density is related with the injected current density as shown in Eq. (2.6). Figure 2.5 shows the relation between gain and injected current density for the active layer thickness of 0.2μm and 1.0μm. The recombination coefficient, B and C, used for calculations are summarized in table 2.1 with the other parameter for calculating the threshold current density of surface emitting lasers. As the gain is increased with high slope for the thin active layer, the thin active layer structure looks like good material. However, the optical confinement factor ξ is reduced for thin active layer structure, and hence there are optimum active layer thickness for the lowest threshold current. We can see large Auger recombination

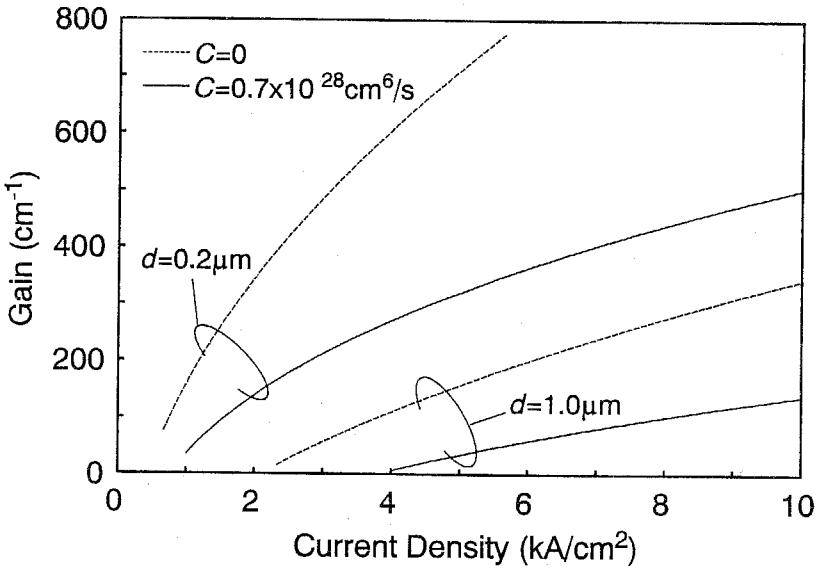

Fig. 2.5 Gain vs. current density characteristics for bulk active layer. The Auger coefficient C is assumed to be 0 and 0.7×10^{-28}cm^6/s.

effect for thin active layer structure because the injected carrier density is larger than that for thick active layer structure under the same injected current.

Next, the threshold current density of surface emitting laser is considered for bulk active layer. The device model for calculation is shown in Fig. 2.6. The threshold current density of bulk active layer is calculated by using Eq. (2.1), (2.5), (2.6). The parameters used in the

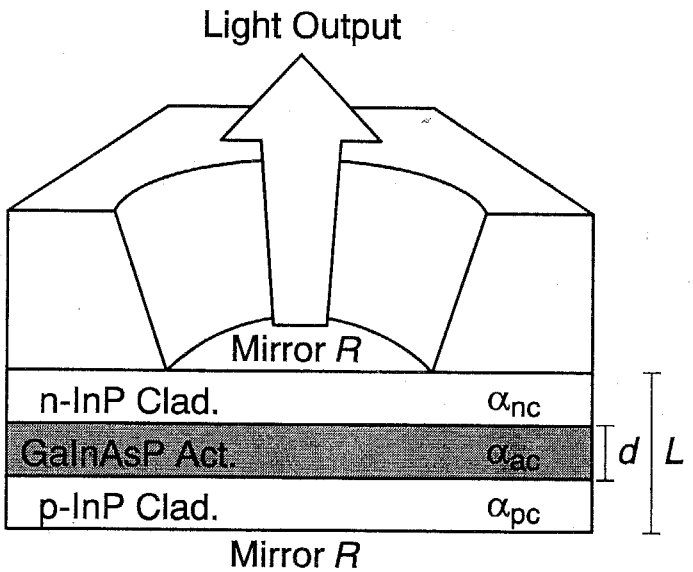

Fig. 2.6 Device model of a GaInAsP/InP surface emitting laser for calculation of threshold current density.

calculations are summarized in table 2.1. Figure 2.7 shows the result of threshold current density against active layer thickness at room temperature. The cavity length L is fixed to 4μm, and hence the cladding layer thickness is changed as active layer thickness. The threshold current density is waved as changing the active layer thickness due to matching factor effect. Considering the current injection condition of conventional semiconductor lasers and light emitting diode, the lasing operation is expected by the reflectivity of over 98% at room temperature. Such high reflectivity is possible by multilayer reflectors described in below section. The threshold current density of bulk active layer is expected to be less than 20kA/cm^2 for 99% reflectivity with 1μm active layer thickness and 5kA/cm^2 is expected for almost 100% reflectivity. However, the expected threshold current density is higher than that of conventional edge emitting lasers with bulk active layer, for example, 1-5kA/cm^2. To realize high performance surface emitting lasers, the threshold current density should be reduced more.

In the above calculations, the cladding layer thickness and absorption coefficients are fixed. Therefore further improvement is expected by optimizing these structure configurations. I considered the reduction of absorption coefficient in cladding layer.

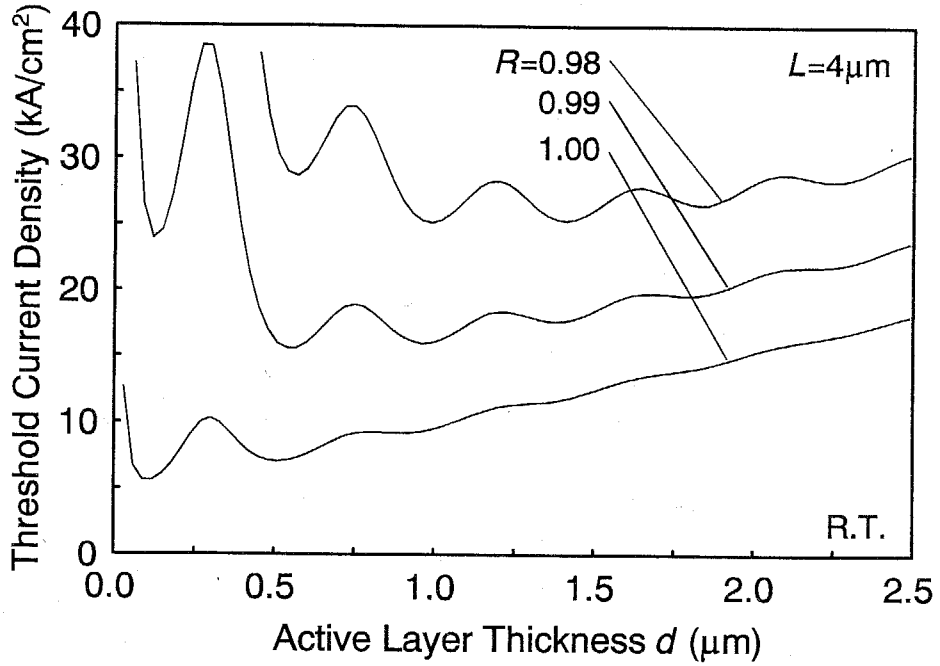

Fig. 2.7 Threshold current density against GaInAsP (λg=1.55μm) bulk active layer thickness for various reflectivities.

Table 2.1 Parameters used in the threshold current density calculation for bulk active layer surface emitting lasers. Reference : a) [22], b) [23].

A_0 a)	2.5×10^{-16} cm^2	α_{ac} b)	60 cm^{-1}
N_{tr} a)	1.2×10^{18} cm^{-3}	α_{nc} b)	10 cm^{-1}
B b)	1.0×10^{-10} cm^3/s	α_{pc} b)	30 cm^{-1}
C b)	0.7×10^{-28} cm^6/s		

2.2.3 Effect of Optical Absorption Reduction in Cladding Layers

The optical absorption in semiconductor [24] is one of problems for lowering threshold. Therefore, the absorption in cladding layer is considered with respect to the threshold current.

For the n-type material, the free carrier (plasma) absorption is important and the absorption coefficient α_{fc} is proportional to the carrier density N as follows;

$$\alpha_{fc} = \frac{e^2\lambda^2}{8\pi^2 ncm\tau} \cdot N \qquad (2.8)$$

where e is electron charge, n is reflective index, m is effective mass and τ is the relaxation time related with diffusion coefficient. Though α_{fc} is less than $10cm^{-1}$ for usual doping concentration, the minimum absorption coefficient is considered to be $10cm^{-1}$ for calculations because the reduction of dominant absorption process appears the other absorption process.

On the other hand, p-type material has large absorption coefficient comparable with n-type material. The valence band of most semiconductors is formed by heavy-hole, light-hole and spin-orbit-sprinting band. In p-type semiconductor, the transition between spin-orbit-spiriting and heavy-hole band is occurred because the valence band is populated with holes. The transition for lasing wavelength is allowed for relatively large wavenumber carrier, and therefore the absorption is increased as increasing p-type doping. Such intervalence band absorption (IVBA) is large for long wavelength because the transition is possible to occur at near center of the Brillouin zone due to small light energy. The absorption coefficient α in p-type material is approximated by next equation;

$$\alpha = \alpha_{\text{int}} + D^{(p)} \cdot p \qquad (2.9)$$

where α_{int} is an intrinsic absorption in the order of less than $10cm^{-1}$, $D^{(p)}$ is the absorption cross section associated with hole transitions and p is hole concentration. The absorption

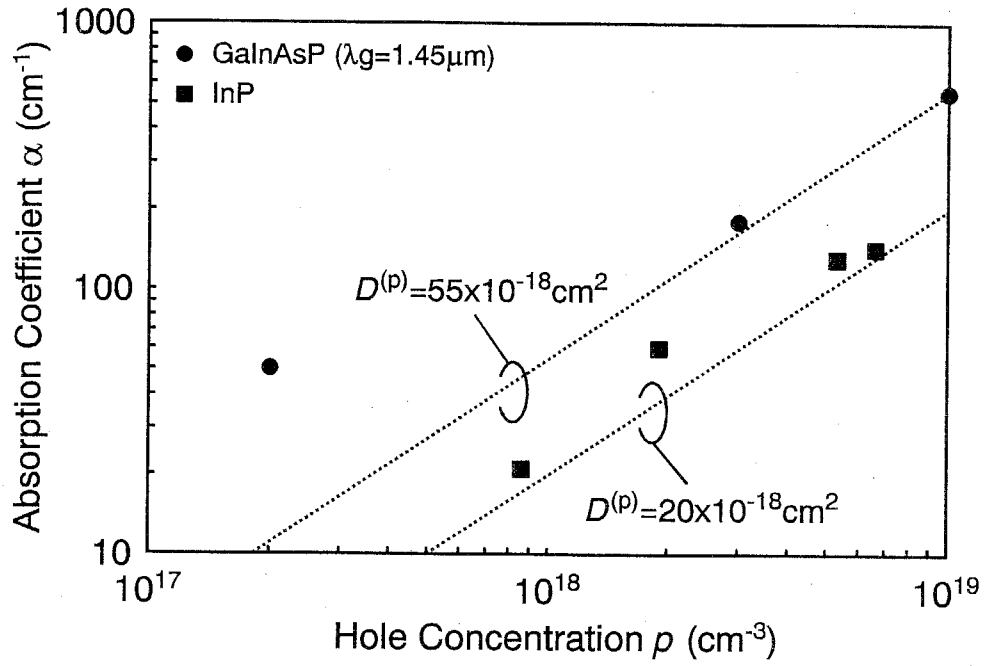

Fig. 2.8 Absorption coefficient of p-type GaInAsP and InP for various hole concentrations. The light wavelength is 1.55μm. The absorption coefficient of InP is result of Ref. 25.

characteristics for p-doped InP have been studied [25]. However, that for GaInAsP which is used as contact layer and semiconductor multilayer for surface emitting lasers is not sufficiently cleared.

In this study, the absorption coefficient of GaInAsP (λg=1.45μm, λg=1.31μm) material is measured to design the surface emitting lasers. The sample grown by CBE had single GaInAsP layer with p-type Be-doping. Figure 2.8 shows measured absorption coefficients of GaInAsP against doping concentrations for 1.55μm wavelength light with the results for Zn-doped InP measured by Casey et al. of Duke University [25]. $D^{(p)}$ is estimated as $20\times10^{-18}cm^2$ and $55\times10^{-18}cm^2$ for GaInAsP of λg=1.31μm and λg=1.45μm, respectively. That for InP was reported as $20\times10^{-18}cm^2$. As the activation energy of IVBA is related with sprit-off energy, the large absorption coefficient for GaInAsP (λg=1.45μm) is considered due to large sprit-energy compared with that of InP. The absorption cross sections are summarized in table 2.2 with the theoretically calculated values for the 1.55μm light.

Next, the effect of inter-valence band absorption (IVBA) loss in the p-cladding layer is examined with respect to the threshold current density of long wavelength surface emitting lasers. As discussed in section 2.1, the threshold gain is reduced by lowering the absorption loss. Assuming the absorption coefficient of p-type material as Eq. (2.9) with the experimental absorption cross-sections in table 2.2 and $\alpha_{int}=0$, the threshold current density of bulk active

Table 2.2 Summary of absorption cross-section $D(p)$ of p-type material for 1.55μm wavelength light. Split-off energy is shown as a reference.

	InP	GaInAsP
Experimental	20 Ref [25, 26]	20 (λg=1.3μm) This study 55 (λg=1.45μm) This study
Theory	48 Ref [25] 5 Ref [26]	50 ($Ga_{0.47}In_{0.53}As$) Ref [26]
Split off energy [27]	0.11 (eV)	0.254 (eV) (λg=1.3μm) 0.314 (eV) (λg=1.55μm) 0.35 (eV) ($Ga_{0.47}In_{0.53}As$)

layer is calculated again.

Figure 2.9 shows the relation between threshold current density of bulk active layer and mirror reflectivity for various doping concentrations in the p-cladding layer. The active layer thickness is optimized for each reflectivity. The absorption in active layer is also assumed to be proportional to the injected carrier density because IVBA is also dominant absorption in

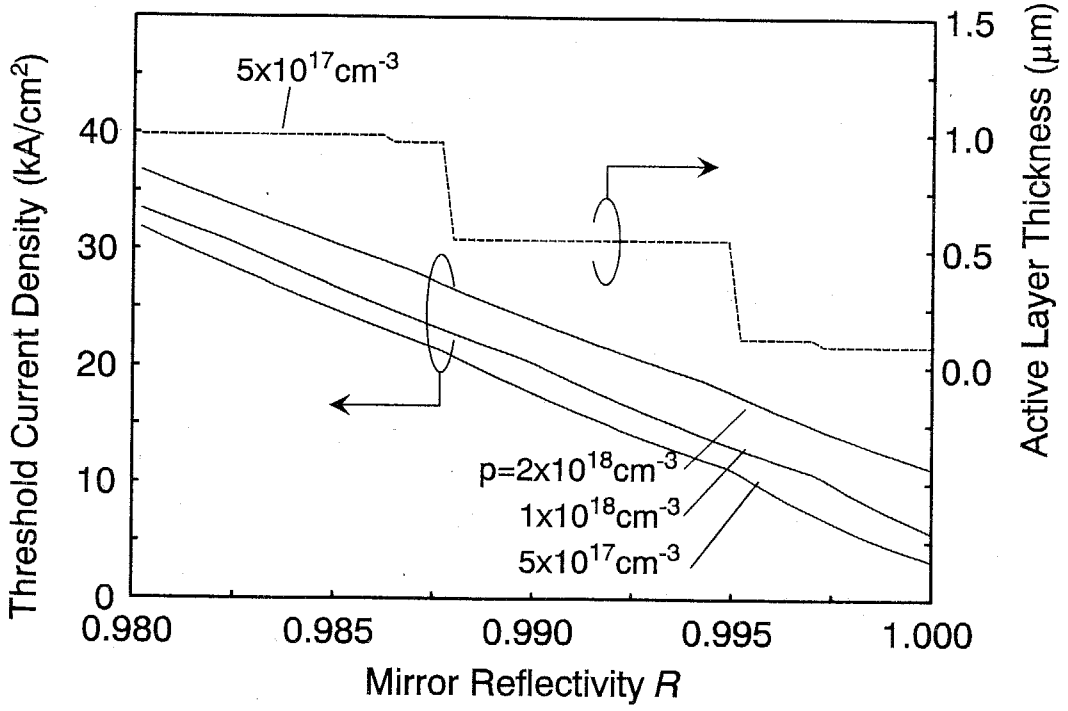

Fig. 2.9 Minimum threshold current density and optimized active layer thickness against mirror reflectivities for various p-doping in cladding layer. Step-like layer thickness is due to matching factor.

the active layer. The absorption cross-section of active layer is assumed to be $55\times10^{-18}cm^{-1}$ which is from the value of GaInAsP (λg=1.45μm). From the result of calculation, the doping concentration in cladding layer affects to the threshold current density strongly. Especially for high reflectivity region, the threshold current reduction ratio is large due to small mirror loss.

As the light absorption is represented as multiple of absorption coefficient and layer thickness, the cladding layer thickness also affects to the threshold current. The threshold current density against reflectivity for various cladding layer thicknesses is shown in Fig. 2.10. In this calculation, both sides of cladding layer thickness are assumed to be the same and the doping concentration of p-cladding layer is assumed to be $1\times10^{18}cm^{-3}$. The cladding layer thickness also effect to the threshold current density strongly. As the result, the threshold current density of less than $5kA/cm^2$ is expected by lowering doping concentration and reducing cladding layer thickness even for bulk active layer surface emitting lasers.

From the result, it is important to reduce the doping concentration and thickness of p-cladding layer for lowering threshold current. However, reducing of doping concentration appears the intrinsic absorption α_{int}, and hence there may be the minimum doping concentration. Furthermore, such low doping and thin cladding layer are not good for current injection because the low doping material has large electrical resistance and the thin layer thickness is also increase the electrical resistance for current flow as discussed in chapter 7.

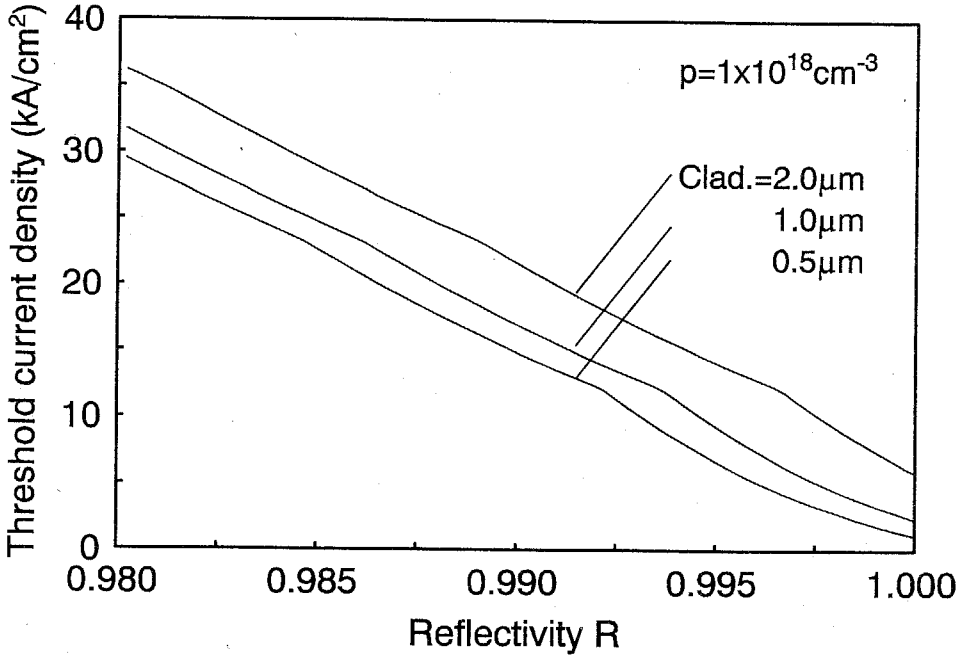

Fig. 2.10 Threshold current density against mirror reflectivity for various cladding thicknesses. The doping concentration in p-cladding layer is assumed at $1\times10^{18}cm^{-3}$.

2.2.4 Threshold Current of Quantum Well Surface Emitting Lasers

Next, the threshold current density of quantum well surface emitting lasers is discussed. First, the relation between quantum well structure and electric field of surface emitting lasers are considered. As the theoretical result for edge emitting lasers, it is known that the unstrained QWs and compressive strained QWs have large TE gain which corresponds to parallel electric field to the surface [7, 28, 29]. On the other hand, tensile strained QWs have large TM gain which corresponds to perpendicular electric field to the surface. Considering the electric field of surface emitting lasers, the electric field should be parallel to the surface and hence the unstrained QW and compressively strained QW is suited for the vertical cavity surface emitting lasers. The relations are shown in Fig. 2.11. Due to such reason, the unstrained QWs and compressively strained QWs are considered in this study.

The gain characteristics for unstrained and strained QWs are also calculated by density matrix theory as mentioned previously. As the simple treatment of quantum wells, the differences from bulk active layers are the step like density of states and increase of matrix momentum as mentioned previous section [7]. However, it should be analyzed considering band mixing effect in the valence band in detail and the band structures are analyzed by Luttinger-Kohn (L-K) Hamiltonian [30]. Lin and Lo calculated the gain characteristics for GaInAs compressively strained QWs by L-K Hamiltonian and lead the empirical formulas of the gain characteristics [31]. However, it is slightly difficult to lead for all composition of GaInAsP which is useful material because the strain and well thickness is selected independently (see chapter 4). It is also difficult to treat the carrier leakage from well to barrier which effect to the effective gain characteristics. From above reasons, I considered the

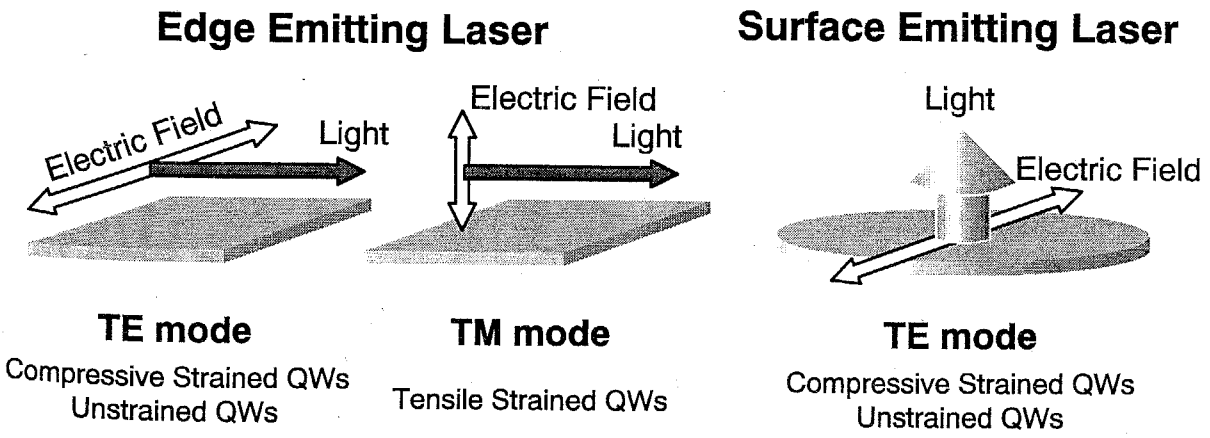

Fig. 2.11 Electric field of edge emitting lasers and surface emitting lasers. The electric field of surface emitting lasers is parallel to the surface which is the same as TE mode of edge emitting lasers.

gain characteristics of quantum wells from the experimental results.

I grow the some types of edge emitting laser wafers with unstrained and strained QW as described in chapter 4. Here I show only the results of the gain characteristics to design the surface emitting lasers. Figure 2.12 shows the experimental gain-current density characteristics of unstrained GaInAs QW, strained GaInAs QW and strained GaInAsP QW for a single QW structure. The well thickness of unstrained and 1% compressively strained GaInAs QW is 35Å and 70Å, respectively. The thickness of GaInAsP well is 65Å and the strain is about 1% compressively. The barrier is GaInAsP (λg=1.2μm) for each structure. Detail structures are shown in chapter 4. The strained GaInAs QW shows five times large gain compared with unstrained GaInAs QW. It is also larger than the gain of strained GaInAsP QW. However, considering the well thickness which is related with confinement factor, the GaInAsP well is superior to the strained GaInAs well because the gain ratio for the same current density is less than 2 though the thickness ratio is about 2.

The threshold current density of QW surface emitting lasers are calculated as well as bulk active layer structures. The cavity lengths are fixed to 4μm and the used absorption coefficients are shown in table 2.1. The well numbers are corresponded to the bulk active layer thickness. The difference from the bulk active layers is that MQW structure is possible to separate the gain region. As shown in previous section, the matching factor effects to the threshold current density strongly if the thickness is enough thin. The idea of periodic gain

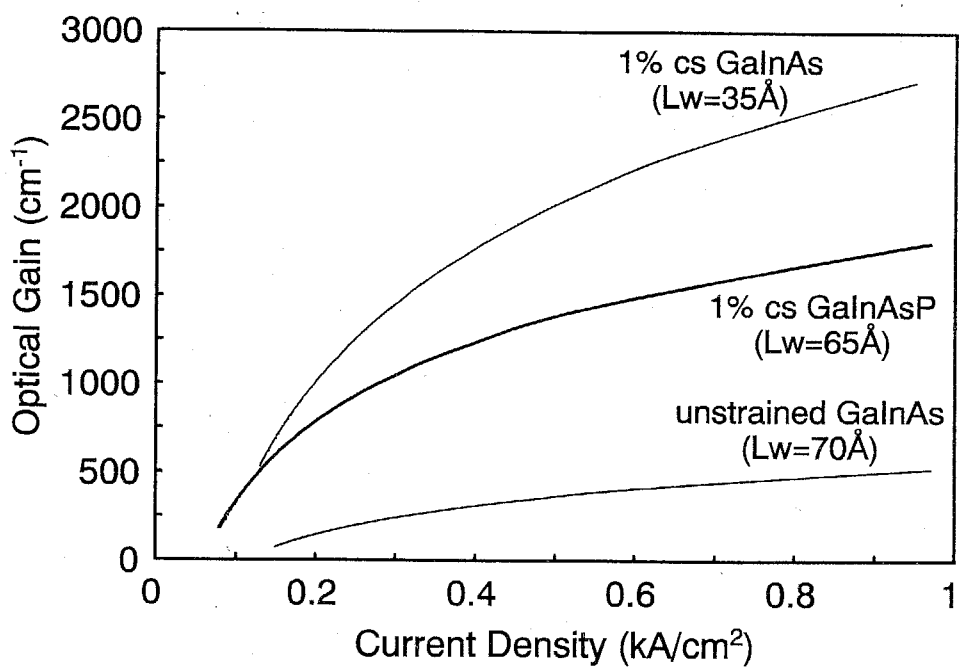

Fig. 2.12 Gain vs. current density for strained/unstrained QWs. The results are calculated from experimental results shown in chapter 5.

structure or matched gain structure is more effective if the active region is separated [1]. In this study, single gain and separate gain structure are considered. As the separate gain structure, two-region structure is considered because of difficulty of uniform carrier injection for multi-gain region structures. The schematic structures are shown in Fig. 2.13.

The calculated threshold current density for GaInAsP 1% compressively strained QWs is shown in Fig. 2.14 using experimentally estimated gain characteristics. The parameters except gain characteristics are the same as the bulk active layer surface emitting lasers. From the result, the separate gain structure is superior. The threshold current density for GaInAsP QWs is possible to reduce less than 1kA/cm^2 at 99.9% reflectivity with 4-12 wells and less than 2kA/cm^2 at 99.5% reflectivity with 8-12 wells. The threshold current density for strained GaInAsP QWs is expected to be about 1/5 of that of bulk active layer.

Figure 2.15 shows the relation between mirror reflectivity versus threshold current density for GaInAsP strained QW surface emitting lasers with separate gain structure. One is 2μm cavity length with doping concentration of p=5×10^{17}cm^{-3} and another structure is 4μm cavity length with p=2×10^{18}cm^{-3}. The threshold current density of about 400A/cm^2 is expected by lowering absorption loss in cladding layer with mirror reflectivity of 99.9%.

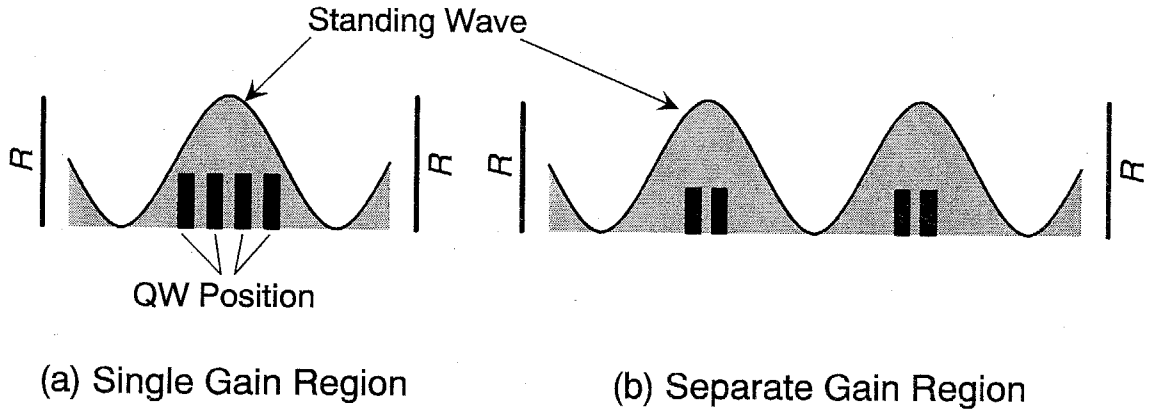

Fig. 2.13 Periodic gain structure with single (a) and separate (b) gain region. In this figure, total well number is assumed to be 4.

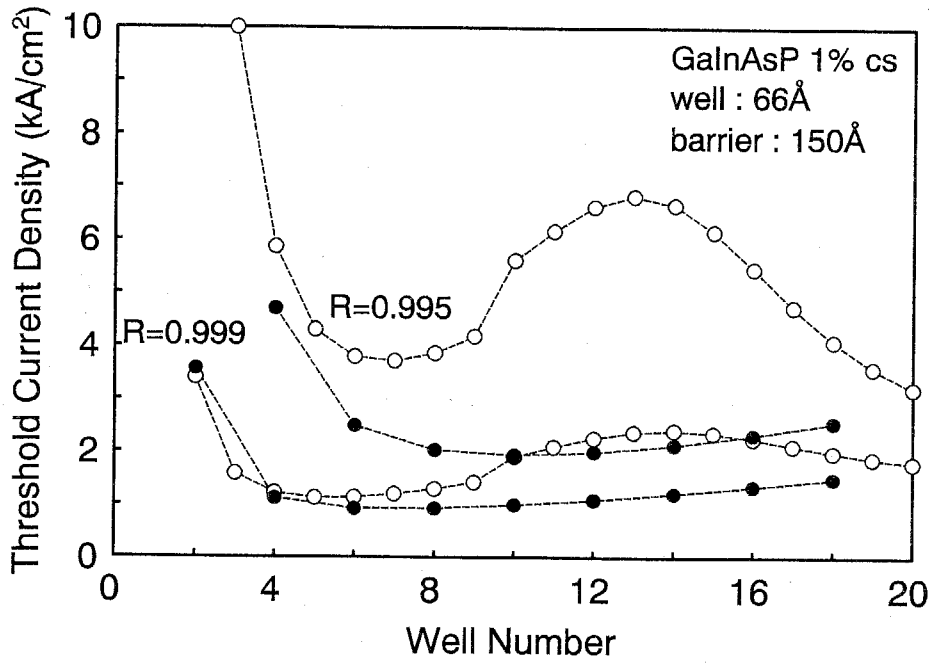

Fig. 2.14 Threshold calculation of GaInAsP strained QW surface emitting laser using experimental gain characteristics. The cavity length is fixed to 4μm and Auger recombination coefficient is neglected.

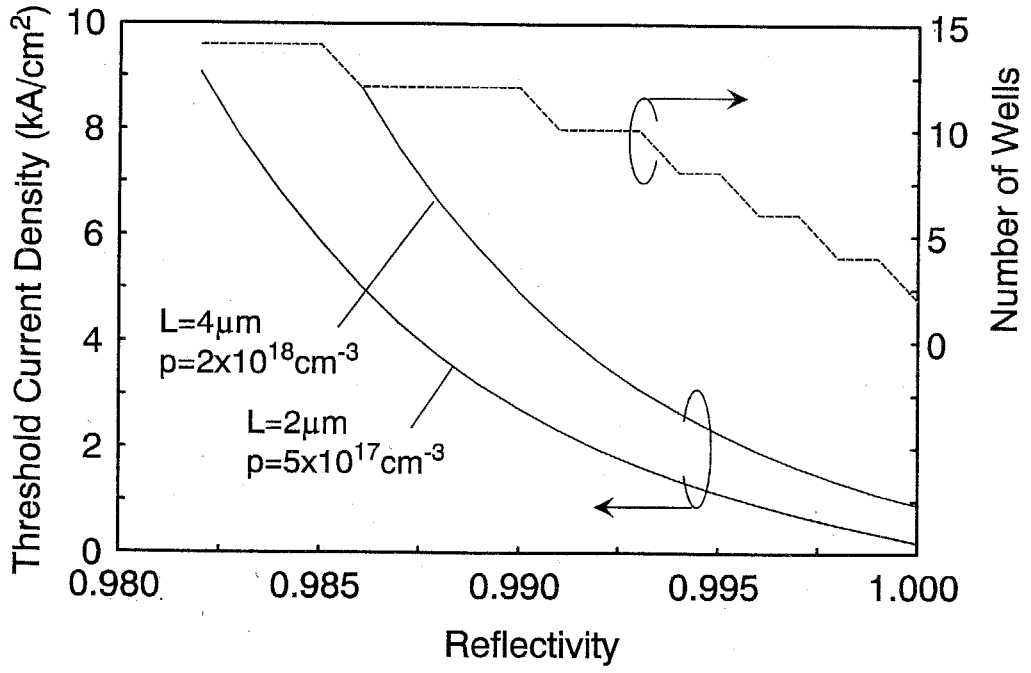

Fig. 2.15 Threshold current density and optimized number of wells against reflectivity for different cladding thickness and doping.

Finally, the relation between threshold current and threshold current density is shown. the threshold current is calculated by multiple of threshold current density and active region area. Fig. 2.16 shows the threshold current versus active region diameter. Threshold current of less than 10mA is possible even if the threshold current density is as large as 10kA/cm^2 which is the value for bulk active layer with 99.5% reflectivity. Furthermore, threshold current of less than 100μA may be realized with strained QW surface emitting laser with active region diameter of few μm. Such low threshold current is as low as the record threshold current of short wavelength surface emitting lasers.

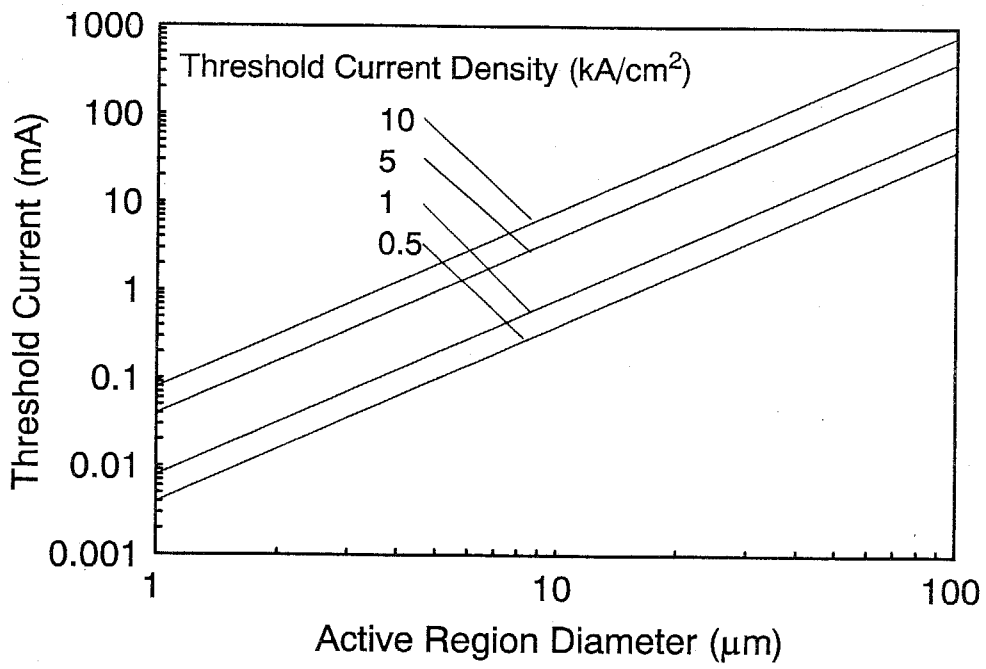

Fig 2.16 Threshold current vs. active region diameter for various threshold current density. Diffraction loss effect and surface carrier recombination effect are not considered in this calculation.

2.3 Design of High Reflectivity Mirrors

2.3.1 Mirrors for Surface Emitting Lasers

As mentioned in previous sections, the reflectivity of surface emitting laser is required at least 98% to realize room temperature operation and over 99.5% for equal laser performance with conventional edge emitting lasers.

As known generally, the power reflectivity at the interface of two materials which

indexes are n_1 and n_2 is represented as $R=(n_1-n_2)^2/(n_1+n_2)^2$. Assuming InP as material n_1 and air as n_2, the reflectivity for 1.55μm wavelength is about 27%. Therefore, the epitaxial surface is not suited as a mirror of surface emitting lasers, though the cleaved facet of edge emitting laser is used as mirrors generally.

At first stage of surface emitting lasers, the gold (Au) on semiconductor surface was used as mirrors [32]. Its reflectivity is expected to be over 90%, theoretically about 94%. Then, SiO_2 was inserted between semiconductor and gold to realize higher reflectivity, and this SiO_2/Au mirror shows the reflectivity of about 98%-98.5% ideally [33]. A surface emitting laser with semiconductor multilayer mirror was demonstrated at about same time [34]. Then, the dielectric multilayer of SiO_2/TiO_2 pairs was utilized [35] and the first room temperature operation was achieved by using dielectric multilayer mirrors for GaAs system [36]. These semiconductor and dielectric multilayer reflectors are possible to achieve over 99% reflectivity theoretically as mentioned below.

The one of advantages of dielectric materials is extremely low optical absorption. To choose dielectric materials, there are some points as follows; (1) large index difference, (2) small thermal resistance, (3) easy to deposition, (4) easy to fabricate micro structure. There are some material systems, for example, SiO_2/TiO_2, SiO_2/Si, MgO/Si, etc. These dielectric material systems have a characteristic of non-electrical conductivity.

On the other hand, semiconductor multilayer reflectors (distributed Bragg reflector : DBR) have a characteristic of electrical conductivity and possibility of growth simultaneously with active layers. As the semiconductor DBR, lattice matching materials are required for epitaxial growth. Therefore, pair of GaInAsP and InP is one of the good materials for long wavelength surface emitting lasers [37, 38]. The other material system lattice matched to InP is also demonstrated for long wavelength mirror, for example, AlAsSb/GaAsSb [39], AlPSb/GaPSb [40], AlAsSb/GaInAs [41], AlGaInAs/InP [42] and InGaAs/InAlAs [43]. However, these novel materials are not suited to the conventional growth system. In recent years, GaAs/AlAs DBRs were demonstrated for long wavelength surface emitting lasers [44]. The multilayers were grown on GaAs substrate and bonded to InP wafers by wafer fusion technique [45, 46]. This fusion technique introduces small crystal defects and deterioration of reflectivity is very little [47].

2.3.2 Design of Multilayer Reflectors for Long Wavelength SE Lasers

In this section, the reflectivity of multilayer mirrors is considered. To calculate the reflectivity of multilayers, the standard matrix method (Appendix A) is used. The material constant of low and high index material is shown in table 2.3 for the wavelength of 1.55μm.

First, the dielectric mirror is considered about the number of pairs and high reflectivity band width. Figure 2.17 shows reflectivities against number of pairs for some dielectric

multilayers. The multilayers are assumed to be formed on InP and the light is incident from InP side. All material systems reach to sufficiently high reflectivity of over 99.8% with less than ten pairs. As described in chapter 5, therefore, Si/SiO_2 multilayers were used in this study as dielectric mirrors because of easy to fabrication with small number of pairs. The theoretical reflectivity spectrum is shown in Fig. 2.18. High reflectivity band width is sufficiently wide, and hence thickness fluctuation is allowed for this mirror.

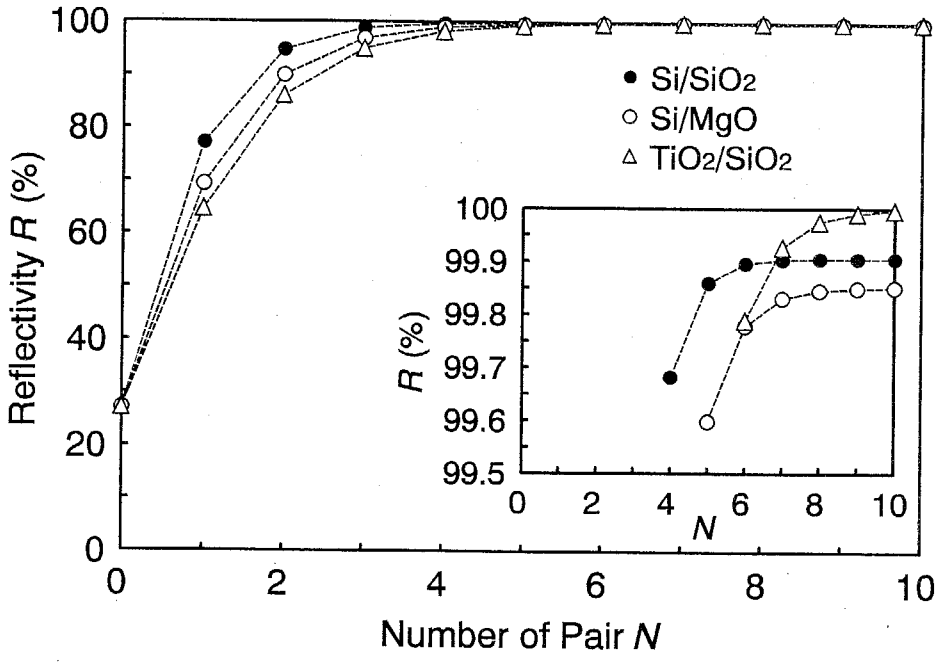

Fig. 2.17 Reflectivity vs. number of pairs for dielectric multilayer mirrors. Inset figure shows zoom of a part of graph.

Table 2.3 Material properties for multilayer reflector material.

Material	index	absorption coefficient (cm^{-1})
Air	1	0
SiO_2	1.45	0
Si	3.2	150
MgO	1.72	0
TiO_2	2.42	0
InP	3.17	10 (n-type), 20×10^{-18}p
GaInAsP (λg=1.45μm)	3.45	10 (n-type), 55×10^{-18}p

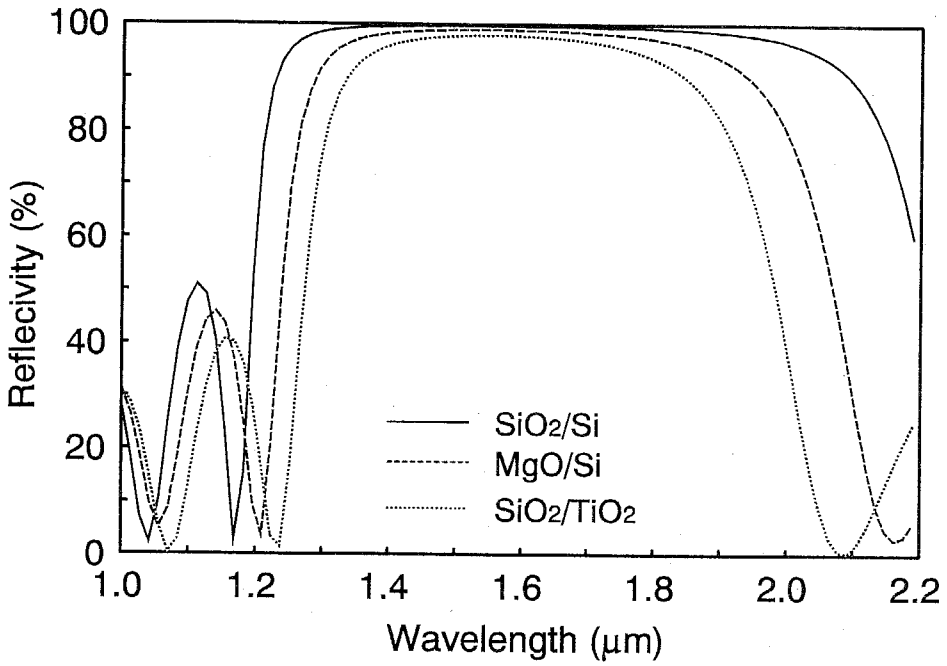

Fig. 2.18 Reflectivity spectrum of dielectric multilayers. The number of pairs is 5 for each system. The center wavelength is set to 1.55μm.

Next, the reflectivity of semiconductor DBRs is considered. The advantage of semiconductor multilayers is possibility of electrical conductivity as mentioned above. However, the carrier doping effects to the optical absorption as free carrier and inter-valence band absorption mentioned in previous section. Here, GaInAsP/InP systems are considered because of easy to grow. Figure 2.19 shows the reflectivity against number of pairs for various doping concentrations. For the n-type DBR, the reflectivity of over 99.5% is possible due to small absorption. On the other hand, the p-type doping of less than $1\times10^{18}cm^{-3}$ is required for achieving over 99.5% reflectivity. GaInAsP/InP DBR is effective for long wavelength surface emitting lasers by controlling the doping concentration. However, the number of pairs for semiconductor DBRs is very large and corresponding thickness becomes very thick.

Some characteristics of important multilayer mirror systems are summarized in table 2.4. In this study, GaInAsP/InP multilayer mirror and Si/SiO_2 multilayer is considered because the GaInAsP system is easy to grow by the epitaxial growth system used in this study, and the Si/SiO_2 mirror has large index difference and easy to deposition and fabrication.

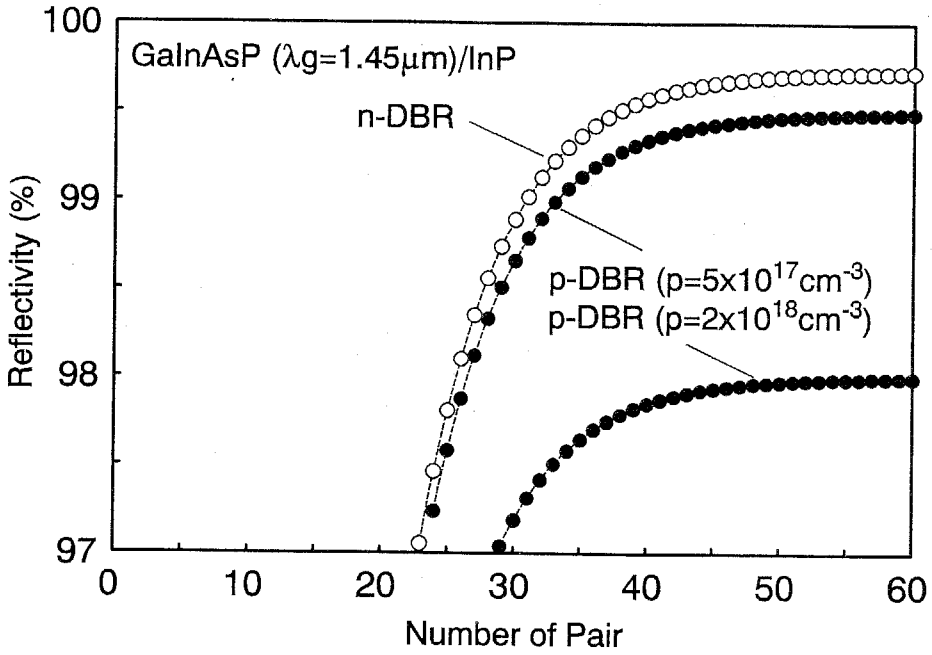

Fig. 2.19 Reflectivity vs. number of pair for GaInAsP (λg=1.45μm) /InP DBR for various doping conditions.

Table 2.4 Summarize of multilayer mirrors and its characteristics.

Material	Max. *R*	Pair for >99%	Thermal Conductivity	Electrical Conductivity	Comment
SiO_2/Si	<99.94	4	fair	fair	easy fabrication
MgO/Si	<99.90	5	excellent	fair	stability?
GaInAsP/InP n-type $p=5\times10^{17}cm^{-3}$ $p=2\times10^{18}cm^{-3}$	 <99.7 <99.4 <98	 31 34 --	fair	excellent	epitaxy
GaAs/AlAs n-type p-type	 <99.9 <99.5	 15 17	good	excellent	wafer fusion

2.3.3 Hybrid Mirror Structure

As described in above section, there exist many types of reflectors. As the summary of reflectors, the dielectric mirror has possibility of extremely high reflectivity with small number of pairs and the semiconductor multilayer should be careful at the doping concentration though it has the advantage of electrical conductivity.

The semiconductor mirror is possible to place at the side of the active layer. On the other hand, the dielectric mirror requires the cladding layer between mirror and active layer. The cladding layer is also absorption medium, therefore the absorption reduces the effective reflectivity of dielectric mirrors.

In this study, I made proposal of the combination of dielectric mirror and semiconductor mirror, and called a hybrid mirror structure. The hybrid mirror structure is shown schematically in Fig. 2.20 with the conventional dielectric mirror and semiconductor mirror structures. For hybrid mirror structure, a part of propagating light from the active layer is reflected at semiconductor mirror region, and hence the light power is lowered gradually in semiconductors. The light absorption is proportional to the light power, and therefore total absorption loss may be reduced by lowering light power in the semiconductor.

Figure 2.21 shows the calculated effective reflectivity, which means the ratio of the incident and reflected light, for hybrid mirror structure and conventional bulk InP cladding layer with dielectric mirror. The horizontal axis shows DBR pair number or thickness of InP layer. The total thickness of DBR is adjusted to the corresponding InP thickness. The dielectric mirror is assumed to be five pairs of Si/SiO_2 multilayer. The increase of semiconductor DBR number reduces the effective reflectivity due to increase of the absorption material thickness. However, for the low doping case of $p=5\times10^{17}cm^{-3}$, the effective reflectivity of hybrid mirror is higher than that of conventional InP cladding structures for all thickness region. For example, the reflectivity of 8 pair DBR is 0.2% higher than that of 2μm thick InP structure. At the reflectivity of over 99%, 0.2% increase of reflectivity is significance. On the other hand, the effective reflectivity for $p=2\times10^{18}cm^{-3}$ is lower than that for InP structure for the thickness of less than about 1.7μm or 7 pairs, however

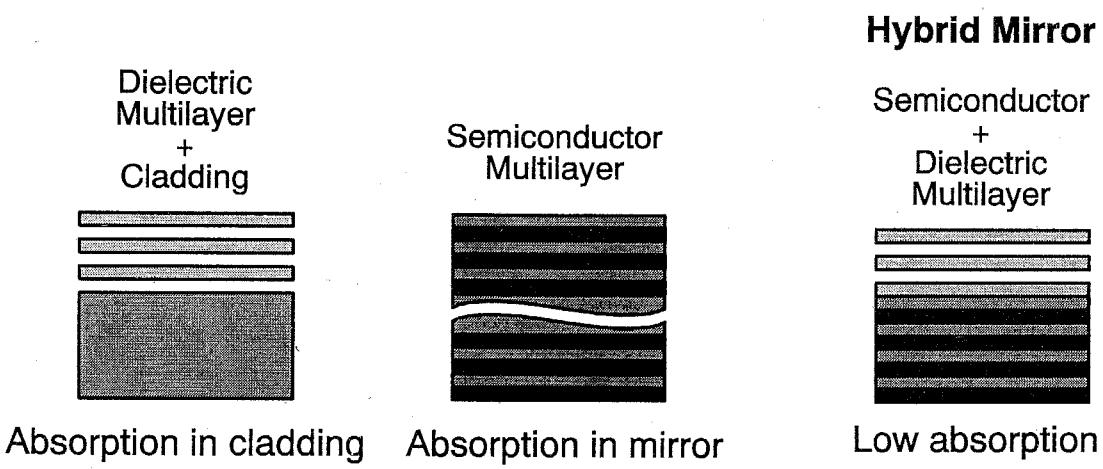

Fig. 2.20 Schematic view of hybrid mirror structure with conventional dielectric mirror structure and semiconductor mirror structure.

for thick or large number of pairs, the hybrid mirror has also the advantage of high reflectivity. For the n-type hybrid mirror, the absorption loss may be as low as that for low p-type doped case. In this way, the hybrid mirror has advantage for long wavelength surface emitting lasers.

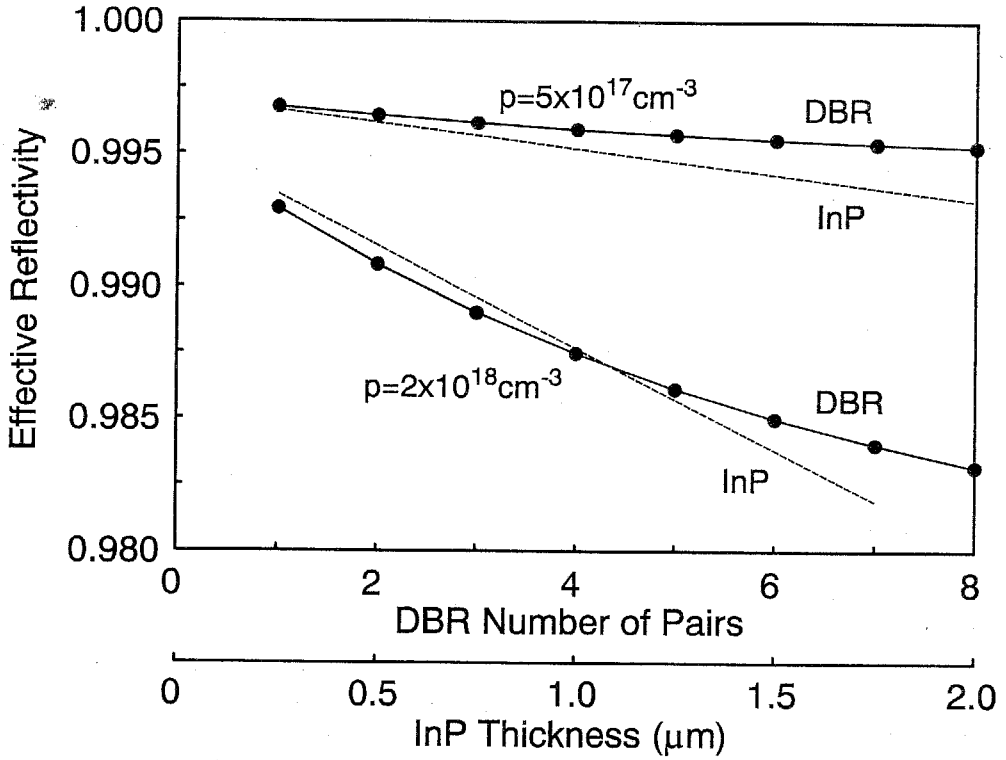

Fig. 2.21 Reflectivity vs. pair number of semiconductor multilayer for hybrid mirror. GaInAsP is assumed to be λg=1.45μm. The reflectivity of InP cladding structure is also shown as the function of InP cladding layer thickness. 5 pair of SiO_2/Si dielectric mirror is assumed.

References

[1] S. W. Corzine, R. S. Geels, J. W. Scott, R. H. Yan, and L. A. Coldren, "Design of Fabry-Perot surface emitting lasers with a periodic gain structure," *IEEE J. Quantum Electron.*, vol. QE-25, pp. 1513-1524, 1989.

[2] G. H. B. Thompson and G. D. Henshall, *Electron. Lett.*, vol. 16, p. 42, 1980.

[3] A. Sugimura, *IEEE J. Quantum Electron.*, QE-18, p. 352, 1982.

[4] M. B. Panish, I. Hayashi, and S. Sumuski, *Appl. Phys. Lett.*, vol. 16, p. 326, 1970.

[5] L. Esaki and R. Tsu, "Superlattice and negative differential conductivity in semiconductors," *IBM J. Res. Develop.*, vol. 14, pp. 61-65, 1970.

[6] for a review, P. S. Zory, Jr., Ed., Quantum Well Lasers, Academic Press, Inc., 1993.

[7] M. Asada, A. Kameyama, and Y. Suematsu, "Gain and intervalence band absorption in quantum-well lasers," *IEEE J. Quantum Electron.*, vol. QE-20, pp. 745-753, 1984.

[8] N. Holonyak, Jr., R. M. Kolbas, R. D. Dupuis, and P. D. Dupkus, *IEEE J. Quantum Electron.*, vol. QE-16, p. 170, 1980.

[9] W. T. Tsang, "Extremely low threshold (AlGa)As modified multiquantum well heterostructure lasers grown by molecular-beam epitaxy," *Appl. Phys. Lett.*, vol. 39, pp. 786-788, 1981.

[10] Y. Arakawa and H. Sakaki, "Multidimensional quantum well laser and temperature dependence of its threshold current," *Appl. Phys. Lett.*, vol. 40, pp. 939-941, 1982.

[11] Y. Arakawa and A. Yariv, "Theory of gain, modulation response, and spectral linewidth in AlGaAs quantum well lasers," *IEEE J. Quantum Electron.*, vol. QE-21, pp. 1666-1674, 1985.

[12] Y. Arakawa and A. Yariv, "Quantum well lasers - gain, spectra, dynamics," *IEEE J. Quantum Electron.*, vol. QE-22, pp. 1887-1899, 1986.

[13] M. Chandrasekhar and F. H. Pollak, "Effects of uniaxial stress on the electro-reflectance spectrum of Ge and GaAs," *Phys. Rev. B*, vol. 15, pp. 2127-2144, 1977.

[14] N. K. Dutta, "Effect of uniaxial stress on optical gain in semiconductors," *J. Appl. Phys.*, vol. 55, pp. 285-288, 1984.

[15] C. S. Adams and D. T. Cassidy, "Effects of stress on threshold, wavelength, and polarization of the output of InGaAsP semiconductor diode lasers," *J. Appl. Phys.*, vol. 64, pp. 6631-6638, 1988.

[16] T. C. Chong and C. G. Fonstad, "Theoretical gain of strained-layer semiconductor lasers in the large strain regime," *IEEE J. Quantum Electron.*, vol. 25, pp. 171-178, 1989.

[17] J. W. Matthews and A. E. Blakeslee, "Defects in epitaxial multilayers," *J. Crystal Growth*, vol. 27, pp. 118-125, 1974.

[18] P. M. J. Maree, J. C. Barbour, J. F. van der Veen, K. L. Kavanagh, C. W. Bulle-Lieuwma, and M. P. A Viegers, "Generation of misfit dislocations in semiconductors," *J. Appl. Phys.*, vol. 62, pp. 4413-4420, 1987.

[19] A. R. Adams, "Band-structure engineering for low-threshold high-efficiency semiconductor lasers," *Electron. Lett.*, vol. 22, pp. 249-250, 1986.

[20] E. Yablonovitch and E. O. Kane, "Reduction of lasing threshold current density by the lowering of valence band effective mass," *J. Lightwave Technol.*, vol. LT-4, pp. 504-506, 1986.

[21] M. Yamada and Y. Suematsu, "Theory of single mode injection lasers taking account of electronic intra-band relaxation," *Jpn. J. Appl. Phys.*, vol. 18, pp. 347-354, 1979.

[22] M. Asada and Y. Suematsu, *IEEE, J. Quantum Electron.*, vol. QE-21, p. 434, 1985.

[23] E. Wintner and E. P. Ippen, "Nonlinear carrier dynamics in $Ga_xIn_{1-x}As_yP_{1-y}$ compounds," *Appl. Phys. Lett.*, vol. 44, pp. 999-1001, 1984.

[24] for a review, J. I. Pankove, Ed., Optical processes in semiconductors, chapter 3, Dover Publications, Inc., New York, 1971.

[25] H. C. Casey, Jr. and P. L. Carter, "Variation of intervalence band absorption with hole concentration in p-type InP," *Appl. Phys. Lett.*, vol. 44, pp. 82-83, 1984.

[26] C. H. Henry, R. A. Logan, F. R. Merritt, and J. P. Luongo, *IEEE J. Quantum Electron.*, vol. QE-19, p. 947, 1983.

[27] for a review, T. P. Pearsall, Ed., GaInAsP Alloy Semiconductors, John Wiley & Sons Ltd., 1982.

R. J. Nicholas, J. C. Portal, C. Houlbert, P. Perrier, and T. P. Pearsall, "An experimental determination of the effective masses for $Ga_xIn_{1-x}As_yP_{1-y}$ alloys grown on InP," *Appl. Phys. Lett.*, vol. 34, pp. 492-494, 1979.

C. Hermann and T. P. Pearsall, "Optical pumping and the valence-band light-hole effective mass in $Ga_xIn_{1-x}As_yP_{1-y}$ ($y \approx 2.2x$)," *Appl. Phys. Lett.*, vol. 38, pp. 450-452, 1981.

[28] M. Yamanishi and I. Suemune, "Comment on polarization dependent momentum matrix elements in quantum well lasers," *Jpn. J. Appl. Phys.*, vol. 23, pp. L35-L36, 1984.

[29] E. P. O'Reilly, G. Jones, A. Ghiti, A. R. Adams, "Improved performance due to suppression of spontaneous emission in tensile-strain semiconductor lasers," *Electron. Lett.*, vol. 27, pp. 1417-1419, 1991.

[30] J. M. Luttinger and W. Kohn, "Motion of electrons and holes in perturbed periodic fields," *Phys. Rev.*, vol. 97, pp. 869-883, 1955.

[31] C. H. Lin and Y. H. Lo, "Empirical formulas for design and optimization of 1.55μm InGaAs/InGaAsP strained-quantum-well lasers," *IEEE Photon. Technol. Lett.*, vol. 5, pp. 288-290, 1993.

[32] H. Soda, K. Iga, C. Kitahara, and Y. Suematsu, "GaInAsP/InP surface emitting injection lasers," *Jpn. J. Appl. Phys.*, vol. 18, pp. 2329-2330, 1979.

[33] S. Uchiyama and K. Iga, "GaInAsP/InP surface emitting injection laser with a ring electrode," *IEEE J. Quantum Electron.*, vol. QE-20, pp. 1117-1118, 1984.

[34] A. Chailertvanitkul, K. Iga, and K. Moriki, "GaInAsP/InP surface emitting laser (λ=1.4 μm, 77K) with heteromultilayer reflector," *Electron. Lett.*, vol. 21, pp. 303-304, 1985.

[35] I. Watanabe, F. Koyama, and K. Iga, "GaInAsP/InP CBH surface-emitting laser with a dielectric multilayer reflector," *Jpn. J. Appl. Phys.*, vol. 26, pp. 1598-1599, 1987.

[36] F. Koyama, S. Kinoshita, K. Iga, "Room-temperature continuous wave lasing characteristics of a GaAs vertical cavity surface-emitting laser," *Appl. Phys. Lett.*, vol. 55, pp. 221-222, 1989.

[37] K. Tai, S. L. McCall, S. N. G. Chu, W. T. Tsang, "Chemical beam epitaxially grown InP/InGaAsP interference mirror for use near 1.55μm wavelength," *Appl. Phys. Lett.*, vol. 51, pp. 826-827, 1987.

[38] D. G. Deppe, N. D. Gerrard, C. J. Pinzone, R. D. Dupuis, and E. F. Schubert, "Quarter-wave Bragg reflector stack of InP-$In_{0.53}Ga_{0.47}As$ for 1.65μm wavelength," *Appl. Phys. Lett.*, vol. 56, pp. 315-317, 1990.

[39] O. Blum, I. J. Fritz, L. R. Dawson, A. J. Howard, T. J. Headley, J. F. Klem, and T. J. Drummond, "Highly reflective, long wavelength AlAsSb/GaAsSb distributed Bragg, reflector grown by molecular beam epitaxy on InP substrate," *Appl. Phys. Lett.*, vol. 66, pp. 329-331, 1995.

[40] H. Shimomura, T. Anan, K. Mori, and S. Sugou, "High-reflectance AlPSb/GaPSb distributed Bragg reflector mirrors on InP grown by gas-source molecular beam epitaxy," *Electron. Lett.*, vol. 30, pp. 314-315, 1994.

[41] K. Tai, R. J. Fischer, A. Y. Cho, and K. F. Huang, "High-reflectivity $AlAs_{0.52}Sb_{0.48}$/GaInAs(P) distributed Bragg mirror on InP substrate for 1.3-1.55μm wavelengths," *Electron. Lett.*, vol. 25, pp. 1159-1160, 1989.

[42] A. J. Moseley, J. Thompson, D. J. Robbins, and M. Q. Kearley, "High-reflectivity AlGaInAs/InP multilayer mirrors grown by low-pressure MOVPE for application to long-wavelength high-contrast-ratio multi-quantum-well modulators," *Electron. Lett.*, vol. 25, pp. 1717-1718, 1989.

[43] I. J. Fritz, B. E. Hammons, A. J. Howard, T. M. Brennan, and J. A. Olsen, "Fabry-Perot reflectance modulator for 1.3μm from (InAlGa)As materials grown at low temperature," *Appl. Phys. Lett.*, vol. 62, pp. 919-921, 1993.

[44] J. J. Dudley, M. Ishikawa, D. I. Babic, B. I. Miller, R. Mirin, W. B. Jiang, J. E. Bowers, and E. L. Hu, "144°C operation of 1.3μm InGaAsP vertical cavity lasers on GaAs substrates," *Appl. Phys. Lett.*, vol. 61, pp. 3095-3097, 1992.

[45] Z. L. Liau and D. E. Mull, "Wafer fusion: A novel technique for optoelectronic device fabrication and monolithic integration," *Appl. Phys. Lett.*, vol. 56, pp. 737-739, 1990.

[46] Y. H. Lo, R. Bhat, D. M. Hwang, M. A. Koza, and T. P. Lee, "Bonding by atomic rearrangement of InP/InGaAsP 1.5μm wavelength lasers on GaAs substrate," *Appl. Phys. Lett.*, vol. 58, pp. 1961-1963, 1991.

[47] R. J. Ram, L. Yang, K. Nauka, Y. M. Houng, M. Ludowise, D. E. Mars, J. J. Dudley, and S. Y. Wang, "Analysis of wafer fusing for 1.3μm vertical cavity surface emitting lasers," *Appl. Phys. Lett.*, vol. 62, pp. 2474-2476, 1993.

Chapter 3

GaInAsP/InP Growth by Chemical Beam Epitaxy

In this chapter, a chemical beam epitaxial technique and its applicability for surface emitting lasers is described. The growth condition of GaInAsP and its crystal quality are discussed, and then the laser wafers are grown and characterized.

3.1 Chemical Beam Epitaxy

3.1.1 Epitaxial Growth Techniques for III/V Alloy Semiconductors

The optical device, for example, laser diodes (LD), light emitting diodes (LED), photo detectors (PD), etc., has commonly thin multilayer structures of alloy semiconductors. Accordingly, highly controllability of layer structures such as thicknesses, compositions and doping concentrations are required for realizing high performance devices, and hence epitaxial growth techniques for III/V alloy semiconductors have been developed and improved to grow the designed layer structure.

There are some growth techniques classified as 1) liquid phase growth method (LPE), 2) vapor phase epitaxial method (VPE) and 3) growth method in ultra-high vacuum.

LPE techniques have been developed since earlier days of epitaxial growth. However, this technique is inferior at the point of thickness controllability and abrupt heterojunctions which are important to design high performance devices.

VPE techniques are classified to two methods. One uses haloid group III materials and another uses metalorganic materials for group III sources. The latter is important technique for the optical devices and the technique is called MOCVD (metalorganic chemical vapor deposition) or OMVPE (organicmetal vapor phase epitaxy) [1]. The advantage of MOCVD is

follows, 1) good composition and thickness controllability by controlling the source gas flow, 2) continuous source supply and easy source exchange, 3) low system cost without ultra-high vacuum system. On the other hand, there are some disadvantages such as 1) existence of flow pattern, turbulence, and intermediate reaction of gases, 2) difficulty of *in-situ* characterization. The advantage is due to gas sources and the disadvantage is due to viscous flow of gas sources.

The growth method in a ultra-high vacuum has the advantage of 1) possibility of atomic layer order growth, 2) *in-situ* characterization. The growth techniques are classified to some methods about source material type. The classification is shown in table 3.1 with the other characteristics. Molecular beam epitaxy (MBE) uses solid sources for both group III and group V [2]. Gas-source MBE (GSMBE) uses solid sources for group III and gas sources for group V [3]. In this growth technique, the group V source is usually supplied by hydride gases and cracked thermally in a growth chamber. As the product of cracked sources is like as that of MBE, the growth mechanism of GSMBE is like as MBE. MOMBE uses metalorganic sources for group III [4]. The growth mechanism is different from MBE and MOMBE because chemical reaction of the group III alkyls is occurred at the substrate surface. The chemical beam epitaxy (CBE), which is used in this study, uses gas sources for both group III and V sources. The variety of gas sources is the same as MOCVD, and hence the advantage of CBE is considered to be combination of MOCVD and MBE.

3.1.2 History of Chemical Beam Epitaxy

The vapor phase growth of alloy semiconductors has been started since late 1950s for bulk crystal growth. The VPE technique for epitaxial growth was suggested at mid 1960s and developed for GaAs microwave devices [5] and GaAsP light emitting diodes (LED) [6]. MOCVD and MBE techniques have been started since late 1960s. The motivations of

Table 3.1 Classification of ultra-high vacuum growth techniques. MOCVD technique is also shown to compare the characteristics.

	MBE	GSMBE	MOMBE	CBE	MOCVD
Pressure (Torr)	$<10^{-9}$	$<10^{-5}$	$<10^{-5}$	$<10^{-4}$	10^{-2}~760
Group III sources	Solid	Solid	Gas	Gas	Gas
Group V sources	Solid	Gas	Solid	Gas	Gas
Dopant sources	Solid	Gas/Solid	Gas/Solid	Gas/Solid	Gas
p-type dopant	Be/Mg	Be/Mg	Be/Mg/C	Be/Mg/C	Zn/C
n-type dopant	Si/Sn	Si/Sn	Si/Sn	Si/Sn	Se/S/Si

MOCVD were simple growth system and good composition/thickness controllability comparable with VPE [1, 7, 8, 9]. On the other hand, the motivations of MBE were atomic layer order growth and study of the quantum structures such as super lattice, quantum wells (QW) and two dimensional electron gas (2DEG) [2, 10, 11, 12].

To combine the advantage of MOCVD and MBE, Morris and Fukui of AT&T Bell Laboratories applied gas sources to MBE in 1974 [13]. They used hydride gases of phosphine (PH_3) and arsine (AsH_3) as group V sources for the MBE system. Since then, Panish of AT&T Bell Laboratories [14] and Calawa of Massachusetts Institute of Technology [15] started to use AsH_3 and PH_3. Panish named the technique gas source MBE (GSMBE) [3] and he has been demonstrated its crystal qualities [16, 17]. The utilization of group V gas sources is necessary to stabilize and control the beam flux ratio because of difficulty of vapor pressure control of solid group V sources. On the other hand, the solid group III source has disadvantages of beam flux change as remain source and necessity of source exchange with exposing a growth chamber to the air. In 1984, Venhoff applied Trimethylgallium (TMGa) for Ga source in MBE, and called this technique MOMBE with using AsH_3 gas for group V sources [4]. At the Third International Conference on Molecular Beam Epitaxy in 1984, Tsang of AT&T Bell Laboratories named chemical beam epitaxy (CBE) as the technique utilizing gas sources for both group V and group III. He grew some III/V alloy semiconductors and demonstrated some devices for showing applicability of CBE grown materials [18,19,20]. The First International Workshop on Chemical Beam Epitaxy was held in 1988 as satellite meeting of the Conference on Molecular Beam Epitaxy. The International Conference on Chemical Beam Epitaxy and Related Growth Technique has been held every year since 1989.

3.1.3 Advantages of Chemical Beam Epitaxy

As mentioned in previous sections, CBE technique is considered to be a combination epitaxial technique of MOCVD at the point of using gas sources and MBE at the point of the growth pressure. The advantage of CBE is summarized as follows.

The advantage of CBE comparing with conventional MBE is;

(1) easy and reproducible composition controls by gas flow control,
(2) source flexibility and easy source exchange.

The first thing is great advantage to grow alloy semiconductors such as GaInAsP which contains two kinds of high vapor pressure materials of phosphorus (P) and arsenic (As) [21, 22]. The second thing is also important to examine source materials for growing high quality crystals [23, 24] and also important to keep a growth chamber from the air.

The advantage compared with MOCVD is follows;

(3) good thickness controllability due to no gas stagnation,

(4) good layer and doping abruptness due to high rate exhaust and relatively low growth temperature which is effective to avoid interdiffusion and/or diffusion of atoms and dopants,

(5) good doping controllability without memory effect.

These advantages are molecular beam nature [18, 19, 20].

3.2 Chemical Beam Epitaxy System and Growth Mechanism

3.2.1 System of Chemical Beam Epitaxy

A CBE system used in this study is shown in Fig. 3.1. The system CBE-32 was manufactured by RIBER Co., France, and some parts of system were modified in this study. Figure 3.2 is a photograph of the system. A schematic view of main unit of CBE system is shown in Fig. 3.3. The CBE system looks like a MBE system around growth chambers and like an MOCVD system around gas lines. For the growth chamber, a turbo molecular pump (TMP) unit (2800ℓ/s for H_2) with a rotary pump is used for high pumping efficiency. To realize low background pressure and to avoid interference between high temperature cells, the liquid nitrogen (LN_2) is filled in shrouds. A TMP unit (330ℓ/s for H_2) with a rotary pump and an ion pump (IP) unit is used for loading chamber. The TMP and IP for the loading chamber are used for achieving low pressure ($<1\times10^{-7}$ Torr) in short time by changing from TMP to IP because the loading chamber is exposed to the air for each wafer loading. On the other hand, the background pressure of the growth chamber before and during growth is typically $<1\times10^{-7}$ Torr and $<5\times10^{-5}$ Torr, respectively. A TMP unit (330ℓ/s for H_2) with a rotary pump is utilized for gas lines. In the growth chamber, a quadrupole mass spectrometer (Q-mass) unit, a reflected high energy electron diffraction (RHEED) unit and a flux gauge are installed for the *in-situ* monitoring.

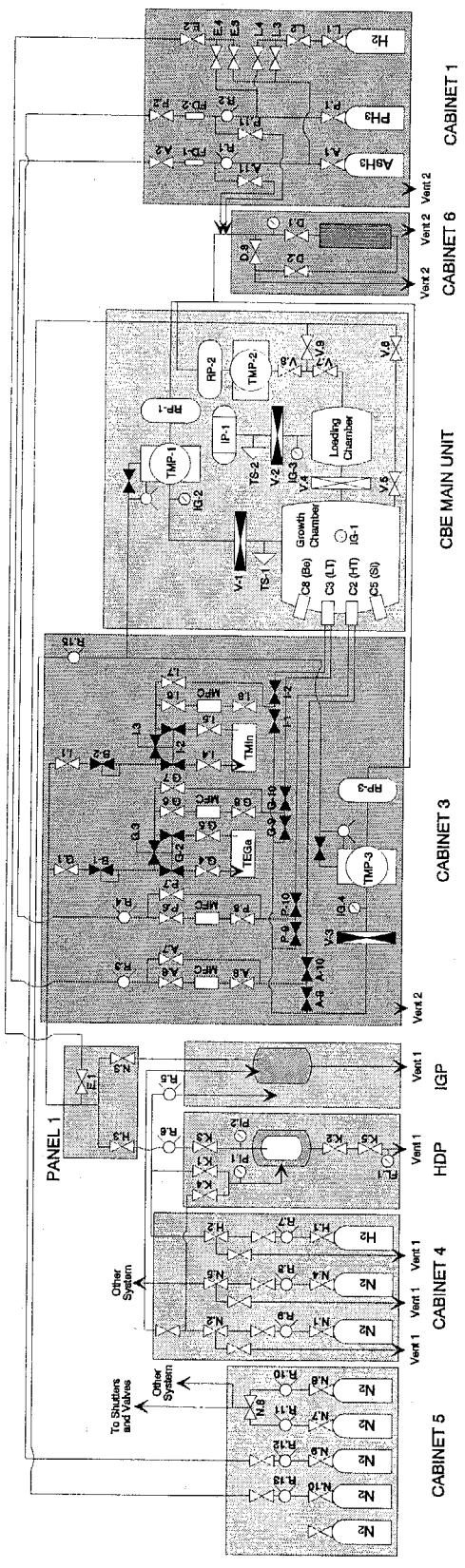

Fig. 3.1 Chemical beam epitaxial system used in this study. In addition to the system in this figure, control system cabinet is installed.

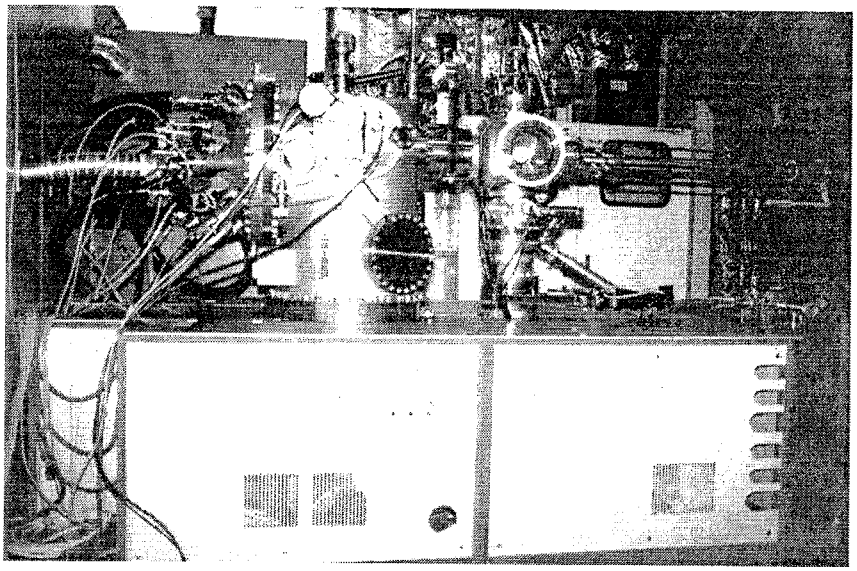

Fig. 3.2 Photograph of a CBE system. The center is a growth chamber and right hand is a wafer loading chamber. The right hand bar is a manipulator for transport a Mo block.

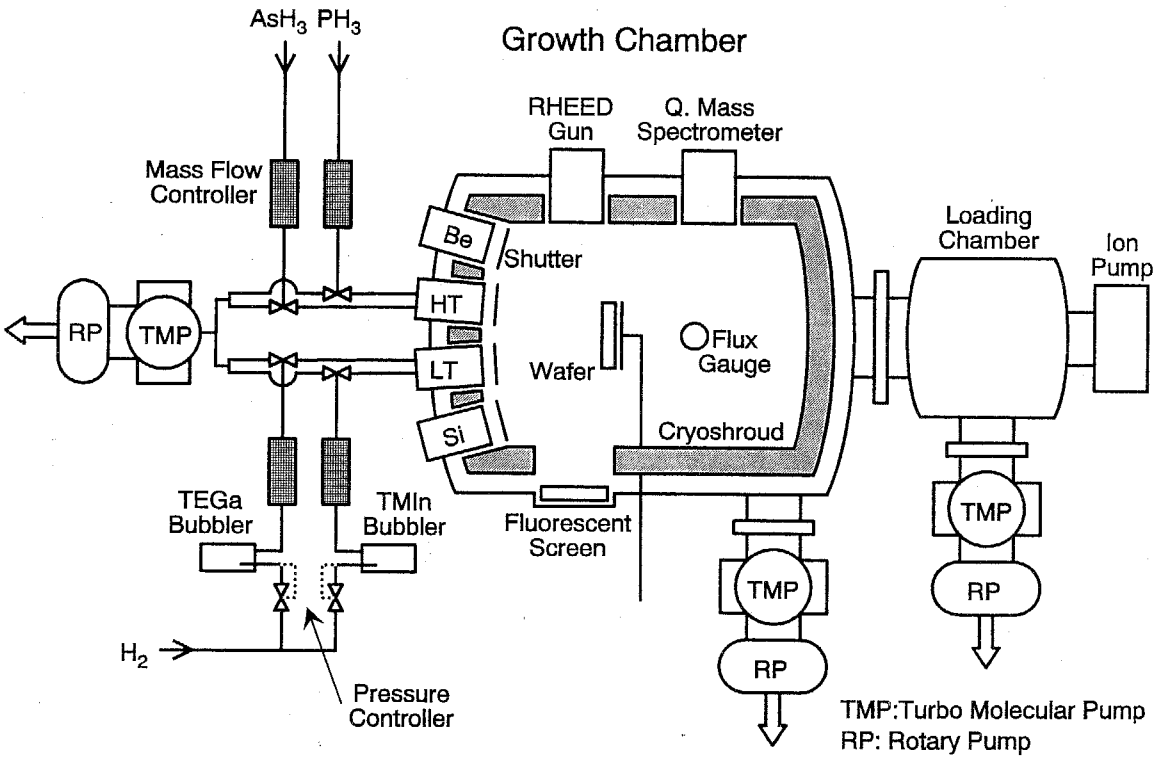

Fig. 3.3 Main unit of chemical beam epitaxial system. The center is growth chamber, the left hand is gas source lines and the right hand is wafer loading chamber. Each element has ultra-high vacuum systems.

The group V sources are pure phosphine (PH_3, 99.999%, 20ℓ cylinder and 20kg/cm^2) and pure arsine (AsH_3, 99.999%, 20ℓ cylinder and 7kg/cm^2). As group III metalorganic sources, trimethylindium (TMIn, 99.9999%, 25g in bubbler) and triethylgallium (TEGa, 99.9999%, 25g in bubbler) are used with H_2 carrier gas. Each gas flow rate is controlled by an electrical mass flow controller (MFC). The valve and flow rate sequence are controlled by computer. The solid sources are utilized for dopant sources of beryllium (Be, 99.999% and 0.03g fragment) for p-type and silicon (Si, 99.9999% and 2g chunk) for n-type. The dopant flux is controlled by cell temperature and mechanical shutter in front of the cells. The dopant sources are exchanged at an interval of about one year, because the doping efficiency is reduced by covering the dopant surface with carbide. Effusion cell crucibles for the dopant sources are made of pyrolytic boron nitride (PBN). A high temperature cell (HT-Cell) is utilized for cracking group V sources. For the group III source, a low temperature cell (LT-Cell) is used not to stick source molecules to chamber wall cooled by LN_2.

3.2.2 Growth Mechanism of CBE

In this section, the growth mechanism of chemical beam epitaxy is described. Figure 3.4 shows a simple schematic view of ideal growth process. The group V hydrides (PH_3 and/or AsH_3) are thermally cracked in HT-Cell. The ideal products are group V dimmers (P_2 and/or As_2), radical hydrogen (H^+), and hydrogen molecules (H_2). The chemical reaction is;

$$2PH_3 \rightarrow P_2 + xH_2 + yH^+ \qquad (3.1)$$
$$2AsH_3 \rightarrow As_2 + xH_2 + yH^+ \qquad (3.2)$$

where $2x + y = 6$. The radical hydrogen plays an important role in the chemical reaction of group III. The group III metalorganic sources (TMIn and/or TEGa) are introduced to growth chamber through the LT-Cell, but any chemical reaction is not occurred at this cell. The metalorganic sources are thermally decomposed on the substrate surface as;

$$In(CH_3)_3 \rightarrow In + 3CH_3 \qquad (3.3)$$
$$Ga(C_2H_5)_3 \rightarrow Ga + 3C_2H_4 + 3H \qquad (3.4).$$

For the chemical reaction of TEGa, the β-elimination process is occurred and ethylene is produced [25]. To form InP or GaAs crystal, a complete pyrolysis is occurred, which is obtained by adding Eq. (3.1) and Eq. (3.3), Eq. (3.2) and Eq. (3.4) together, respectively. The ideal reactions on the substrate surface are follows;

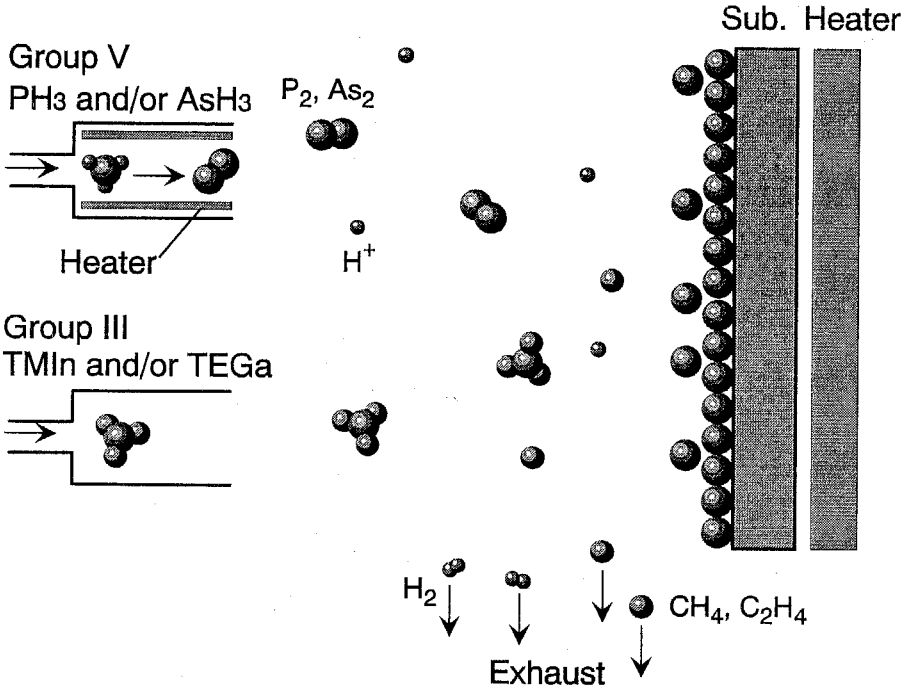

Fig. 3.4 Schematic view of ideal growth process of chemical beam epitaxy.

$$2In(CH_3)_3 + P_2 + xH_2 + yH^+ \rightarrow 2InP + 6CH_4 \quad (3.5)$$

$$2Ga(C_2H_5)_3 + As_2 + xH_2 + yH^+ \rightarrow 2GaAs + 6C_2H_4 + 6H_2 \quad (3.6).$$

In these reactions, it is adequate not to indicate the hydrides because of presence of only cracked hydride products on the ideal substrate surface.

The detail of growth processes at the surface is divided into the next steps; (1) absorption of molecules, (2) surface reaction, (3) surface diffusion and (4) incorporation into lattice site. Schematic reaction steps are shown in Fig. 3.5 for the group III (a) and for the group V (b). In these steps, the temperature of substrate is very important. One of the role of temperature is to dissociate group III alkyls. To increase the reaction rate, it is required above 350°C-400°C. However, at such relatively low temperature, the grown layers are amorphous or polycrystal and the layer contains many carbons (C) originated from undissociated and partially dissociated metalorganic sources. To obtain high quality epitaxial layer, more high temperature is required. On the other hand, excess high temperature takes place desorption or re-evaporation of the group III and group V atoms. Hence, excess high temperature influences crystal quality strongly because the vapor pressure of group V materials such as phosphorus (P) and arsenic (As) is high. To suppress the desorption or re-evaporation of group V atoms, sufficient molecules, ideally dimmers, should be supply, and hence the ratio of group III and group V gas sources, named V/III ratio, is usually high.

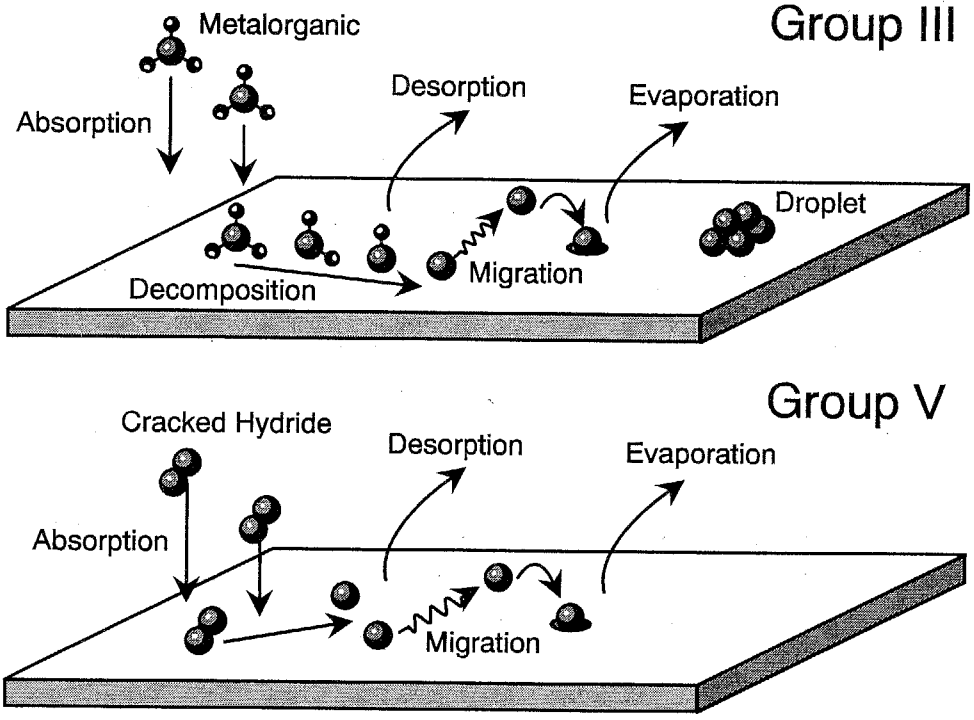

Fig. 3.5 Simple reaction processes on substrate surface. The reactions are shown independently for group III and group V materials.

3.3 Growth and Characterization of InP and GaInAsP

3.3.1 Preparation for Growth

In this section, some important growth preparations are described.

(1) Group III metalorganic:

The preparation for group III sources is determination of gas flow range. The controllability of growth rate and composition is determined by vapor pressure of sources, pressure of carrier gas (H_2) and the range of MFCs. The vapor pressure is given as;

$$\log(p(Torr)) = 10.520 - \frac{3014}{T(K)} \quad \text{(for TMIn)} \quad (3.7)$$

$$\log(p(Torr)) = 9.172 - \frac{2532}{T(K)} \quad \text{(for TEGa)} \quad (3.8).$$

In this study, the temperatures of TMIn and TEGa are set to 25°C-30°C, and the vapor pressure is less than 10 Torr. The pressure of H_2 carrier gas is controlled at typically 30 Torr.

Under this condition, the flow rate is given as follows;

$$TMIn(sccm) = \frac{p_{TMIn}}{p_{TMIn} + p_{H_2}} \times MFC_{TMIn}(sccm) \times Flow_{TMIn}(\%) \qquad (3.9)$$

$$TEGa(sccm) = \frac{p_{TEGa}}{p_{TEGa} + p_{H_2}} \times MFC_{TEGa}(sccm) \times Flow_{TEGa}(\%) \qquad (3.10)$$

where "MFC" means the range of mass flow controller and "Flow" means the electrically set flow ratio of MFC. The maximum range is determined by considering the growth rate and controllability of the composition, and hence 12-20 sccm MFCs were used in this study.

(2) Cells:

High temperature cell (HT-Cell), low temperature cell (LT-Cell) and dopant (Be and Si) cells are kept at 200°C while the system doesn't operate. HT-Cell is baked at 1100°C-1150°C for one hour to keep and stabilize the cracking efficiency for each day. After the baking, liquid nitrogen (LN_2) is filled into the shroud, and then HT-Cell temperature is lowered to operation temperature of 850°C-1000°C and simultaneously LT-Cell temperature is set to operation temperature of 100°C. Dopant cells and their shutters are baked for 30 minutes at 1250°C for Si cell and 1100°C for Be cell. After the baking, Si cell and Be cell are lowered to the standby temperature of 500°C and 450°C, respectively.

Here, the operation temperature of HT-Cell is described. The cell elements shown in Fig. 3.6 are tried with some materials of PBN or tantalum (Ta) to obtain high cracking efficiency.

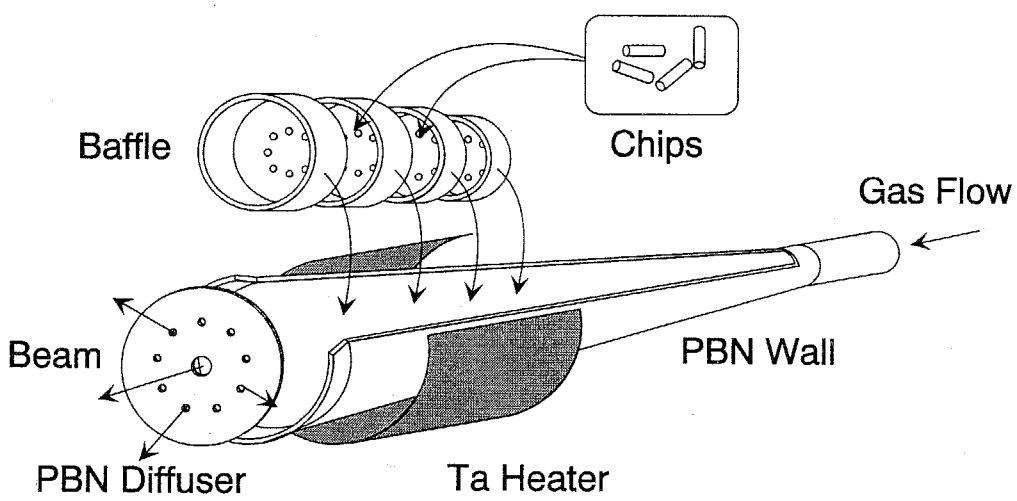

Fig. 3.6 Cracking cell for group V sources. Baffles and chips are made of PBN or Ta.

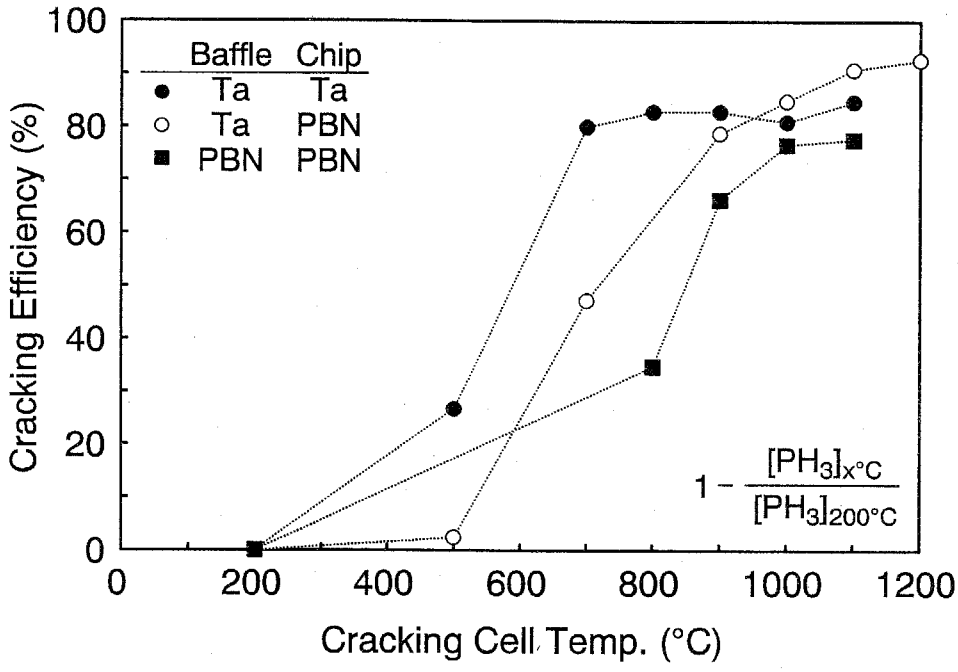

Fig. 3.7 HT-Cell cracking efficiency for PH_3 gas (1sccm). Three marker types show the difference of cell elements shown in Fig. 3.6.

Figure 3.7 shows the measured cracking efficiency for PH_3 gas. The measurement is carried out by Q-mass. The efficiency is large for Ta element at low temperature. This phenomenon is result of catalysis of Ta metal for the hydrides [3]. However, the cracking efficiency with Ta elements is gradually reduced by changing of surface quality of elements, and hence the growth condition is also changed. Therefore, almost growths of this study have been carried out using PBN cell which is stable for long term use.

(3) InP Substrate:

The preparation of InP substrate is following. The substrate used in this study is n-type (Sn-doped, $n=2\times10^{18}cm^{-3}$), p-type (Zn-doped, $p=2\times10^{18}cm^{-3}$) and semi-insulating (s.i.) type (Fe-doped) InP oriented to <100> direction. The substrate is cleaved to the size of from 5×5 mm^2 to 20×20 mm^2, and then it is cleaned in boiling trichroroethylene, acetone and methanol for about 10 minutes. After rinsed in the water, the substrate is etched chemically in the solution of H_2SO_4:H_2O_2:H_2O = 3:1:1. The etching conditions are follows; 80°C for 60sec for n-type, 0°C for 30sec for p-type and 60°C for 30sec for s.i.-type. Immediately, the substrate is rinsed in deionized water and then the substrate is into methanol. The substrate is dried and mounted on the molybdenum (Mo) holder with indium (In) solder. At the same time, InSb fragment (<1×1mm^2) is also mounted at the side of InP substrate. Then the holder is loaded to loading chamber, and after reaching to high vacuum (<10^{-7} Torr), the holder is moved to

growth chamber. The substrate temperature is gradually (about 30-60min) up with exposing phosphine gas to avoid phosphorus desorption. At the temperature of 525°C which is exactly decided by the melting point of InSb, the thermal cleaning is taken place for 1-5 minutes to evaporate the surface oxide. Then the temperature is set to growth temperature of 500°C typically. During the growth, the temperature is monitored by an infrared (λ=2μm) pyrometer which is calibrated by melting point of InSb.

3.3.2 Characterization Method of Epitaxial Layers

In this study, some crystal characterization methods are used, for example, X-ray diffraction (XRD), photoluminescence (PL) and doping concentration measurement. In addition, the surface morphology observation by optical microscope is important characterization technique. As the other characterization techniques, roughness measurement and scanning electron microscope (SEM) are used for thickness and growth rate measurement. Some measurement system used in this study are mentioned in following.

(1) X-ray diffraction (XRD):

X-ray diffraction measurement is utilized for determination of lattice mismatch. The crystal quality is also estimated from the line width and intensity of diffraction curve. Furthermore, the periodicity of thin multilayers such as multi-quantum wells (MQWs) is possible to measure as mentioned in chapter 4. In this study, a double crystal XRD system was used and the X-ray wavelength is Cu:kα1 (λ=1.540Å). The lattice mismatch $\Delta a/a$ is calculated by;

$$\frac{\Delta a}{a} = \frac{\Delta\theta}{\tan(\theta)} \qquad (3.11)$$

where $\Delta\theta$ is deviation of diffraction angle between epitaxial layer peak and substrate peak θ. For the InP substrate, 2θ is 63.34 (deg) for Cu:kα1. The measured lattice mismatch is corresponding to the thickness perpendicular to the surface. For estimation of the amount of strain or the free-standing lattice constant, it is necessary to apply next equation;

$$\frac{\Delta a_0}{a} = \frac{C_{11}}{C_{11}+2C_{12}} \cdot \frac{\Delta a}{a} \qquad (3.12)$$

$$\Delta a_0 \approx \frac{\Delta a}{2} \quad (\because C_{11} \approx 2C_{12}) \qquad (3.13)$$

where Δa_0 is deviation for the substrate and C_{ij} are elastic stiffness constants.

(2) Photoluminescence (PL):

PL measurement technique is used for characterizing the bandgap energy (Eg) and crystal quality. These characteristics are measured by the peak wavelength (λg), line width (FWHM: full width at half maximum) and emission intensity. Figure 3.8 shows the PL measurement system used in this study. The excitation light sources are a Nd:YAG laser (λ =1.064μm) for pumping narrow bandgap GaInAsP (λg>1.2μm) and a He-Ne laser (λ=0.6328 μm) for pumping GaInAsP and InP (λg=0.92μm). As a detector, germanium (Ge) and silicon (Si) PIN photodiodes is used. The PL signals are measured using lock-in technique. The measurement is taken place at room temperature and 77K.

We can determine the compositional ratio x and y of lattice matched $Ga_xIn_{1-x}As_yP_{1-y}$ from the PL emission wavelength using next equations;

$$Eg = 1.35 - 0.72y + 0.12y^2 \qquad (3.14)$$

$$x \approx 0.47y \qquad (3.15).$$

where Eg is bandgap energy of GaInAsP and corresponds to the PL peak wavelength. For the case of the lattice mismatch $Ga_xIn_{1-x}As_yP_{1-y}$, determination of the compositional ratio is slightly difficult because the emission peak wavelength is changed by strain. The relation between lattice mismatch and emission wavelength is discussed in next chapter.

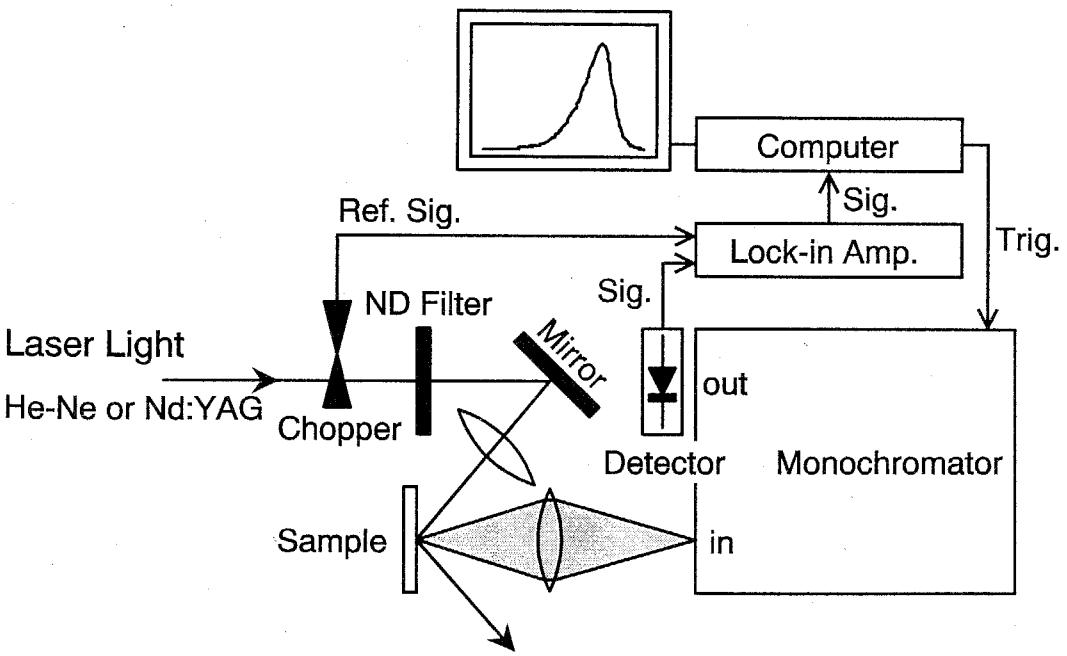

Fig. 3.8 Photoluminescence (PL) measurement system. He-Ne laser and Nd:YAG laser are used as excitation light sources.

3.3.3 Growth Conditions and Characterization of InP and GaInAsP

The growth conditions of CBE technique is examined by 1) growth temperature, 2) V/III ratio, 3) gas flow rate i.e. growth rate. An important thing is that V/III ratio is related to cracking efficiency of HT-Cell which is changed by cell temperature.

The growth conditions are determined by the results of surface morphology, PL emission intensity and FWHM, and residual doping concentration. For example, the surface morphology of InP epitaxial layer is very sensitive to the growth temperature. Figure 3.9 shows the surface morphology of InP under different growth temperatures. The flow rate of TMIn and PH_3 was 0.7sccm and 10sccm, respectively and then V/III ratio was about 14. The growth rate was about 1.0μm/hour.

Surface defect observed under high growth temperature is related with phosphorus desorption and it is modified by control of V/III ratio or by increase of PH_3 cracking efficiency. As the result of growth under various conditions, the range of growth condition for good crystal quality was achieved. The typical growth conditions are summarized in table 3.2.

The photoluminescence spectra are shown in Fig. 3.10 for various bandgap GaInAsP. In this figure, the peak intensities of samples are normalized. All the samples are undoped and the thicknesses are about 0.5μm with InP buffer layer. Some samples have InP capping layer. The substrate surface and epitaxial surface have defects or surface states, so the nonradiative carrier recombination occurs. Hence the double heterostructure with InP buffer layer and InP capping layer emitted strongly. The line widths (FWHM) are slightly varied for each sample. The reasons may be due to alloy broadening and difference of density of states. The PL line width and its intensities are as well as that of LPE grown wafers prepared in our laboratory. The result shows the good crystal quality of CBE grown wafers.

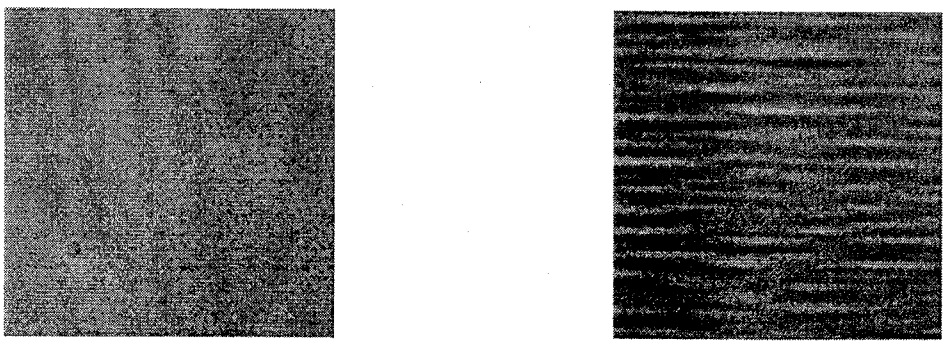

Tg=500°C　　Tg=525°C

Fig. 3.9 Photograph of surface morphologies of epitaxial InP layer for different growth temperature. The HT-Cell is made of PBN and the temperature is set to 850°C. (growth rate: 1.0μm/h, V/III=14)

Table 3.2 Summary of typical growth conditions.

TMIn Bubbler Temp./Press.		25°C/2.58Torr
TEGa Bubbler Temp./Press.		25°C/4.78Torr
Carrier Gas Press.		30Torr
Max. TMIn Flow		1.58 sccm
Max. TEGa Flow		1.64 sccm
Max. PH_3 Flow		15.2 sccm
Max. AsH_3 Flow		8.0 sccm
Cracking Cell Temp.		850°C (PBN)
Low Temp. Cell		100°C
Growth Temperature		500°C
Substrate Rotation		20-40 rpm
Background Press.		<5×10^{-5}Torr (during growth)
InP	Growth rate	1.0-1.5μm/h
	TMIn Flow	0.6-1.0sccm
	V/III ratio	10-15
GaInAsP (λg=1.15-1.55μm)	Growth rate	1.5-2.0μm/h
	V/III ratio	5-12
GaInAs	Growth rate	1.5-2.5μm/h
	V/III ratio	2-4

Figure 3.11 shows the relation between gas flow ratio of group III and group V sources and PL peak wavelength at growth temperature of 500°C. In this figure, all samples have lattice mismatch of less than 0.1%. The dashed lines are the relation between compositional ratio of lattice matched GaInAsP and bandgap energy calculated by Eq. (3.14) and (3.15). From the result, the gas flow ratio is not agreement with the compositional ratio. This phenomenon indicates the existence of nonlinearity for dissociation rate and/or sticking efficiency. For narrower bandgap GaInAsP, group III ratio is only slightly changed and it make difficult the control of lattice mismatch. However, in real growth, the wide range of bandgap energy material is possible to grow by controlling the gas flow ratio accurately.

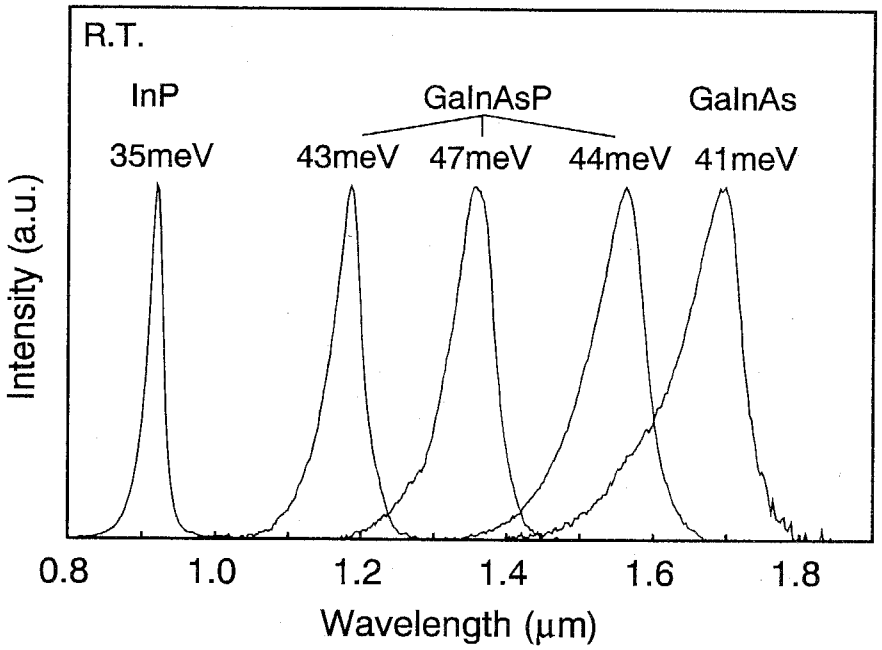

Fig. 3.10 Typical photoluminescence spectra of InP, GaInAsP (λg=1.2μm, 1.35μm, 1.55μm), GaInAs at room temperature. All samples are non-doped and the thickness is about 0.5μm. InP sample was grown on s.i.-type InP substrate because s.i.-type InP hardly emitted.

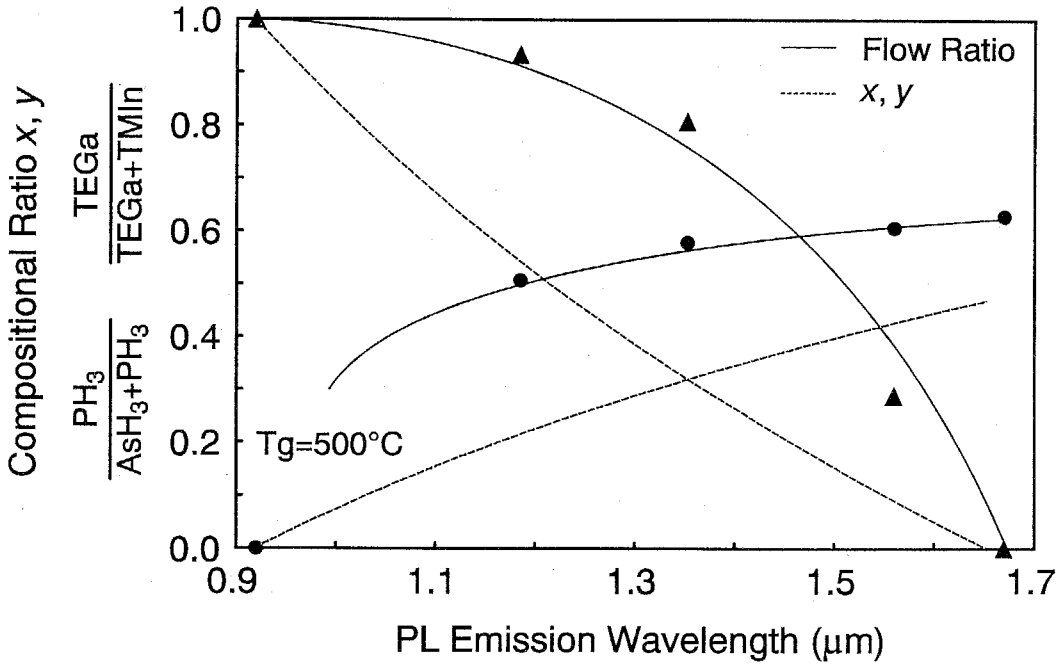

Fig. 3.11 Gas flow ratios for group III and Group V. All samples of GaInAsP are lattice matched to InP ($\Delta a/a<\pm 0.1\%$). The dotted lines show compositional ratio of Ga and P calculated by Eq. (3.14) and (3.15).

Next, the doping controllability is described. The required doping range of surface emitting laser wafer is from $10^{17}cm^{-3}$ to mid $10^{19}cm^{-3}$ without deterioration of crystal quality and surface morphologies. The residual impurity level is typically $1\times10^{16}cm^{-3}$ for InP and $1\times10^{15}cm^{-3}$ for GaInAs under typical growth condition. The doping control was carried out by controlling the temperature of dopant cells. Figure 3.12 shows an example of the doping profile measured by C-V etching profiler. The sample has two layers of InP which is grown under different growth rate of 1.0μm/h and 1.5μm/h. The doping is n-type by Si for the same Si cell temperature of 1090°C. The top layer of 1.5μm/h region is $n=4\times10^{17}cm^{-3}$ and 1.0μm/h region is $n=7\times10^{17}cm^{-3}$. The doping concentration is inversely proportional to the growth rate for the same dopant cell temperature.

The relation between doping concentration and Si cell temperature is shown in Fig. 3.13 (a) for InP and GaInAsP. Figure 3.13 (b) shows that of Be dopant. In these figures, the growth rates of the samples are not the same. However, the doping concentrations are almost determined by cell temperature because the difference of growth rates is not so large. From the result, doping concentration is proportional to the vapor pressure of the dopant sources, and hence precise doping level control is possible by only setting the cell temperature.

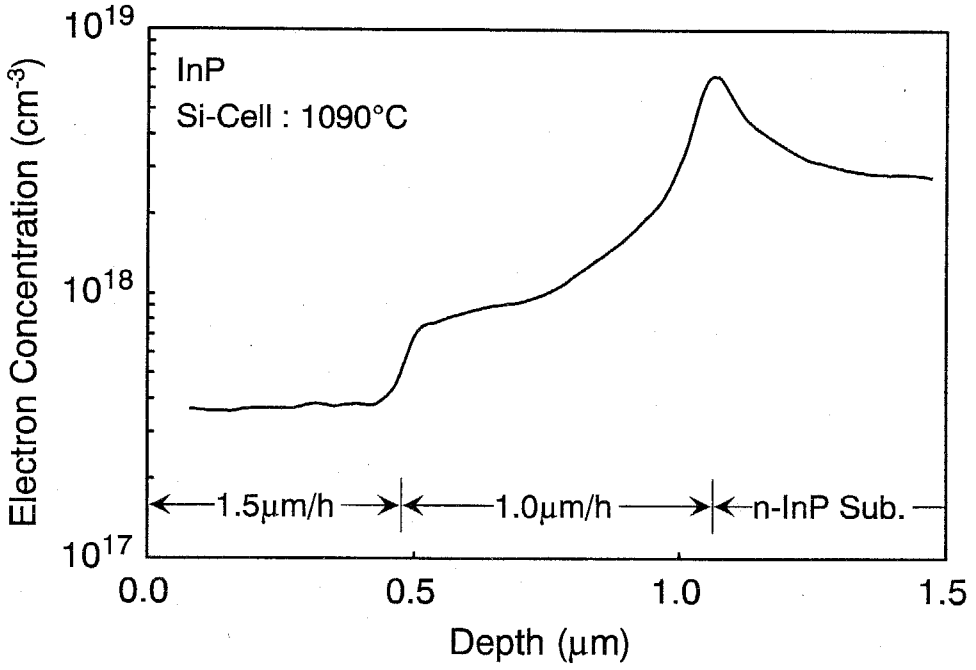

Fig. 3.12 Example of doping depth profile. The sample has two InP layers with different growth rate. Si (n-type) cell temperature is the same for both layer growths.

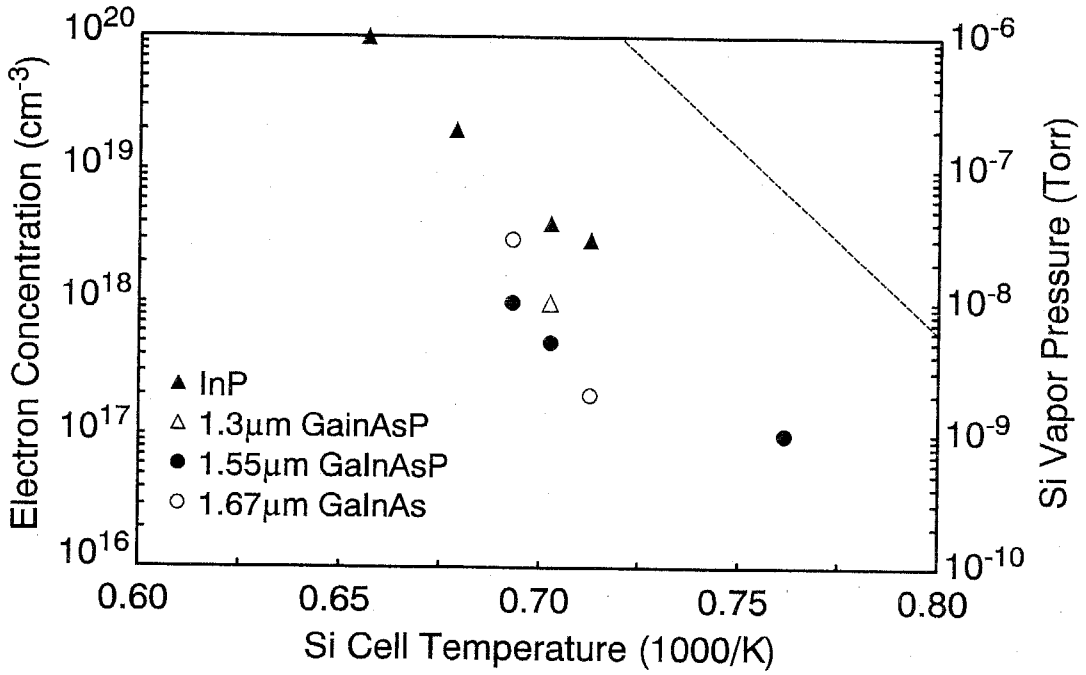

(a) n-type : Si doping

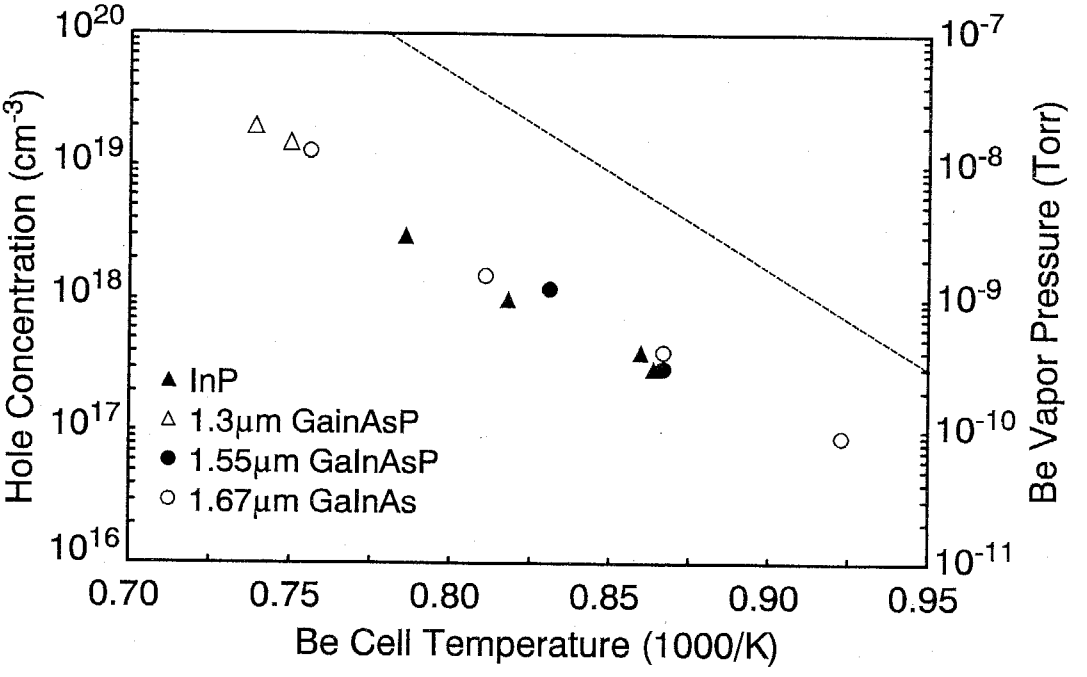

(b) p-type : Be doping

Fig. 3.13 Carrier concentration of InP, GaInAsP, GaInAs versus Si (a), Be (b) cell temperatures.

3.3.4 Growth of GaInAsP/InP Multilayer Reflector

As mentioned above section, InP and GaInAsP materials are successively grown by CBE at the point of compositional controllability and doping controllability. For realizing surface emitting lasers, the thickness controllability is also important because the epitaxial layer thickness is directly related to the lasing wavelength. The layer thickness is controlled by the growth time and the effective group III gas flow represented by Eq. (3.9) and (3.10). The gas flow is controlled by MFC, however the effective group III gas flow is changed by the temperature of bubblers and gas lines, so the temperature of the growth system is required to stable. In this study, the roughness measurement system was used to observe accurate thickness. This technique has very small error (few 10Å) for wide thickness range (0.01μm to few μm), though the selective etching between substrate and epitaxial layer is necessary. For measurement of ultra-thin layers such as QWs, we can determine the thickness of period from the X-ray diffraction curve of periodic structure. (The detail is mentioned in chapter 4.) Using these techniques, the growth thickness and growth rate is determined.

The semiconductor distributed Bragg reflector (DBR) or multilayer reflector is useful for surface emitting lasers as discussed in chapter 2. To realize DBR, both thickness and composition controllability are required because the optical path length is composed of the refractive index and the thickness. As the demonstration of applicability of CBE, GaInAsP/InP DBR was grown. The reflectivity spectrum of DBR is shown in Fig. 3.14 by

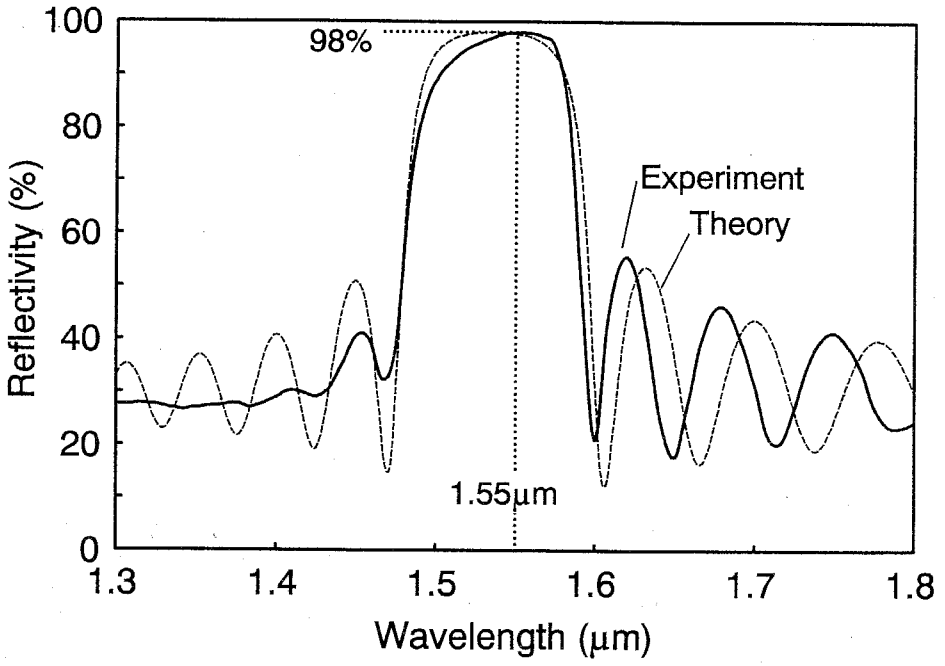

Fig. 3.14 Spectrum of semiconductor multilayer reflector. The structure consists 24pair of GaInAsP (λg=1.45μm, 1110Å) and InP (1220Å).

solid curve. InP and GaInAsP (λg=1.45μm) are selected as low and high index material, respectively. The DBR was grown on the InP substrate consisted 24pairs of InP (1220Å) and GaInAsP (1110Å) and total thickness was about 5.5μm. InP is doped at $n=1\times10^{18}cm^{-3}$ and GaInAsP is doped at $n=6\times10^{17}cm^{-3}$. The peak reflectivity was 1.55μm wavelength which was designed wavelength and the peak reflectivity was 98%. The measured reflectivity is good agreement with calculated one. It indicates the good controllability of the thickness and composition with good surface morphology. Furthermore, the thickness and composition fractuation may be negligible during growth. To apply the DBR to the surface emitting lasers, it is required more high reflectivity to obtain low threshold current. On the other hand, these results are enough to grow hybrid mirror-type surface emitting lasers.

In addition to the thickness controllability, thickness uniformity is also important characteristics to obtain uniform lasing characteristics. Figures 3.15 (a) and (b) show the thickness uniformity with substrate rotation (a) and without rotation (b) during growth. To measure the thickness variation, the cavity resonance wavelength is measured for the wafer of hybrid-mirror surface emitting lasers shown in chapter 5. From the Fig. 3.15 (a), the uniformity is less than 1% at the center of Mo block for the area of $10\times12mm^2$, and at the off-center, that is about 2%. The non-uniformity at the off-center position is due to non-uniformity of thermal distribution because the off-center position is not used for usual growth. For the non-rotation case, the uniformity for center and off-center position are worse comparable with that for rotation case. The reason of non-uniformity is difference of arrival rate of molecular beam and thermal distribution. Substrate rotation and using usual position is important to obtain uniform characteristic devices.

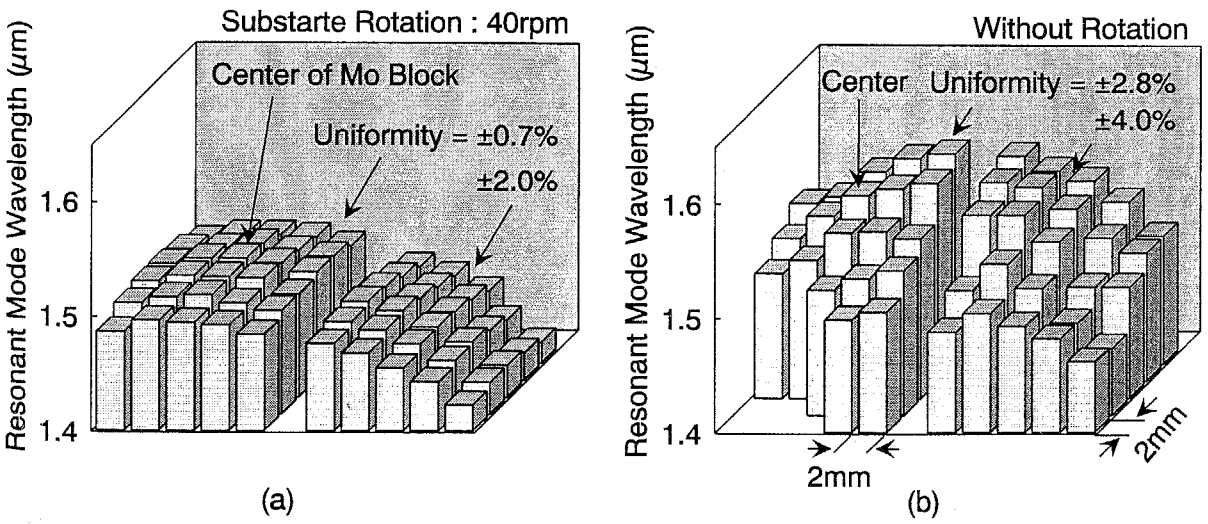

Fig. 3.15 Thickness uniformity measurement by measure the resonance mode wavelength.

3.4 Evaluation of GaInAsP/InP Laser Wafers

3.4.1 Growth and Fabrication of Laser Structures

In this section, wide-stripe-contact lasers were fabricated in order to evaluate the crystal quality as the laser materials.

The grown wafer structure and fabricated laser structure is shown in Fig. 3.16. The wafer was designed to utilize not only stripe-contact lasers but also surface emitting lasers. The active layer thickness of 1.0μm is designed to lase at room temperature as discussed in chapter 2. The structure consists of a 0.3μm n-GaInAsP (λg=1.3μm, $2\times10^{18}cm^{-3}$) etch stop layer which is required to fabricate the surface emitting laser structure. A 1.0μm-2.0μm n-InP ($2\times10^{18}cm^{-3}$) cladding layer is grown on the etch stop layer. The active layer is bulk GaInAsP (λg=1.55μm) and the thickness is 1.0μm. Then a 1.0μm-1.5μm p-InP ($5\times10^{17}cm^{-3}$) cladding layer and a 0.25μm p^+-GaInAsP (λg=1.3μm, $2\times10^{19}cm^{-3}$) contact layer is grown.

The fabrication process of stripe lasers is not so complicated. The SiO_2 insulator layer was deposited thickness of about 1500-2000Å by spattering technique. Then, the substrate was polished to about 100μm. The stripe width was 50μm by photolithography technique. The electrode material was evaporated AuGe (about 1000Å) for n-substrate side and Au/Zn/Au (250Å/500Å/1000Å) for p-side. The annealing process is performed independently for each side. The annealing temperature and time are 440°C with 2min for n-side and 410°C with 2min for p-side.

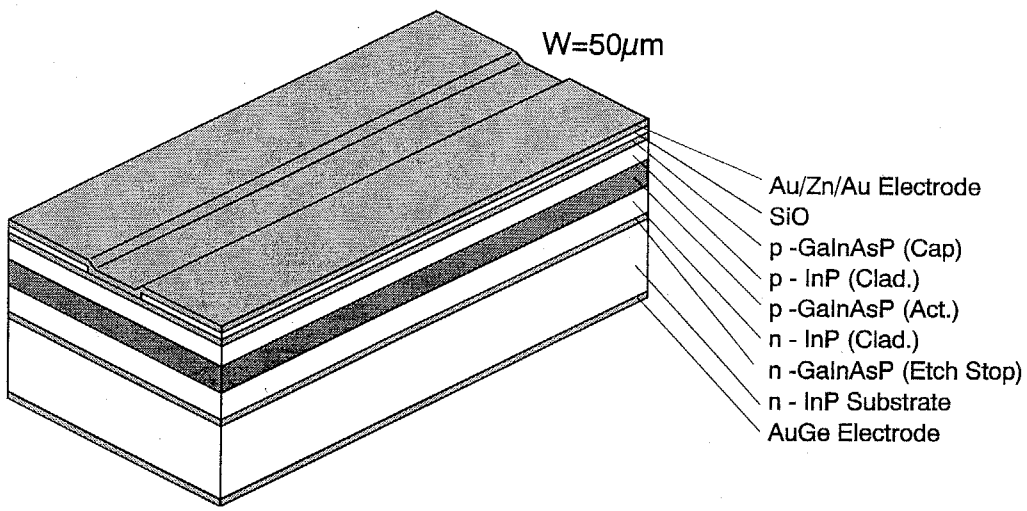

Fig. 3.16 Stripe contact laser structure for evaluating the laser material quality. The etching stop layer is grown to applying surface emitting lasers.

3.4.2 Evaluation of Stripe Contact Laser Characteristics

The laser wafer was cleaved to each devises and mounted without any solder. The cavity length was varied about from 200μm to 500μm. The measurement was performed under pulsed condition to avoid the thermal effect at room temperature. The threshold current density of 5.0kA/cm^{2}μm was observed for minimum threshold and averaged threshold current density was 6-7kA/cm^{2}μm. These values are almost comparable to the laser device with the same structure grown by liquid phase epitaxial method (LPE) in this laboratory [26]. The obtained threshold current density is also plotted against the active layer thickness in Fig. 3.17 compared with some other results obtained by CBE [27, 28]. The dashed line represents theoretically estimated values. The value for 1.0μm active layer thickness is in agreement with the theoretical value and other CBE-grown lasers. From the result, the laser material grown in this study has almost the same crystal quality with the other CBE-grown materials and sufficient to apply the surface emitting lasers.

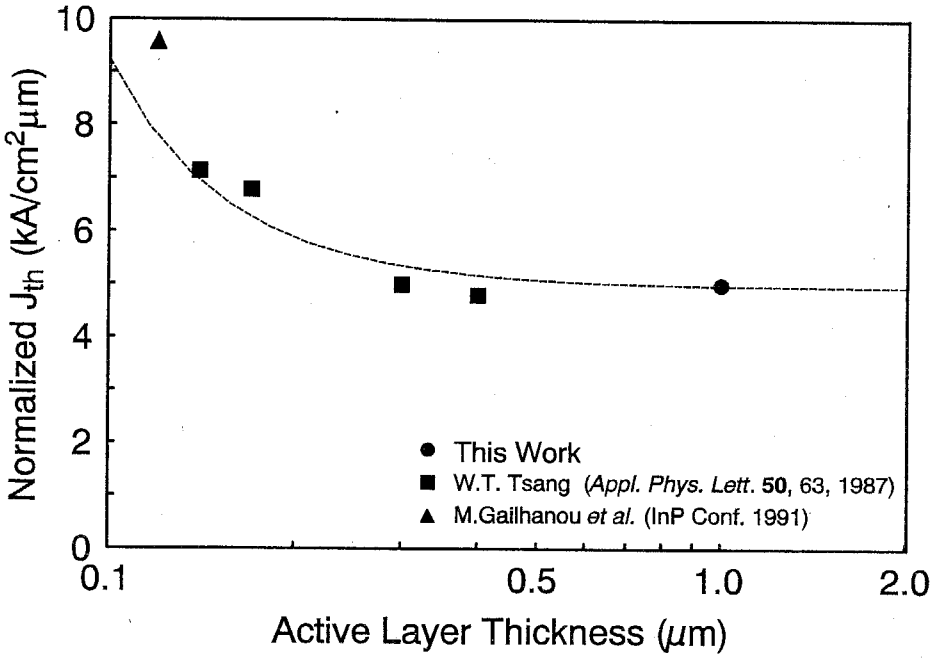

Fig. 3.17 Normalized threshold current density vs. active layer thickness.

References

[1] for a review, G. H. Olsen, "Vapor-phase epitaxy of GaInAsP," in GaInAsP Alloy semiconductors, T. P. Pearsall, Ed., John Wiley & Sons Ltd., New York, 1982.

[2] A. Y. Cho, "Recent developments in molecular beam epitaxy," *J. Vac. Sci. Technol.*, vol. 16(2), p. 275, 1979.

[3] M. B. Panish, and S. Sumski, "Gas source molecular beam epitaxy of $Ga_xIn_{1-x}As_yP_{1-y}$," *J. Appl. Phys.*, vol. 55, p. 3571, 1984.

[4] E. Venhoff, W. Pletschen, P. Balk, and H. Lüth, "Metalorganic CVD of GaAs in a molecular beam system," *J. Crystal Growth*, vol. 55, p. 30, 1981.

[5] J. R. Knight, D. Effer, and P. R. Evans, *Solid State Electron.*, vol. 8, p. 178, 1965.

[6] J. J. Tietjen and J. A. Amick, *J. Electrochem. Soc.*, vol. 113, p. 724, 1966.

[7] H. M. Manasevit, "Single-crystal GaAs on insulating substrate," *Appl. Phys. Lett.*, vol. 12, p. 156, 1968.

[8] H. M. Manasevit, and W. J. Simpson, "The use of metal-organics in the preparation of semiconductor materials, the formation of In-group V compounds and alloys," *J. Electrochem. Soc.*, vol. 116, p. 1725, 1969.

[9] H. M. Manasevit, *J. Crystal Growth*, vol. 13, p. 306, 1972.

[10] A. Y. Cho, *J. Vac. Sci. Technol.*, vol. 8, p. 531, 1971.

[11] L. L. Chang, L. Esaki, W. E. Howard, and K. Ludeke, *J. Vac. Sci. Technol.*, vol. 10, p. 11, 1973.

[12] A. Y. Cho, and J. R. Arthur, *Prog. Solid State Chem.*, vol. 10, p. 157, 1975.

[13] F. J. Morris, and H. Fukui, "A new GaAs, GaP, and $GaAs_xP_{1-x}$ vacuum deposition technique using arsine and phosphine gas," *J. Vac. Sci. Technol.*, vol. 11, p. 506, 1974.

[14] M. B. Panish, "Molecular beam epitaxy of GaAs and InP with gas source for As and P," *J. Electrochem. Soc.*, vol. 127, p. 2729, 1980.

[15] A. R. Calawa, "On the use of the AsH_3 in the molecular beam epitaxial growth of GaAs," *Appl. Phys. Lett.*, vol. 38, pp. 701-703, 1981.

[16] M. B. Panish, H. Temkin, and S. Sumski, "Gas source MBE of InP and $Ga_xIn_{1-x}P_yAs_{1-y}$: materials properties and heterostructure lasers," *J. Vac. Sci. Technol.*, vol. B3, p.657, 1985.

[17] M. B. Panish, H. Temkin, R. A. Hamm, and S. N. G. Chu, "Optical properties of very thin GaInAs(P)/InP quantum wells grown by gas source molecular beam epitaxy," *Appl. Phys. Lett.*, vol. 49, pp. 164-166, 1986.

[18] W. T. Tsang, "Chemical beam epitaxy of InGaAs," *J. Appl. Phys.*, vol. 58, p. 1416, 1985.

[19] W. T. Tsang, E. F. Schubert, T. H. Chiu, J. E. Cunningham, E. G. Barkhart, J. A. Ditzenberger, and E. Agyekun, "Growth of high-quality $Ga_xIn_{1-x}As_yP_{1-y}$ by chemical beam epitaxy," *Appl. Phys. Lett.*, vol. 51, pp. 761-763, 1987.

[20] W. T. Tsang, "Chemical beam epitaxy of $Ga_{0.47}In_{0.53}As$/InP quantum wells and heterostructure devices," *J. Crystal Growth*, vol. 81, p. 261, 1987.

[21] W. T. Tsang, F. K. Reinhart, and J. A. Ditzenberger, "1.3-μm wavelength GaInAsP/InP double heterostructure lasers grown by molecular beam epitaxy," *Appl. Phys. Lett.*, vol. 41, pp. 1094-1096, 1982.

[22] G. D. Holah, F. L. Eisele, E. L. Meeks, and N. W. Cox, "Growth of InGaAsP by molecular beam epitaxy," *Appl. Phys. Lett.*, vol. 41, pp. 1073-1075, 1982.

[23] G. J. Davies, P. J. Skevington, J. C. Morris, A. C. Jones, S. Rushworth, J. S. Foord, and C. L. Levoguer, "Some comparisons of chemical beam epitaxy InGaAs/InP growth using triethylgallium, triisopropylgallium and triisobutylgallium sources," *J. Crystal Growth*, vol. 136, p. 133, 1994.

[24] D. A. Bohling, C. R. Abernathy, and K. F. Jensen, "Chemical/surface mechanistic considerations in the design of novel precursors for metalorganic molecular beam epitaxy," *J. Crystal growth*, vol. 136, p. 118, 1994.

[25] G. B. Stringfellow, Ed., Organicmetallic Vapor-Phase Epitaxy: Theory and Practice, Academic Press, Boston, 1989.

[26] K. Iga, H. Soda, T. Terakado, and S. Shimizu, "Lasing characteristic of GaInAsP/InP surface emitting lasers," *Trans. IECE*, vol. E68, pp. 91-97, 1985.

[27] W. T. Tsang, "GaInAsP/InP double heterostructure lasers emitting at 1.5μm grown by chemical beam epitaxy," *Appl. Phys. Lett.*, vol. 50. pp. 63-65, 1987.

[28] M. Gailhanou, L. Goldstein, P. A. Buffat, P. Brosson, B. Fernier, and J. Benoit, *The Third International Conference on Indium Phosphide and Related Materials*, Apr., 1991, Cardiff, Wales, UK, paper PD11.

Chapter 4

Growth and Characterization of Quantum Well Structures

In this chapter, growth capabilities of ultra-thin layers by CBE are investigated and the applicability of quantum wells to surface emitting lasers is also described.

4.1 Growth of Unstrained/Strained GaInAs/InP Quantum Wells

4.1.1 Growth of Quantum Well Structures

The quantum well structure is one of superior active layer material as described in chapter 2. To apply QW structures to the active layer of surface emitting laser, it is important to optimize the growth techniques and investigate QW characteristics.

Figure 4.1 shows a schematic structure of grown samples for investigation QW characteristics. In this section, all samples are grown with InP barriers and GaInAs wells because the layer structure is relatively simple. The sample with GaInAsP barriers is discussed in next section. Grown samples consist 10 GaInAs wells and 11 InP barriers. The GaInAs well is lattice matched to InP or compressively strained. The gas valve sequence of barrier to next barrier is shown in Fig. 4.2 for GaInAs/InP QWs and GaInAsP/InP QWs. To avoid the desorption of group V atoms, group V gases are always supplied. For GaInAs well structure, the group V gas of phosphine and arsine is used in only InP and GaInAs, respectively, and the group III gas of TEGa is only used in GaInAs. Therefore, GaInAs/InP MQWs don't require the flow rate change for any gas under the same TMIn flow condition and the growth interruption time is only 3sec. The growth rate described in chapter 3 corresponds to about 1-2 monolayer (ML) per seconds. Therefore, the growth interruption time effects to the structure and its characteristic strongly because the growth time of well is

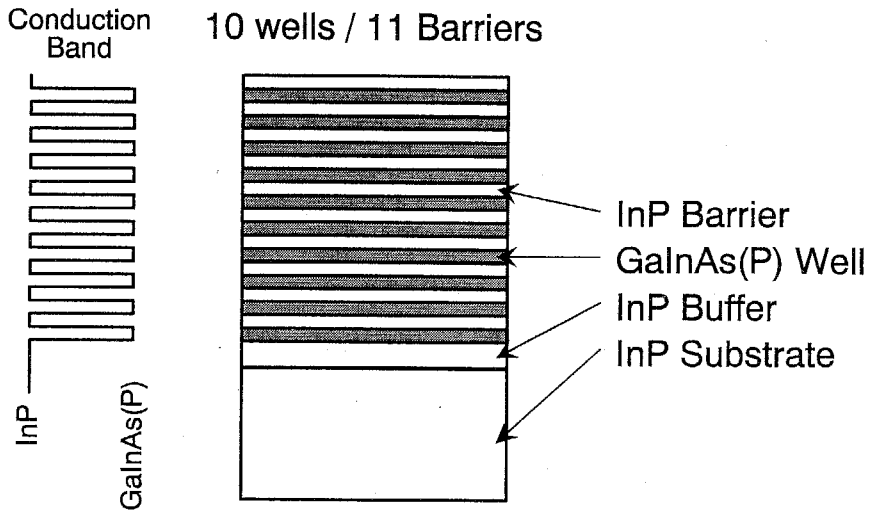

Fig. 4.1 Schematic view of GaInAs/InP quantum well structure grown for characterizing the unstrained/strained QWs.

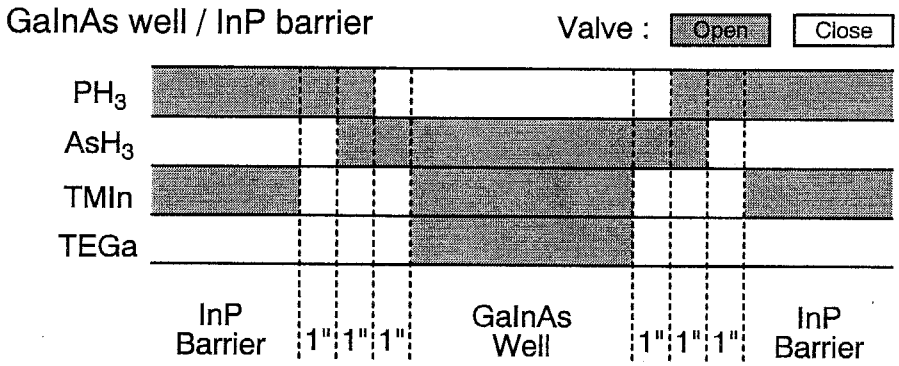

Fig. 4.2 Valve sequences for GaInAs well structure with InP barrier. The growth interruption time is controlled to 3 seconds.

usually less than few 10 seconds. Though it is known that such growth interruption is effective to obtain flat and abrupt interface [1], the growth interruption causes to reduce the PL intensity slightly due to increase of interface recombination.

4.1.2 Determination of Quantum Well Structures

The quantum well structure consists structural parameters of thickness and composition for both well and barrier. The composition is classified to bandgap energy and strain. In this study, X-ray diffraction measurement is used to determine the thickness and strain of QWs [2, 3, 4]. We can determine the composition of GaInAs from the strain because the lattice constant of ternary material such as GaInAs is fixed against the composition.

First, the estimation method of the QW period is mentioned. The satellite peaks originated from QW periodicity is observed in X-ray diffraction curve. Figure 4.3 shows an example of X-ray diffraction curve of GaInAs/InP MQW structure with theoretically calculated curve (Appendix B). As satellite peaks are observed symmetry for this sample, the well is considered to be lattice matched to InP substrate. We can see satellite mode of ±6th. This result indicates the good periodicity of QWs and good abruptness at each interface.

For (m00) X-ray diffraction, the period D of QW structure is estimated from Bragg condition and represented as;

$$D = \frac{a \cdot \tan(\theta)}{m \cdot \Delta\theta} \qquad (4.1)$$

where a is averaged lattice constant of MQW and 5.8688Å for lattice matched QW. m is usually 4 because the diffraction signal is large compared with other number. θ is fundamental (0th) satellite peak angle and 2θ is 63.34 (deg) for lattice matched QWs which is the same as InP substrate angle as described in chapter 3. Δθ is angle spacing between 0th and 1st satellite peak. If there are two samples with the same growth condition except growth time of either barrier or well, the thickness of well and barrier is completely determined by simultaneous

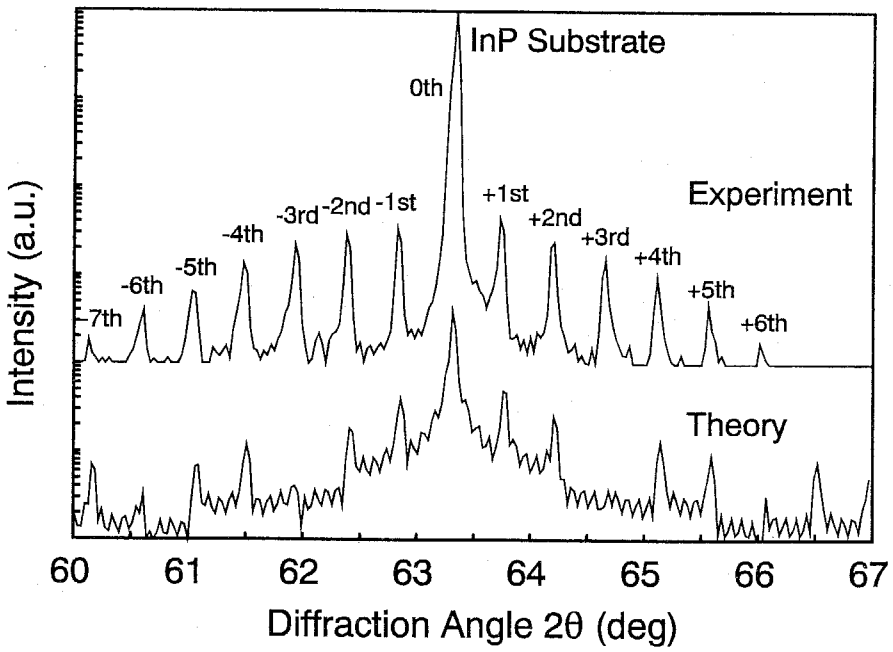

Fig. 4.3 Satellite signal in X-ray diffraction curve for unstrained GaInAs/InP 10QW. The well and barrier thickness is estimated to be 80Å and 150Å, respectively.

equation with respect to each thickness. The growth rate of each material is calculated from the thickness and growth time. The period of QW shown in Fig. 4.2 is estimated to be 230Å (78ML) and the sample is estimated to consists 80Å (27ML) GaInAs well and 150Å (51ML) InP barrier. For the lattice matched $Ga_{0.47}In_{0.53}As$/InP QW, barrier and well thicknesses are all of structure parameters.

The X-ray diffraction curve for strained GaInAs/InP QWs are shown in Fig. 4.4. The QW period of 188Å (64ML) is estimated from Eq. (4.1). The barrier and well thickness is determined by the same method of lattice matched QWs. The fundamental (0th) peak angle is shifted by the averaged QW monolayer thickness. For the compressively strained QWs, the 0th peak is placed at small diffraction angle comparable with InP peak because the compressively strained material has larger lattice constant than InP. The strain of well is determined by fitting the envelope curve of each peaks with theoretically calculated diffraction pattern. We can see good agreement between the measured and calculated curves. The error of structure parameter, thickness and strain, may be less than one ML and less than ±0.05% strain by this fitting method. As the result, the structure shown in Fig. 4.4 consists 8ML 1.0% compressively strained GaInAs well and 56ML InP barrier.

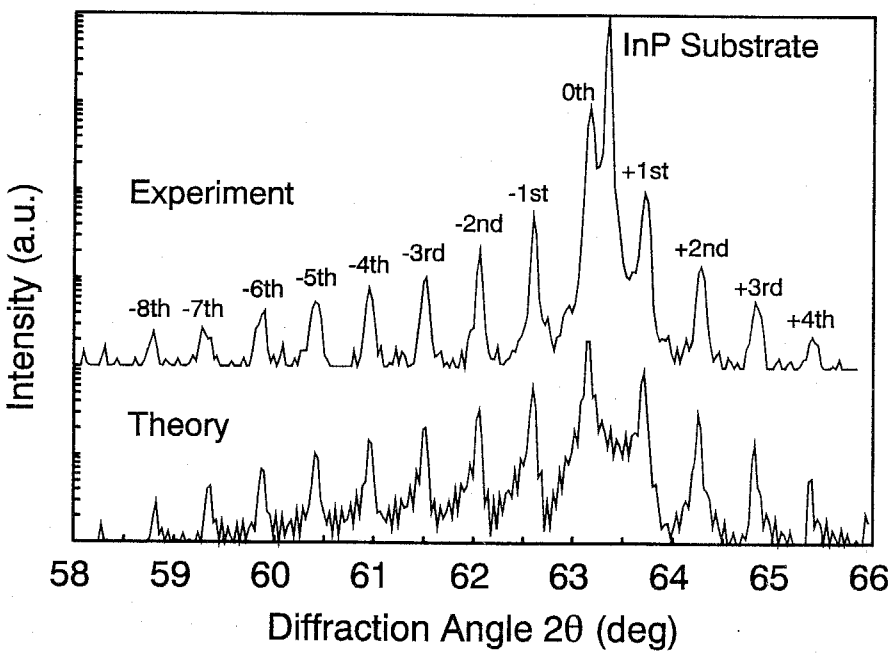

Fig. 4.4 X-ray diffraction pattern for compressively strained GaInAs/InP 10QW. Well strain is 1%. The well and barrier thickness is 24Å and 164Å, respectively. The 0th peak is positioned at the small diffraction angle to the InP substrate peak.

4.1.3 Evaluation of Quantum Well Characteristics

The characteristics of quantum well structures are evaluated by PL measurement at room temperature and 77K. The PL measurement system is the same as shown in chapter 3. For low temperature measurement, samples are dipped into the liquid nitrogen (LN_2) in the transparency glass receptacle.

Figure 4.5 shows the emission peak wavelength for various unstrained/strained GaInAs/InP QWs at room temperature. The well thicknesses were proportional to the growth time. Dashed lines represent theoretically estimated transition energy using effective mass approximation (Appendix C). The parameters used in calculation is shown in table 4.1. The band discontinuity ΔEc is referred from the result of Cavicchi et al. [5]. Though ΔEc is important parameter for design of device structure, it is one of not fully cleared parameter for GaInAsP/InP system [6, 7]. Furthermore, the strain effects confuse the determination of its discontinuity [8]. However, the measured emission peaks are good agreement with theory and the results indicate good controllability of emission wavelength.

Figure 4.6 shows the PL linewidth for 1% compressively strained $Ga_{0.32}In_{0.68}As/InP$ QWs at 77K and room temperature. At 77K, almost samples show the linewidth of around 16meV. These linewidth are comparable or better than some of strained or unstrained QWs

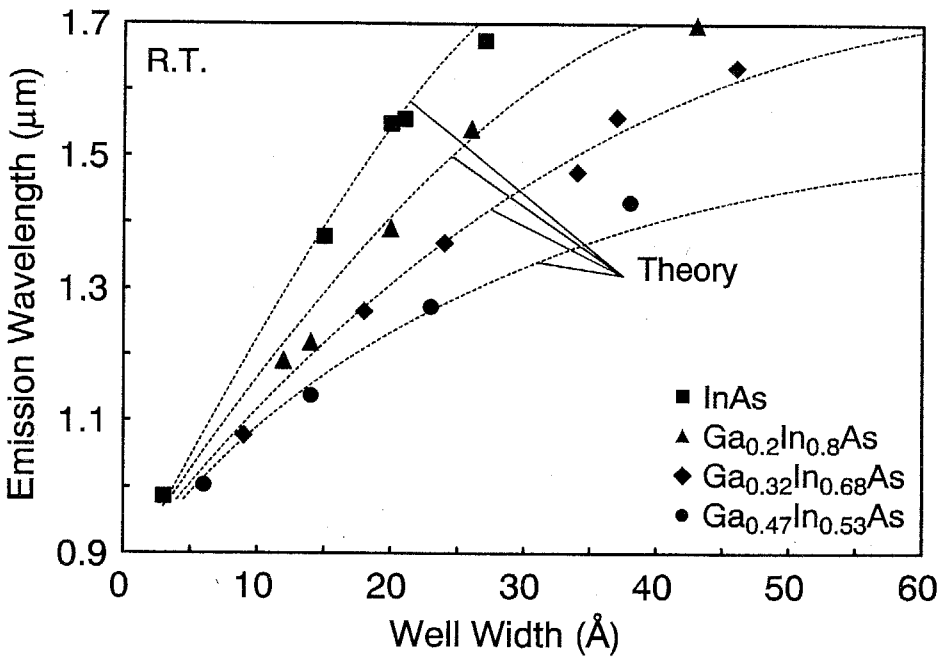

Fig. 4.5 PL Emission wavelength versus well thickness for various strained/unstrained GaInAs/InP QWs. Dashed lines show the theoretically calculated results.

Table 4.1 Parameters for emission energy calculation.

	InP	$Ga_{0.47}In_{0.53}As$	$Ga_{0.32}In_{0.68}As$	$Ga_{0.20}In_{0.80}As$	InAs
Strain ε (%)	-	0	1.0	1.8	3.2
Bandgap energy Eg (eV)	1.35	0.75	0.64	0.55	0.42
Conduction band offset (eV)	-	0.30	0.32	0.40	0.48
Electron mass m_e (m_0)	0.08	0.044	0.037	0.032	0.023
Heavy hole mass m_{hh} (m_0)	0.56	0.43	0.42	0.42	0.41

grown by others [8, 9]. The linewidths at room temperature are about 30meV. These values are narrower than that of bulk as shown in chapter 3. This is due to step-like density of states of QW structure. On the other hand, the linewidth is rapidly increased for the well thickness less than 20Å. Such linewidth increases for QWs have been reported and considered as follows. Singh and Bajaj considered the broadening mechanism as the result of alloy disorder in the barrier and/or well region and furthermore the importance of the interface roughness was discussed [10]. Welch et al. reported the reasons as the transfer of electrons from the cladding layer to the well and interface roughness [11]. Considering the reason as the interface roughness, the result in this study indicates that CBE grown samples have good interface uniformity and small fluctuation less than two monolayers. On the other hand, I observed small sub-peaks in the slope of short wavelength region for some samples. Such sub-peaks may be originated not only from the layer fluctuation but also from transition about second quantized level and/or light hole band. These sub-peaks broaden the emission linewidth, and therefore the linewidth does not always show the crystal quality or interface roughness.

Figure 4.7 shows the photoluminescence peak intensity against well thickness for different strain of 1% ($Ga_{0.32}In_{0.68}As$), 2% ($Ga_{0.2}In_{0.8}As$) and 3% (InAs) QWs. Intensities are relative to the sample of $Ga_{0.2}In_{0.8}As$ with a 20Å well thickness. We can see strong intensities around the 20Å well thickness for all three composition. Intensity decrease below the 20Å well width may caused by not only thickness and compositional fluctuations as previously described but also reduction of total well thickness which corresponds absorption layer thickness of excitation light. Furthermore, I consider another reason of intensity reduction. From the simple analysis of quantized energy for valence band, the energy difference between quantized energy and barrier band edge is decreased rapidly below 20Å well width. However, I can not explain the relation among the emission intensity and the band structure in detail.

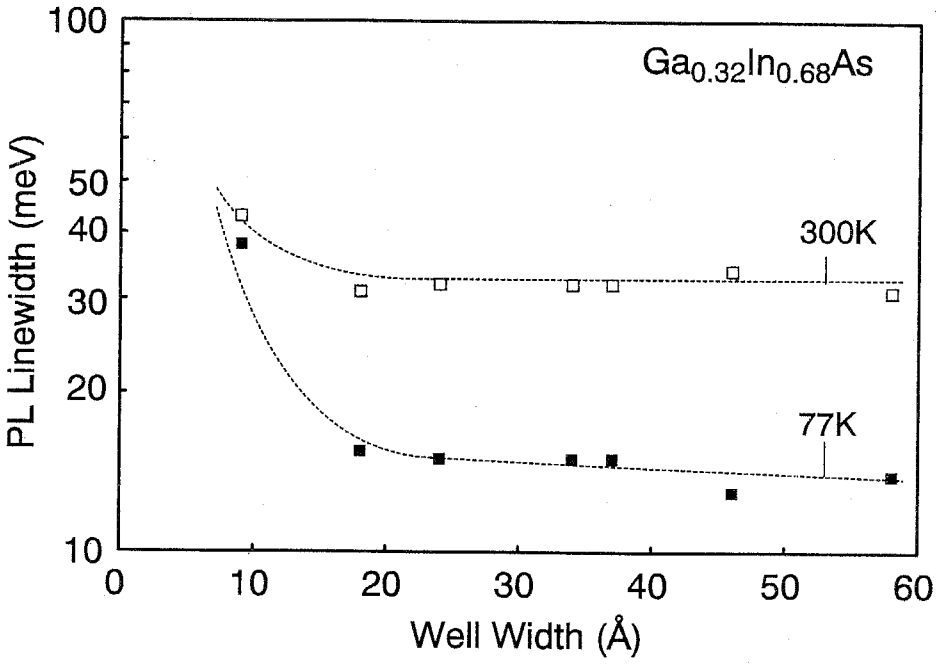

Fig. 4.6 Photoluminescence linewidth for various well thicknesses of 1% compressively strained GaInAs/InP QWs. The linewidth increase for less than 20Å well is due to interface roughness.

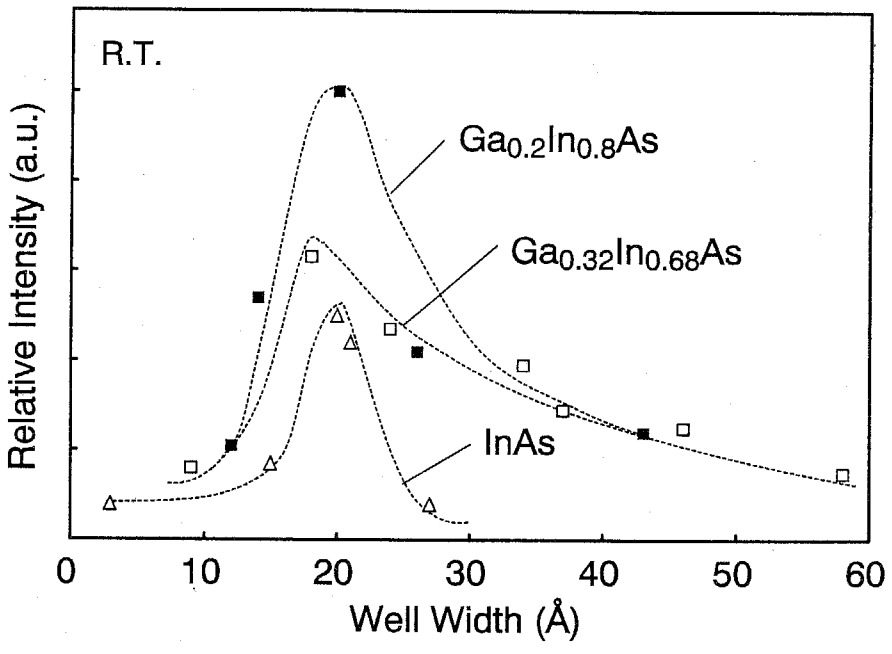

Fig. 4.7 Relative PL intensity of strained quantum wells against well thickness.

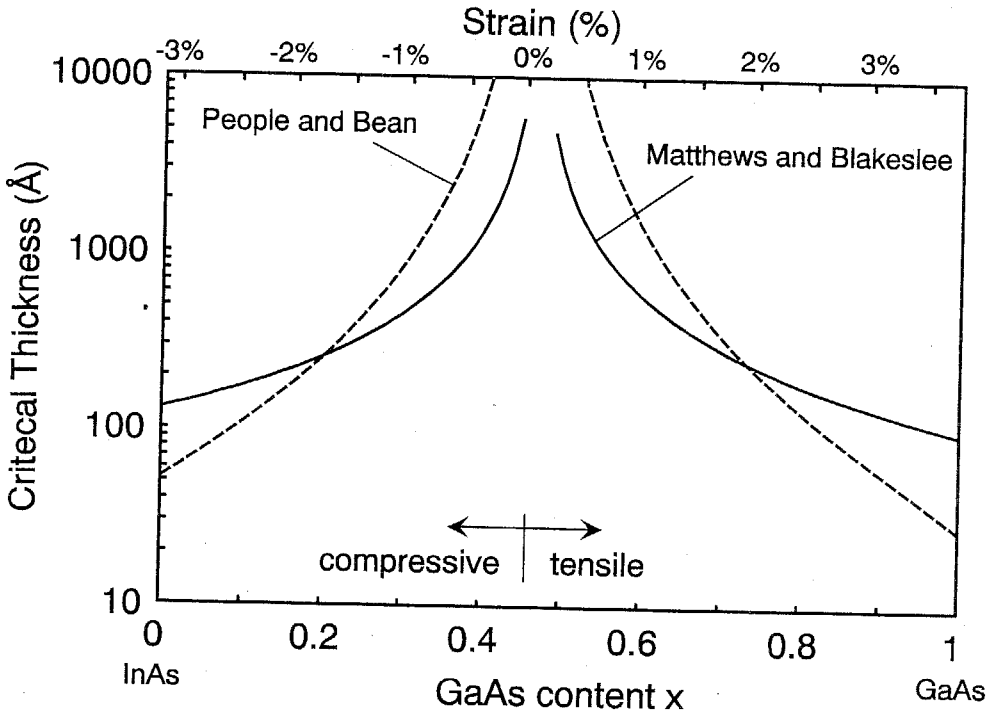

Fig. 4.8 Critical layer thickness Lc for $Ga_xIn_{1-x}As$/InP heterostructures.

Intensity decrease above 20Å well widths may be not due to degradation of crystal quality since linewidths shown in Fig. 4.6 are similar. However, the intensity reduction of the highest strain sample of InAs/InP QWs is considered due to the result of deterioration of crystal quality because the intensity decreased extremely rapidly.

It is known that the thick layer of strained material has misfit dislocations by the lattice mismatch, however sufficiently thin films are possible to grow without dislocations. Such strained material without dislocations is named pseudomorphic crystal and the limitation thickness is called critical layer thickness. The layer thickness of strained material should be less than the critical thickness to obtain good crystal quality. The critical layer thickness *Lc* is estimated from the energy balance model by People and Bean [12] and the mechanical equilibrium model by Matthews and Blakeslee [13] as follows;

$$Lc = \left(\frac{a}{32\sqrt{2}\pi\varepsilon^2}\right)\left(\frac{1-\upsilon}{1+\upsilon}\right)\ln\left(\frac{Lc\sqrt{2}}{a}\right) \qquad \text{(People et al.) (4.2)}$$

$$Lc = \left(\frac{a}{\sqrt{2}\pi|\varepsilon|}\right)\left(\frac{1-0.25\upsilon}{1+\upsilon}\right)\left(\ln\left(\frac{Lc}{\sqrt{2}a}\right)+1\right) \qquad \text{(Matthews et al.) (4.3)}$$

where a is lattice constant of free standing material and ε is strain and υ is Poisson's ratio. The

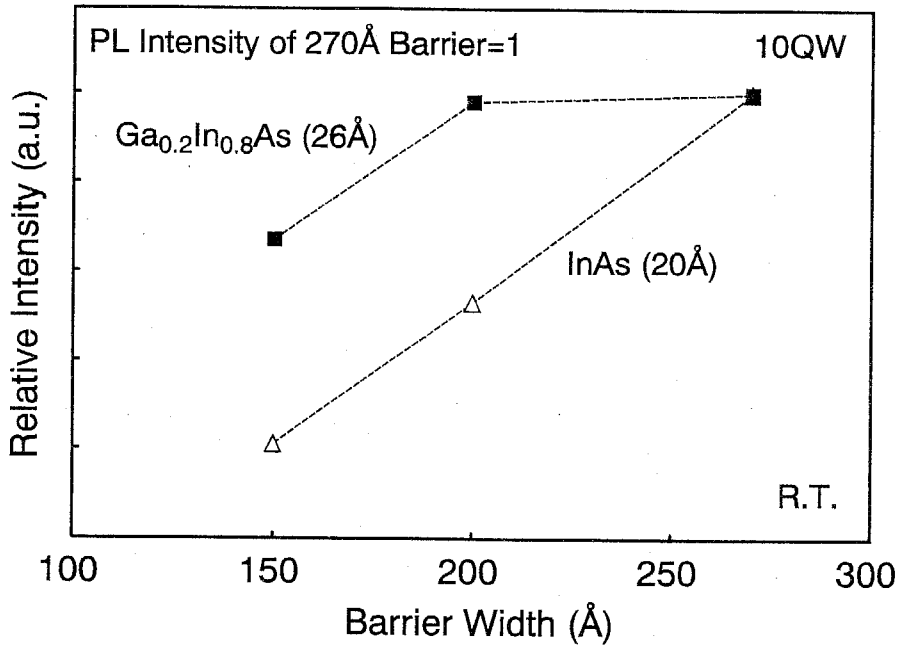

Fig. 4.9 PL intensity of strained quantum well as a function of InP barrier thickness. The samples emitted at 1.55μm wavelength. The InAs samples require thick barrier thickness in spite of thin well thickness.

results for $Ga_xIn_{1-x}As$ on InP are shown in Fig. 4.8. The thermal effect between growth temperature and room temperature, and multilayer effect such as MQW has not been fully cleared. However, it is important that the critical thickness limits the structure of strained QWs and the intensity reduction for above 20Å well of InAs/InP samples may be due to critical thickness.

To avoid the deterioration of crystal quality due to critical thickness, it is important that each layer thickness is less than critical layer thickness. However, the thickness of multilayer structure is considered to be related with averaged strain and total thickness. In order to sustain the coherency of structure to InP substrate, InP barrier must be thick enough to accommodate the well stress. Photoluminescence intensities were measured for various barrier thicknesses with the same well thickness. The result for $Ga_{0.2}In_{0.8}As$/InP with 28Å well and InAs/InP with 20Å well are shown in Fig. 4.9. For high compressively strained material of InAs, it is required a thick barrier to keep the high quality crystal.

As summary of this section, I grow the quantum well structures with InP barriers by chemical beam epitaxy with good thickness and composition controllability. The unstrained/strained QWs show good photoluminescence. To apply the quantum well to laser active layer, it is necessary to consider critical thickness effect.

4.2 Strain Compensated GaInAsP/GaInAsP Quantum Wells

4.2.1 Strain Compensated Quantum Wells

The strained QW is expected to have high differential gain and small transparency current density for higher strained material [14, 15]. Usually, the optimized structure for edge emitting laser has few numbers of QWs for lowering threshold current, and the differential gain and good temperature characteristic require more large number of wells. As described in chapter 2, the surface emitting laser also requires about 6-12 wells. However, the critical thickness is one problem for designing strained QW structures as described in previous section. To avoid the structure limitation related with critical thickness, strain-compensated strained layer superlattice by Miller et al. [16] and zero-net-strain structure by Seltzer et al. [17] were proposed. Both techniques consist of barriers which have opposite strain against the well strain. By introducing opposite strain into the barrier, it is realized small or zero averaged strain structure. For the strain compensated structure, some superior results are reported about the crystal qualities, laser characteristics and the reliability [18, 19, 20, 21]. Such strain compensated structures usually consist GaInAsP barriers to form the opposite strain.

To design such GaInAsP/GaInAsP strain-compensated structure, there exist some structure parameters as follows; 1) number of wells, 2) well strain, 3) well bandgap energy, 4)

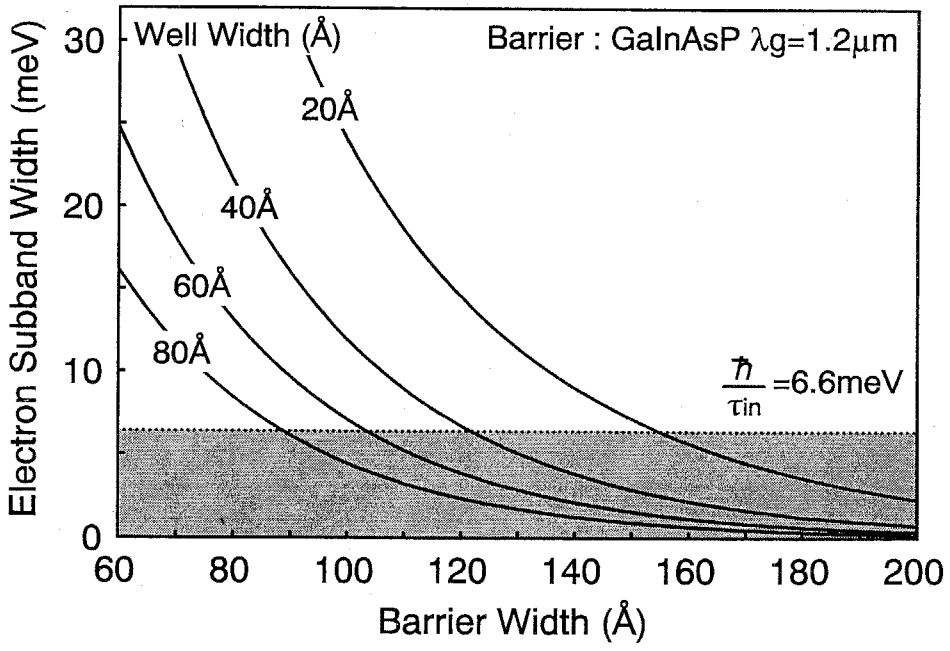

Fig. 4.10 Subband width of multiple quantum wells against barrier widths. the barrier material is assumed GaInAsP of λg=1.2μm (Eg=1.03eV).

well thickness, 5) barrier strain, 6) barrier bandgap energy, 7) barrier thickness. In this study, the emission wavelength is considered to be 1.55μm. This wavelength limits the range of well strain, bandgap energy and thickness. On the other hand, the bandgap energy of barrier is related with the carrier confinement and uniform carrier injection to each well. In this study, the barrier bandgap energy is set to 1.2μm-1.25μm. The barrier thickness is designed by considering energy coupling of the MQWs and matching factor described in chapter 2. From the point of matching factor, thin barrier thickness is superior since the QWs are densely placed around the peak of standing wave. However, thin barrier thickness causes to energy coupling of each well. The coupling energy calculated by Penney-Kronig model is shown in Fig. 4.10 as function of barrier width for various well thicknesses. In this calculation, the barrier is assumed to be GaInAsP of λg=1.2μm and the well bandgap is set to be the emission wavelength of 1.55μm for each well thickness. The conduction band offset ratio is assumed to be 0.4. From the result, 100-150Å barrier thickness is required for sufficient energy separation.

4.2.2 Growth and Characterization of Strain Compensated QWs

The strain compensated structure is composed by GaInAsP barriers. As the compressively strained QW is required for surface emitting lasers, the barrier is designed to be tensile strained material. Figure 4.11 shows the schematically drawn strain compensated QW structure for characterization. The structure has tensile GaInAsP barriers and compressive GaInAs(P) wells. The numbers of wells are 3 to 10 and typically 5. The InP buffer and InP capping layer was also grown. The valve sequences for GaInAsP barrier structures are shown in Fig. 4.12. Usually, the barrier and well has large and small group V ratio, respectively, and

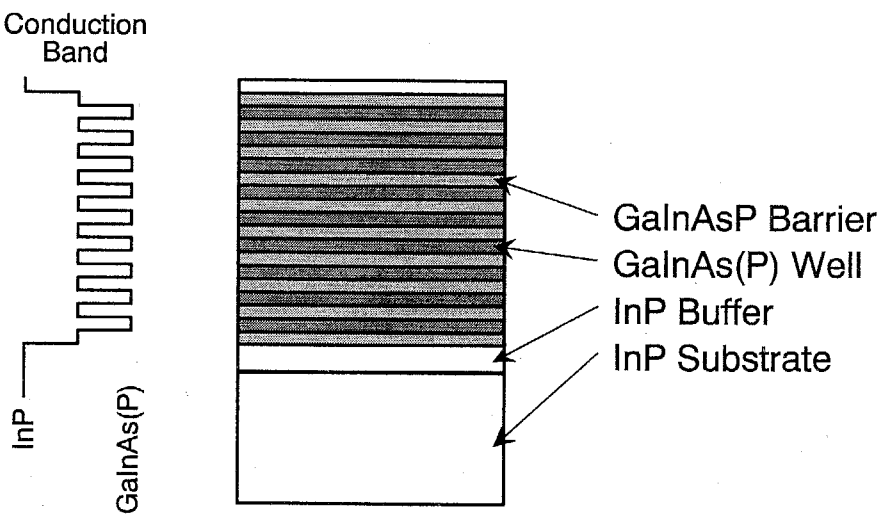

Fig. 4.11 Schematic view of strain compensated GaInAsP/GaInAsP QWs and its conduction band profile. The well numbers are from 3 to 10.

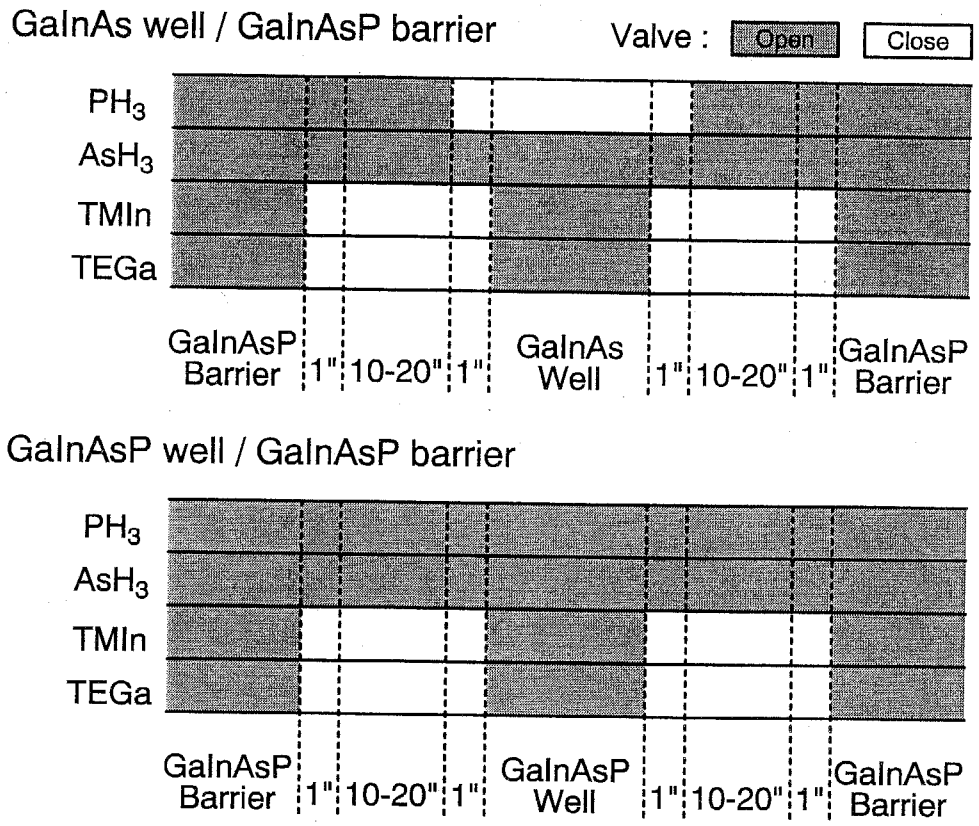

Fig. 4.12 Valve sequence for GaInAs and GaInAsP wells structure with GaInAsP barriers.

therefore the flow rate change time, in short growth interruption, is required for about 10-20sec because all sources have one gas line in this study.

The structure parameter is also determined by satellite peaks of X-ray diffraction curves as well as GaInAs/InP MQWs though the determination of the bandgap energy for both well and barrier is difficult. The bandgap energy is estimated from the GaInAsP/InP QW and GaInAsP bulk growth conditions, and from the emission peak wavelength considering bandgap change due to strain effect and quantum effect. However, the strain is almost exactly determined by the curve fitting of X-ray diffraction curves as well as strained GaInAs/InP QWs. Figures 4.13 (a) and (b) show the X-ray diffraction curve with theoretically calculated result. The sample has 5 wells of compressively strained GaInAsP and 6 barriers of tensile strained GaInAsP. The barrier composition is about λg=1.25μm and the bandgap energy of well is about 0.75eV. The thickness of barrier is estimated to be 120Å (41ML) and the well thickness is 80Å (27ML). We can also determine GaInAsP/GaInAsP QW thickness and strain of both barrier and well from X-ray diffraction pattern. The X-ray pattern is good agreement with theoretical curves. This indicates that the interface of such GaInAsP/GaInAsP QWs is good and abrupt as well as GaInAs/InP QWs.

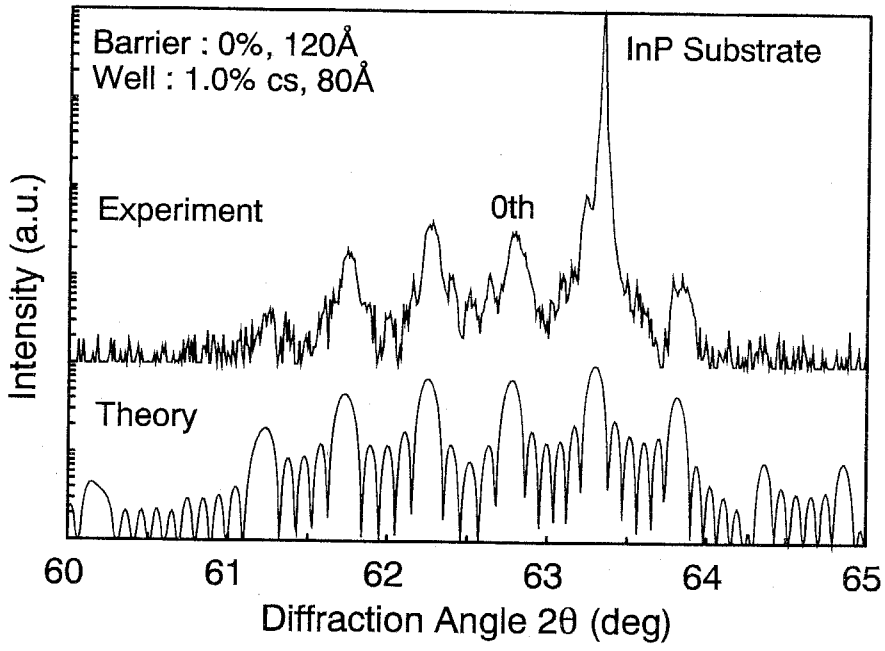

(a) lattice matched barrier

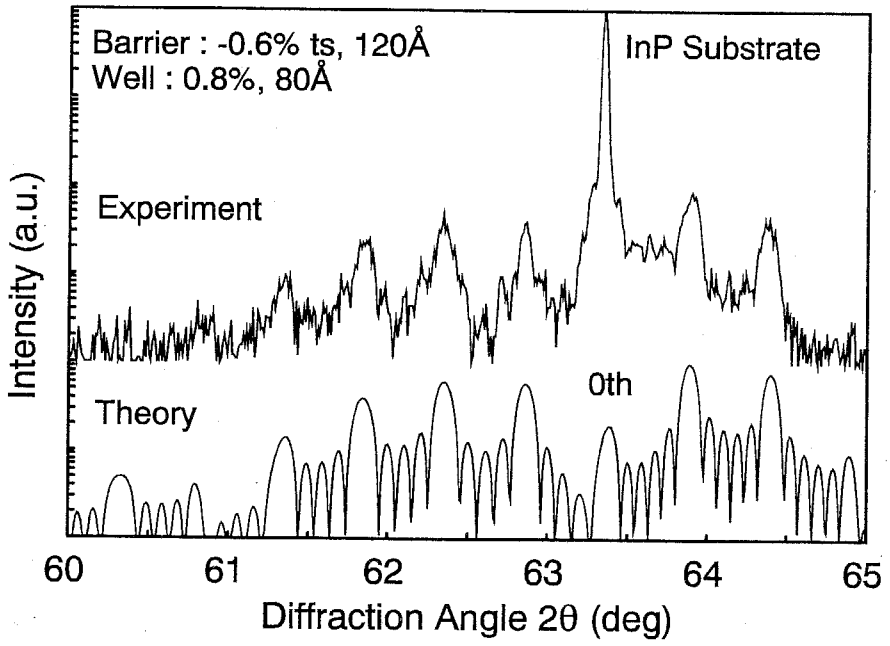

(b) zero-net strain

Fig. 4.13 X-ray diffraction curves for GaInAsP/GaInAsP 5 well structure. (a) Barrier is lattice matched to substrate. (b) zero-net strain.

Figure (a) shows the result for lattice matched barrier structure and the well strain is about 1%. The averaged strain estimated by 0th peak of satellite peaks is about 0.4%. The critical thickness of 0.4% strain material is estimated to be about 1500Å from the result in Fig. 4.8. As total thickness of this structure is about 1000Å (5QW×(120Å+80Å)), it is less than critical thickness. However, the structure may have crystal defects by strain if the number of well is larger than 10. On the other hand, the structures shown in Fig. (b) have 0.8 % compressively strained well with 0.6% tensile barrier and the averaged strain is almost 0%. Then the 0th peak is overlapped to the InP substrate peak. For this zero-net strain, the critical thickness may be considered to be infinite because averaged strain is zero.

As mentioned above, strain compensated QWs have many structural parameters. However, the thickness and bandgap energy of well are fixed by destination wavelength and that of barrier are limited as mentioned above. Therefore, the rest freedoms of the parameters are number of wells and barrier strain. In this study, the grown numbers of quantum wells were from 3 to 10 for GaInAsP barrier structures. Figure 4.14 shows the photoluminescence intensity against well number for GaInAsP/GaInAsP structures. The samples contain the un-compensated, strain compensated and zero-net strain structures. The well thickness is 65Å or 90Å and the well strain is 0.8-0.9% compressively. The barrier thickness is 120-140Å of GaInAsP (λg=1.25μm). The intensities are rapidly decreased for the well number of larger than 7. The structures with InP barriers shown by closed circles are not decreased for 10 wells.

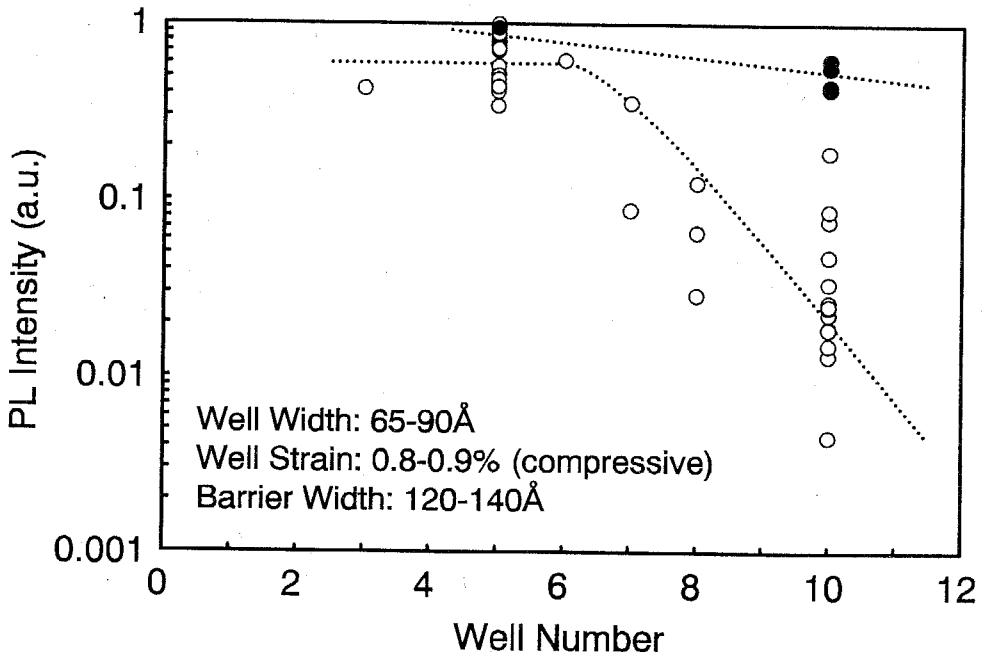

Fig. 4.14 PL Intensity vs. well number for GaInAsP/GaInAsP (open circle) and GaInAsP/InP (closed circle) strained quantum wells.

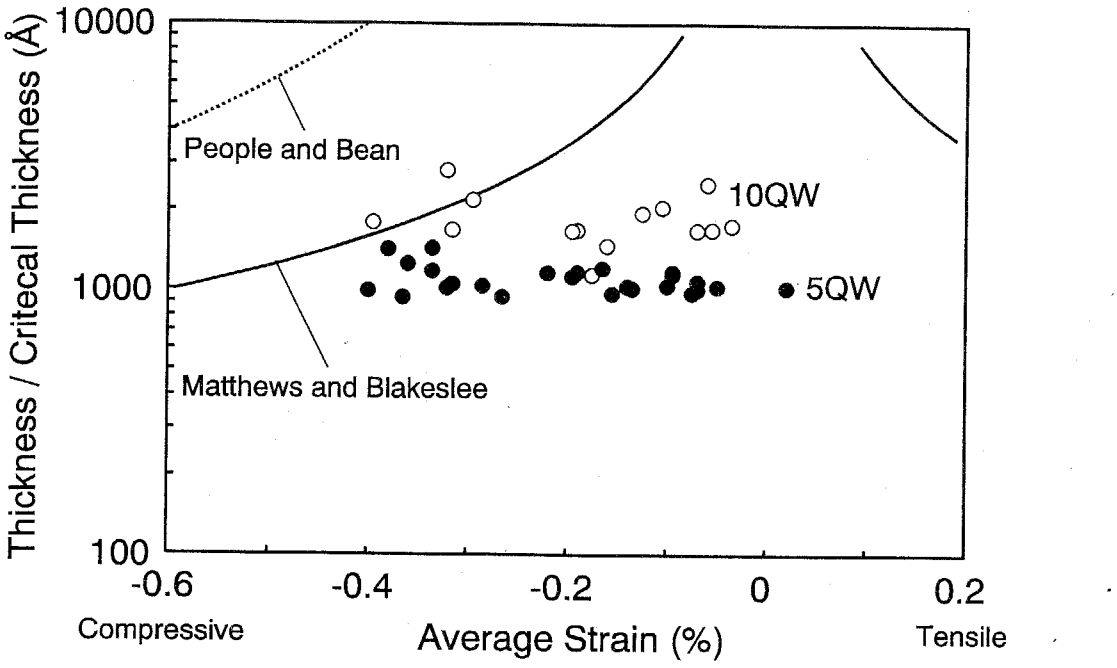

Fig. 4.15 Total thickness vs. average strain for grown samples. Total thickness of almost samples are less than critical thickness.

Figure 4.15 shows the total thickness of MQW structure against averaged strain for all samples shown in Fig. 4.14. The total thickness of almost samples is less than critical thickness. Considering that InP barrier structure shows good crystal quality even for the 10 well in spite of un-compensated structure, deterioration of PL intensity is considered due to not only critical thickness but also growth mechanism of GaInAsP alloy semiconductors. Smith et al. reported crystal qualities of strain compensated structures grown at various temperatures [18]. In their report, the lower growth temperature inhibits the compositional clustering for the GaInAs/GaInAs strain compensated structures grown by MOCVD. Though the growth temperature of CBE is lower than MOCVD, the result in this study is not so good. Further optimization of growth condition is required for realizing better crystal quality.

In this way, GaInAsP/GaInAsP strained QW structures with relatively large number of wells (>6) are difficult under the growth condition used in this study. This result limits the device design. However, growth of less than 6 QWs is enough to apply the QW structures to the surface emitting lasers because the optimized QW structure described in chapter 2 consist two gain regions with 4-6 wells.

Next, the characteristics of strain compensated QWs related with barrier strain is considered. Figure 4.16 shows the relation between PL intensity and averaged strain for 5 QW structures. The well strain is 0.8% compressively and the thickness is 65Å or 90Å. The barrier thickness is 140Å for all samples and the emission wavelength is around 1.55μm.

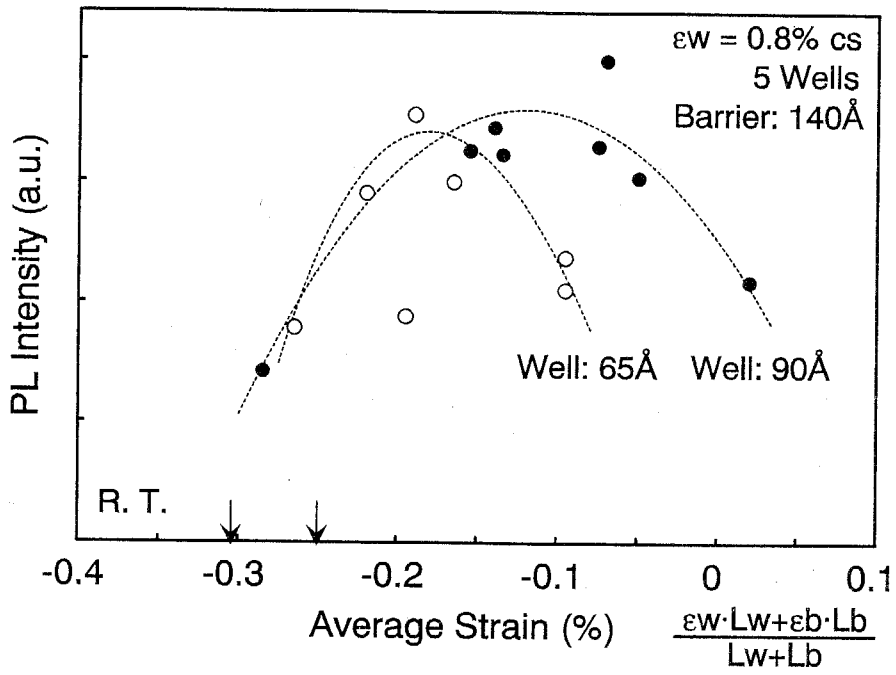

Fig. 4.16 PL intensity vs. averaged strain of strain compensated QWs. The well thickness is 65Å or 90Å with 0.8% compressively strained. The barrier thickness is fixed to 140Å and its strain is varied under tensile condition. Arrows show the unstrained barrier structures.

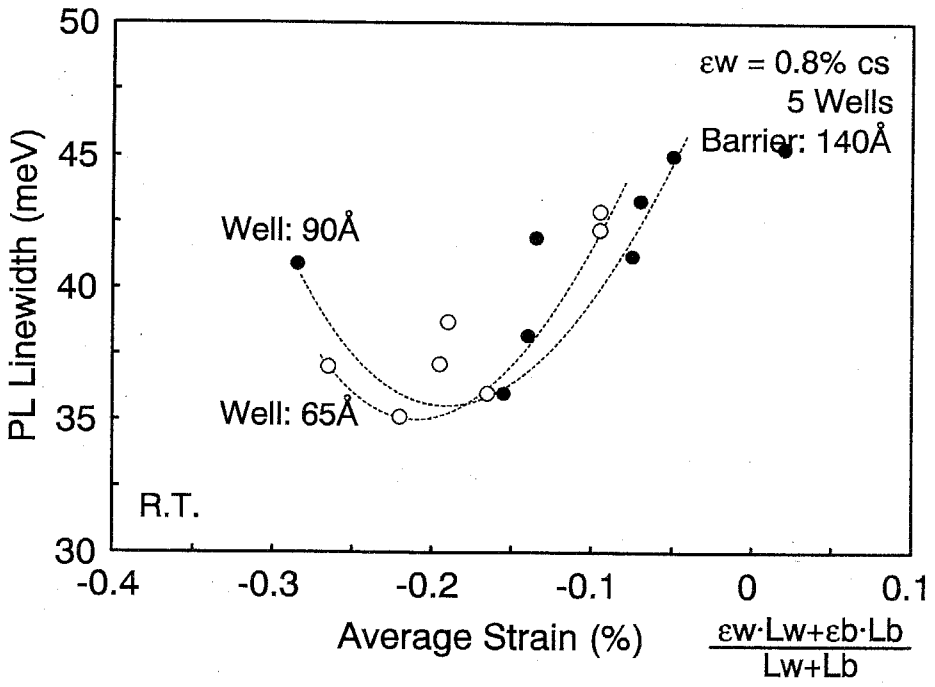

Fig. 4.17 PL linewidth vs. averaged strain at room temperature. The linewidth is minimum at around intensity maximum condition.

The averaged strain for lattice matched barrier is 0.25% for 65Å well and 0.31% for 90 Å well. Of course, the average strain of zero net strain structure is 0%. From the result, the highest PL intensity is obtained at neither the lattice matched barrier condition nor the zero-net condition. The result of PL intensity shows that the intermediate average strain is superior. Figure 4.17 shows the result of PL linewidth against averaged strain. The line widths also support the good QW property at the condition of intermediate barrier strain. From the result of PL intensity and linewidth, the intermediate barrier strain is considered to be good for active layer. However, the intensity decrease for other barrier structure is not so large compared with large well number structure shown in Fig. 4.14. I think the deterioration of large well number structure is due to crystal defect such as misfit dislocation because the linewidth was not so strange and nearly equal to the small well number structure. On the other hand, the barrier strain changed structure show difference of linewidth according to the intensity. I did not measure total intensity of each structure. The total intensity might be the same for each structure because the small peak intensity samples had wide linewidths. It may indicate small crystal defects and the PL spectra show the change of band structure.

4.3 Growth and Characterization of GaInAsP/InP Quantum Well Lasers

4.3.1 Unstrained GaInAs QW Laser

To evaluate QW structures for applying to surface emitting lasers, QW laser wafers were grown and fabricated to stripe contact lasers.

First, unstrained $Ga_{0.47}In_{0.53}As$ QW lasers were fabricated to stripe contact lasers. The grown wafer structure is shown in Fig. 4.18. The laser wafer has 10 $Ga_{0.47}In_{0.53}As$ lattice matched wells with 11 GaInAsP (λg=1.3μm) barriers. The wafer consists etching stop layer for applying to surface emitting laser. Usually, the separate confinement heterostructure (SCH) is introduced in QW edge emitting lasers because the optical confinement factor is increased [22]. However, the grown wafer has no SCH layer because the surface emitting laser doesn't require such SCH layer. On the other hand, the optical field extends to the cladding layer and the confinement factor is reduced if SCH layer does not exist for the conventional edge emitting laser. However, the confinement factor of the structure shown in Fig. 4.18 is 13% due to large number of wells, though the confinement factor is increased to 15.0% if SCH layer is introduced. The confinement factor is calculated by Appendix D.

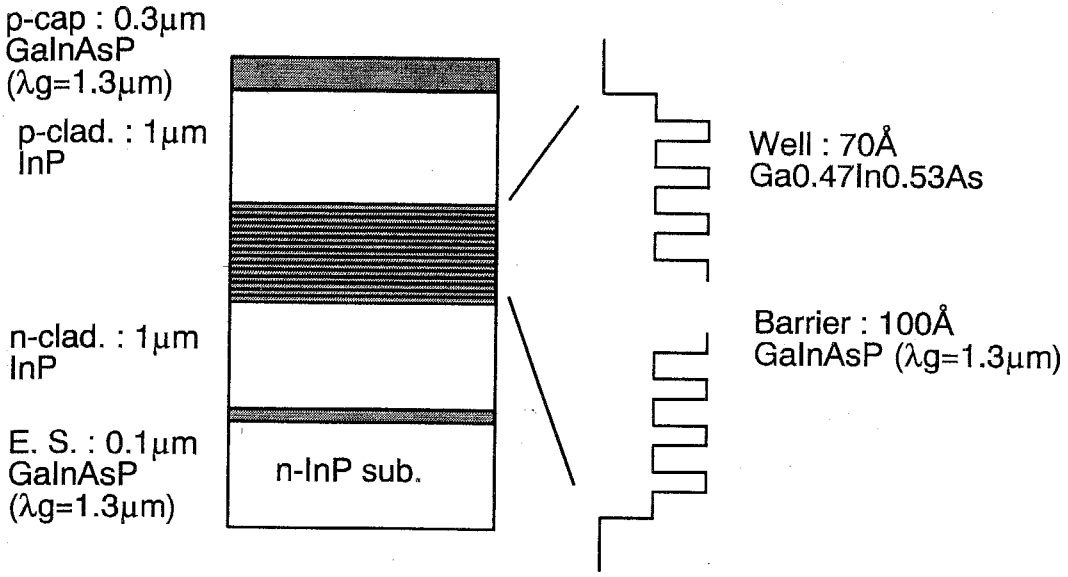

Fig. 4.18 Schematic structure of unstrained $Ga_{0.47}In_{0.53}As$ QW laser wafer. The right hand of drawing is schematic conduction band structure.

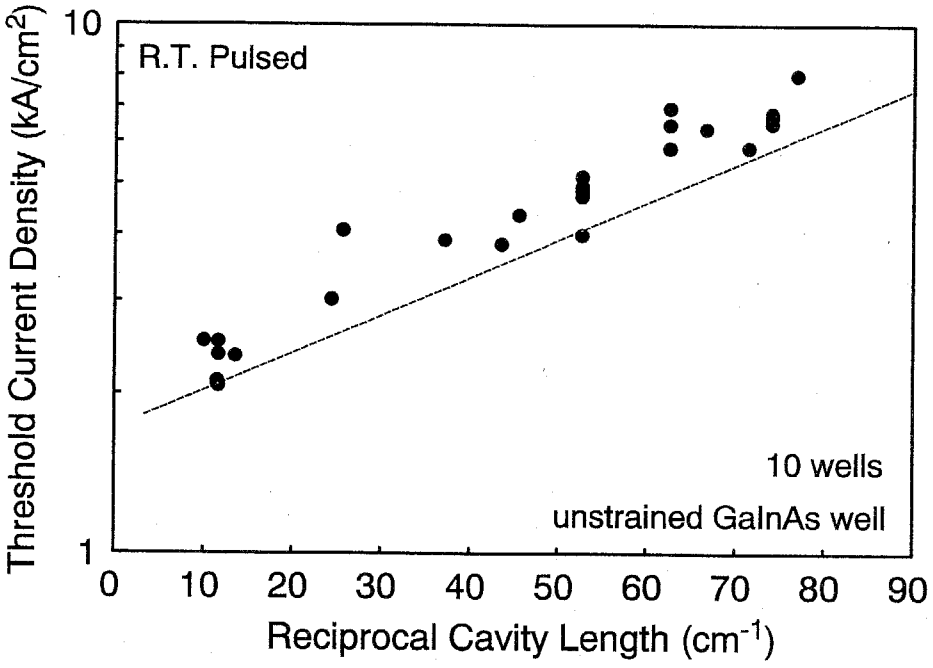

Fig. 4.19 Threshold current density against reciprocal cavity length for unstrained 10QW lasers.

Figure 4.19 shows the threshold current density against cavity length for unstrained QW lasers. The fabricated laser structure is 50μm wide stripe contact laser (see chapter 3). The minimum threshold current density was 2.0kA/cm² and 200A/cm²/QW at 1mm cavity length.

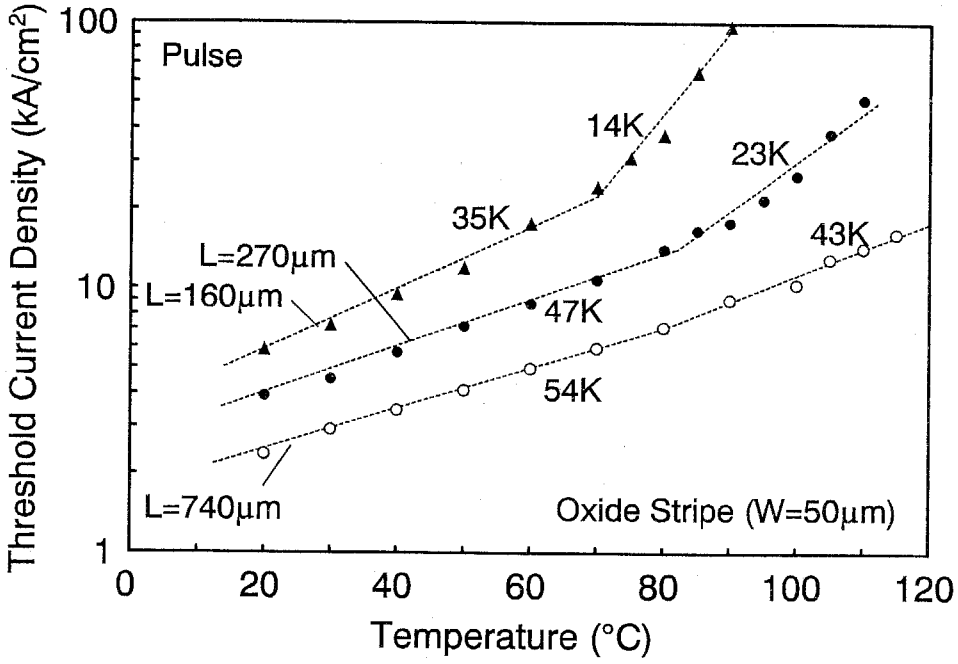

Fig. 4.20 Temperature characteristics for unstrained GaInAs QW lasers. The laser consists 10 wells without SCH layer.

The threshold current for infinite cavity length is estimated to be 150A/cm²/QW. The threshold current density is higher than previously reported 1.55μm-GaInAsP/InP unstrained QW lasers [23, 24]. However, the threshold current density per well is not so large compared with reported values. Therefore, the characteristics of quantum well lasers grown by CBE are enough good and applicable to surface emitting lasers. The gain characteristics shown in chapter 2 are calculated from the result of this threshold current density per well. The threshold gain g_{th} at each cavity length is given as;

$$g_{th} = \frac{1}{\Gamma}\cdot\alpha + \frac{1}{\Gamma\cdot L}\ln\left(\frac{1}{R}\right) \qquad (4.4)$$

where R is mirror reflectivity and assumed to be 0.3. The optical confinement factor Γ is calculated from the multilayer slab waveguide and 13.3% in this case. The absorption coefficient α is the fitting parameter for the theoretically estimated QW laser characteristic represented as [25];

$$J_{th} = N_w J_0 \exp\left(\frac{\alpha + \frac{1}{L}\ln\left(\frac{1}{R}\right)}{\Gamma G_0}\right) \qquad (4.5)$$

where N_W is number of wells. α is assumed to be 15cm^{-1} with J_0=140A/cm^2 and G_0=500cm^{-1}. A dashed line shown in figure is theoretically fitted line.

The temperature dependence of threshold current density is shown in Fig. 4.20. The temperature characteristic is measured for three different cavity lengths. The result shows good temperature characteristic for the long cavity length device due to small mirror loss and low threshold carrier density. The characteristic temperature T_0 of 54K for 740μm cavity device is good agreement with other reported value [26].

4.3.2 Strained GaInAs QW Lasers

As described in above section, unstrained QW lasers grown by CBE showed good lasing characteristics. To realize much high performance laser, strained QW lasers were also grown and fabricated to edge emitting lasers. Next, the lasing characteristic of strained GaInAs QW lasers are shown. The laser structure is shown in Fig. 4.21. The lasers consist five 1.0% compressively strained GaInAs with 0.1% tensile GaInAsP (λg=1.25μm) barriers. The well and barrier thickness is 35Å and 150Å, respectively. The wafers are not for surface emitting lasers and the SCH layer is introduced for both sides with thickness of 1500Å. The confinement factor was increased from 2.3% to 3.6% by introducing SCH layer. Figure 4.22 shows the result for compressively strained GaInAs well lasers. The minimum threshold current density was 960A/cm^2 (192A/cm^2/QW). The threshold current density per well looks like that of unstrained QW lasers, however more low threshold is expected for long cavity

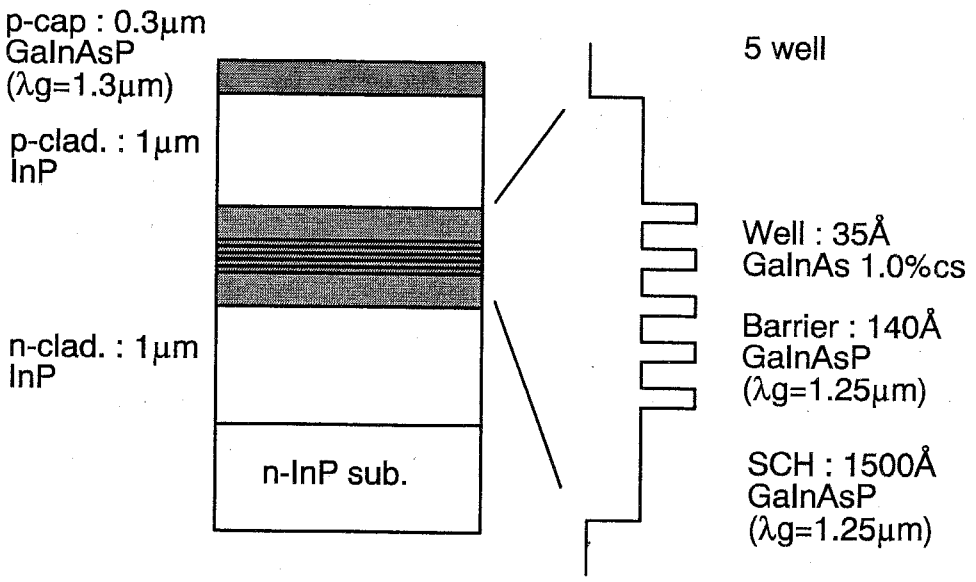

Fig. 4.21 Schematic wafer structure for GaInAs compressively strained 5QW lasers. SCH layer is introduced.

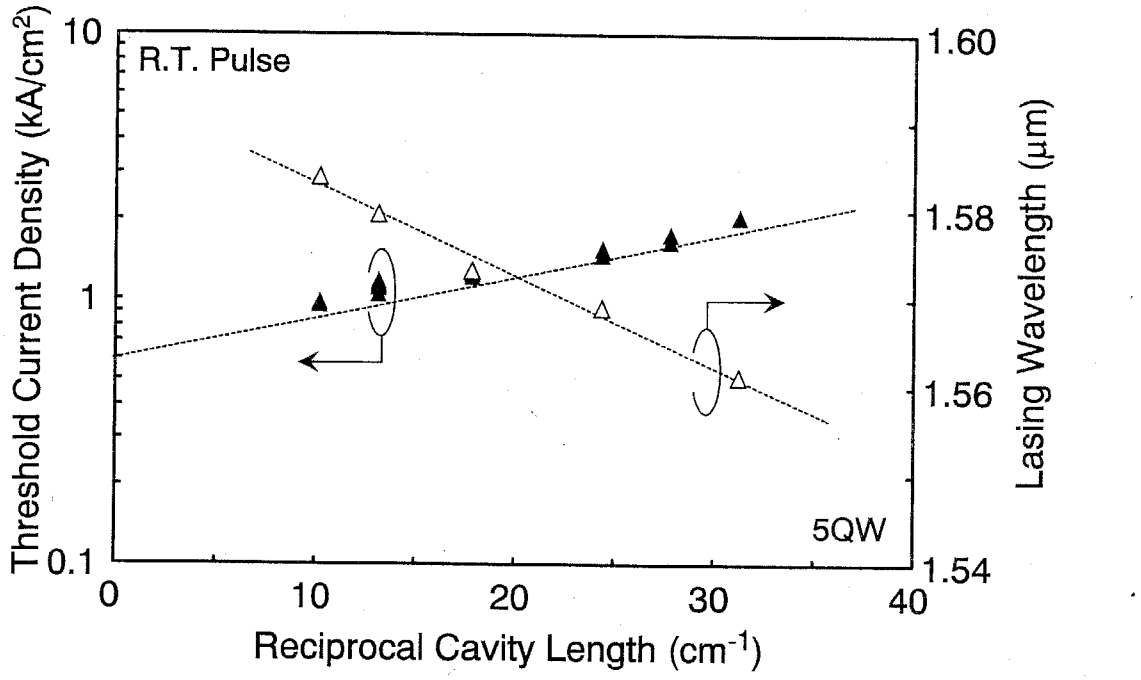

Fig. 4.22 Threshold current and lasing wavelength of strained GaInAs QW lasers against reciprocal cavity length.

length because the optical confinement factor of strained GaInAs well structure is small due to thin well thickness. The estimated threshold current for infinite cavity length is 120A/cm^2/QW. The lasing wavelength is shifted as increasing the threshold current density due to carrier filling.

4.3.3 Strain Compensated GaInAsP QW Lasers

Finally, lasing characteristics of strained GaInAsP QW lasers are shown. The laser structure is like as strained GaInAs QW lasers as shown in Fig. 4.22. The well number is 5 and the SCH layer of 1000Å is also introduced to increase the confinement factor. The well thickness is 65Å due to wide bandgap compared with compressively strained GaInAs and strain is 1.0% compressively. The barrier structure is thickness of 150Å and strain of 0.2% tensile which is selected from the result described in previous sections. The optical confinement factor is increased from 4.9% to 6.8% by SCH layer. The large confinement factor compared with strained GaInAs well is due to wide well thickness. The SEM photograph of a part of active layer is shown in Fig. 4.23. We can see the successively grown SCH strained GaInAsP/GaInAsP MQW structure. The threshold current density against reciprocal cavity length is shown in Fig. 4.24. The minimum threshold current density was 450A/cm^2 and 90A/cm^2/QW. The threshold current of infinite cavity length is estimated to be 72A/cm^2/QW. This result is most superior in QW lasers grown in this study. Recently, a low

threshold current ranging from 100 to 170A/cm2 were reported with strained GaInAs(P)/InGaAsP single-QW devices for 1.55μm wavelength [26, 24, 27]. Though such single QW structure has a disadvantage of small optical confinement, the result in this study is considered to be sufficiently low threshold compared with other grown devices.

The estimated gain characteristics are shown again in Fig. 4.25. In this figure, the vertical axis means the modal gain. The confinement factor of surface emitting laser is defined as ratio of active layer thickness and cavity length considering matching factor. However, the cavity length is changed for each structure. Therefore, the λ-cavity is assumed in the figure. As described in chapter 2, the most superior quantum well is considered to be GaInAsP compressively strained QW structure with tensile barrier.

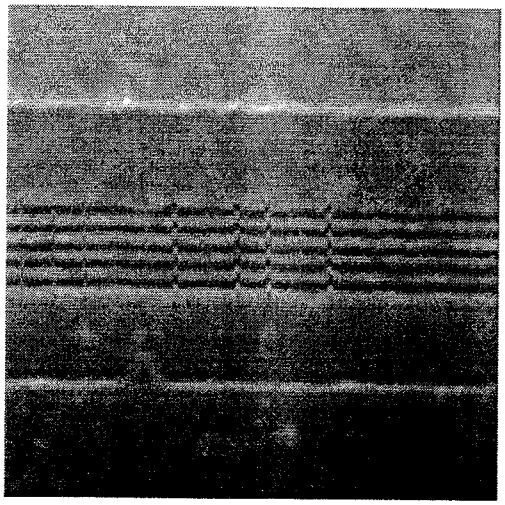

Fig. 4.23 SEM photograph of GaInAsP/GaInAsP strain compensated 5 QW laser active layer.

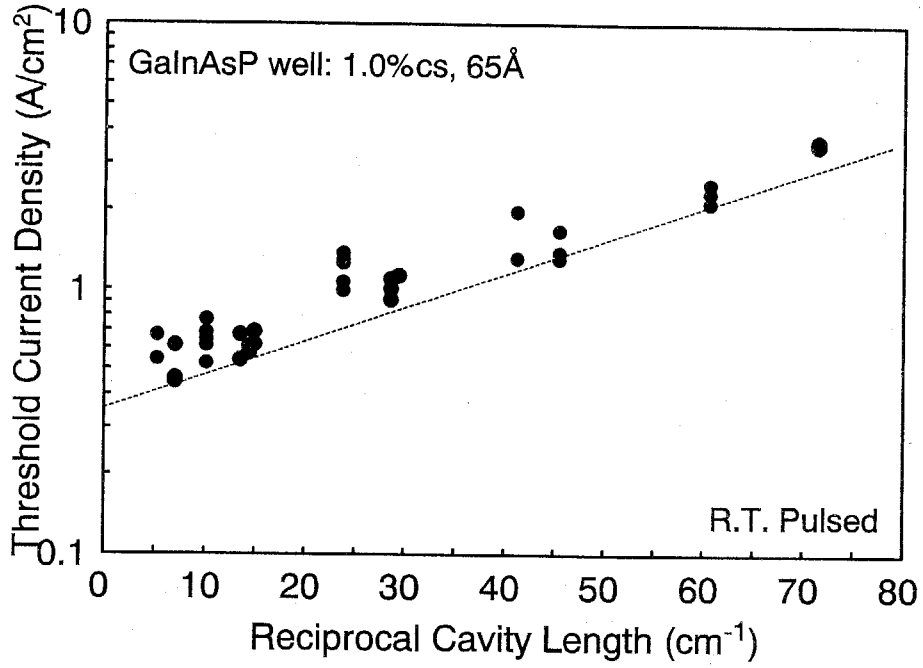

Fig. 4.24 Threshold current density vs. reciprocal cavity length for GaInAsP strain compensated structure.

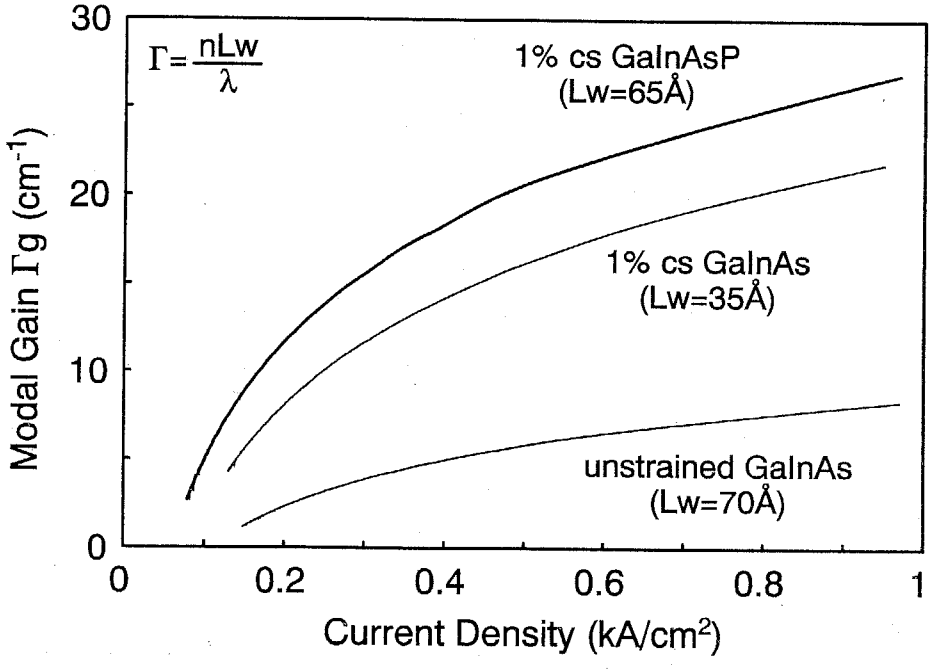

Fig. 4.25 Modal gain for various QW structures estimated from lasing threshold current of edge emitting lasers. The confinement factor is considered as ratio between well width and laising wavelength of 1.55μm.

References

[1] M. Tanaka, H. Sakaki, and J. Yoshino, Jpn. J. Appl. Phys., 25, L155, 1986.

[2] M. Sugawara, M. Kondo, S. Yamazaki, and K. Nakajima, "Exact determination of superlattice structures by small-angle x-ray diffraction method," *Appl. Phys. Lett.*, vol. 52, pp. 742-744, 1988.

[3] A. T. Macrander, S. Lau, K. Strege, and S. N. G. Chu, "Nondestructive measurement of layer thickness in double heterostructures by x-ray diffraction," *Appl. Phys. Lett.*, vol. 52, pp. 1985-1986, 1988.

[4] W. Y. Choi and C. G. Fonstad, "Determination of the layer structure of embedded strained InGaAs multiple quantum wells by high resolution x-ray diffraction," *Appl. Phys. Lett.*, vol. 62, pp. 2815-2817, 1993.

[5] R. E. Cavicchi, D. V. Lang, D. Gershoni, A. M. Sergent, J. M. Vandenberg, S. N. G. Chu, and M. B. Panish, "Admittance spectroscopy measurement of band offsets in strained layers of $In_xGa_{1-x}As$ grown on InP," *Appl. Phys. Lett.*, vol. 54, pp. 739-741, 1989.

[6] S. R. Forrest, P. H. Schmidt, R. B. Wilson, and M. L. Kaplan, "Relationship between the conduction-band discontinuities and band-gap differences of InGaAsP/InP heterojunctions," *Appl. Phys. Lett.*, vol. 45, pp. 1199-1201, 1984.

[7] B. R. Nag and S. Mukhopadhyay, "Band offset in $InP/Ga_{0.47}In_{0.53}As$ heterostructures," *Appl. Phys. Lett.*, vol. 58, pp. 1056-1058, 1991.

[8] T. Y. Wang and G. B. Stringfellow, "Strain effects on GaxIn1-xAs/InP single quantum wells grown by organicmetallic vapor-phase epitaxy with $0 \leq x \leq 1$," *J. Appl. Phys.*, vol. 67, pp. 344-352, 1990.

[9] Y. Kawaguchi and H. Asahi, "High-temperature observation of heavy-hole and light-hole excitons in InGaAs/InP multiple quantum well structures grown by metalorganic molecular beam epitaxy," *Appl. Phys. Lett.*, vol. 50, pp. 1243-1245, 1987.

[10] J. Singh and K. K. Bajaj, "Role of interface roughness and alloy disorder in photoluminescence in quantum-well structures," *J. Appl. Phys.*, vol. 57, pp. 5433-5437, 1985.

[11] D. F. Welch, G. W. Wicks, and L. F. Eastman, "Luminescence line shape broadening mechanisms in GaInAs/AlInAs quantum wells," *Appl. Phys. Lett.*, vol. 46, pp. 991-993, 1985.

[12] R. People and J. C. Bean, "Calculation of critical layer thickness versus lattice mismatch for GexSi1-x/Si strained-layer heterostructures," *Appl. Phys., Lett.*, vol. 47, pp. 322-324, 1985. Erratum: *Appl. Phys. Lett.*, vol. 49, p. 229, 1986.

[13] J. W. Matthews and A. E. Blakeslee, "Defects in epitaxial multilayers," *J. Crystal Growth*, vol. 27, pp. 118-125, 1974.

[14] S. W. Corzine, R. H. Yan, and L. A. Coldren, "Theoretical gain in strained InGaAs/AlGaAs quantum wells including valence-band mixing effects," *Appl. Phys. Lett.*, vol. 57, pp. 2835-2837, 1990.

[15] P. W. A. Mc Ilroy, A. Kurobe, and Y. Uematsu, "Analysis and application of theoretical gain curves to the design of multi-quantum-well lasers," *IEEE J. Quantum Electron.*, vol. QE-21, pp. 1958-1963, 1985.

[16] B. I. Miller, U. Koren, M. G. Young, and M. D. Chien, "Strain-compensated strained-layer superlattices for 1.5μm wavelength lasers," *Appl. Phys. Lett.*, vol. 58, pp. 1952-1954, 1991.

[17] C. P. seltzer, S. D. Perrin, M. C. Tatham, and D. M. Cooper, "Zero-net-strain multiquantum well lasers," *Electron. Lett.*, vol. 27, pp. 1268-1270, 1991.

[18] A. D. Smith, A. T. R. Briggs, K. Scarrott, X. Zhou, and U. Bangert, "Optimization of growth conditions for strain compensated $Ga_{0.32}In_{0.68}As/Ga_{0.61}In_{0.39}As$ multiple quantum wells," *Appl. Phys. Lett.*, vol. 65, pp. 2311-2313, 1994.

[19] A. T. R Briggs, P. D. Greene, and J. M. Jowett, "Gain and threshold characteristics of strain-compensated multiple-quantum-well lasers," *IEEE Photon. Technol. Lett.*, vol. 4, pp. 423-425, 1992.

[20] C. P. Seltzer, S. D. Perrin, M. J. Harlow, R. Studd, and P. C. Spurdens, "Long-term reliability of strain-compensated InGaAs(P)/InP MQW BH lasers," *Electron. Lett.*, vol. 30, pp. 227-229, 1994.

[21] M. Silver and E. P. O'Reilly, "Optimization of long wavelength InGaAsP strained quantum-well lasers," *IEEE J. Quantum Electron.*, vol. 31, pp. 1193-1200, 1995.

[22] W. T. Tsang, "A graded-index waveguide separate-confinement laser with very low threshold and a narrow Gaussian beam," *Appl. Phys. Lett.*, vol. 39, pp. 134-137, 1981.

[23] W. T. Tsang, M. C. Wu, L. Yang, Y. K. Chen, and A. M. Sergent, "Strained-layer 1.5μ m wavelength InGaAsP/InP multiple quantum well lasers grown by chemical beam epitaxy," *Electron. Lett.*, vol. 26, pp. 2035-2036, 1990.

[24] P. J. A. Thijs, J. J. M. Binsma, L. F. Tiemeijer, and T. van Dongen, "Submilliamp threshold current (0.62mA at 0°C) and high output power (220mW) 1.5μm tensile strained InGaAs single quantum well lasers," *Electron. Lett.*, vol. 28, pp. 829-830, 1992.

[25] P. W. A. Mc Ilroy, A. Kurobe, and Y. Uematsu, "Analysis and application of theoretical gain curves to the design of multi-quantum-well lasers," *IEEE J. Quantum Electron.*, vol. QE-21, pp. 1958-1963, 1985.

[26] W. T. Tsang, F. S. Choa, M. C. Wu, Y. K. Chen, A. M. Sergent, and P. F. Sciortino, Jr., "Very low threshold single quantum well graded-index separate confinement heterostructure InGaAs/InGaAsP lasers grown by chemical beam epitaxy," *Appl. Phys., Lett.*, vol. 58, pp. 2610-2612, 1991.

[27] N. Yamamoto, K. Yokoyama, T. Yamanaka, and M. Yamamoto, "Very low threshold graded-index separate-confinement-heterostructure strained InGaAsP single-quantum-well lasers," *Electron. Lett.*, vol. 30, pp. 243-244, 1994.

Chapter 5

Fabrication and Performances of CBE Grown GaInAsP/InP Surface Emitting Lasers

In this chapter, fabrication processes of surface emitting lasers grown by chemical beam epitaxy are mentioned, and then lasing characteristics of bulk active layer surface emitting lasers are discussed.

5.1 Structures of GaInAsP/InP Surface Emitting Lasers

In chapter 2, design of active layer and mirror structures for surface emitting lasers are already discussed. Such structures are directly related with the threshold current density. On the other hand, threshold current is represented as multiple of the threshold current density and active region area, and hence the design of device structure is important to obtain low threshold current devices.

There exist some methods to reduce the active region. The schematic view of current confinement structures is shown in Fig. 5.1. Usually, the current confinement is performed at p-side because the mobility of holes is smaller than that of electrons, and hence the electrodes shown in figures are p-side. The simple limitation of the active region is achieved by localized electrode (a). The mesa capping layer (b) is more effective to limit the active region due to small current spreading in capping layer. Further limitation is achieved by limitation in cladding layer (c). This structure is possible to confine the current without spreading in cladding layer. However, these limitation techniques still remain the lateral carrier diffusion in the active layer. The most effective structure for current confinement is limitation in the active layer (d). Table 5.1 shows the current confinement positions and realized structures. The electrode confinement structure corresponds to the stripe contact edge emitting lasers as

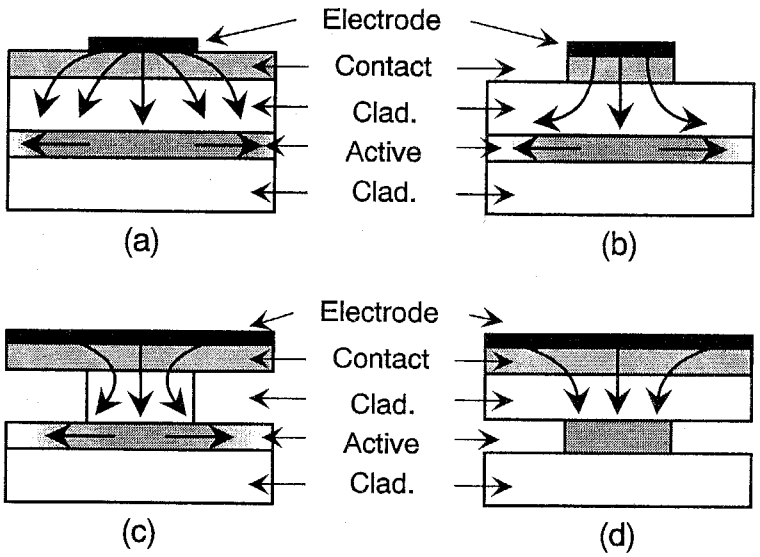

Fig. 5.1 Schematic view of current confinement structure. The current confinement is performed at (a) electrode, (b) contact layer, (c) cladding layer and (d) active layer.

fabricated in chapter 5 and this structure was realized as the first surface emitting laser [1]. Current confinement at contact layer was reported as mesa cap structure [2]. This structure has advantages of relatively good current confinement and relatively easy fabrication. The cladding confinement structure was realized as the selective oxidation technique in the GaAs/AlAs mirror system of short wavelength surface emitting lasers and achieved the lowest threshold current [3]. The active layer confinement structures have been studied much and various techniques are reported such as buried heterostructure (BH) [4], ion implanted [5], air post structure [6], and buried by insulator material such as polyimide [7], SiO_2, etc.

A simple structure such as mesa cap structure is enough to evaluate the lasing threshold current density. On the other hand, the efficient current confinement structure is necessary to obtain low threshold current devices.

Next, the geometric arrangement of electrode is considered. The current flow path of vertical cavity surface emitting laser is parallel to the optical path. Accordingly, the electrode position is the same or near the mirror position as shown in Fig. 5.2. The first stage of surface emitting lasers used gold (Au) as both electrode and mirror [8] and hence the geometric arrangement was straight for electrode, mirror and optical path. As well as the Au mirror, the semiconductor multilayer reflectors become both current flow path and mirror. On the other hand, the ring electrode structure [1] is required for dielectric material mirrors. In this structure, the lateral position of optical path is equal to the mirror but the electrode is separated from the mirror. However, I chose the dielectric multilayer mirror for both sides

because the dielectric multilayer has potentiality of high reflectivity. As a result, the ring electrode structure was applied for epitaxial side and the holing structure (ring electrode structure in wide sense) was utilized for substrate side. The worry of the current injection for the ring electrode is considered in chapter 7.

Table 5.1 Table of confined structure used by surface emitting lasers.

Confinement at	structure	References
(a) electrode	circular electrode	Uchiyama et. al [1], etc.
(b) contact layer	mesa-cap (low mesa)	Uchiyama et. al [2], etc.
(c) cladding layer	selective oxidation	Huffaker et. al [3], etc.
(d) active layer	buried heterostructure ion (H^+) implantation air post selective etching	Okuda et. al [4], etc. Y. H. Lee et. al [5], etc. Y. H. Lee, et. al [6], etc. Wada et. al [7], etc.

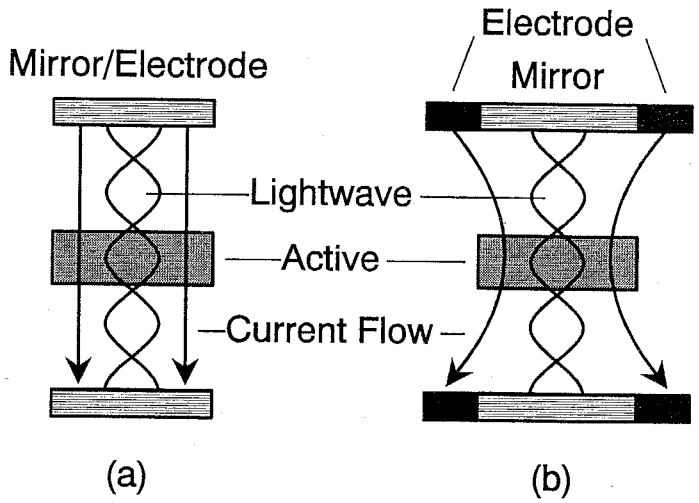

Fig. 5.2 Geometrical arrangement of mirror / electrode / optical path. (a) Mirror and electrode is same lateral position by electrical conductive mirror. (b) Electrode is separated from mirror by insulating mirror.

5.2 Mesa-Cap Type Surface Emitting Lasers with Bulk Active Layers

5.2.1 Growth and Fabrication of Mesa-Cap Type Surface Emitting Lasers

From the result of threshold current density analysis discussed in chapter 2, the room temperature operation is expected by the conventional bulk active layer structure with active layer thickness of 1μm even if the mirror reflectivity is as low as 99%. Figure 5.3 shows the wafer structure grown by CBE which was the same wafer grown in chapter 3. Cladding layer thickness was 1.0μm for n-side ($n=2\times10^{18}cm^{-3}$) and 1.5μm for p-side ($p=5\times10^{17}cm^{-3}$), respectively. The active layer thickness was 1.0μm of GaInAsP ($\lambda g=1.55\mu m$) and its doping concentration was $3\times10^{17}cm^{-3}$ by p-type. The capping layer was $p=2\times10^{19}cm^{-3}$ doped GaInAsP ($\lambda g=1.3\mu m$) and the thickness was 0.25μm. The cavity length of this wafer was about 4μm and the longitudinal mode spacing was estimated to be 0.07-0.08μm (70-80nm). As described in chapter 3, the edge emitting laser of this wafer showed $5kA/cm^2\mu m$ at room temperature pulsed condition.

The first fabricated devices were mesa cap type. The current confinement of this structure is performed by suppression of current spreading at mesa-etched capping layer. The advantage of this type is relatively easy fabrication processes and sufficient structure to evaluate fundamental lasing characteristics. Here, the fabrication processes of this mesa cap structure are mentioned. The corresponding processes are shown in Fig. 5.4.

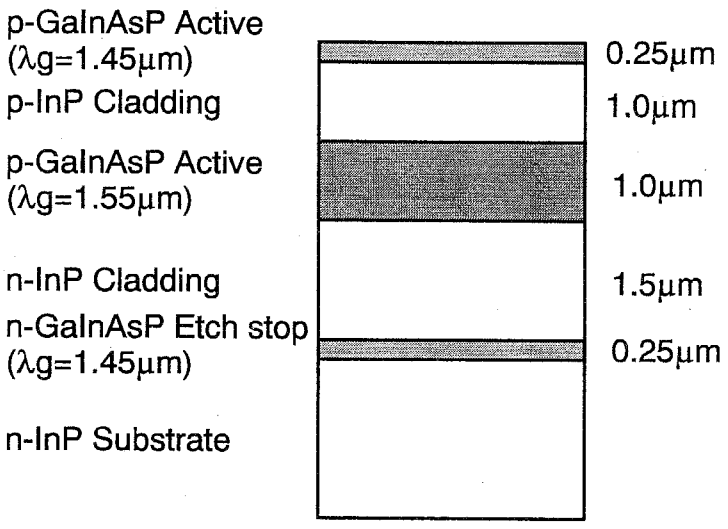

Fig. 5.3 Wafer structure for surface emitting laser with bulk active layer.

(1) wafer growth and preparation for fabrication

The wafer for surface emitting lasers was successively grown by CBE as shown in Fig. 5.3. The backside of grown wafers was smeared by indium (In) solder which was utilized to mount on Mo-block. Indium was removed by HgCl solution in the supersonic cleaner, and then the substrate was rinsed in acetone. The substrate was then cleaned in boiling trichroroethylen, acetone, and methanol for about 10 minutes. This cleaning method is named organic solvent cleaning in this thesis.

(2) mesa-cap formation

As etching mask for formation of mesa-cap structure, positive type resist was used. The mask was 30μm diameter dot with 600μm pitch. The mesa-cap structure is formed by selective etching technique between capping (GaInAsP) and p-cladding (InP) layer by solution of H_2SO_4:H_2O_2:H_2O=3:1:1 at 20°C. Therefore, the mesa height was capping layer thickness. The resist mask was removed and cleaned by organic solvent.

(3) insulator deposition

As an electrical insulator layer, SiO_2 was evaporated with the thickness of about 3000Å by RF spattering technique with Ar gas.

(4) substrate polishing

To success the holing process as mentioned below, the thickness of substrate side was thinned to about 100μm by polishing, and then the backside was finished to mirror like surface.

(5) n-electrode formation

N-side electrode metal was evaporated to the substrate side. The n-electrode was gold-germanium alloy (AuGe), and the thickness was 5000Å. The electrode was also used as an etching mask of the holing process. To form the hole in the metal layer, the photolithography was performed with 400μm diameter dot mask of 600μm pitch. The lithography system was double-side type and the center of dot was adjusted to the center of p-side mesa. The AuGe metal was etched by kalium-iodine (KI) solution, and then rinsed in deionized water. After removal of photo resist and cleaned by organic solvent, annealing for metalization was performed at 440°C for 2 minutes and the color of metal was changed from brownish-gold to silver.

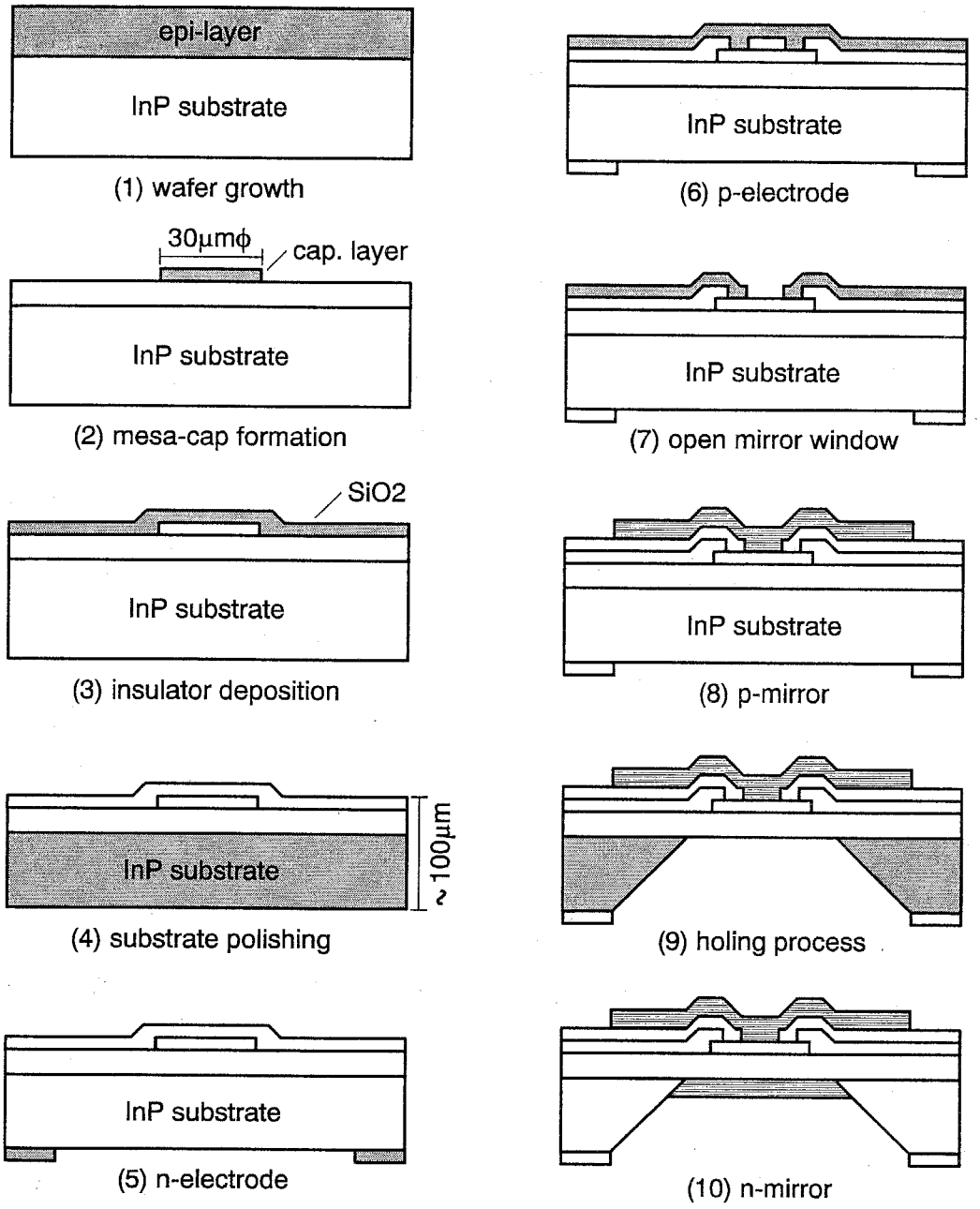

Fig. 5.4 Fabrication processes of mesa-cap type surface emitting lasers.

(6) p-electrode formation

To expose the contact layer on the mesa, SiO_2 was removed by photolithography using ring mask. The ring had inner and outer diameter of 10μm and 20μm, respectively. After removing the photo resist, p-side electrode metals were evaporated. The layer structure was Au/Zn/Au=250Å/500Å/1000Å. Then, the metals were annealed at 410°C for 2 minutes. The color was changed from gold to gold-silver.

(7) mirror window opening

To open the mirror window at the center of mesa, the photolithography process was performed using 10μm diameter dot mask. The etching was carried out by two steps. First, the electrode material was etched by KI solution, and then SiO_2 was etched by BHF. The SiO_2 plays important role to keep the epitaxial surface flatness because annealing process occurs interdiffusion of semiconductor and metal, and hence the surface may be slightly damaged.

(8) p-mirror formation

The p-side dielectric multilayer mirror was formed by electron beam (EB) evaporation system [9]. In this study, the mirror materials were Si and SiO_2 for high and low index material, respectively. The number of pairs used in this study was four with the first layer of SiO_2, and the finally SiO_2 layer was evaporated considering the reflection phase of gold. The evaporation rate and the thickness were monitored by X'tal and optical thickness monitoring system because the index of evaporated material was different from bulk material [10]. The substrate temperature was set to 250°C and the oxygen (O_2) was introduced for the case of SiO_2 evaporation with the pressure of 1×10^{-4}Torr. The evaporation rate was about 3Å/sec for SiO_2 and 0.3Å/sec for Si, respectively. The signal of optical monitor system was shown in Fig. 5.5. In this study, the monitoring light source was 1.3μm DFB laser and the destination

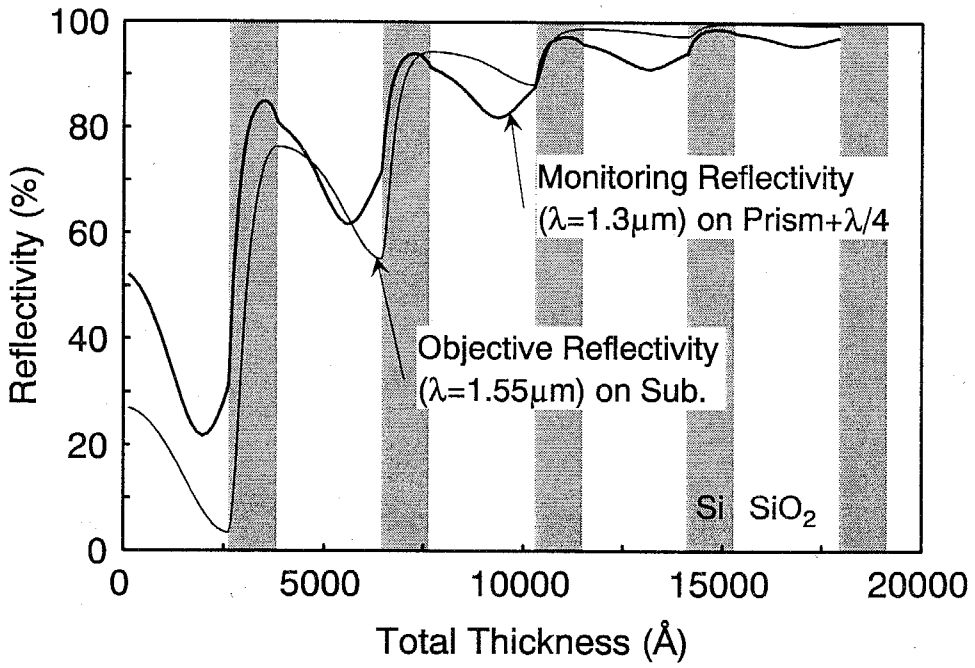

Fig. 5.5 Theoretical signal of optical monitoring system. In this study, the destination wavelength is different from monitoring light wavelength. The bold line is monitoring and light line is reflectivity of device.

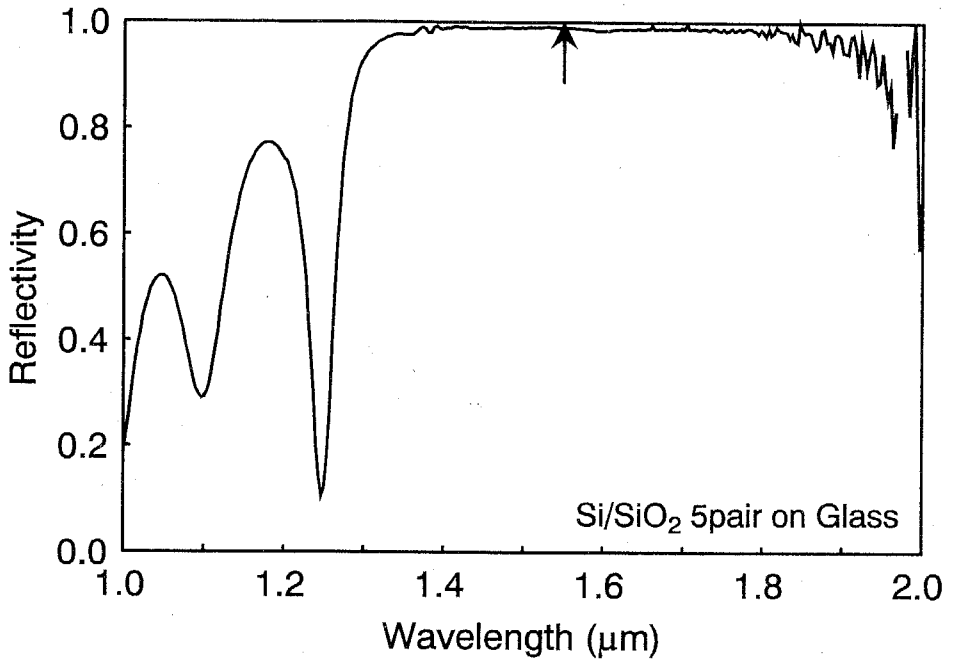

Fig. 5.6 Measured reflectivity spectrum of Si/SiO_2 dielectric multilayers. The number of pair is 5 pair.

wavelength was 1.55μm. To form the reflector for 1.55μm wavelength range, the 1.55μm wavelength light source is most suitable because the material change of Si and SiO_2 is carried out at peak and bottom of valley of monitoring signal. If the light wavelength is different from destination wavelength, the thickness correction is required by X'tal thickness monitor for each layer.

The reflectivity spectrum is shown in Figure 5.6. High reflectivity of over 99% and wide wavelength range of high reflectivity was observed as well as theoretical results shown in chapter 2 because the index difference between Si and SiO_2 are enough large.

As the evaporated mirror covers the whole area of p-side, it is required to remove the mirror and expose the p-side electrode. This process was simply carried out by photolithography of 400μm diameter adjusted to center of mesa and then the multilayer was etched away by BHF solution, thought the boundary was unseemly. Finally, the gold (Au) was evaporated on the dielectric mirror to obtain higher reflectivity. Theoretical reflectivity is over 99.9% for 4.5 pair SiO_2/Si with Au reflector.

(9) Holing process

To form a short cavity, holing process was performed [11]. Fortunately, etching selectivity between InP substrate and GaInAsP etching stop layer is very large, so the etching process is very simple. The etching mask is n-side electrode of AuGe. The InP substrate was

etched by hydrochloric acid ($HCl:H_2O$ = 3:1) for 10-15 minutes at 20°C (6-8μm/min). The etching was stopped perfectly at the interface of GaInAsP etching stop layer, and the mirror like surface was appeared. Then, the etching stop layer was also etched away selectively by $H_2SO_4:H_2O_2:H_2O$ = 3:1:1 solution. Due to selectivity of surface orientation, the bottom form of the hole became like as a cat eye.

(10) n-mirror formation

As well as p-side mirror, Si and SiO_2 multilayer were evaporated to n-side. The number of pair was four and the last layer was Si. Theoretically estimated reflectivity was 99.7% for this configuration. The mirror etching is also performed as well as p-side.

The finished mesa cap laser structure is shown in Fig. 5.7.

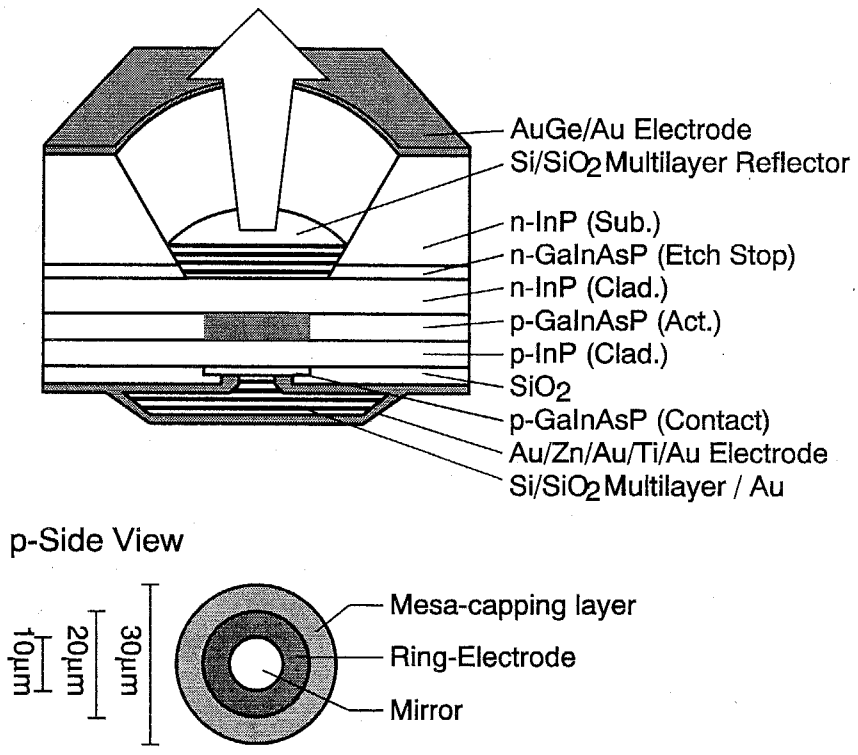

Fig. 5.7 Schematic view of mesa-cap type surface emitting laser structures and p-side view.

5.2.2 Lasing Characteristics of Mesa-Cap Surface Emitting Lasers

The surface emitting laser was successively fabricated to mesa-cap type structure. The wafer was cleaved or cut to independent devices, and then it mounted to measure the device characteristics without metal solder.

The lasing characteristic of light output against current (I-L) and lasing spectrum was measured at 77K under continuous wave (CW) condition. Figure 5.8 shows an I-L curve and lasing spectrum of the lowest threshold device in the first fabricated wafer. This is the first lasing operation grown by chemical beam epitaxy. The threshold current was 2.7mA. The threshold current density estimated from the area of near field pattern (NFP) at room temperature was 455A/cm^2. The threshold current and its current density were the lowest value of all the long wavelength surface emitting lasers reported formally. The light output power was about 90μW at two times of I_{th}. The output power was very small and slope efficiency was estimated to be about 33μW/mA = 0.03W/A. The differential quantum efficiency η_d was estimated to be 3.8%. Such small output power and small efficiency are due to large ineffective current of mesa-cap structure because the current flows the area about 10 times of mirror area. The lasing spectrum of this device at $1.1 \times I_{th}$ (~3mA) is also shown in Fig. 5.8. The lasing wavelength was 1.43μm and the linewidth was less than resolution of spectrum analyzer (2Å). The lasing wavelength was far from 1.55μm due to bandgap change

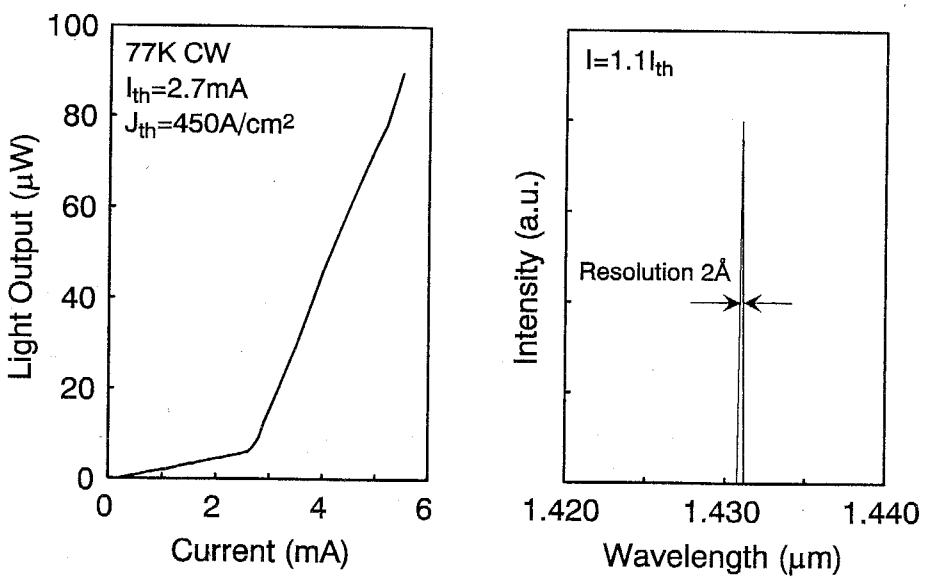

Fig. 5.8 Light output vs. current and lasing spectrum for 30μm diameter mesa-cap device. This result was the first observation of lasing operation for surface emitting lasers grown by CBE. Lasing threshold was 2.7mA under 77K continuous wave operation.

by temperature of about dEg/dT ~-0.3meV/K. The wavelength shift was good agreement with estimated value. We can see single mode operation. Such single mode operation is due to wide longitudinal mode spacing of short cavity surface emitting lasers and it is advantage of vertical cavity surface emitting lasers as mentioned in chapter 1. From the current voltage characteristics, the differential resistance was about 70Ω ($1.6\times10^{-4}\Omega cm^2$) at 77K and 30Ω ($7\times10^{-5}\Omega cm^2$) at room temperature. As such high resistance is due to small electrode area, it is important to reduce the specific contact resistance.

This device was not lased at room temperature CW and pulsed condition. However, I observed spontaneous emission spectra at room temperature CW condition. Figure 5.9 shows a spectrum under room temperature CW condition. Three Fabry-Perot modes were observed due to wide emission spectrum width under room temperature. The mode spacing was estimated about 75-80nm and this value agrees with the longitudinal mode spacing estimated from the grown cavity length.

The temperature characteristics of lasing threshold current are mentioned in next section with the other devices.

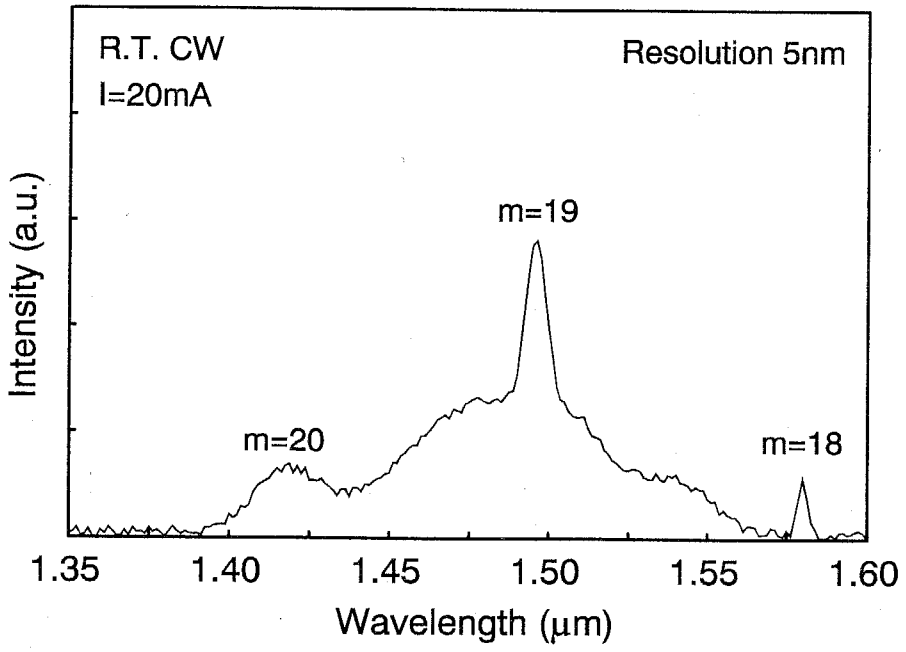

Fig. 5.9 Emission spectrum under room temperature. The peaks of 1.42μm, 1.50μm and 1.58μm are Fabry-Perot modes and m means longitudinal mode number. This device lased at 1.40μm under 77K CW condition with threshold current of 8mA.

5.2.3 Surface Emitting Lasers with Low Absorption Capping Layer

Next, a laser wafer with small optical absorption structure was grown and fabricated to mesa-cap surface emitting lasers. To reduce the optical absorption in highly doped p-capping layer, the capping layer structure was improved from previous wafer. The thickness was reduced from 0.25μm to 0.10μm, and the doping concentration was lowered from $2\times10^{19}cm^{-3}$ to $1\times10^{19}cm^{-3}$. By such configurations, the reduction of absorption loss in capping layer is expected to be about 1/5. The over all structure except capping layer is the same as the previous wafer shown in Fig. 5.3. The fabricated structure is also the same as the structure shown in Fig. 5.7.

The lasing characteristics under 77K CW condition are shown in Fig. 5.10. The minimum threshold current was 2.6mA at the lasing wavelength of 1.46μm. The threshold current density estimated from room temperature NFP was $575A/cm^2$. Improvement from the first lasing device mentioned above was not observed. The reason may be that the absorption loss is very small at low temperature, and the superior gain characteristics under low temperature also covered the loss difference. The worry of electrical characteristic such as differential resistance in capping layer was not observed though the hole concentration was low. However, the diameter of room temperature NFP was reduced compared with previous structure. The reason may be due to small current spreading in capping layer.

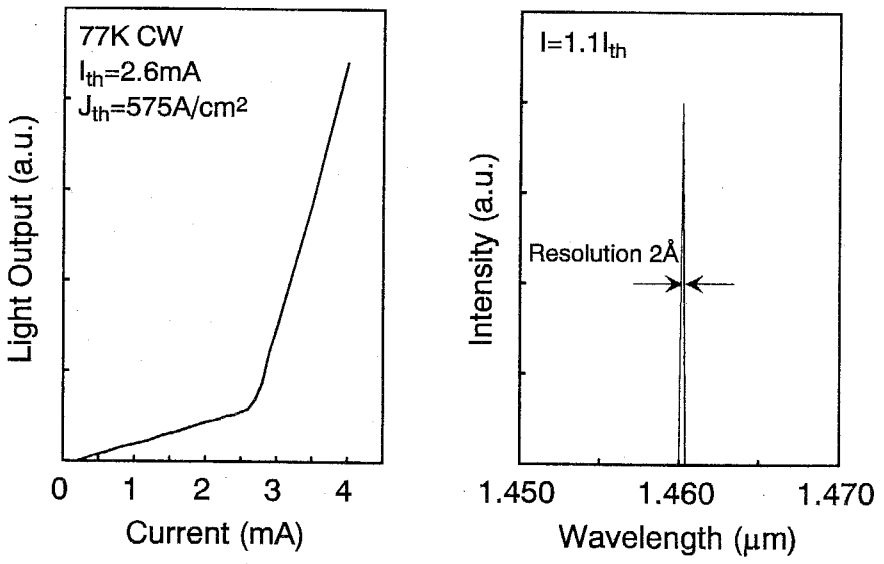

Fig. 5.10 Lasing characteristics for low absorption capping layer structure device. The threshold current was very slightly lowered against previous device at 77K CW condition.

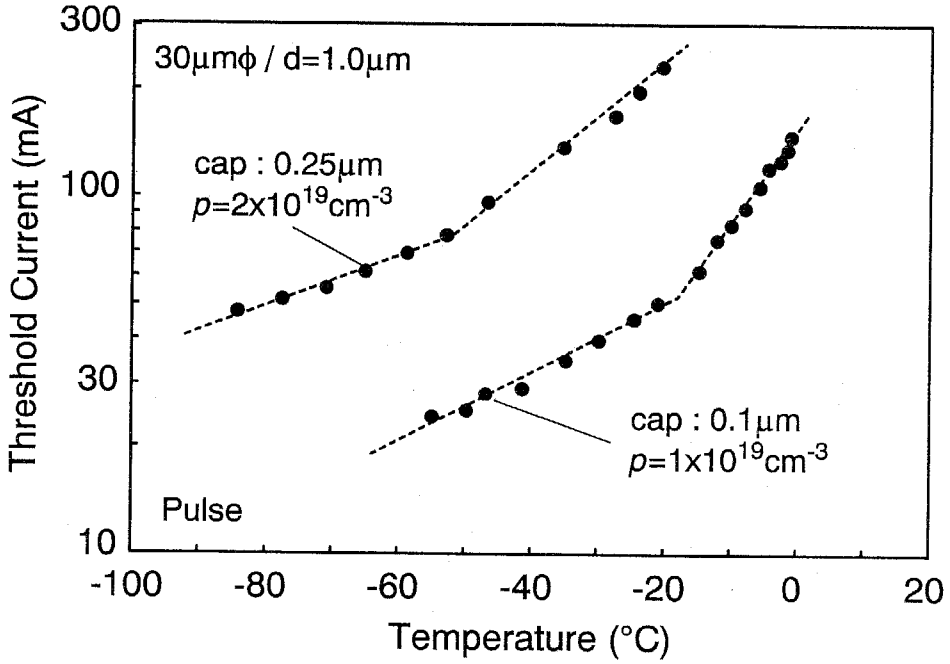

Fig. 5.11 Temperature characteristics of surface emitting lasers. The difference of two structures is thickness and doping concentration of capping layer.

Next, the temperature characteristic under pulse condition is discussed for two type structures. Temperature characteristics were measured in cooled mixture of methanol and ethanol for range from about -100°C to room temperature.

The temperature characteristics of threshold current are shown in Fig. 5.11. A former device which has 0.25μm thick capping layer with $p=2\times10^{19}cm^{-3}$ operated up to -20°C. The threshold current and its density was 230mA and 33kA/cm^2, respectively at maximum operating temperature. Thus any devices with thick capping layer did not lased at room temperature. On the other hand, the devices with low absorption capping layer structure was operated up to slightly higher temperature, and the maximum operating temperature was -1°C. At this temperature, the threshold current of later device was 147mA and the corresponding current density was 21kA/cm^2. The temperature characteristic difference between two devices seems not so large. However, the threshold current of later device was only 50mA at -20°C and the value was only about 1/5 compared with former device. The decrease of threshold current was considered due to reduction of optical absorption in capping layer because the inter-valence band absorption has large temperature sensitivity.

From the result, the absorption reduction in the cavity is effective for lowering threshold. On the other hand, the threshold current and maximum operating temperature was different from each device on the same wafer. In next section, it is discussed about this phenomenon.

5.3 Gain-Resonance Matching of Surface Emitting Lasers

5.3.1 Lasing Wavelength Dependence of Threshold Current

In the first fabricated wafers mentioned in previous section, the threshold current was ranged from 2.7mA to 30mA for tested 42 devices. From the measurement of lasing characteristics, I had found that there was a tendency which strongly depends on the wafer position for the threshold current and lasing wavelength. Figure 5.12 shows the threshold current and lasing wavelength of devices against wafer position. The lasing wavelength looks like gradually changed for the device positions. The threshold current was high at the changing position of lasing wavelengths.

As the surface emitting laser is a single longitudinal mode laser because of short cavity length, the variation of lasing wavelength is considered due to the difference of cavity lengths. The uniformity of thickness and composition is good enough under the substrate rotation condition during growth as mentioned in chapter 3. However the laser wafer shown in Fig. 5.12 was grown without substrate rotation to introduce intentional nonuniformity in layer thickness. Figure 5.13 shows the relation between threshold current and lasing wavelength of whole devices shown in Fig. 5.12. The tendency is clearly observed from this figure.

I considered the reason of this tendency as the result of a gain spectrum. Conventional edge emitting lasers have usually very short longitudinal mode spacing comparable with surface emitting lasers. Hence, the edge emitting laser is possible to lase at almost gain peak wavelength as shown in Fig. 5.14 (a). On the other hand, the surface emitting laser doesn't always lase at gain peak wavelength because of its wide longitudinal spacing as shown in Fig. 5.14 (b).

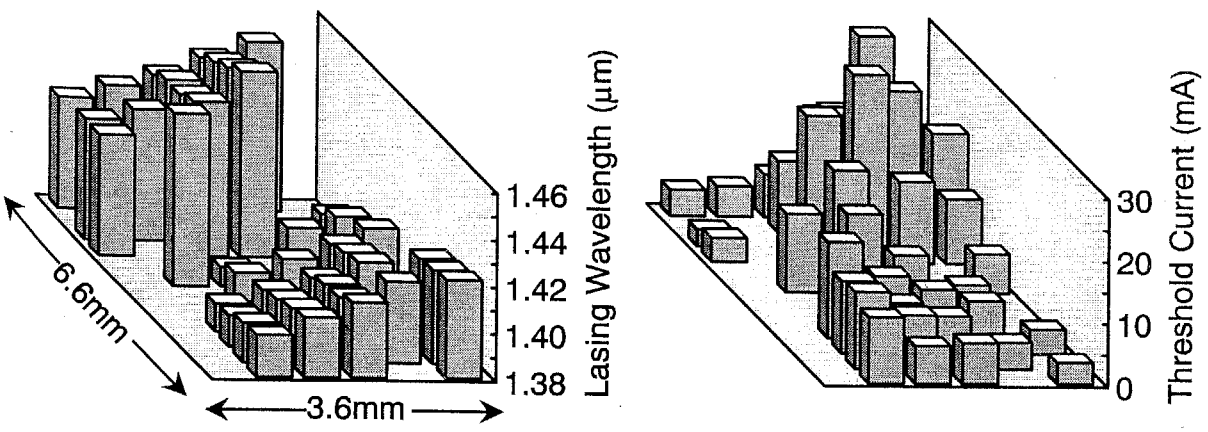

Fig. 5.12 Wafer position dependence of lasing wavelength and threshold current for one wafer. The device pitch is 600μm.

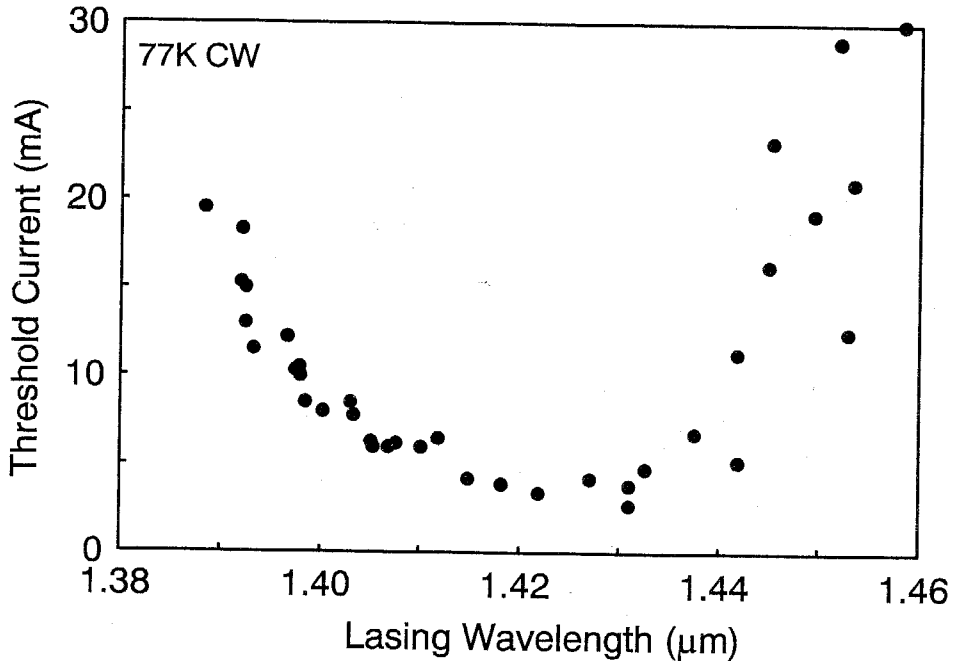

Fig. 5.13 Threshold current against lasing wavelength for devices on one wafer. The measurement was performed under 77K CW condition. The active layer diameter is about 30μm.

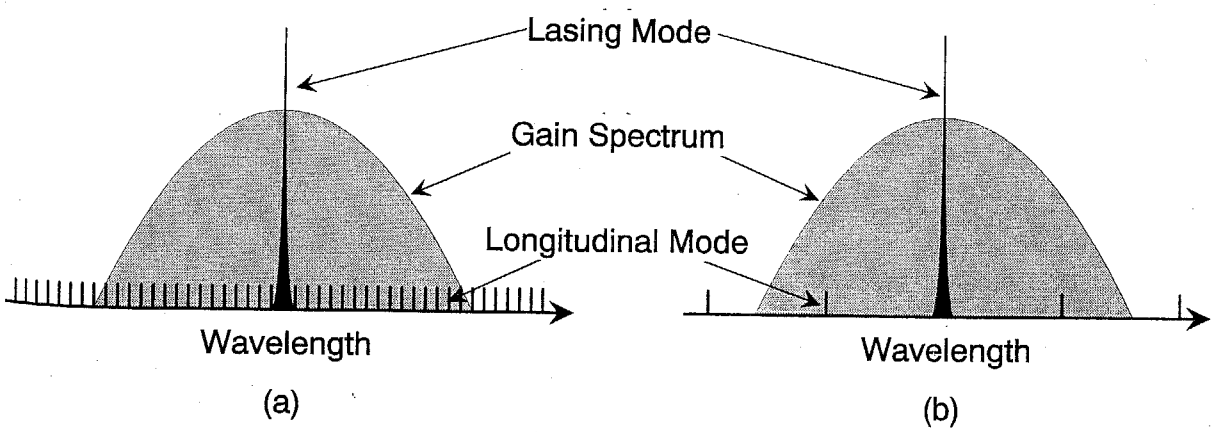

Fig. 5.14 Relation between gain spectrum, longitudinal mode and lasing mode for edge emitting lasers (a) and surface emitting lasers (b).

Figure 5.15 shows the theoretically calculated result of relation between threshold current density and lasing wavelength considering gain spectrum. The gain characteristics were calculated using the density matrix theory with intraband relaxation time. The bandgap energy of 0.86eV (1.44μm) was assumed for the GaInAsP at 77K. The threshold gain was assumed to be 100cm^{-1} which was calculated by mirror reflectivity of 99.5% and absorption coefficient of 10cm^{-1} in the 4μm cavity consisting 1μm active layer thickness. The gain spectrum is also shown in the figure for minimum threshold current condition. The threshold current density is gradually increased for below 1.43μm and rapidly increased for above 1.43μm. The experimental results shown in Fig 5.13 also show such tendency but the increase at short wavelength region was relatively rapidly. The reason may be due to thermal effect because the measurement was carried out under CW condition, and hence the bandgap energy was changed to narrow bandgap energy by heating. As the result, excess current was required for shorter wavelength region. This phenomena may also effect to reduce the increase of threshold current for longer wavelength region

Next, the wavelength dependence on threshold current is considered for room temperature condition. To calculate the threshold current, the bandgap energy of GaInAsP is assumed to be 0.77eV (1.62μm) to obtain peak gain at 1.55μm. The absorption coefficient is 10cm^{-1} for each cladding layer. The carrier density dependence absorption is assumed in the active layer with absorption cross section of 55×10^{-18}cm^2 (see chapter 2). The mirror reflectivity is assumed to be 99.7%. The results are shown in Fig. 5.16 for nonradiative

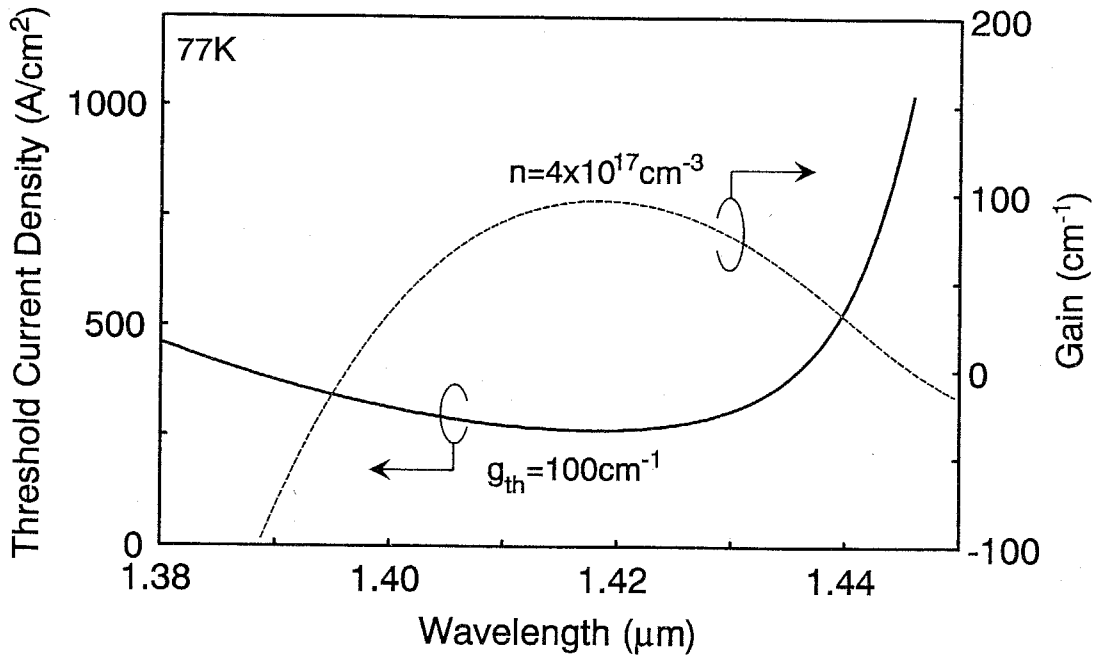

Fig. 5.15 Theoretical threshold current density vs. lasing wavelength at 77K.

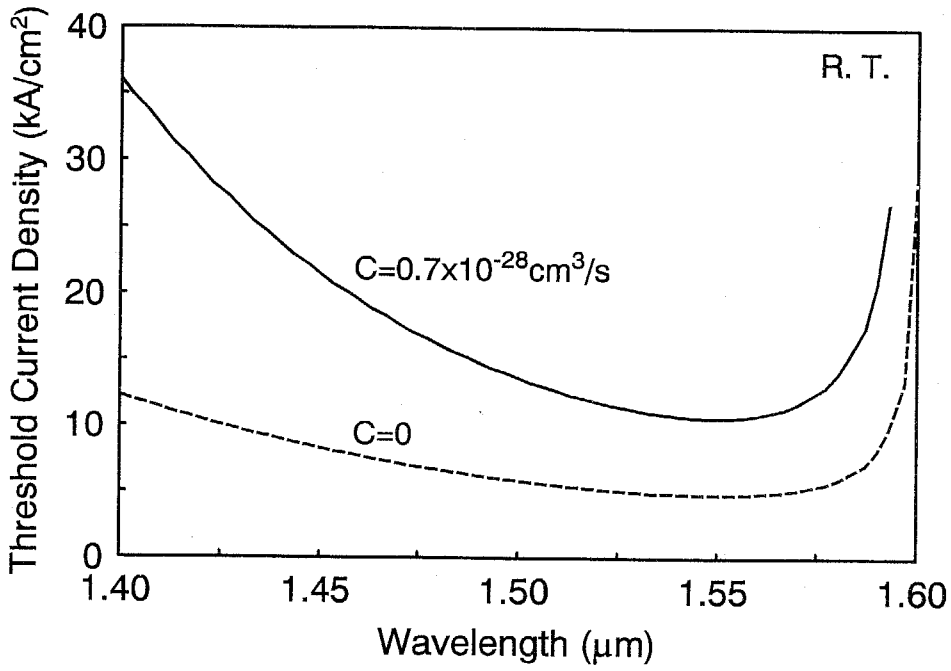

Fig. 5.16 Theoretical threshold current density vs. lasing wavelength at room temperature for different Auger recombination coefficients.

recombination coefficient C of 0.7×10^{-28}cm^6/s and 0 with radiative recombination coefficient B of 1.0×10^{-10}cm^3/s. Though the gain spectrum is relatively wide wavelength range at room temperature, the low threshold current wavelength range becomes narrow due to non-radiative recombination.

5.3.2 Gain-Resonance Matching Effect on Temperature Characteristics

The bandgap energy is changed by temperature as mentioned above. In this section, the temperature dependence of threshold current is examined in detail for long wavelength surface emitting lasers.

The temperature characteristics for two devices are shown in Fig. 5.17. These two devices were chosen from the first lasing wafer. The threshold current for sample A was increased monotonically as temperature rise. The sample A was lased at short wavelength compared with gain peak wavelength at 77K. The threshold current change is considered due to not only gain reduction but also mismatching of the gain peak and oscillation wavelength because the gain spectrum is shifted to long wavelength as the temperature rise. It is considered that the sample lased at equal or shorter wavelength than gain peak behave such temperature characteristic and the behavior looks like that of conventional lasers. As the result, the sample A was oscillated only up to about 110K. On the other hand, the sample B was oscillated up to 150K though the sample lased at far short wavelength from the gain peak at

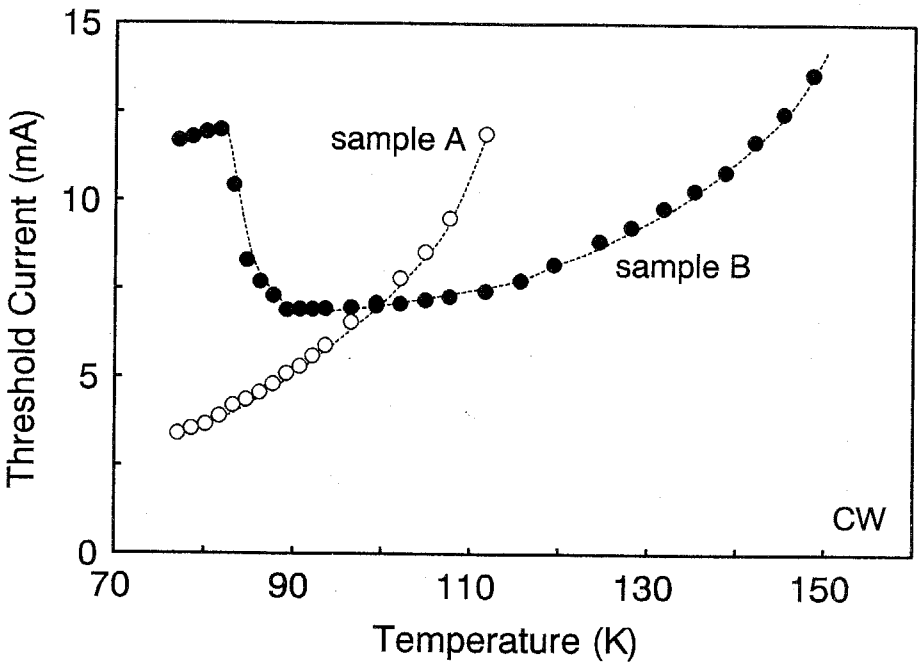

Fig. 5.17 Temperature characteristics of two type lasers. The lasing wavelength of sample A at 77K is matched or slightly shorten against gain peak wavelength. Sample B oscillated at far short wavelength against gain peak wavelength at 77K but the next mode in long wavelength was oscillated above 80K.

77K. The threshold current is increased as temperature rise at near 77K by the same reason as previous device. However, the lasing mode was hopped to next long wavelength mode at 82K and the lasing wavelength was changed to the longer wavelength than gain peak. As the gain peak is shifted to long wavelength, the oscillation wavelength match to the gain peak at 90K. Following behavior is the same as previous device. It is also reported that the temperature characteristics of threshold behave unique for GaAs system surface emitting lasers [12, 13, 14].

As the summary of this chapter, I realized the first achievement of a CBE grown GaInAsP/InP surface emitting laser. The lasing characteristic was drastically improved by lowering absorption loss in capping layer. On the other hand, the threshold current and the temperature characteristic is much related with gain peak wavelength. To obtain low threshold and higher operating temperature, the design of lasing wavelength (which is 1.55μm in this study) and the gain peak wavelength is very important because the longitudinal mode spacing is wide for surface emitting lasers. Though the analysis for quantum well active layer is not carried out in this study, the matching may be more important because the gain spectrum is considered to be narrow.

References

[1] S. Uchiyama, and K. Iga, "GaInAsP/InP surface emitting injection laser with a ring electrode," *IEEE J. Quantum Electron.*, vol. QE-20, pp. 1117-1118, 1984.

[2] K. Iga, H. Soda, T. Terakado, and S. Shimizu, "Lasing characteristics of improved GaInAsP/InP surface emitting injection lasers," *Electron. Lett.*, vol. 19, pp. 457-458, 1983.

[3] D. L. Huffaker, D. G. Deppe, K. Kumar, and T. J. Rogers, "Native-oxide defined ring contact for low threshold vertical-cavity lasers," *Appl. Phys. Lett.*, vol. 65, pp. 97-99, 1994.

[4] H. Okuda, H. Soda, K. Moriki, Y. Motegi, and K. Iga, "GaInAsP/InP surface emitting injection laser with buried heterostructures," *Jpn. j. Appl. Phys.*, vol. 20, pp. L563-566, 1981.

[5] Y. H. Lee, B. Tell, K. Brown-Goebeler, J. L. Jewell, "Top-surface-emitting GaAs four-quantum-well lasers emitting at 0.85μm," *Electron. Lett.*, vol. 26, pp. 710-711, 1990.

[6] Y. H. Lee, J. L. Jewell, A. Scherer, S. L. McCall, J. P. Harbison, and L. T. Florez, "Room-temperature continuous-wave vertical-cavity single-quantum-well microlaser diodes," *Electron. Lett.*, vol. 25, pp. 1377-1378, 1989.

[7] H. Wada, D. I. Babic, D. L. Crawford, T. E. Reynolds, J. J. Dudley, J. E. Bowers, E. L. Hu, J. L. Merz, B. I. Miller, U. Koren, and M. G. Young, "Low-threshold, high-temperature pulsed operation of InGaAsP/InP vertical cavity surface emitting lasers," *IEEE Photon. Technol. Lett.*, vol. 3, pp. 977-979, 1991.

[8] H. Soda, K. Iga, C. Kitahara, and Y. Suematsu, "GaInAsP/InP surface emitting injection lasers," *Jpn. J. Appl. Phys.*, vol. 18, pp. 2329-2330, 1979.

[9] I, Watanabe, F. Koyama, and K. Iga, "GaInAsP/InP CBH surface-emitting laser with a dielectric multilayer reflector," *Jpn. J. Appl. Phys.*, vol. 26, pp. 1598-1599, 1987.

[10] M. Oshikiri, F. Koyama, and K. Iga, "Optical thickness monitoring in dielectric multilayer deposition for surface emitting laser reflectors," *IEICE*, vol. J74-C-I, pp. 340-345, 1991.

[11] Y. Motegi, H. Soda, and K. Iga, "Surface-emitting GaInAsP/InP injection laser with short cavity length," *Electron. Lett.*, vol. 18, pp. 461-463, 1982.

[12] P. L. Gourley, S. K. Lyo, and L. R. Dawson, "High-efficiency, continuous-wave, epitaxial surface-emitting laser with pseudomorphic InGaAs quantum well," *Appl. Phys. Lett.*, vol. 54, pp. 1397-1399, 1989.

[13] P. L. Gourley, S. K. Lyo, T. M. Brennan, and B. E. Hammons, "Lasing threshold in quantum well surface emitting lasers: many-body effects and temperature dependence," *Appl. Phys. Lett.*, vol. 55, pp. 2698-2700, 1989.

[14] B. Tell, K. F. Brown-Goebeler, R. E. Leibenguth, F. M. Baez, and Y. H. Lee, "Temperature dependence of GaAs-AlGaAs vertical cavity surface emitting lasers," *Appl. Phys. Lett.*, vol. 60, pp. 683-685, 1992.

Chapter 6

Low Threshold Current GaInAsP/InP Surface Emitting Lasers

In this chapter, low threshold current GaInAsP/InP surface emitting lasers are fabricated and characterized. To reduce the threshold current density, a hybrid mirror structure was introduced. A current confinement structure was also fabricated. Furthermore, quantum well surface emitting lasers were considered for further reduction of threshold current density.

6.1 Hybrid-Mirror Surface Emitting Lasers

6.1.1 Growth and Fabrication of Hybrid-Mirror Surface Emitting Lasers

As described in chapter 2, hybrid mirror structure is effective to increase the effective reflectivity, and hence the structure is expected to reduce the threshold current density. In this section, a long wavelength surface emitting laser with hybrid mirror structure was grown and fabricated to the surface emitting lasers. The schematic view of the wafer structure is shown in Fig. 6.1. The wafer has 8 pair of GaInAsP (λg=1.45μm)/InP multilayer reflector (DBR) for n-side. The each layer thickness is corresponding to $\lambda/4$ (λ=1.55μm) optical thickness and the thickness of InP and GaInAsP is 1220Å and 1110Å, respectively. The bottom GaInAsP layer is also used as an etching stop layer. The n-cladding layer is $3\lambda/4$ and 0.36μm. The doping concentration of n-InP and n-GaInAsP is $2\times10^{18}cm^{-3}$ and $1\times10^{18}cm^{-3}$, respectively. The active layer is undoped GaInAsP (λg=1.55μm) and the thickness is 0.44μm which corresponds to $4\lambda/4$. As the optimum active layer thickness is reduced by higher mirror reflectivity, the thickness is designed thinner for hybrid-mirror laser wafers than that for conventional wafer shown in Fig. 5.3. The p-cladding layer has the thickness of $7\lambda/4$ and doping concentration of $1\times10^{18}cm^{-3}$. The GaInAsP (λg=1.3μm) capping layer is designed as a

low absorption structure with doping concentration of $1\times10^{19}cm^{-3}$ and thickness of $\lambda/4$ (0.11μm). In this way, all the layer thickness is designed as multiple of $\lambda/4$ and the lasing wavelength is controlled as λ. Such design is important to realize a low threshold surface emitting lasers because gain-resonance matching is necessary for optimized threshold current as described in chapter 5.

Figure 6.2 shows a reflectivity spectrum of a hybrid-mirror laser wafer. The reflectivity was measured from the epitaxial surface side. The dip at 1.55μm wavelength is the cavity resonance mode. The cavity is formed by 8 pair GaInAsP/InP multilayer reflector and epitaxial layer surface. In the figure, the theoretical reflection spectrum is also shown by dashed line. The experimental results are good agreement with theoretical results.

The wafers are fabricated to mesa-cap structures as shown in Fig. 6.3. The mesa diameters are 30μm and 20μm for two wafers but wafer structures are the same. The small mesa diameter structure is fabricated to realize low threshold with small current spreading in capping layer. The fabrication processes are almost the same as described in previous chapter, however the holing process is carried out for only InP substrate because the etching stop layer is designed as a part of multilayer reflector. The mirror is Si/SiO_2 multilayers for both side and the number of pairs is 4.5 for p-side with gold (Au) and 4 for n-side. Though the hybrid mirror is effective for realizing high reflectivity, it does not perform as reflector at low temperature because the mirror is adjusted to 1.55μm at room temperature and the high

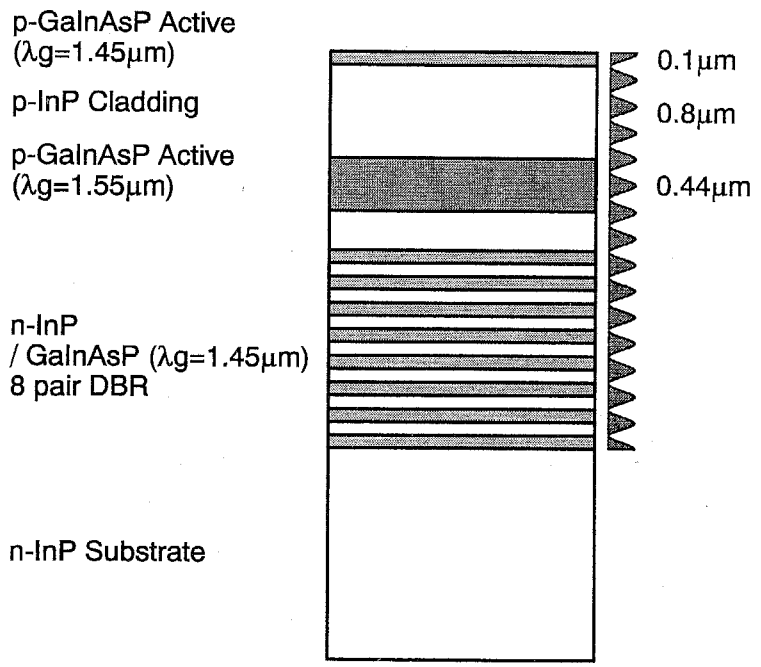

Fig. 6.1 Hybrid mirror surface emitting laser wafer grown by CBE. The wave form shows the schematic view of standing wave in the cavity.

reflectivity band width is not so wide.

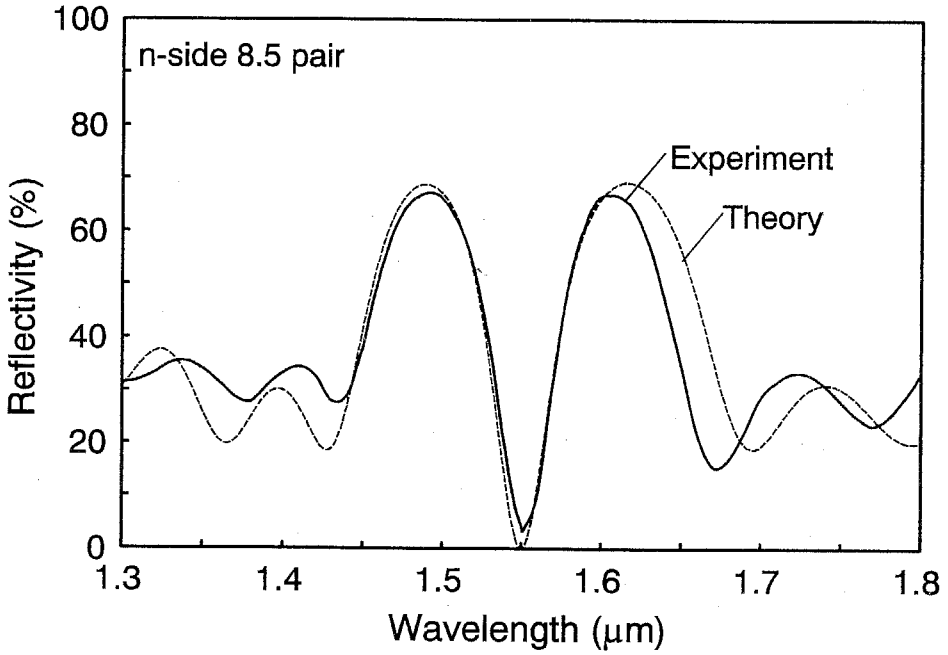

Fig. 6.2 Reflectivity spectrum of hybrid mirror laser wafer. The dashed line is theoretically calculated spectrum.

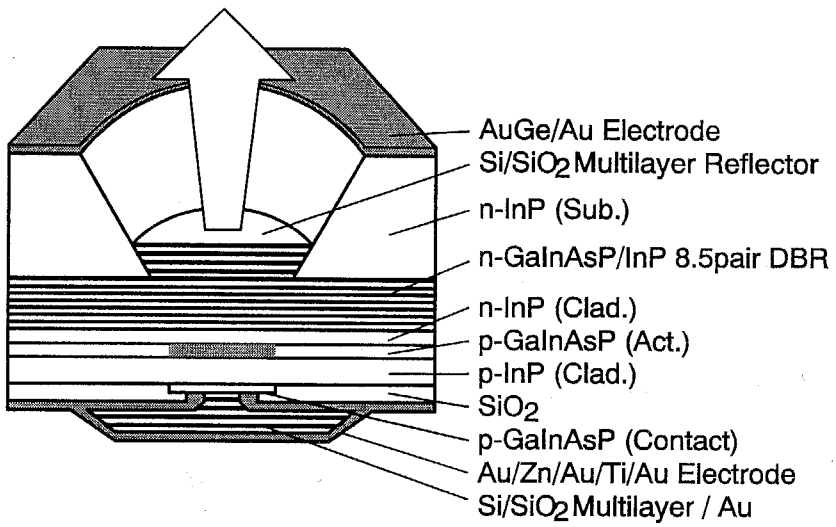

Fig. 6.3 Schematic view of a mesa-cap type surface emitting laser structure with n-hybrid mirror. This schematic view shows the 30μm diameter mesa type.

6.1.2 Lasing Characteristics of Hybrid-Mirror Surface Emitting Lasers

The minimum threshold current of 30μm diameter devices was 5.4mA. This value was about two times higher than the device shown in previous chapter. Considering the thinned active layer thickness, the threshold current is estimated about half of previous devices at low temperature. The reason of high threshold current is due to effect of gain and resonance mode mismatching. As the wafers for hybrid mirror devices were grown with substrate rotation, the thickness uniformity was superior than the wafers grown in chapter 5. Therefore the lasing wavelength is not so distributed and the lasing wavelength range was from 1.41μm to 1.44μm and from 1.49μm to 1.50μm. The two wavelength range is considered to be due to difference longitudinal mode number. This wavelength range is smaller than previous wafers without substrate rotation. The matching of gain peak wavelength and oscillation wavelength was considered to be occur in 1.47-1.48μm. In this way, it does not always show good lasing characteristics if the operating temperature is different from designed temperature.

The lowest threshold current of 1.0mA was observed for 20μm diameter mesa structure and its threshold current density was 320A/cm^2 as shown in Fig. 6.4. This threshold current and its density were lower than previous devices. The wafer for 20μm diameter devices was also grown with substrate rotation. Therefore the lasing wavelength of each device was

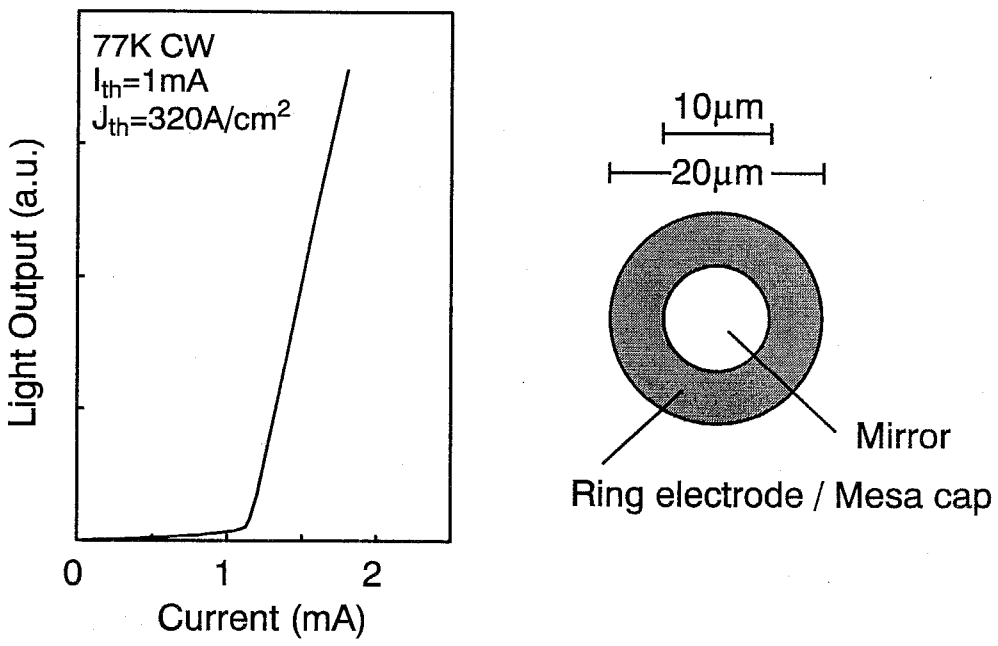

Fig. 6.4 I-L characteristic of mesa-cap surface emitting laser with n-hybrid mirror structure. The threshold current of 1.0mA is the lowest in mesa-cap type surface emitting lasers. The mesa diameter is 20μm with ring-electrode of outer/inner diameter of 20μm/10μm.

distributed narrow wavelength range from 1.49μm to 1.52μm. The gain peak wavelength is considered to be slightly shorter wavelength. Further reduction of threshold current is expected if the gain and oscillation wavelength is matched at 77K.

The temperature characteristics of hybrid-mirror structures are follows. The maximum operating temperature was 11°C for 30μm diameter mesa device and it is the highest operation temperature of CBE grown surface emitting lasers under pulse operation. Figure 6.5 shows the temperature characteristics of the hybrid-mirror device with that of previous devices. The threshold current was 97mA at maximum operating temperature. The corresponding current density was 18kA/cm^2 which was estimated from the measured NFP of 26μm diameter. The estimated reflectivity from the threshold current density is about 99.0% by theoretical calculation described in chapter 2. The maximum operating temperature and its threshold current exhibit superior characteristics to previous devices. The threshold current at -20°C and 0°C were about 20mA and 60mA, respectively. These threshold currents are about half and 1/10 of that of conventional devices. The notable result is due to high reflectivity of hybrid-mirror structure. The characteristic temperature T_0 was 20K at near room temperature for hybrid mirror surface emitting lasers. The temperature characteristics for previous devices were also not so large at near room temperature. The reported characteristic temperature for conventional edge emitting lasers are about 40K for GaInAsP (λg=1.55μm) bulk active layer.

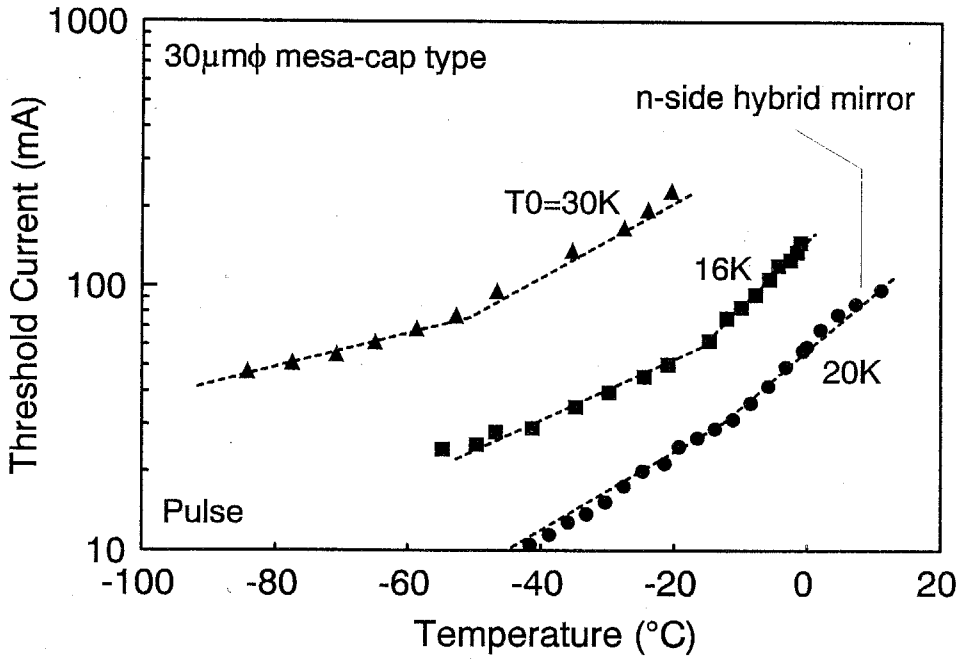

Fig. 6.5 Temperature characteristics of n-hybrid mirror surface emitting lasers (closed circle). Triangle and square makers represent the same result shown in Fig. 5.11.

Up to this time, almost reported long wavelength surface emitting lasers which operated at room temperature indicated small characteristic temperatures at near room temperature. Of course, characteristic temperatures of long wavelength semiconductor lasers are not so large comparable with that of short wavelength lasers because the optical absorption is increased as temperature rise. However, the value is worse for surface emitting lasers than for conventional edge emitting lasers. I considered that one of the reason may be originated from current injection problem of ring-electrode and it is discussed in next chapter.

The temperature characteristics under CW condition are shown in Fig. 6.6 for 20μm diameter hybrid mirror structure device. The maximum operating temperature was -84°C and that was far from the result under pulse operation because of thermal heating of continuous current. However, this temperature was highest for the GaInAsP/InP surface emitting lasers under CW condition at that time. The threshold current was varied for temperature but different from that of conventional edge emitting lasers. The reason is also the same as described in chapter 5. On the other hand, the lasing wavelength was changed gradually with 1.1Å/K which is less than conventional long cavity lasers and good agreement with distributed feedback (DFB) lasers [1, 2]. This small wavelength change is common for single mode lasers and the wavelength change corresponds to the refractive index change against temperature.

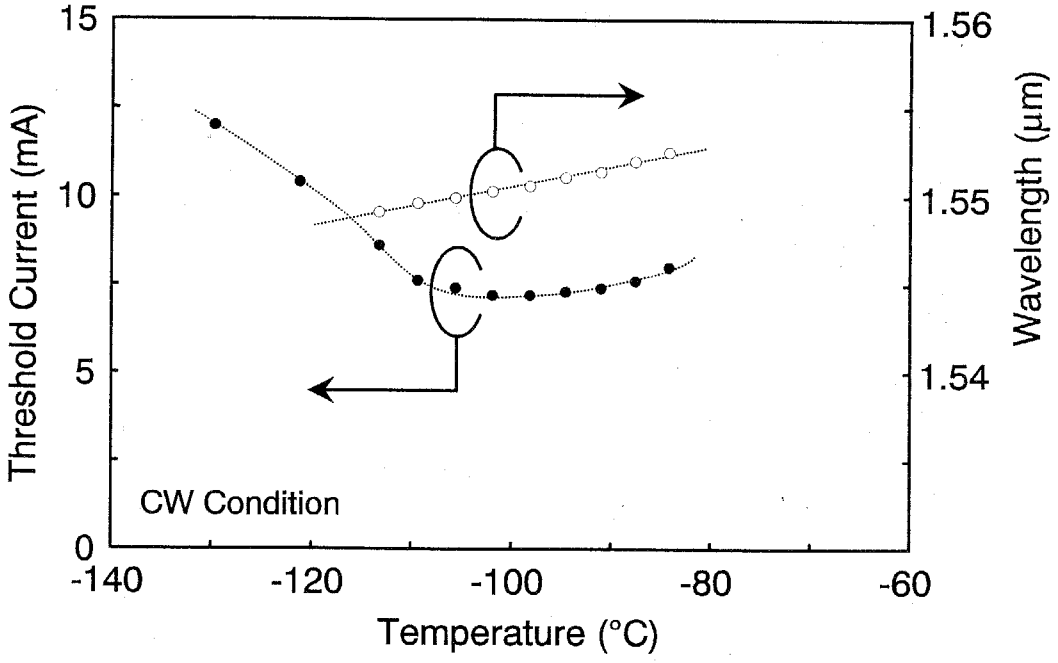

Fig. 6.6 CW temperature characteristics for 20μm diameter mesa-cap structure with n-side hybrid-mirror. The maximum operating temperature of -84°C was highest value at that time.

6.2 Polyimide Buried Mushroom Structure Lasers

6.2.1 Growth and Fabrication of Mushroom Structure Lasers

Next, a current confinement structure was fabricated to demonstrate a low threshold current. The fabricated current confinement structure is one of current limitation at active layer and called mushroom structure. The fabrication processes are like as mesa cap structure except formation process of the mushroom like mesa structure. The wafer for this mushroom structure is n-hybrid mirror type. First, fabrication processes are shown.

After the wafer growth and cleaning, SiO_2 for mesa etching mask was deposited by spattering technique about 1000Å. The SiO_2 was etched remaining 30μm diameter circle as well as mesa cap structure. Then the formation of mushroom structure is performed as follows; 1) GaInAsP capping layer etching by H_2SO_4:H_2O_2:H_2O = 3:1:1, 2) InP p-cladding layer etching by HCl:H_2O = 3:1, 3) GaInAsP active layer etching by H_2SO_4:H_2O_2:H_2O = 3:1:1.

The active layer etching is important to obtain controlled small active area which is smaller than SiO_2 mask and p-cladding layer. To control the area, the etching rate is very important because we can not see the active region through the cladding and capping layer.

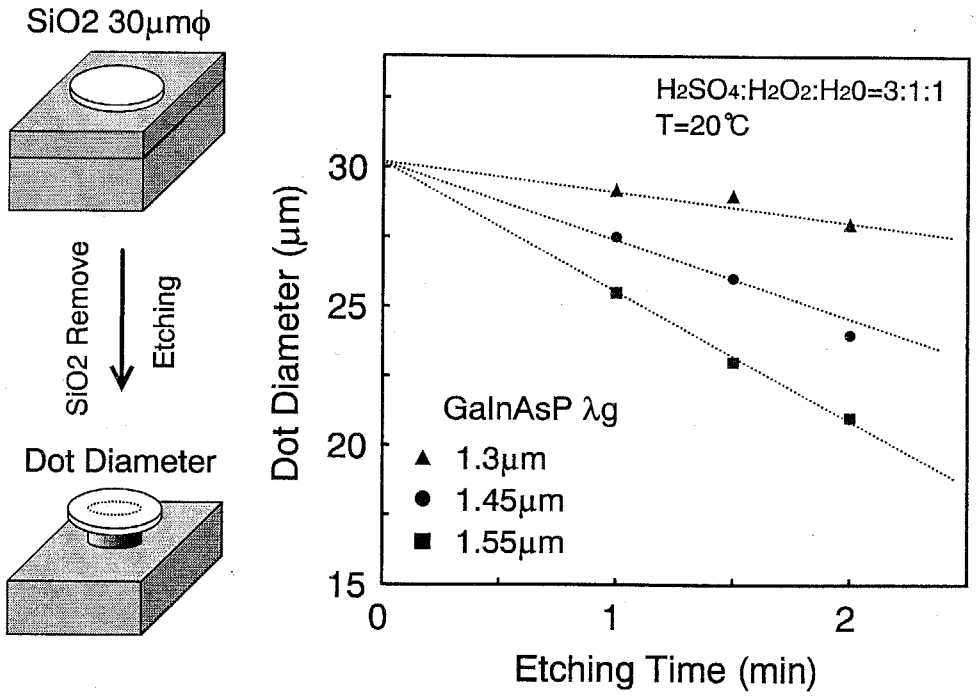

Fig. 6.7 Etching rate of GaInAsP. Etching rate is represented as the remain dot diameter.

Table 6.1 Etching rate of GaInAsP <110> direction by H_2SO_4:H_2O_2:H_2O = 3:1:1 (20°C)

GaInAsP λg	1.3μm	1.45μm	1.55μm
etching rate	0.6μm/min	1.8μm/min	2.3μm/min

To success the formation of small active area, the etching rate of GaInAsP was measured for H_2SO_4:H_2O_2:H_2O solution. The measurement results are shown in Fig. 6.7. To adjust the condition to the real device, the vertical axis of graph is represented as remained mesa diameter. The sample for measurement of etching rate consists single GaInAsP layer on InP substrate and the thickness is about 0.5μm. The samples are covered by SiO_2 and the SiO_2 is etched remaining 30μm diameter area. Then the etching is carried out at 20°C in the solution. The GaInAsP composition is λg=1.3μm, 1.45μm and 1.55μm. From the result, narrow band gap material (long wavelength material) has high etching rate. As the etching is progressed unhomogeneously, the remained area is square shape. The etching rate is summarized in table 6.1.

After formation of mushroom structure, the mesa is buried by polyimide which also plays an electrical insulator layer. The polyimide used in this study has sensitization as

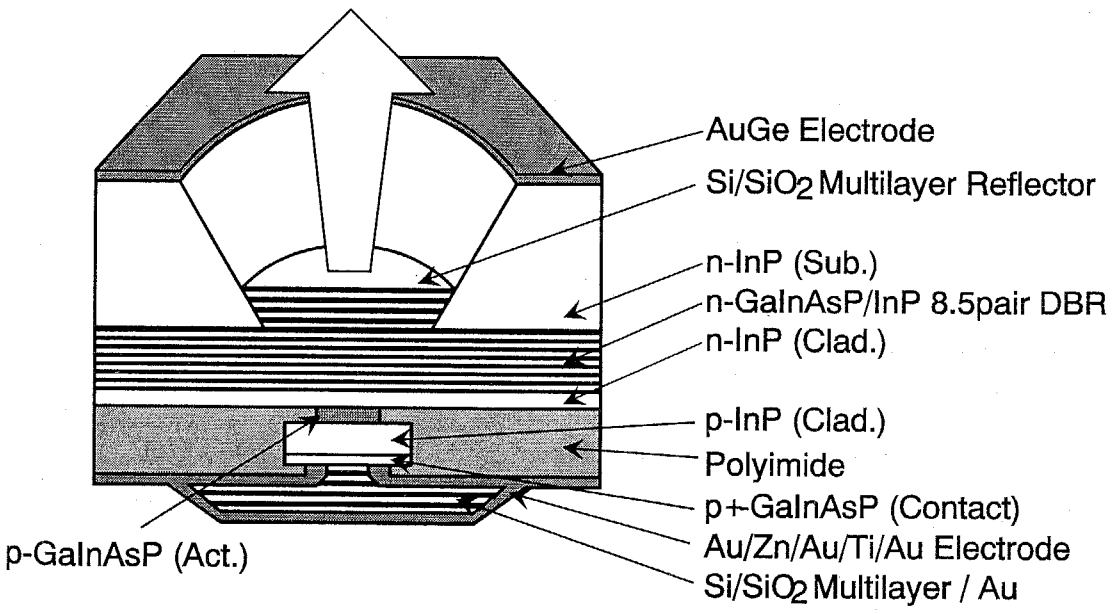

Fig. 6.8 Schematic structure of mushroom type surface emitting laser with n-side hybrid mirror.

negative type for the light, and so the electrode and mirror window at the center of mesa is opened by conventional photolithography technique. The following processes are like as that of mesa-cap structures and hence the processes are omitted here. The schematic structure of mushroom type surface emitting laser with hybrid mirror is shown in Fig. 6.8. The name of mushroom is from the shape of the active region which is smaller than cladding layer.

6.2.2 Lasing Characteristics of Mushroom Structure Lasers

The lasing characteristics of mushroom type structure are shown in Fig. 6.9. The threshold current of 0.3mA was obtained under 77K CW condition and this threshold is the lowest threshold current at 77K for long wavelength surface emitting lasers. The device has $10\times10\mu m^2$ of active area and this area is about 1/3 - 1/7 of the current flow area of mesa-cap structures. The threshold current density of $300A/cm^2$ is good agreement with that of mesa-cap structures. However, the yields of completely fabricated devices were very little, and so the lower threshold devices will be expected if the fabrication process is improved. The temperature characteristic of this device is not so good. The reason of this is also due to difficulty of fabrication.

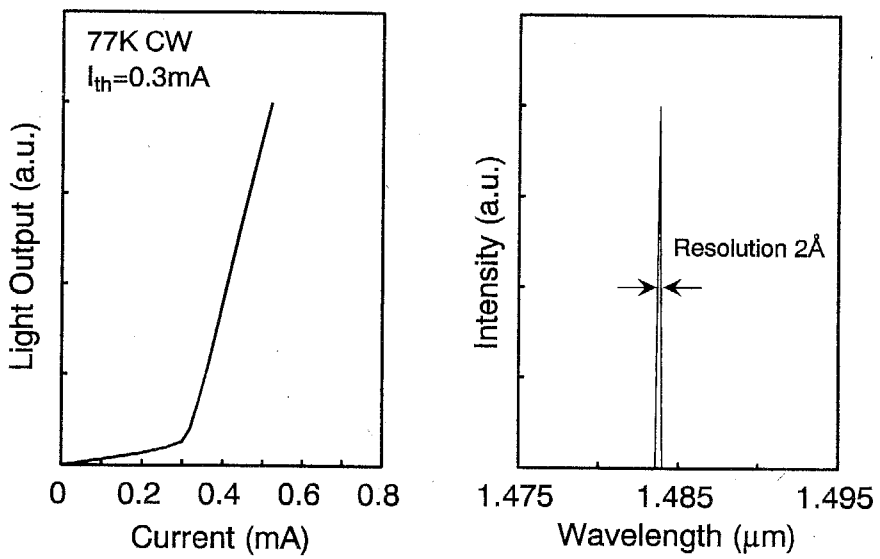

Fig. 6.9 Lasing characteristics of a mushroom type surface emitting laser shown in Fig. 6.8 under 77K CW condition. Threshold current of 0.3mA is the lowest in GaInAsP/InP surface emitting lasers.

6.3 Strain Compensated Quantum Well Surface Emitting Lasers

6.3.1 Growth and Fabrication of Strain Compensated QW SE Lasers

As discussed in previous section, good lasing characteristics were achieved by bulk active layer structure. From the lasing characteristics of edge emitting laser, much higher performance is expected by applying quantum well active layer. I also tried to fabricate the quantum well surface emitting lasers.

The grown structure for surface emitting lasers is shown in Fig. 6.10. The active layers have 8 or 10 quantum wells separated to two regions considering large matching factor as described in chapter 2. The well is 65Å thick and 1.0% compressively strained GaInAsP. On the other hand, the barrier is 150Å thick and 0.6% tensile strained GaInAsP which form the strain-compensated structure. The strain-compensation is not zero-net strain from the result of photoluminescence measurement discussed in chapter 4. The λg of the barrier is 1.2μm. The separator between two quantum well regions is GaInAsP of λg=1.2μm lattice matched to InP. The separator thickness is 1258Å and 1040Å for the structure of 8QW and 10QW, respectively. This thickness is determined that the two quantum well regions fit to the peak of standing wave. In this structure, any semiconductor mirror did not exist, however the doping concentration of p- and n-cladding layer is lowered to reduce the absorption loss. The doping

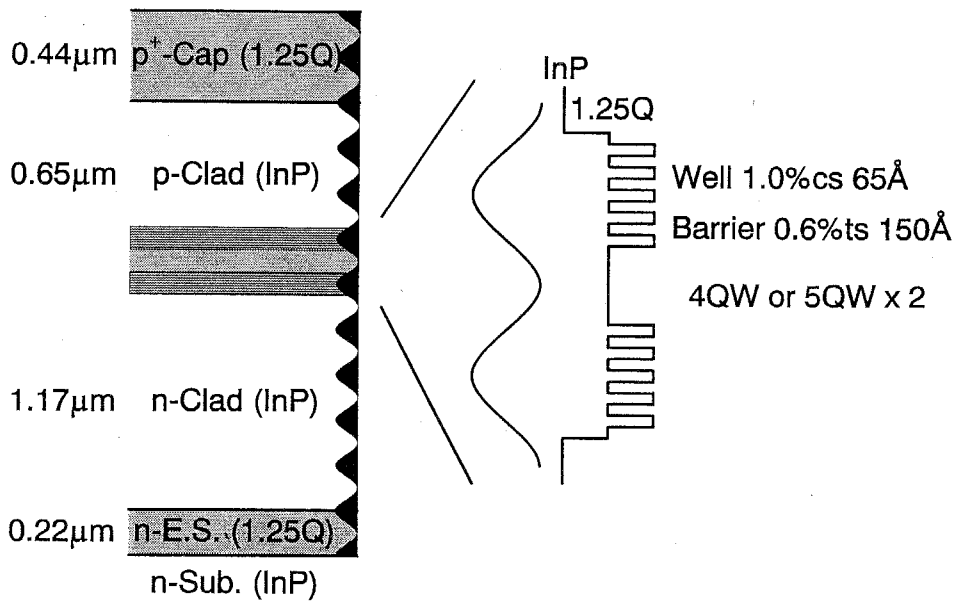

Fig. 6.10 Schematic structure of strained QW surface emitting lasers. The active region has 8 or 10 wells separated to two groups. The active region structure is strain-compensated strained QWs.

concentration of n- and p-cladding layer is $n=5\times10^{17}cm^{-3}$ and $p=2\times10^{17}cm^{-3}$, respectively. The thickness of cladding layer is 1.17μm ($9\times\lambda/4+\alpha$) and 0.65μm ($5\times\lambda/4+\alpha$) for n- and p-side, respectively. InP of thickness of α is inserted to the side of active layer to adjust the total cavity thickness to multiple of $\lambda/4$. The capping layer thickness of 0.44μm is thicker than that of previous devices because the capping layer of mirror region is etched away to reduce the absorption loss. It is more effective to avoid absorption loss than the thin capping layer thickness and low doping concentration.

The lasing characteristics of this wafer of edge emitting lasers are follows. The minimum threshold current density was $2.5kA/cm^2$ at 500μm cavity length and it corresponded to be $250A/cm^2/QW$. The relation between threshold current density and reciprocal cavity length is shown in Fig. 6.11. The expected threshold current for infinite cavity length is about $160A/cm^2/QW$ and this value is higher than result of conventional edge emitting laser wafer with SCH layers as shown in chapter 4. The deterioration of threshold current density is due to un-optimized structure for edge emitting lasers such as thin p-cladding layer and nothing of SCH layer.

The fabricated laser structure is mesa cap type and mushroom type as shown in Fig. 6.12. The layers around mesa of the previous devices shown in chapter 5 are etched away except mesa region, and hence these structures have very thin layer at the hole. The modified structure fabricated in this section is etched away only around mesa by using ring mask.

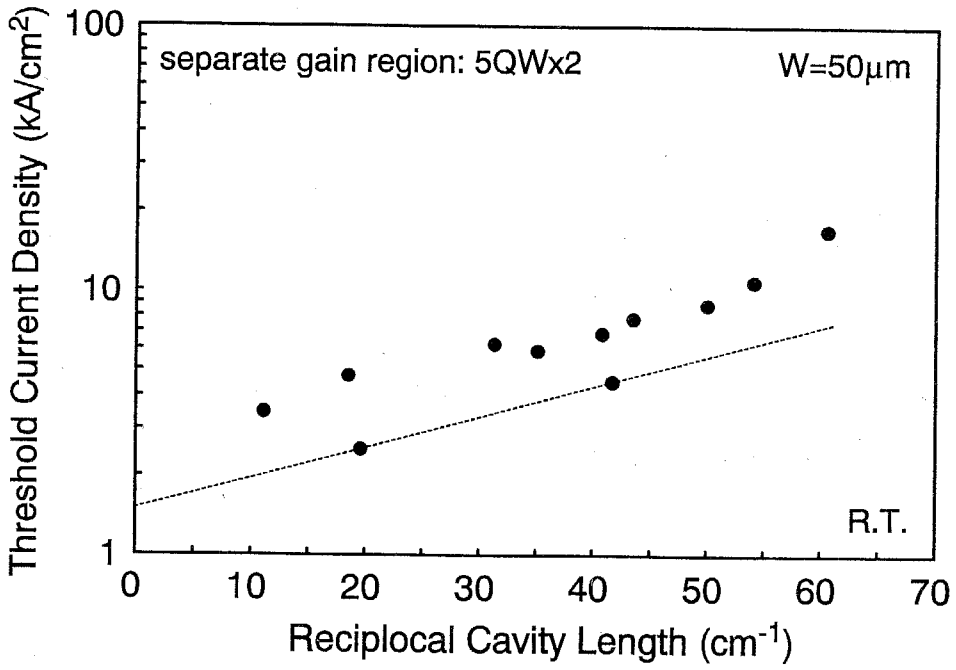

Fig. 6.11 Edge emitting laser characteristics for separate gain region structure.

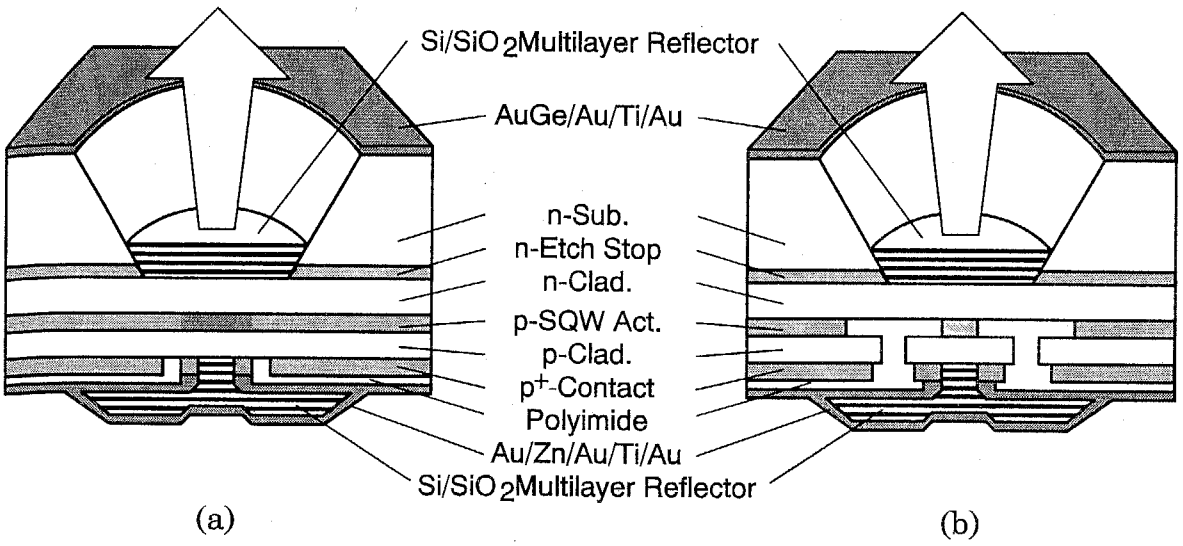

Fig. 6.12 Mesa-cap type (a) and mushroom type (b) surface emitting lasers with strain compensated MQWs. These structures are different from previous structure at the point of remaining of layers around mesa.

6.3.2 Characteristics of Strain Compensated QW SE Lasers

Up to the present, the lasing operation have not been obtained for QW surface emitting lasers grown by CBE yet. Figure 6.13 shows spectra under 77K CW condition for 10QW×2 separate gain structure. We can see two Fabry-Perot modes especially in injection current of 3mA. Theoretically calculated longitudinal spacing is about 130nm though the observed value is 44nm. Thus the unknown peaks are observed. I consider that the origin of short wavelength peak may be formed between n-side mirror and p-side ring electrode. The wavelength difference from the destination cavity is due to thickness difference with/without capping layer. The destination cavity consists 18×(λ/4) thickness but the undesirable cavity consists 18 ×(λ/4) with 4×(λ/4) capping layer thickness. The theoretical reflection spectrum is shown in Fig. 6.14. In this calculation, n-mirror is assumed to be one-pair Si/SiO_2 and p-mirror is 1.5-pair Si/SiO_2 with gold. The cavity is 18×(λ/4) InP. For undesirable cavity, the cavity also consists GaInAsP (λg=1.4μm) of 4×(λ/4) thickness with gold mirror. We can see two different wavelength modes near 1.4μm as well as experimentally observed mode. Thus undesirable mode may be due to another cavity mode. The destination cavity is successively fabricated, however the lasing was not observed due to offset of gain peak wavelength and cavity mode wavelength under 77K.

In this study, high performance QW surface emitting laser has not been realized yet. However, there are some study for QW long wavelength surface emitting lasers [3, 4, 5]. These results show better lasing characteristics than bulk active layer.

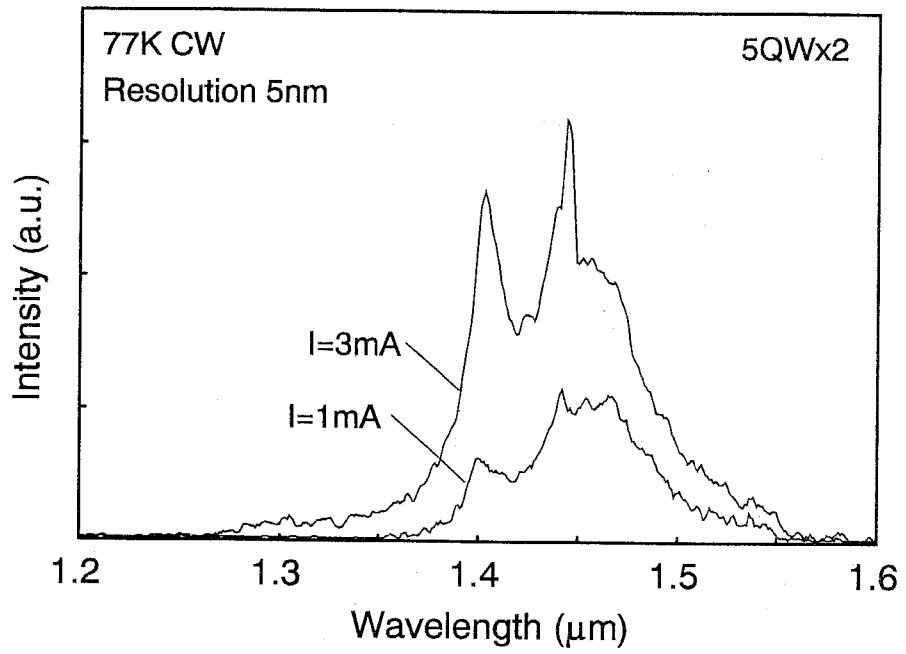

Fig. 6.13 Spectra of 5QW×2 separate gain structure under 77K CW condition. The device structure is mushroom type but the active layer area is relatively large (about 25×25μm²).

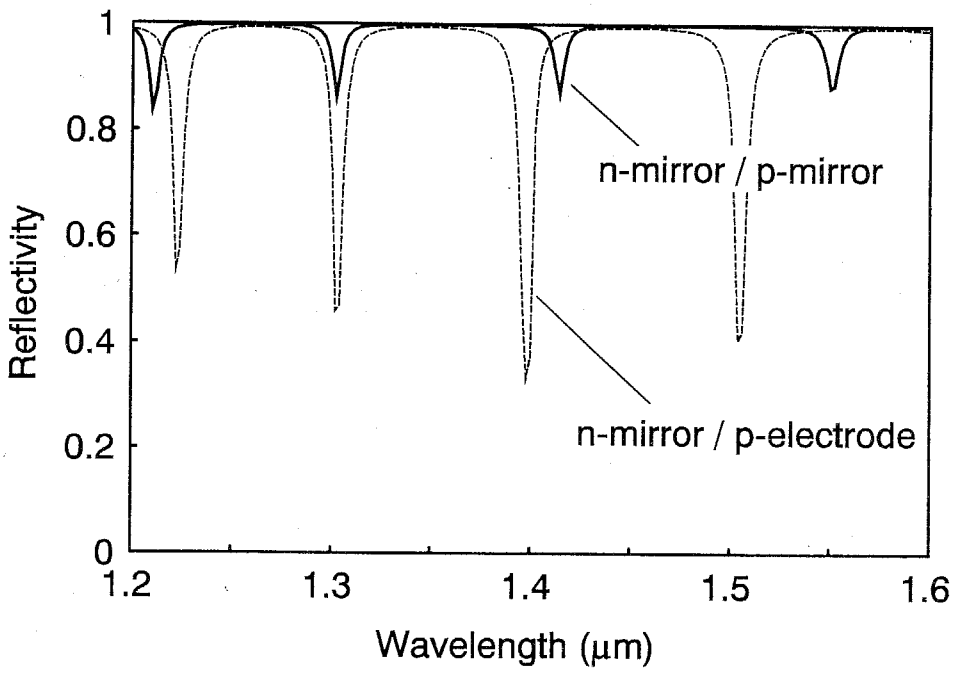

Fig. 6.14 Longitudinal mode wavelength calculation by analysis of reflectivity spectrum. The assumed cavity structure is described in the text.

References

[1] K. Sakai, K. Utaka, S. Akiba, and Y. Matsushima, "1.5μm range InGaAsP/InP distributed feedback lasers," *IEEE J. Quantum Electron.*, vol. 18, p. 8, 1982.

[2] T. Tanbun-ek, S. Suzaki, S. Wang, F. Koyama, S. Arai, and Y. Suematsu, "Static characteristics of 1.5-1.6μm GaInAsP/InP buried heterostructure butt-jointed built-in integrated lasers," *IEEE J. Quantum Electron.*, vol. QE-20, pp. 131-140, 1984.

[3] K. Uomi, S. J. B. Yoo, A. Scherer, R. Bhat, N. C. Andreadakis, C. E. Zah, M. A. Koza, and T. P. Lee, "Low threshold, room temperature pulsed operation of 1.5μm vertical-cavity surface-emitting lasers with an optimized multi-quantum well active layer," *IEEE Photon. Technol. Lett.*, vol. 6, pp. 317-319, 1994.

[4] C. H. Lin, C. L. Chua, Z. H. Zhu, F. E. Ejeckam, T. C. Wu, and Y. H. Lo, "Photopumped long wavelength vertical-cavity surface-emitting lasers using strain-compensated multiple quantum wells," *Appl. Phys. Lett.*, vol. 64, pp. 3395-3397, 1994.

[5] D. I. Babic, K. Streubel, R. P. Mirin, N. M. Margalit, J. E. Bowers, E. L. Hu, D. E. Mars, L. Yang, and K. Carey, "Room-temperature continuous-wave operation of 1.54μm vertical-cavity lasers," *IEEE Photon. Technol. Lett.*, vol. 7, pp. 1225-1227, 1995.

Chapter 7

Discussions for Improving Surface Emitting Laser Characteristics

In this chapter, surface emitting laser characteristics are discussed in detail about current-voltage characteristic for p-type DBR and lateral current uniformity of ring-electrode structure. Then, future development of high performance long wavelength surface emitting lasers are considered.

7.1 Electrical Characteristics of p-Type Multilayer Reflectors

7.1.1 Electrical Characteristics of p-GaInAsP/InP DBR

To realize high performance long wavelength surface emitting lasers, it is required to realize high reflectivity mirrors as described in chapter 2. For long wavelength surface emitting lasers, a GaInAsP/InP multilayer distributed Bragg reflector (DBR) is important mirror because of lattice matching material to InP substrate and high productivity by continuous growth with active layer. I applied the n-type GaInAsP/InP multilayer to the surface emitting lasers as hybrid mirror described in chapter 6. The GaInAsP/InP DBRs applied to the n-side mirror of the long-wavelength surface emitting lasers are also reported and the lasers show good lasing characteristics [1, 2, 3, 4].

On the other hand, the p-type semiconductor DBR has realized only as fused GaAs/AlAs mirror structure for long wavelength surface emitting lasers [5]. I also considered to apply the p-type semiconductor multilayer mirror as a hybrid mirror. The schematic laser wafer structures are shown in Fig. 7.1 with previously described wafers grown by CBE. The structure (a) has no DBR structure which is the first lasing surface emitting laser grown by CBE. The structure (b) consists of an 8-pair GaInAsP/InP DBR for the n-side and the structure (c) has a 5-pair DBR for the p-side and an 8-pair DBR for the n-side. The

composition of GaInAsP layer of DBR is λg=1.45μm and lattice matched to InP. The doping levels of the p-DBR are $1\times10^{18}cm^{-3}$ for InP and $2\times10^{18}cm^{-3}$ for GaInAsP, and that of n-DBRs are $1\times10^{18}cm^{-3}$ for InP and $2\times10^{18}cm^{-3}$ for GaInAsP. The p-capping layers are also grown on the top of epitaxial layers with $p=1\times10^{19}cm^{-3}$. The active layer is undoped-GaInAsP (λg=1.55 μm). These wafers were fabricated to mesa-cap type surface emitting laser structures. However, the lasing operations are achieved only for structure (a) and (b) and double-side hybrid mirror lasers (c) are not lased even under 77K.

I considered one of the reasons as its high electrical resistance. Figure 7.2 shows current-voltage characteristics of each structure at room temperature. The two structures without DBR and with only n-side DBR show very similar characteristics. The obtained result indicates that the n-type DBR does not affect to the electric characteristics so much. However, the p-side DBR causes an excess bias of 0.5V at $5kA/cm^2$. This value is equivalent to a 0.1V excess bias for one p-DBR pair.

It is known that the p-type semiconductor DBRs has difficulty of high electrical resistance at the heterojunction. This high resistance at the p-type DBR had been reported as a serious problem in short wavelength surface emitting lasers using AlAs/GaAs DBRs. Some methods to reduce the excess bias at AlAs/GaAs DBR have been reported, for example, using a graded layer, and high delta doping at the hetero-interface [6, 7, 8, 9]. Although theoretical study is required to design the optimum DBR structure, the theoretical modeling of electrical characteristics for p-type DBRs has not been fully cleared yet [10, 11, 12, 13].

In this section, I made proposal of analysis method of the current-voltage characteristic of p-type GaInAsP/InP DBR structure taking the light- and heavy-hole transmission tunneling

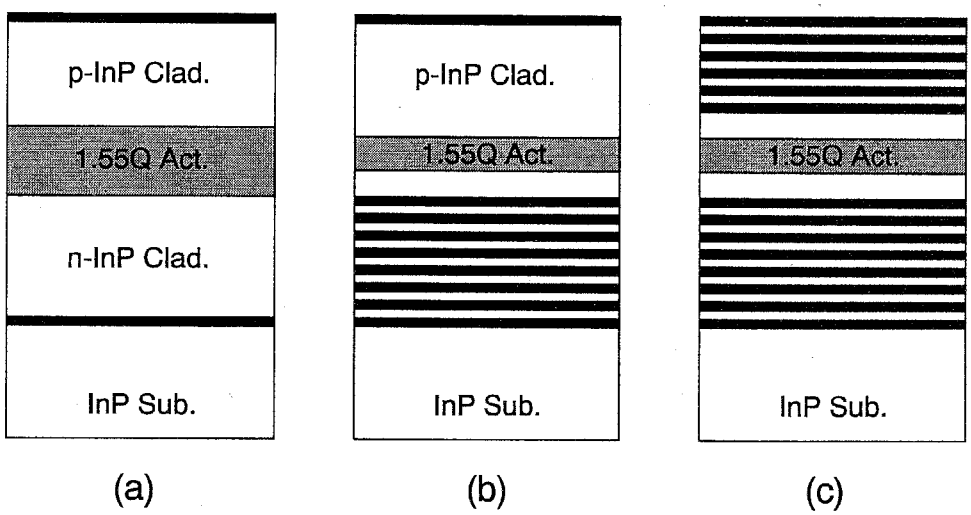

Fig. 7.1 Laser wafers for examine the current-voltage characteristics in semiconductor multilayer regions.

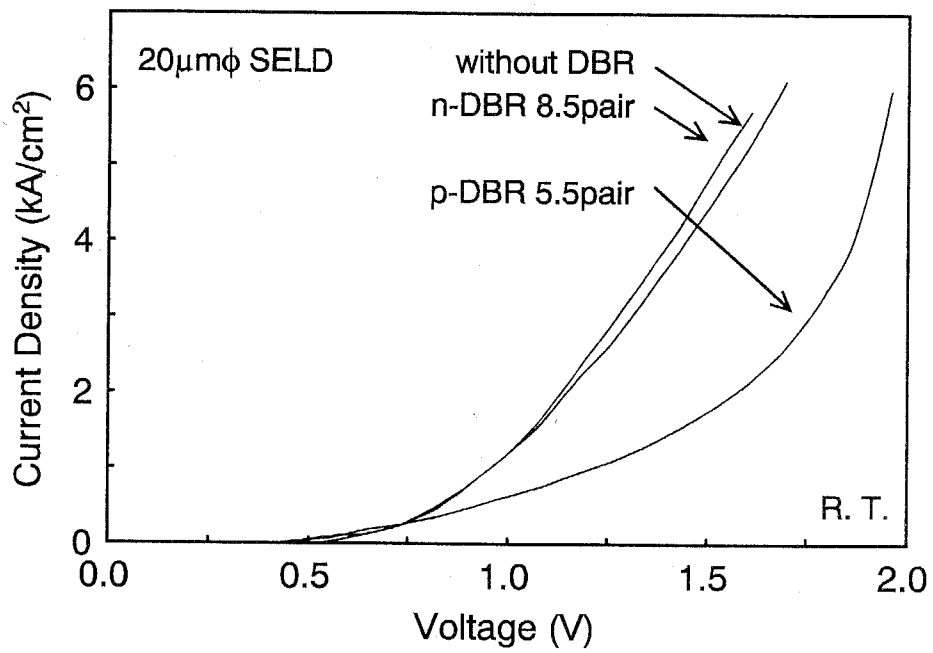

Fig. 7.2 Experimental current-voltage characteristics for various laser structures.

into account.

7.1.2 Modeling of Current Flow at p-Type Heterojunction

I consider the current-voltage characteristic of p-type DBRs taking the carrier tunneling at heterointerface into account. Figure 7.3 is a schematic energy-band diagram of a part of p-GaInAsP/InP DBR. The GaInAsP and InP are high and low index material, respectively. The heterointerface is assumed to be abrupt. The doping profile in each layer is assumed to be uniform and any delta- or graded-doping is not considered. In the figure, two kinds of the heterojunctions marked forward- and reverse-bias is shown. The distinction of the two heterojunctions is a result from the direction of the current flow, and the current is assumed to flow from right to left in the figure. At the forward-bias interface, holes move from the wide band-gap material to narrow one. The reverse-bias means the opposite situation.

The hetero-spikes may exist at these hetero-interface and these spikes obstruct the transport of holes remarkably for the reverse-bias condition. In the n-type DBR, the hetero-spikes also exist, but the electrons distribute in wide energy width at near room-temperature due to small effective mass. On the other hand, holes distribute at near valence-band edge due to the large density of states. Therefore, both the thermionic emission which means the carrier transport over the hetero-spikes and the tunneling transport should be considered for the hole current. The hole tunneling transmission current of p-GaAs/AlAs DBRs was calculated by

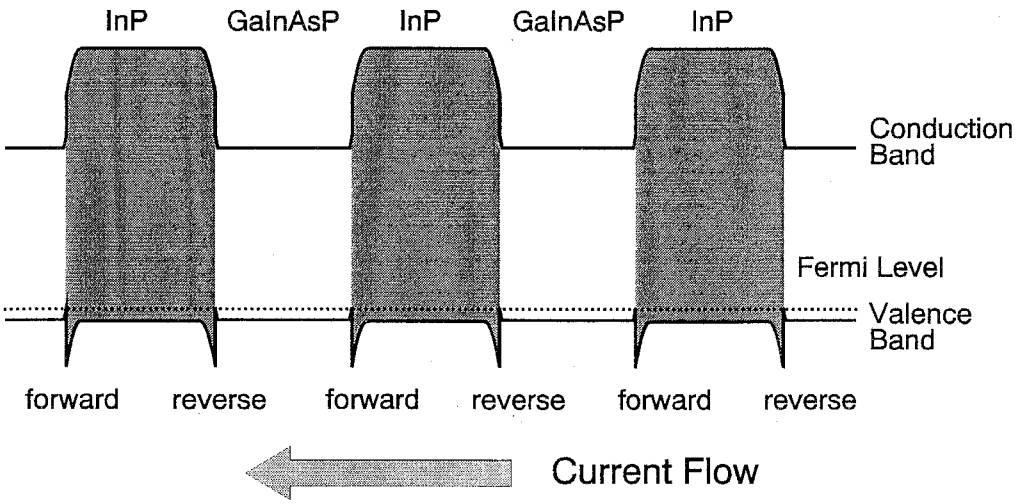

Fig. 7.3 Band diagram of GaInAsP/InP p-type DBR. The potential spike in valence band is classified to two types for the current flow direction as forward bias and reverse bias.

Zeeb and Ebeling [12], however they dealt with only the heavy-hole tunneling current and the light-hole transmission tunneling is neglected. In considering the tunneling transport, the tunneling probability is important and it relates with the effective mass of the carriers. Since the light-holes have smaller effective mass than the heavy-holes, the tunneling probability of light hole may be large. Then I consider a new carrier transport model of p-type GaInAsP/InP DBRs which include both light- and heavy-hole tunneling effects.

To calculate the tunneling probability, the potential barrier profile is required for the biased conditions. At first, the energy band diagram of p-isotype GaInAsP/InP heterostructure is calculated under bias conditions by using Poisson's equation. We can calculate smoothly the potential barrier profile of the abrupt interface structure because the depletion region exists only in the wide band-gap material of InP. The potential profile is calculated by using the condition of edge energies and the thickness of the depletion region. The edge energies are defined by equality of the interface electric displacement at two material [14];

$$\left\{2\varepsilon_1 qN_1\left[\frac{kT}{q}\left(\exp\frac{q(V_{D1}-V_1)}{kT}-1\right)-(V_{D1}-V_1)\right]\right\}^{1/2}=\left[2\varepsilon_{21}qN_2(V_{D2}-V_2)\right]^{1/2} \quad (7.1)$$

where the subscripts of 1 and 2 means narrow and wide bandgap material, respectively. ε is the dielectric constant. V_D and V are the built-in potential and the applied bias, respectively. The built-in potential is calculated as the difference of vacuum energy in two materials, and therefore $V_D = f1 - f2$ where $f1$ and $f2$ are Fermi-energy of each material. V_{D1}, V_{D2}, V_1, and

V_2 are the portion of the built-in potential and applied bias ($V_D = V_{D1} + V_{D2}$, $V = V_1 + V_2$). The depletion layer thickness d is calculated as;

$$d = \left[\frac{2\varepsilon_2 (V_{D2} - V_2)}{qN_2} \right]^{1/2} \qquad (7.2)$$

For the calculation of fermi-energy, the density of states of light- and heavy-hole is taken into account by following reduced effective mass m*;

$$m^* = \left(m_{lh}^{\frac{3}{2}} + m_{hh}^{\frac{3}{2}} \right)^{\frac{2}{3}} \qquad (7.3)$$

where m_{lh} and m_{hh} is the effective mass of light- and heavy-hole, respectively. The relation between Fermi-energy E_f and hole concentration N is calculated by the following relation,

$$N = \int_{-\infty}^{Ev} \frac{1}{2\pi^2} \left(\frac{2m^*}{\hbar^2} \right)^{\frac{3}{2}} \sqrt{Ev - E} \frac{1}{1 + \exp\left(-\frac{E - E_f}{kT} \right)} dE \qquad (7.4)$$

where Ev is the edge energy of the valence band. The values of parameters are shown in table 7.1 with the other parameter used in the following calculations.

The calculated band profiles are shown in Fig. 7.4 for various bias conditions. The wide bandgap material is InP and the narrow one is GaInAsP (λg=1.45μm). The hole concentrations of GaInAsP and InP are both 2×10^{18}cm^{-3}. The potential profile of the accumulation region in GaInAsP is schematically drown. We can see that the potential barrier height is slightly changed by reverse bias, but the barrier thickness is changed enormously.

Table 7.1 Material parameters for calculation of I-V characteristics [15].

Material	InP	GaInAsP (λg=1.3μm)	GaInAsP (λg=1.45μm)
Band-gap (eV)	1.350	0.954	0.855
Valence band offset (eV)	--------	0.238	0.297
Heavy-hole mass m_{hh} (m_0)	0.56	0.5	0.5
Light-hole mass m_{lh} (m_0)	0.120	0.072	0.068
Dielectric constant	12.4	13.3	13.6

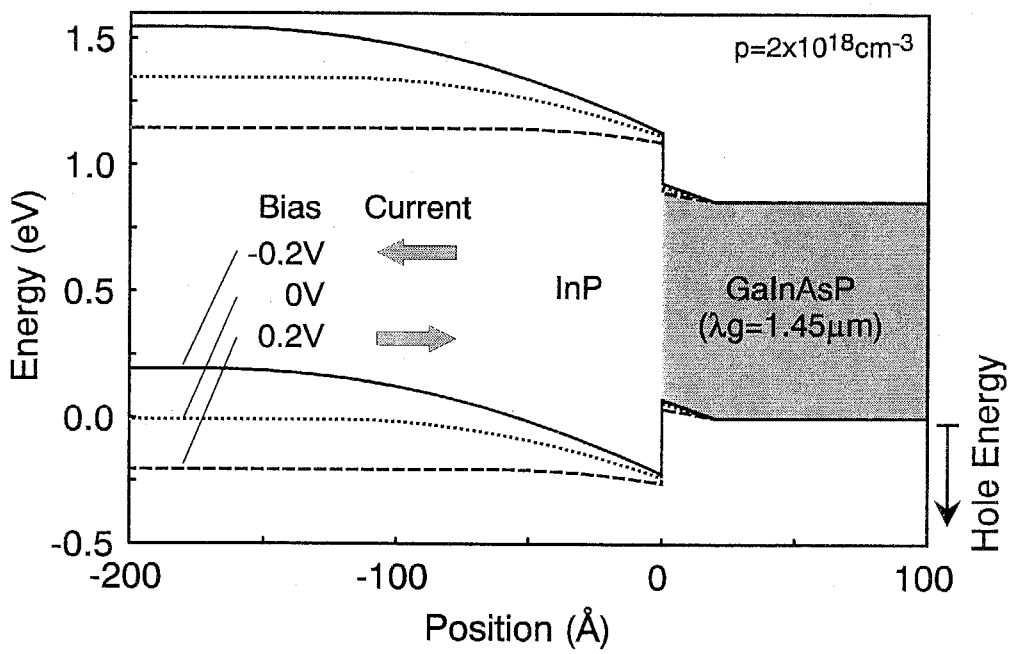

Fig. 7.4 Band profiles under bias/non-bias condition. The valence band energy of GaInAsP is fixed to 0eV.

The transmission probability is analyzed by considering the potential profile of the depletion region and the accumulation region effect is neglected. However, the tunneling transport is occur at high hole energy enormously, because the tunneling probability is large at high hole energy. So the accumulation region which is near band edge may affect very small.

The transmission probability is calculated by using the potential profile of the energy barrier by the method of the multiple potential approximation [16]. Figure 7.5 shows the transport probability of the light- and heavy-hole at GaInAsP/InP hetero-interface for 0V and -0.2V bias condition. The transmission probability of the light hole increases at smaller hole energy than that of the heavy-hole, and the energy difference is about 50meV. From the comparison of zero and -0.2V bias condition, the transmission probability shifts toward lower energy for both light and heavy hole under reverse bias condition. The amount of energy reduction for the light-hole is larger than that for the heave-hole. These phenomena are caused by the small effective mass of the light-hole.

The current-voltage characteristics are calculated using the transmission probability [16]. Assuming the hole energy E_z, which means the longitudinal energy for slanting incidence to the hetero-interface, the current density for each energy E_z is given by;

$$J(E_z) = \frac{q m_t^* kT}{2\pi^2 \hbar^3} D(E_z) \times \ln\left(\frac{f_2}{f_1}\right) \qquad (7.5)$$

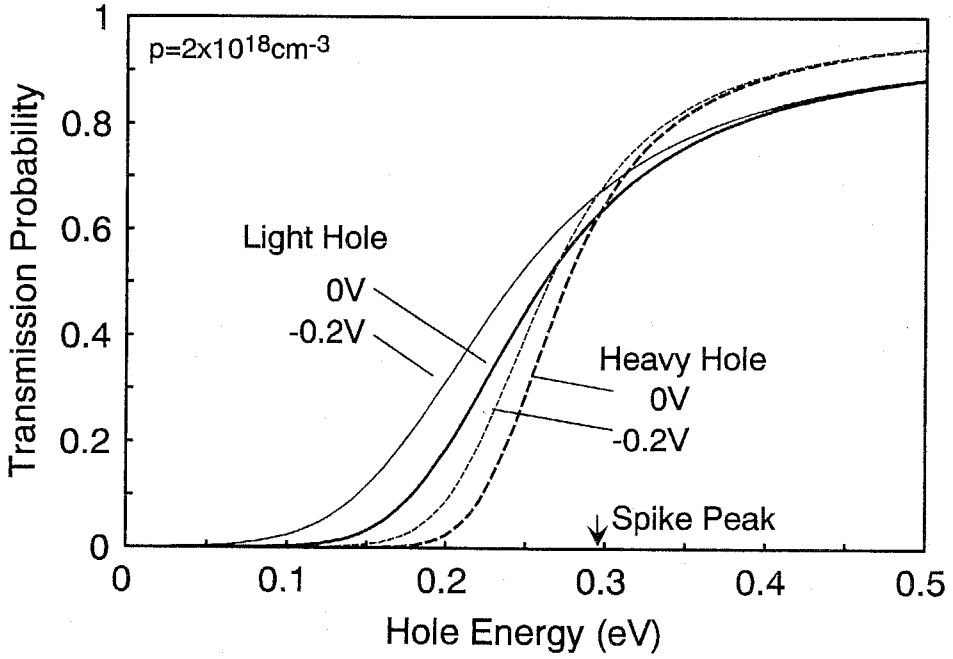

Fig. 7.5 Transmission probability at hetero interface. Light hole transmission probability is larger at near band edge than heavy hole one.

where $D(E_z)$ is the transmission probability for the energy E_z, f_1 and f_2 are Fermi-distribution functions for the wide and narrow band-gap material, respectively. The effective mass m_t* is;

$$m_t^* = \frac{m_{1hh} m_{2hh}}{m_{1hh} + m_{2hh}} \qquad (7.6)$$
$$m_t^* = \frac{m_{1lh} m_{2lh}}{m_{1lh} + m_{2lh}}$$

for the heavy- and light-hole tunneling transmission, respectively. The total current density is calculated by the integration of $J(E_z)$ for all valence band energy;

$$J = \int_{-\infty}^{Ev} J(E_z) dE_z \qquad (7.7)$$

Thus, the total current is related strongly with Fermi-Dirac distribution, transmission tunneling probability and effective mass.

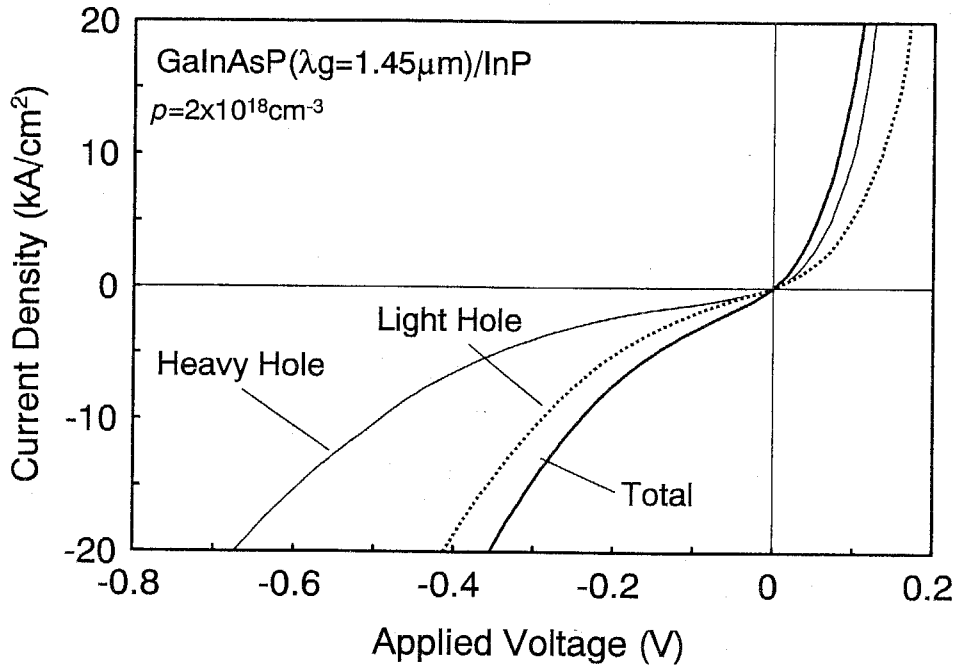

(a) p-GaInAsP (λg=1.45μm)/InP heterojunction.

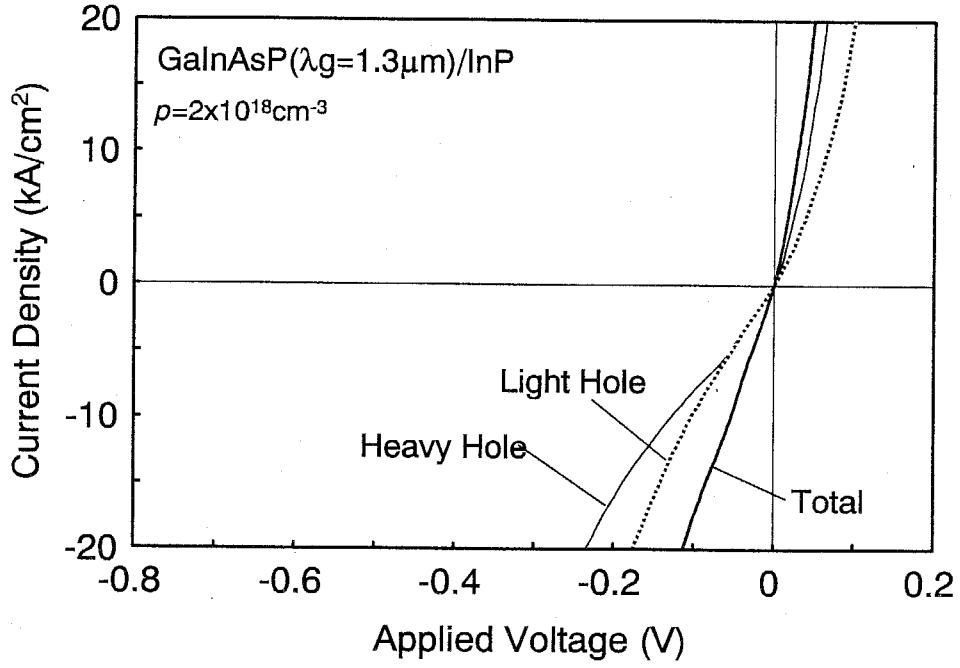

(b) p-GaInAsP (λg=1.3μm)/InP heterojunction.

Fig. 7.6 Current-voltage characteristics of p-GaInAsP/InP iso-type heterostructure. The doping concentration of each material is assumed to be $2\times10^{18}cm^{-3}$.

Figures 7.6 (a) and (b) show the theoretical current-voltage characteristics for the light- and heavy-hole transmission current and the total current means the sum of these two currents. Figure 7.6 (a) is a result for the high potential barrier height of GaInAsP (λg=1.45μm)/InP and (b) is result for the low barrier height of GaInAsP (λg=1.3μm)/InP. The hole concentrations of GaInAsP and InP are assumed to be both $2\times10^{18}cm^{-3}$. We can see the large rectification in total current of GaInAsP (λg=1.45μm)/InP case and little rectification in that of GaInAsP (λg=1.3μm)/InP case. Though the Fermi-energy and the carrier distributions are almost the same for two cases, the tunneling probability of GaInAsP (λg=1.3μm) case is larger at small hole energy than that of GaInAsP (λg=1.45μm) case. Then the contrast is owing to the difference of the potential barrier height. From the result, utilization of the small barrier height is effective to reduce the excess bias.

It is noted that the light-hole current is larger than the heavy-hole current for both GaInAsP cases under the reverse bias condition. The density of states for heavy-hole is larger than that of light-hole, so the number of the carriers in each hole energy is large for the heavy-hole. However, the tunneling transmission probability is large for the light-holes (shown in Fig. 7.5), so the tunneling transmission current for the light-hole is larger than that of the heavy-hole. From the result, the light-hole current is dominant in the total current for the reverse bias condition, especially in the case of GaInAsP (λg=1.45μm)/InP hetero-structure. The light-hole current of reverse bias condition may be dominant generally for the large

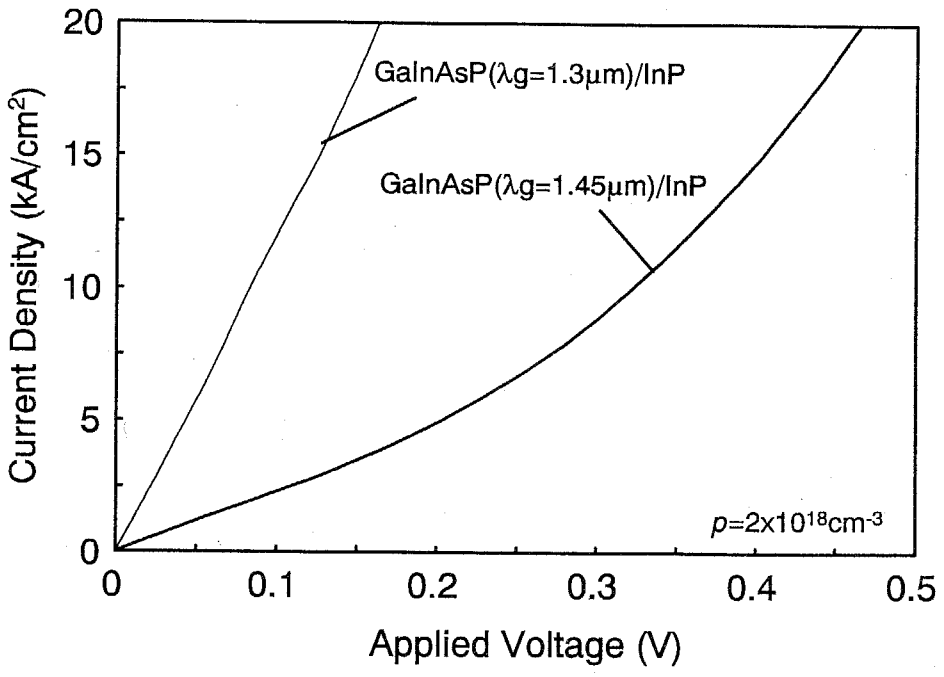

Fig. 7.7 Current-voltage characteristics for one pair DBR which consists of one forward bias and one reverse bias junction.

potential barrier case. On the other hand, the dominant current for forward bias condition is the heavy-hole current because the applied bias reduces the hetero-barrier height and the thermionic emission current which means the current flow over the potential barrier increase.

The current-voltage characteristics of multiple-pair p-DBR are calculated by considering the stacks of the same number of forward- and reverse-bias heterojunctions. The calculated current-voltage characteristic for the set of one forward- and one reverse-bias heterojunction, which means one-pair DBR, is shown in Fig. 7.7 corresponding to the Fig. 7.6 (a) and (b). If we assume the current density of 5kA/cm^2, the excess bias in one pair is required about 0.05V and 0.2V for the case of GaInAsP (λg=1.3μm) and GaInAsP (λg=1.45μm), respectively. The total excess bias of multiple-pair DBR is calculated from the sum of number of heterojunction pairs. Such excess bias is one of the thermal sources, and it should be reduced.

Next, the hole concentration dependence is considered. The Fermi-energy is related with the current density greatly. Figure 7.8 shows the current-voltage characteristics of various doping designs for one-pair GaInAsP (λg=1.45μm)/InP DBR. From the figure, two lines which are the same hole concentration of 2×10^{18}cm^{-3} in InP show nearly same current-voltage characteristics, though the hole concentrations in GaInAsP are different. The lines of the hole concentration of 1×10^{18}cm^{-3} in InP show larger excess bias than the other lines. This results show that the high doping in wide band-gap material is effective to reducing the excess bias and the high doping in the narrow band-gap material is not so necessary. It is important point

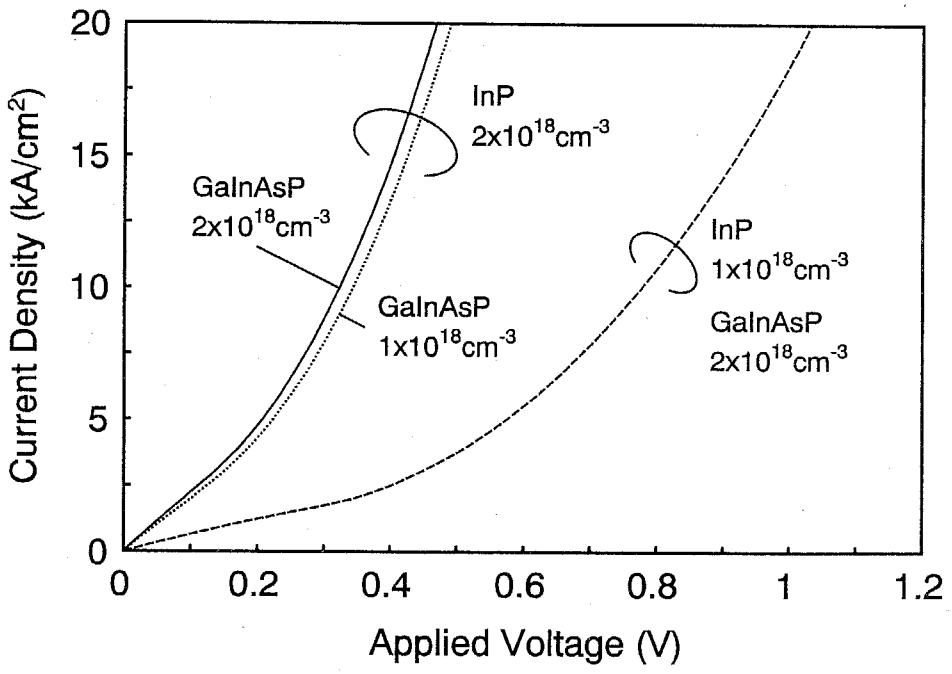

Fig. 7.8 Current-voltage characteristic of one pair GaInAsP(λg=1.45μm)/InP DBR for various hole concentration configurations.

to realize the low excess bias and low absorption mirror because the narrow bandgap material has large absorption cross section as described in chapter 2.

As a summary of this section, I characterized the electrical characteristics of p-DBR structures for the long-wavelength surface emitting lasers. The CBE grown p-DBR structure indicates 0.1V excess bias for one DBR pair. This excess bias is smaller than the estimated value theoretically. However, the difference between experimental and theoretical results is enough small considering the difficulty of measurement of the actual band discontinuity and fermi levels, because the tunneling probability is very sensitive to these parameters. The current-voltage characteristic of a p-type GaInAsP/InP heterojunction is calculated by considering the light- and heavy-hole transmission tunneling current. The light-hole current is dominant for the reverse-bias heterojunction. The absorption of p-DBR for the long-wavelength material is much influenced by hole concentration, so the highly acceptor doping only in InP is effective for low excess bias and high reflectivity mirror. These results may be helpful for the design of the high performance p-DBR and also high performance GaInAsP/InP surface emitting lasers.

The calculation program is shown in Appendix E.

7.2 Lateral Current Uniformity of Ring Electrode Structures

7.2.1 Examination of Current Injection for Surface Emitting Lasers

As mentioned in previous chapters, I selected the dielectric multilayer mirror because of the potentiality of extremely low absorption loss. As the dielectric mirror is not electrical conductive material, the electrode arraignment is designed as the ring structure for epitaxial side. As the result of ring electrode structure, the current flow is not uniform at the active region which means the region just below the mirror.

To examine the lateral current injection, a near field pattern (NFP) of surface emitting laser structure is observed as shown in Fig. 7.9. The device structure is the same as mushroom structure shown in chapter 6, but the mirror is not deposited. The device has 15μm diameter mirror window. The intensity profile of the center line is shown below the NFP. The intensity profile is measured for various injection current density. The intensity profile is shown in Fig. 7.10. The intensity at low injected current density is considered to be enough uniform. As increasing the current density, the nonuniformity is increase.

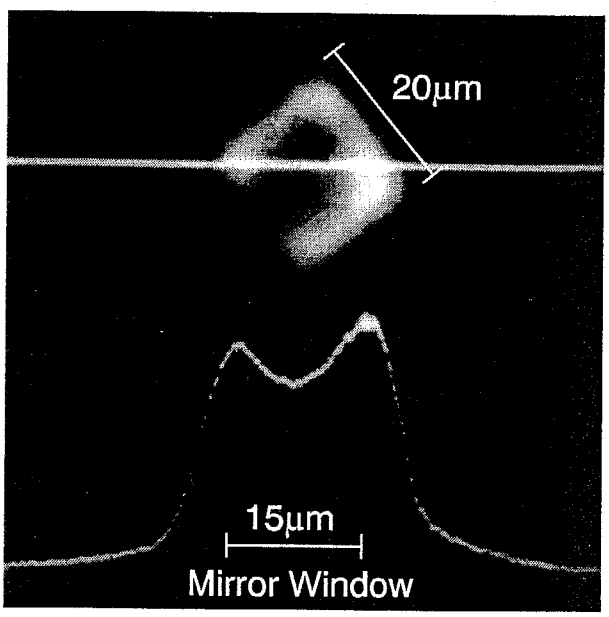

Fig. 7.9 Photograph of NFP for surface emitting LED.

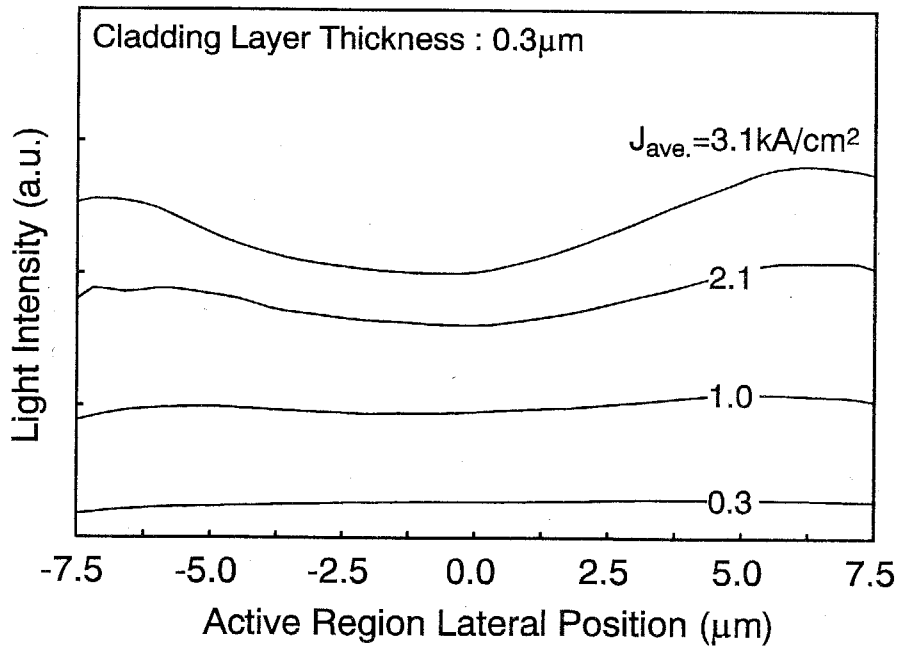

Fig. 7.10 Intensity profile for various injection current density.

7.2.2 Modeling and Computerize of Current Flow

To consider the current uniformity, the current flow is calculated by the finite element method (FEM). The schematic model structure and the schematic arrangement of FEM

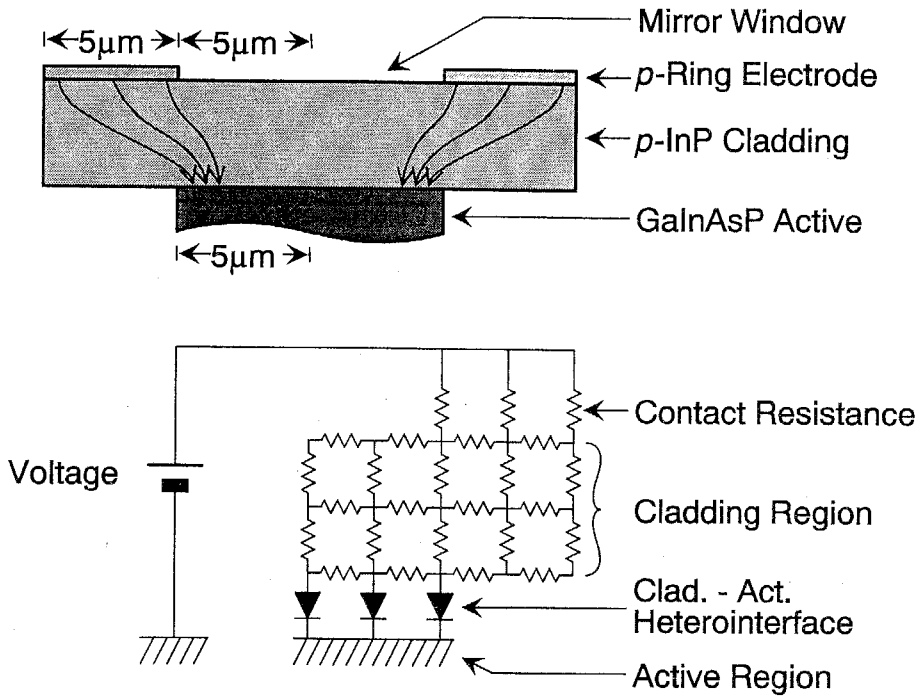

Fig. 7.11 Schematic device model and element arrangement for analysis.

elements are shown in Fig. 7.11. The ring electrode has inner and outer radius of 5μm and 10 μm and the mirror window is opened at the center of the mesa with 10μm diameter. The cladding layer of InP is 20μm diameter and the active layer is 5μm radius. In this calculation, the active layer is assumed to be the same voltage. As the structure is assumed to be cylindrical three dimensional structure, the calculation is carried out by two dimension.

Figure 7.12 shows one element cut out from the cladding region. The resistance network is formed with two kinds of resistance. One is parallel to the surface and another is perpendicular to the surface.

The resistance perpendicular to the surface $R^{\perp}$ is represented as;

$$R_m^{\perp} = \frac{\Delta h}{S_m} \cdot \frac{1}{\sigma} \qquad (7.8)$$

where m is the number of element against radius direction. Δh is height of element. σ is conductivity of material. S_m is area of the element and represented as;

$$S_m = \left(\left(r + \frac{\Delta r}{2} \right)^2 - \left(r - \frac{\Delta r}{2} \right)^2 \right) \pi \cdot \frac{d\theta}{2\pi} = m \Delta r^2 \cdot d\theta \qquad (7.9).$$

The element for θ direction is the same condition and hence the resistance is shown as;

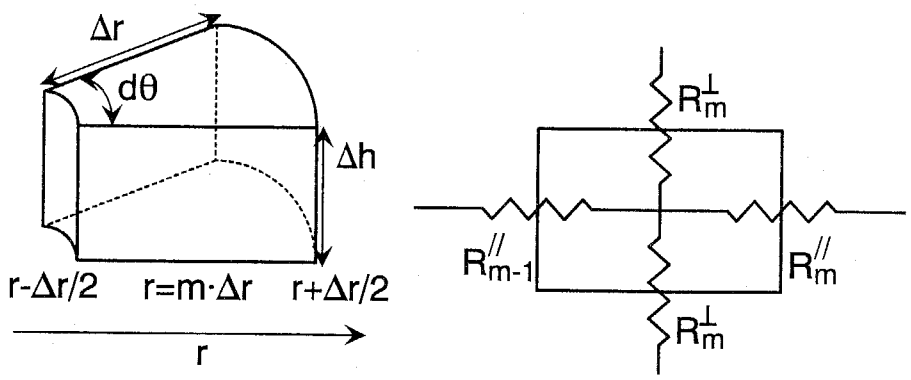

Fig. 7.12 Schematic view of element structure and names of resistance.

$$R_m^{\perp} = \frac{\Delta h}{2m\pi\Delta r^2 \cdot \sigma} \qquad (7.10).$$

On the other hand, the resistance parallel to the surface $R^{//}$ is;

$$R_m^{//} = \frac{dr}{S_m^{//}} \cdot \frac{1}{\sigma} \qquad (7.11).$$

$S^{//}$ is represented as;

$$S_m^{//} = 2\pi r \cdot \frac{d\theta}{2\pi} \cdot \Delta h \qquad (7.12).$$

Integration for r direction from r-Δr to r+Δr and θ direction from 0 to 2π, the resistance is shown as;

$$R_m^{//} = \ln\left(\frac{m+\frac{1}{2}}{m-\frac{1}{2}}\right) \cdot \frac{1}{2\pi \cdot dh \cdot \sigma} \qquad (7.13).$$

As a result, the resistance of each element is changed from the material conductivity.

The contact resistance at the interface between cladding layer and electrode is assumed to be $1\times10^{-5}\Omega cm^2$. Furthermore, the non-linearity of heterointerface between active layer and cladding layer is considered using current-voltage characteristic of the tunneling current as described in previous section.

By placing the each resistance and non-linear element, two dimensional resistance network is formed and the calculation is carried out by applying the voltage (Appendix F). Figure 7.13 shows the current density against active layer radius position. The cladding layer

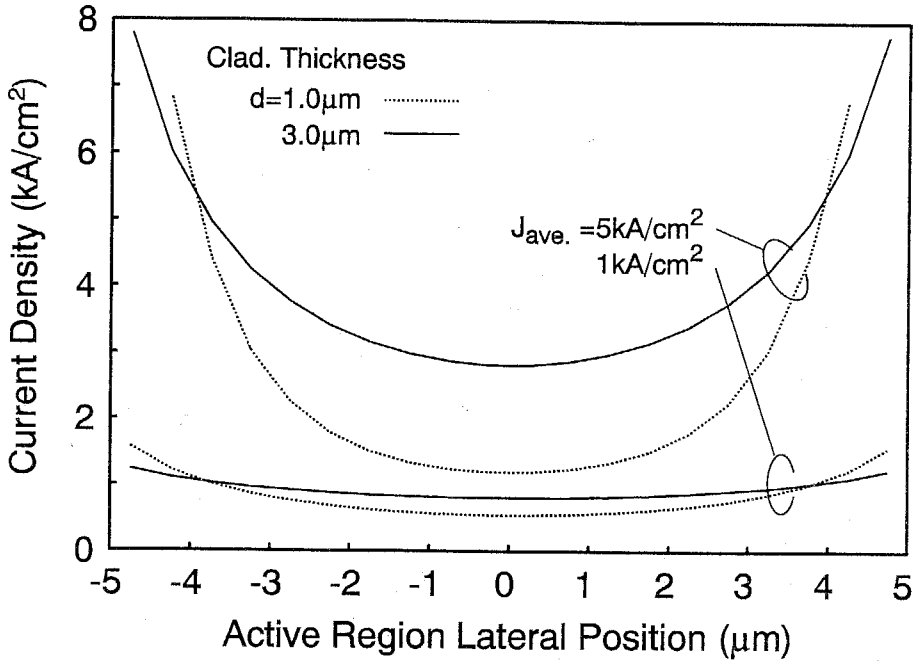

Fig. 7.13 Lateral current uniformity for different cladding thickness at high and low injection current.

is assumed to be 1μm or 3μm. The injected current is assumed to be 1kA/cm^2 and 5kA/cm^2. The injected current means the averaged current density for the active layer area. The uniformity at low injected current is good for both cladding thickness structures. However, non-uniformity is appeared at high injected current condition. Especially, the thin cladding layer structure shows worse non-uniformity. If the non-linearity element is not considered, the current flow pattern is not changed by the applied voltage. Hence, the increase of non-uniformity is due to non-linearity of current-voltage characteristics at hetero-interface between cladding layer and active layer. In this calculation, I neglected the active layer and n-cladding layer. The non-linearity of current-voltage characteristics in p-n junction may be more effective, and therefore the non-uniformity may be large if the p-n junction is considered.

From the figure, increase of p-cladding layer thickness and lowering threshold current are effective for reducing non-uniformity. However, the current non-uniformity is increased for high current to obtain high output power even if the threshold is reduced. Also, the thick cladding layer structure is not good to reduce the absorption in cladding layer.

As the bulk material has homogeneous resistance, the resistance change by doping concentration is not effective for uniform current injection because the current flow pattern is fixed for homogeneous materials though the total resistance is changed. To realize current spreading, it is required to insert unhomogeneous material. If the material has lower resistance for the parallel to the surface than perpendicular to the surface, the carriers spread in the layer.

In this study, I make proposal of the insertion of the narrow bandgap material (GaInAsP) in the cladding layer as the current spreading layer. The spreading layer is also homogeneous material but the interfaces between spreading layer and cladding layer have non-linear I-V characteristics. Figure 7.14 shows the schematic view of surface emitting laser structure with a current spreading layer. The difference from the conventional structure is only the GaInAsP layer. The calculated result for the spreading layer structure is shown in Fig. 7.15 with the result of conventional structure. The current-voltage characteristics at the interfaces are the same as the result for previous section. The current spreading layer is effectively performed. If the spreading layers are utilized as the semiconductor mirror such as hybrid mirror, it may be more effective.

As the other method to avoid the non-uniformity, small active region structure is effective as shown in Fig. 7.16. The current density at the center of active region with 6μm diameter structure is increased comparable with 10μm diameter structure. The limitation of minimum active region area is determined by the diffraction loss. The diffraction loss of 6μm diameter structure may be not serious. As the diffraction loss is related with the cavity length, more consideration is needed for accurate analysis.

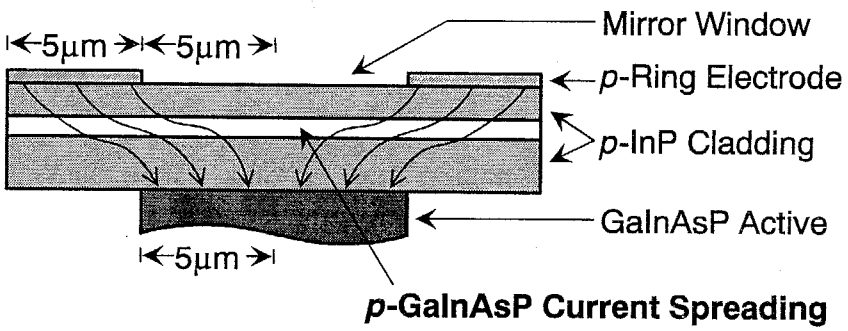

Fig. 7.14 Schematic view of current spreading layer structure.

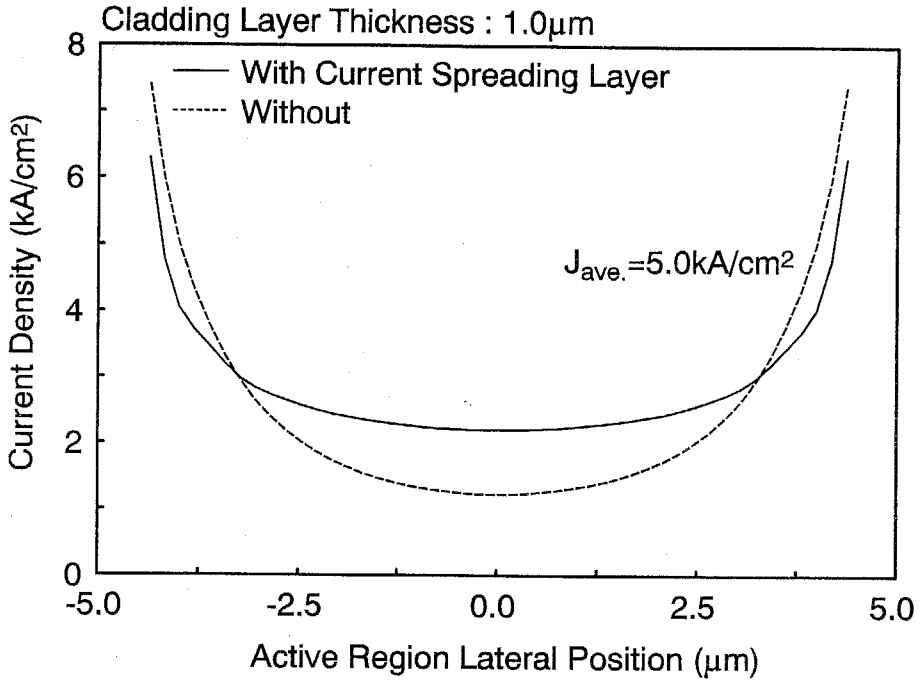

Fig. 7.15 Lateral current uniformity for current spreading layer structure. The dashed line shows for structure without current spreading layer.

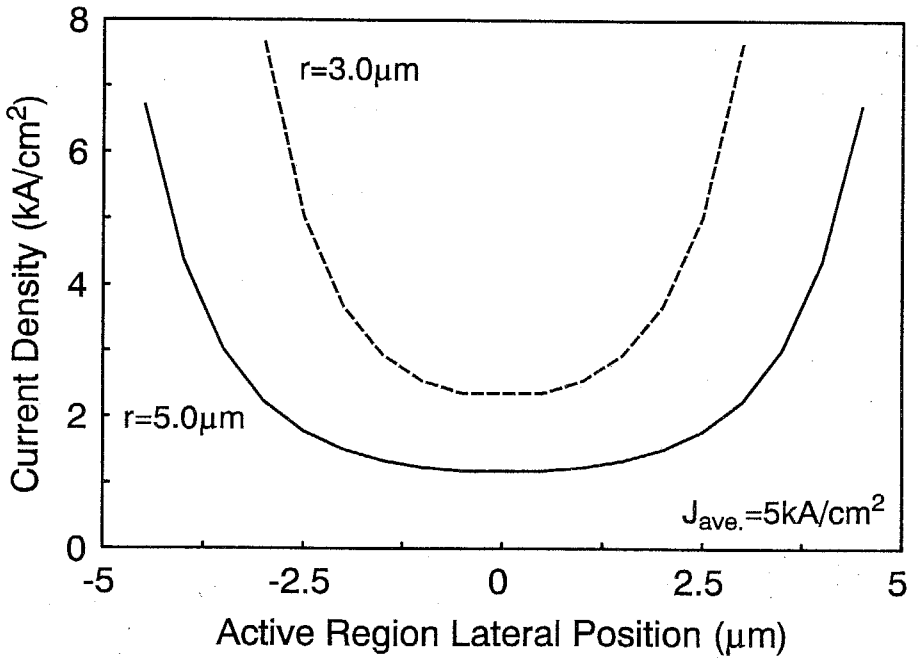

Fig. 7.16 Lateral current uniformity for different active radius at high and low injection current.

7.3 Future Development of High Performance Surface Emitting Lasers

In the previous chapter, some lasing characteristics of long wavelength surface emitting lasers were described and some problems were cleared as discussed above. The obtained lasing characteristics were pulsed operation at near room temperature, CW operation with 0.3mA threshold current at 77K and CW operation up to -84°C. These results are extremely improved compared with results reported formerly of this study. On the other hand, other research on long wavelength surface emitting lasers achieved room temperature operation under not only pulsed operation but also CW operation. The highest performance is considered to be 33°C CW operation, 2.3mA threshold current under CW room temperature (23°C) condition and 1.8mA threshold under room temperature pulsed operation by Babic et al. of UCSB in 1995 [17]. The maximum operating temperature is 150°C under photopumped condition by Lin et al. of Cornell University, in 1994 [18]. Thus the operating temperature of injection devices is not sufficient for practical use in this time, but the potentiality is considered to be indicated by photopumped condition. The threshold current of few mA is sufficiently low compared with commercial edge emitting devices. Thus the long wavelength surface emitting laser has capability of real use though there are still some problems to realize high performance operation.

I consider some problems about long wavelength surface emitting lasers consisting problems considered in above section.

1. Intervalence band absorption
2. Auger nonradiative recombination
3. Lateral current uniformity
4. Uniform carrier injection to each well
5. Carrier leakage from well
6. Carrier leakage to cladding layer
7. Thermal problem

Intervalence band absorption (IVBA) in cladding layer or capping layer is reduced by lowering doping concentration as described in chapter 2. The doping concentration in cladding layer is related with electrical resistance and carrier injection problem of problem #3 and #6. The IVBA and Auger recombination in active layer are expected to be decreased by strained QWs. In fact, reduction efficiency of IVBA and Auger recombination ratio is not completely cleared. Furthermore, the optimum structure such as strain and well thickness is complicated problem because the optimum condition may be changed by modal gain.

Lateral current uniformity is considered in previous section. The current spreading layer

and small active region may be effective to reduce the nonuniformity. The design of optimum structure is important to realize high performance. In short, the current-voltage characteristic at each heterointerface, carrier diffusion in active layer and lateral (transverse) optical field should be considered.

For multi-quantum well structure, the uniform carrier injection is one of problems. The carrier transport is performed by thermionic emission and tunneling transport across the barrier. GaInAsP/InP system has large valence band offset and small conduction band offset. As the density of states in valence band is large, low barrier height is required for uniform carrier injection because the Fermi-energy is near the band edge. However, utilization of narrow bandgap barrier material is not good for conduction band because the coupling and leakage to barrier may be increase due to low barrier height for electron. To solve the problem, there are two approaches. One is using of strained materials. The composition change and strain deformation of band structure are expected about strain material. Another method is utilization of the other material. AlGaInAs/InP is considered to be one of superior material for long wavelength region. This material has the advantage of using only one group V material of arsenic (As). This material has large conduction band offset and small valence band offset. Recently, another advantage was proposed for this material by N. Ohnoki of Tokyo Institute of Technology in 1995 [19]. The strained AlAs ultra-thin layer in the cladding layer has capability of oxidation as well as AlAs/GaAs system. Using this technique, the current confinement structure may be achieved. Another interesting material of GaInNAs/GaAs was proposed in recent time [20]. The advantage of this material is large (small) conduction (valence) band offset and possibility of using GaAs substrate. This material has been just started to develop by Kondow et al. and the potential is unknown up to this time.

The electron leakage to cladding layer may also become one of problem. The reason is follows. The potential spike between active layer and p-cladding layer is large for GaInAsP/InP system due to large valence band offset. Holes, which are injected from p-cladding layer, feel the spike, and hence excess bias is required as well as the phenomena described in previous section. This excess bias reduces the potential barrier height for electron in the active layer [21]. This problem is expected to be solved by introducing a thin layer (BDR : band discontinuity reduction layer [22]) which has intermediate bandgap energy between active layer and cladding layer or by high delta doping at the interface. Furthermore, multi-quantum barrier (MQB) structure is considered to be effective to suppress the electron leakage [23, 24].

A thermal problem is important to realize high performance lasers. The excess temperature rising due to CW operation with small thermal conductivity causes limitation of maximum operating temperature. Of course, threshold current (density) reduction is effective to lowering power consumption. However, the other optimization is required to realize good

temperature characteristics. One is reduction of electrical resistance at ohmic contact, heterojunction and structural dependence resistance such as very thin layer of ring electrode structure and low doping concentration. Another is reduction of thermal resistance. The first room temperature operation in long wavelength surface emitting laser has magnesium oxide (MgO)/Si multilayer reflector. This material system has superior thermal conductivity compared with Si/SiO_2 multi layer and GaInAsP/InP multilayer. In addition, the introduction of buried heterostructure with InP is also effective to obtain the thermal dissipation from active region. Combining these techniques with optimized heat sink structure, the lasing threshold and its temperature characteristics are expected to be improved.

A high performance long wavelength surface emitting laser will be realized in near future by further improvement of device structure and growth/fabrication techniques.

References

[1] A. Chailertvanitkul, K. Iga, and K. Moriki, "GaInAsP/InP surface emitting laser (λ=1.4 μm, 77K) with heteromultilayer Bragg reflector," *Electron. Lett.*, vol. 21, pp. 303-304, 1985.

[2] Y. Imajo, A. Kasukawa, S. Kashiwa, and H. Okamoto, "GaInAsP/InP semiconductor multilayer reflector grown by metalorganic chemical vapor deposition and its application to surface emitting laser diode," *Jpn. J. Appl. Phys.*, vol. 29, pp. L1130-L1132, 1990.

[3] T. Tadokoro, H. Okamoto, Y. Kohama, T. Kawakami, and T. Kurokawa, "Room temperature pulsed operation of 1.5μm GaInAsP/InP vertical-cavity surface-emitting laser," *IEEE Photon. Technol. Lett.*, vol. 4, pp. 409-411, 1992.

[4] M. A. Fisher, Y.-Z. Huang, A. J. Dann, D. J. Elton, M. J. Hralow, S. D. Perrin, J. Reed, I. Reid, and M. J. Adams, "Pulsed electrical operation of 1.5-μm vertical-cavity surface-emitting lasers," IEEE Photon. Technol. Lett., vol. 7, pp. 608-610, 1995.

[5] D. I. Babic, J. J. Dudley, K. Streubel, R. P. Mirin, J. E. Bowers, and E. L. Hu, "Double-fused 1.52-μm vertical-cavity lasers," *Appl. Phys. Lett.*, vol. 66, pp. 1030-1032, 1995.

[6] K. Tai, L. Yang, Y. H. Wang, J. D. Wynn, and A. Y. Cho, "Drastic reduction of series resistance in doped semiconductor distributed Bragg reflectors for surface-emitting lasers," *Appl. Phys. Lett.*, vol. 56, pp. 2496-2498, 1990.

[7] K. L. Lear, S. A. Chalmers, and K. P. Killen, "Low threshold voltage vertical cavity surface-emitting laser," *Electron. Lett.*, 29, pp. 584-586, 1993.

[8] M. Sugimoto, H. Kosaka, K. Kurihara, I. Ogura, T. Numai, and K. Kasahara, "Very low threshold current density in vertical-cavity surface-emitting laser diodes with periodically doped distributed Bragg reflectors," *Electron. Lett.*, vol. 28, pp. 385-387, 1992.

[9] G. Reiner, E. Zeeb, B. Möller, M. Ries, and K. J. Ebeling, "Optimization of planar Be-doped InGaAs VCSEL's with two-sided output," *IEEE Photon. Technol. Lett.*, vol. 7, pp. 730-732, 1995.

[10] G. W. Yoffe, "Rectification in heavily doped p-type GaAs/AlAs heterojunctions," *J. Appl. Phys.*, vol. 70, pp. 1081-1083, 1991.

[11] E. F. Schubert, L. W. Tu, G. J. Zydzik, R. F. Kopf, A. Benvenuti, and M. R. Pinto, "Elimination of heterojunction band discontinuities by modulation doping," *Appl. Phys. Lett.*, vol. 60, pp. 466-468, 1992.

[12] E. Zeeb and K. J. Ebeling, "Potential barriers and current-voltage characteristics of p-doped graded AlAs-GaAs heterojunctions," *J. Appl. Phys.*, vol. 72, pp. 993-999, 1992.

[13] R. F. Nabiev, C. J. Chang-Hasnain, "Voltage drop in n- and p-type Bragg reflectors for vertical-cavity surface-emitting lasers," *IEEE Photon. Technol. Lett.*, vol. 7, pp. 733-735, 1995.

[14] R. L. Anderson, "Experiments on Ge-GaAs heterojunctions," *Solid-State Electron.*, vol. 5, pp. 341-351, 1962.

[15] for a review, T. P. Pearsall ed., GaInAsP alloy semiconductor, John Wiley & Sons Ltd., 1982.

[16] Y. Ando and T. Itoh, "Calculation of transmission tunneling current across arbitrary potential barriers," *J. Appl. Phys.*, vol. 61, pp. 1497-1502, 1987.

[17] D. I. Babic, K. Streubel, R. P. Mirin, N. M. Margalit, J. E. Bowers, E. L. Hu, D. E. Mars, L. Yang, and K. Carey, "Room-temperature continuous-wave operation of 1.54-μm vertical cavity lasers," *IEEE Photon. Technol. Lett.*, vol. 7, pp. 1225-1227, 1995.

[18] C. H. Lin, C. L. Chua, Z. H. Zhu, F. E. Ejeckam, T. C. Wu, and Y. H. Lo, "Photopumped long wavelength vertical-cavity surface emitting lasers using strain-compensated multiple quantum wells," *Appl. Phys. Lett.*, vol. 64, pp. 3395-3397, 1994.

[19] private discussion in laboratory. The result of oxidation may be presented in near future.

[20] M. Kondow, A. Niwa, and K. Uomi, "A proposal of laser-diodes for optical fiber communications using a novel material of GaInNAs," *The 42nd Spring Meeting, 1995, The Japan Society of Applied Physics and Related Societies*, paper 29a-ZG-5, 1995.
K. Kondow and K. Uomi, " A proposition for laser-diodes fabricated on Si Wafers using novel materials of GaNAs and GaNP," paper 30p-ZH-14, 1995.

[21] R. F. Kazarinov and M. R. Pinto, "Carrier transport in laser heterostructures," *IEEE J. Quantum Electron.*, vol. 30, pp. 49-53, 1994.

[22] A. Takemoto, K. Matsumoto, H. Nishiguchi, T. Takiguchi, Y. Nakajima, E. Omura, and M. Aiga, "Improvement of high power/high temperature operation of long wavelength laser diodes by band discontinuity reduction layer," *13th IEEE International Semiconductor Laser Conf.*, Takamatsu, Japan, paper D-7, 1992.

[23] K. Iga, H. Uenohara, and F. Koyama, "Electron reflectance of multiquantum barrier (MQB)," *Electron. Lett.*, vol. 22, pp. 1008-1010, 1986.

[24] T. Takagi, F. Koyama, and K. Iga, "Photoluminescence study of electron wave confinement in multi-quantum barrier (MQB)," *Jpn. J. Appl. Phys.*, vol. 29, pp. L1969-L1972, 1990.

Chapter 8

Conclusion

I have performed this study to realize 1.55μm GaInAsP/InP surface emitting lasers. The purpose of this work is, 1) design and optimization of 1.55 μm GaInAsP/InP surface emitting laser structure, 2) establishment of chemical beam epitaxial technique for applying to surface emitting lasers and 3) realization of 1.55μm surface emitting lasers and investigation of laser characteristics. The results obtained in this study are summarized as follows.

1. Design and optimization of GaInAsP/InP surface emitting laser structures

i) I designed GaInAsP/InP surface emitting laser structures. The threshold current density of less than 10kA/cm^2 was possible for bulk active layer structure. Further improvement is expected by compressively strained quantum wells. The estimated threshold current density for separate gain structure was less than 2kA/cm^2 with 99.5% reflectivity. Though these threshold currents are slightly high compared with conventional edge emitting lasers, the room temperature operation is expected.

ii) I suggested that the optical absorption reduction in cladding layer is effective to reduce the threshold current. By reducing the p-cladding layer doping concentration and its layer thickness, the estimated threshold current is reduced to about half of previous values and the performance may become equal or superior compared with the conventional laser.

iii) I made proposal of a hybrid mirror structure which contains semiconductor and dielectric multilayer reflectors. The effective reflectivity of hybrid mirror was increased about 0.2% comparable with conventional dielectric mirror structure at the reflectivity of over 99% range. This result indicates that the hybrid mirror may effectively reduce the threshold current.

2. Establishment of CBE techniques for surface emitting laser

i) The chemical beam epitaxial (CBE) technique was established for growth of surface emitting laser wafers. The growth of semiconductor multilayer reflector indicated good controllability of thickness and composition with good surface morphology. Furthermore, the lasing characteristic of edge emitting lasers with bulk active layer was as well as LPE grown devices. Thus the applicability of CBE for surface emitting lasers were implied.

ii) To apply quantum well (QW) structures to surface emitting lasers, I also investigated the QW structure grown by CBE. I suggested that GaInAsP/GaInAsP strain-compensated QWs had optimum compensation condition. Under this condition, the QW edge emitting laser showed 450A/cm^2 threshold current density. This result makes possibility of very low threshold current QW surface emitting lasers.

3. Realization of low threshold surface emitting lasers in long wavelength region

i) A GaInAsP/InP surface emitting laser grown by CBE was realized for the first time. Furthermore, the low threshold and higher temperature operation were accomplished by low absorption loss structure. By introducing n-type hybrid mirror, the operation temperature was improved up to 11°C under pulse condition, and -84°C CW operation was achieved. A mushroom structure showed 0.3mA threshold current at 77K which is the lowest value for GaInAsP/InP surface emitting lasers. Though the lasing operation of a QW surface emitting laser has not achieved yet, the low threshold device is expected by establishing the fabrication process.

ii) I suggested the importance of matching of gain-oscillation wavelengths. The optimized design about the gain peak wavelength and oscillation wavelength may bring the low threshold current and superior temperature characteristics.

iii) I considered a new carrier transport model of p-type DBRs which include both light- and heavy hole tunneling current. The light hole tunneling current is considered to be dominant for reverse biased condition. This analysis of current flow model may be helpful for the design of p-type DBR and bring high performance surface emitting lasers.

iv) I examined about lateral current uniformity of the ring electrode structure. The result indicated deterioration of lasing characteristics at high injection current conditions such as high output power, high temperature operation, etc. The current spreading layer and small active region is expected to reduce the non-uniformity current injection.

I have designed and demonstrated the world level low threshold GaInAsP/InP surface emitting lasers grown by CBE. The laser characteristics at present are still far from practical use. However, I believe that the results obtained in this study will become the basis of further improvement of long wavelength surface emitting laser characteristics and promise the progress of new generation optical communications and interconnections.

Appendix

The appendix A-F show the computer programs for calculations in this study. The followings are the computer hardware and software used for all calculations.

Hardware : IBM-compatible (Dell Computer Corp., TEL 03-5466-4419)
CPU : Intel Pentium (120MHz)
RAM : 32Mbyte
Software : OS : Microsoft Windows 95
Mathcad 5.0 PLUS (MathSoft Inc., TEL 03-5476-9802)

A. Reflection of Multilayer Reflector (Program A)

The theoretical treatment of reflection of multilayer reflector (DBR : distributed Bragg reflector) is described in detail in Ref. 1-3. Here, the method is summarized simply. The propagation of plane wave is considered in a homogeneous medium. Using the Maxwell's equation, the electrical and magnetic fields at the each interface are considered for the forward and backward propagation wave. From the field continuity at boundary between the medium (i-1) and (i), the next conditions are obtained;

$$E_{i-1}^{+R} + E_{i-1}^{-R} = E_i^{+L} + E_i^{-L} \qquad \text{(A.1)}$$

$$\frac{n_{i-1}}{c \cdot \mu_0} E_{i-1}^{+R} - \frac{n_{i-1}}{c \cdot \mu_0} E_{i-1}^{-R} = \frac{n_i}{c \cdot \mu_0} E_i^{+L} - \frac{n_i}{c \cdot \mu_0} E_i^{-L} \qquad \text{(A.2)}$$

where E is electric field and n is refractive index. c and μ_0 is the light velocity in a vacuum space and permeability, respectively. Considering each boundary condition, the relation between electric field of first (i=0) and last (i=N+1) medium is calculated by multiplication of coefficient matrix for electric field in Eq. (A.1) and (A.2). As the result, the relation is represented as;

$$\begin{bmatrix} E_0^{+R} \\ E_0^{-R} \end{bmatrix} = \begin{bmatrix} S_{11} & S_{12} \\ S_{21} & S_{22} \end{bmatrix} \begin{bmatrix} E_{N+1}^{+L} \\ E_{N+1}^{-L} \end{bmatrix} \qquad \text{(A.3).}$$

From the Eq. (A.3), the power reflectivity R is calculated as;

$$R = \left|\frac{E_0^{-R}}{E_0^{+R}}\right|^2 = \left|\frac{S_{21}}{S_{11}}\right|^2 \qquad \text{(A.4)}$$

where the incident light is E_0^{+R}. In the equations, the refractive index n is possible to exchange the complex index $n^*(=n-j\cdot k)$. k is extinction coefficient and related with absorption coefficient α as $k=\alpha\cdot\lambda/4\pi$.

The program is possible to calculate any hybrid mirror structure. In this program, reflectivity spectrum and reflectivity as a function of number of pair are calculated. Reflective index of dielectric materials is shown in Ref. 4 and refractive index of GaInAsP is shown in Ref. 5.

B. X-ray Diffraction Pattern from GaInAsP/GaInAsP Superlattice (Program B)

A program to calculate X-ray diffraction pattern from superlattice [6] is presented. The superlattice structure is assumed to be GaInAsP/GaInAsP and the thickness has monolayer unit. Elastic constants are shown in Ref. 7.

C. Emission Wavelength of GaInAs/InP Quantum Well (Program C)

Quantized energy is estimated from finite energy potential well using effective mass approximation. The potential profile is assumed to be rectangle. Quantized energies E_i satisfy the next relation.

$$\frac{m_w}{m_b}\cdot\frac{K_b}{K_w} = \tan\left(K_w\cdot L - \frac{n\pi}{2}\right) \quad (n\geq 0) \qquad \text{(A.5)}$$

where wave number K_w and K_b satisfy $K_w=\sqrt{2m_wE}/\hbar$, $K_b=\sqrt{2m_b(V-E)}/\hbar$. m_w and m_b is the effective mass in the well and barrier, respectively. L_w is the well width and V is potential barrier height. Integer (n+1) means quantum number. The emission energy is calculated by the sum of bandgap energy of well and the lowest quantized energy in the conduction and valence band as $E=E_g^{well}+Ec_1+Ev_1$. The program shows the emission wavelength and quantized energy of conduction and valence band.

D. Optical Confinement Factor of Multilayer Slab Waveguide (Program D)

The fundamental of theory is like as multilayer reflector. The program is made for calculating the TE mode. The optical field, confinement factor and propagation coefficient are calculated for the given index, thickness and active layer position.

E. Hole Tunneling Transmission Current at Heterointerface (Program E)

The hole tunneling transmission current is calculated in the program. The theory is described in chapter 7. The calculation procedure is follows. First, Fermi energy in both narrow and wide gap materials is calculated. Then, the built in potentials and depletion width are computed to obtain the potential profile by using Anderson model [8]. Using multistep potential approximation [9], the transmission probabilities for each energy are calculated. Finally, integration for each hole energy is carried out for multiplication of density of states, transmission probability and Fermi-Dirac distribution. In the program, the current value is calculated for one bias voltage, and hence current-voltage characteristics are drawn by giving various voltage.

F. Current Flow of Ring Electrode Structure (Program F)

To calculated current spreading characteristics by small computer system, the element number of FEM is only about few hundred. However, it is enough to estimate current-voltage characteristics. In this program, the analysis is carried out for regular condition. The nonlinearity at the heterointerface is calculated by appendix E and the calculation is carried out until convergence of current and voltage condition.

Reference

[1] M. Born and E. Wolf, *Principle of Optics*, Pergamon, New York, 1965.

[2] Z. Knittl, *Optics of thin films*, John Wiley & Sons Ltd., New York, 1976.

[3] T. Sakagchi, F. Koyama, and K. Iga, "Design and fabrication of a surface emitting laser using semiconductor distributed Bragg reflector," *The Review of Laser Eng.*, vol. 18, pp. 137-145, 1990.

[4] S. Uchiyama and S. Kashiwa, "GaInAsP/InP SBH surface emitting laser with Si/Al_2O_3 mirror," *Electron. Lett.*, vol. 31, pp. 1449-1450, 1995.

[5] T. P. Pearsall, *GaInAsP Alloy Semiconductors*, John Wiley & Sons Ltd., New York, 1982.

[6] J. M. Vandenberg, R. A. Hamm, M. B. Panish, and H. Temkin, "High-resolution x-ray diffraction studies of InGaAs(P)/InP superlattices grown by gas-source molecular-beam epitaxy," *J. Appl. Phys.*, vol. 62, pp. 1278-1283, 1987.

[7] H. Nagai, S. Adachi, and T. Fukui, *III-V Mixed Crystals*, Corona Publishing Co., Ltd., Japan, 1988.

[8] R. L. Anderson, "Experiments on Ge-GaAs heterojunctions," *Solid State Electron.*, vol. 5, pp. 341-351, 1962.

[9] Y. Ando and T. Itoh, "Calculation of transmission tunneling current across arbitrary potential barriers," *J. Appl. Phys. Lett.*, vol. 61, pp. 1497-1502, 1987.

Program A
Reflection of Multilayer Reflector

Material ID, Refractive Index and Absorption Coefficient

$$\begin{bmatrix} \text{Air} \\ \text{SiO2} \\ \text{Si} \\ \text{MgO} \\ \text{TiO2} \\ \text{Au} \end{bmatrix} := \begin{bmatrix} 0 \\ 1 \\ 2 \\ 3 \\ 4 \\ 5 \end{bmatrix} \qquad DEn := \begin{bmatrix} 1 \\ 1.45 \\ 3.2 \\ 1.72 \\ 2.42 \\ 0.257 - j \cdot 6.82 \end{bmatrix} \qquad DE\alpha := \begin{bmatrix} 0 \\ 0 \\ 150 \\ 0 \\ 0 \\ 0 \end{bmatrix}$$

$InP := rows(DEn)$

$DBR := InP + 1$

$Cap := InP + 2$

$$GaInAsP := \begin{pmatrix} 0.92 \\ 1.25 \\ 1.35 \end{pmatrix}$$ Wavelength of GaInAsP

$$\alpha := \begin{pmatrix} 10 \\ 20 \\ 50 \end{pmatrix}$$

Refractive Index of GaInAsP

$$E0(y) := 3.391 - 1.652 \cdot y + 0.863 \cdot y^2 - 0.123 \cdot y^3$$

$$Ed(y) := 28.91 - 9.278 \cdot y + 5.626 \cdot y^2$$

$$Eg(y) := 1.35 - 0.775 \cdot y + 0.149 \cdot y^2$$

$$\eta(y) := \frac{\pi \cdot Ed(y)}{2 \cdot E0(y)^3 \cdot \left(E0(y)^2 - Eg(y)^2\right)}$$

$$nn(E,y) := Re\left(\sqrt{1 + \frac{Ed(y)}{E0(y)} + \frac{Ed(y)}{E0(y)^3} \cdot E^2 + \frac{\eta(y)}{\pi} \cdot E^4 \cdot \ln\left(\frac{2 \cdot E0(y)^2 - Eg(y)^2 - E^2}{Eg(y)^2 - E^2}\right)}\right)$$

$y := 0 \qquad As\_y(\lambda g) := root\left(Eg(y) - \frac{1.2398}{\lambda g}, y\right)$

$$Index(\lambda, \lambda g) := nn\left(\frac{1.2398}{\lambda}, As\_y(\lambda g)\right)$$

Wavelength Range of Reflectivity Spectrum

$reso := 100 \qquad i := 0 .. reso \qquad \lambda_i := \lambda s + \frac{\lambda e - \lambda s}{reso} \cdot i$

Refractive Index for Each Layer and Wavelength

$j := 0 .. rows(DEn) - 1$

$$n_{j,i} := DEn_j - i \cdot \frac{\lambda_i \cdot 10^{-4}}{4 \cdot \pi} \cdot DE\alpha_j \qquad nc_j := DEn_j - i \cdot \frac{\lambda c \cdot 10^{-4}}{4 \cdot \pi} \cdot DE\alpha_j$$

$j := 0 .. rows(GaInAsP) - 1$

$$n_{j+InP,i} := Index\left(\lambda_i, GaInAsP_j\right) - i \cdot \frac{\lambda_i \cdot 10^{-4}}{4 \cdot \pi} \cdot \alpha_j \qquad nc_{j+InP} := Index\left(\lambda c, GaInAsP_j\right) - i \cdot \frac{\lambda c \cdot 10^{-4}}{4 \cdot \pi} \cdot \alpha_j$$

$j := 0 .. rows(n) - 1$

λ/4 Thickness for Each Layer

$$d_j := \left(\frac{\lambda c}{4 \cdot \mathrm{Re}(nc_j)}\right)$$

Phase Shift for Each Layer and Wavelength

$$\Phi_{j,i} := 2 \cdot \frac{\pi}{\lambda_i} \cdot d_j \cdot n_{j,i} \qquad \Phi c_j := 2 \cdot \frac{\pi}{\lambda c} \cdot d_j \cdot nc_j$$

Matrix

$$U(m,i) := \begin{bmatrix} \cos(\Phi_{m,i}) & \frac{i}{n_{m,i}} \cdot \sin(\Phi_{m,i}) \\ i \cdot n_{m,i} \cdot \sin(\Phi_{m,i}) & \cos(\Phi_{m,i}) \end{bmatrix} \qquad Uc(m) := \begin{bmatrix} \cos(\Phi c_m) & \frac{i}{nc_m} \cdot \sin(\Phi c_m) \\ i \cdot nc_m \cdot \sin(\Phi c_m) & \cos(\Phi c_m) \end{bmatrix}$$

$$B(m,i) := \begin{pmatrix} 1 & 1 \\ n_{m,i} & -n_{m,i} \end{pmatrix} \qquad Bc(m) := \begin{pmatrix} 1 & 1 \\ nc_m & -nc_m \end{pmatrix}$$

Layer Structure for Reflectivity Spectrum

$$S(i) := B(InP,i)^{-1} \cdot (U(SiO2,i) \cdot U(Si,i))^{Nn} \cdot B(Air,i)$$

Layer Structure for Reflectivity against Pair Number

$$SN(N) := Bc(InP)^{-1} \cdot (Uc(DBR) \cdot Uc(InP))^{N} \cdot Uc(Cap) \cdot Bc(Air)$$

Reflectivity Spectrum Calculation

$$R_i := \left(\left|\frac{S(i)_{1,0}}{S(i)_{0,0}}\right|\right)^2 \cdot 100$$

Reflectivity Calculation

$$NN := 0 .. N$$

$$RN_{NN} := \left(\left|\frac{SN(NN)_{1,0}}{SN(NN)_{0,0}}\right|\right)^2 \cdot 100$$

Conditions and Results

Center Wavelength $\lambda c \equiv 1.55$

Wavelength Range $\lambda s \equiv 1.0$ $\lambda e \equiv 2.2$

Number of DBR pairs $Nn \equiv 4$

Pair Number Range $N \equiv 40$

Maximum Reflectivity $\max(R) = 99.68$

Reflectivity $RN_{30} = 95.564$

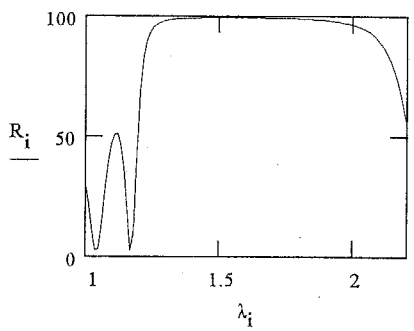

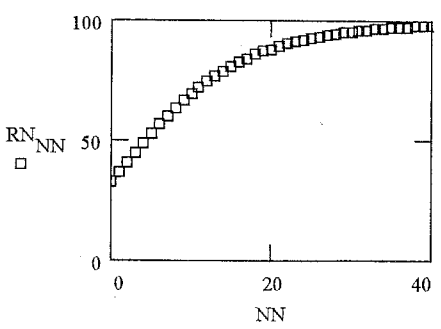

Program B
x-Ray Diffraction Pattern from GaInAsP/GaInAsP Superlattice

Lattice Constant of InP Substrate

$$dInP := \frac{5.8688}{2}$$

Cu : $K\alpha_1$ $\lambda \equiv 1.5405$

$\theta InP \equiv 63.34$

Lattice Constant of Free Standing Barrier and Well

$$db0 := (5.4512 \cdot xb \cdot (1 - yb) + 5.8688 \cdot (1 - xb) \cdot (1 - yb) + 6.0584 \cdot (1 - xb) \cdot yb + 5.6533 \cdot xb \cdot yb) \cdot \frac{1}{2}$$

$$dw0 := (5.4512 \cdot xw \cdot (1 - yw) + 5.8688 \cdot (1 - xw) \cdot (1 - yw) + 6.0584 \cdot (1 - xw) \cdot yw + 5.6533 \cdot xw \cdot yw) \cdot \frac{1}{2}$$

Elastic Stiffness Constants

$$Cb11 := 14.12 \cdot xb \cdot (1 - yb) + 10.22 \cdot (1 - xb) \cdot (1 - yb) + 8.329 \cdot (1 - xb) \cdot yb + 11.88 \cdot xb \cdot yb$$

$$Cb12 := 6.253 \cdot xb \cdot (1 - yb) + 5.76 \cdot (1 - xb) \cdot (1 - yb) + 4.526 \cdot (1 - xb) \cdot yb + 5.38 \cdot xb \cdot yb$$

$$Cw11 := 14.12 \cdot xw \cdot (1 - yw) + 10.22 \cdot (1 - xw) \cdot (1 - yw) + 8.329 \cdot (1 - xw) \cdot yw + 11.88 \cdot xw \cdot yw$$

$$Cw12 := 6.253 \cdot xw \cdot (1 - yw) + 5.76 \cdot (1 - xw) \cdot (1 - yw) + 4.526 \cdot (1 - xw) \cdot yw + 5.38 \cdot xw \cdot yw$$

Lattice Constant of Strained Barrier and Well

$$db := \left[\left(1 + \frac{2 \cdot Cb12}{Cb11} \right) \cdot \frac{db0 - dInP}{dInP} + 1 \right] \cdot dInP \qquad dw := \left[\left(1 + \frac{2 \cdot Cw12}{Cw11} \right) \cdot \frac{dw0 - dInP}{dInP} + 1 \right] \cdot dInP$$

Averaged Lattice Constant of QW

$$d0 := \frac{n \cdot db + m \cdot dw}{n + m}$$

x-Ray Scattering Factor (Molecule Mass Approximation)

$$Fb := 69.72 \cdot xb + 114.82 \cdot (1 - xb) + 74.92 \cdot yb + 30.97 \cdot (1 - yb)$$

$$Fw := 69.72 \cdot xw + 114.82 \cdot (1 - xw) + 74.92 \cdot yw + 30.97 \cdot (1 - yw)$$

Diffraction Pattern Calculation

$$i := 0 .. \frac{\theta e - \theta s}{d\theta} \qquad \theta_i := \theta s + i \cdot d\theta \qquad \overrightarrow{h := \left(2 \cdot d0 \cdot \sin\left(\frac{\theta}{2} \cdot \frac{\pi}{180} \right) \cdot \frac{1}{\lambda} \right)}$$

$$\overrightarrow{A := \sum_{N=0}^{n-1} \exp\left[2 \cdot \pi \cdot i \cdot \left(N + \frac{1}{2} \right) \cdot \frac{db}{d0} \cdot h \right]}$$

$$\overrightarrow{B := \sum_{N=0}^{m-1} \exp\left[2 \cdot \pi \cdot i \cdot \left(N + \frac{1}{2} \right) \cdot \frac{dw}{d0} \cdot h \right]}$$

$$\overrightarrow{P := \sum_{s=0}^{p-1} \exp\left[2 \cdot \pi \cdot i \cdot s \cdot \left(\frac{n \cdot db + m \cdot dw}{d0} \right) \cdot h \right]}$$

$$\overrightarrow{I := \left| Fb \cdot A + \exp\left(2 \cdot \pi \cdot i \cdot n \cdot h \cdot \frac{db}{d0} \right) \cdot \left(Fw \cdot B + \exp\left(2 \cdot \pi \cdot i \cdot m \cdot h \cdot \frac{dw}{d0} \right) \cdot Fb \cdot A \right) \cdot P \right|}$$

$$\overrightarrow{I := \frac{I}{\max(I)}}$$

0th Diffraction Peak (2θ) $\theta 0th := 2 \cdot \operatorname{asin}\left(\frac{\lambda}{d0}\right) \cdot \frac{180}{\pi}$

Strain (%) $\varepsilon b := \frac{db0 - dInP}{db0} \cdot 100$ $\varepsilon w := \frac{dw0 - dInP}{dw0} \cdot 100$ $\varepsilon := \frac{d0 - dInP}{dInP} \cdot 100$

Conditions and Results

Barrier monolayers	n ≡ 32
Well monolayers	m ≡ 25
Pairs	p ≡ 4
Barrier Thickness	n·db = 93.1
Well Thickness	m·dw = 74.4
One Period Thickness	n·db + m·dw = 167.5
Net Strain	ε = 0.136

$Ga_xIn_{1-x}As_yP_{1-y}$

Barrier Material xb ≡ 0.532 yb ≡ 1

Strain (%) εb = −0.443

Well Material xw ≡ 0.365 yw ≡ 1

Strain (%) εw = 0.706

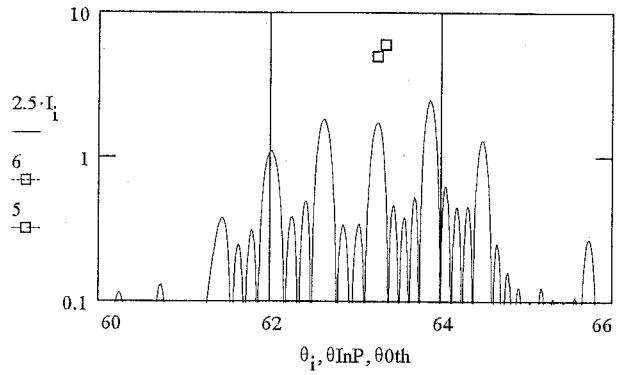

0th Diffraction Peak (2θ)

θ0th = 63.238

Start Angle	θs ≡ 60
Stop Angle	θe ≡ 66
Step Angle	dθ ≡ 0.004

Program C
Emission Wavelength of GaInAs/InP Quantum Well

Free Electron Mass $m0 := 9.1093897 \cdot 10^{-31}$ [kg]

Electron Charge $e := 1.60217733 \cdot 10^{-19}$ [C]

Planck's Constant $hbar := 6.582122 \cdot 10^{-16}$ [eVs]

Band Discontinuity

$dEc := offset \cdot (Egb - Egw)$ $dEv := (1 - offset) \cdot (Egb - Egw)$

Wave Number

$$Kw(E, mw) := \frac{\sqrt{2 \cdot mw \cdot m0 \cdot E \cdot e}}{hbar \cdot e} \qquad Kb(E, mb, V) := \frac{\sqrt{2 \cdot mb \cdot m0 \cdot (V - E) \cdot e}}{hbar \cdot e}$$

Quantized Energy Calculation Function

$E := 10^{-4}$

$$En(L, mw, mb, V) := Re\left(root\left(atan\left(\frac{mw}{mb} \cdot \frac{Kb(E, mb, V)}{Kw(E, mw)}\right) - Kw(E, mw) \cdot \frac{L \cdot 10^{-10}}{2}, E\right)\right)$$

Range of Well Thickness

$i := 0..35$ $L_i := \frac{5.8688}{2} \cdot (i + 1)$

Quantized Energy

$\overrightarrow{Ec := En(L, mcw, mcb, dEc)}$ $\overrightarrow{Eh := En(L, mhw, mhb, dEv)}$

Emission Wavelength

$$\overrightarrow{\lambda ch := \frac{1.2398}{Ec + Eh + Egw}}$$

Conditions and Results

	Barrier	Well		
Bandgap Energy	$Egb = 1.35$	$Egw = 0.75$	Band Offset Ratio	$offset = 0.4$
Effective Mass	$mcb = 0.08$	$mcw = 0.041$	Band Discontinuity	$dEc = 0.24$
	$mhb = 0.56$	$mhw = 0.50$		$dEv = 0.36$

Emission Wavelength vs. Well Width

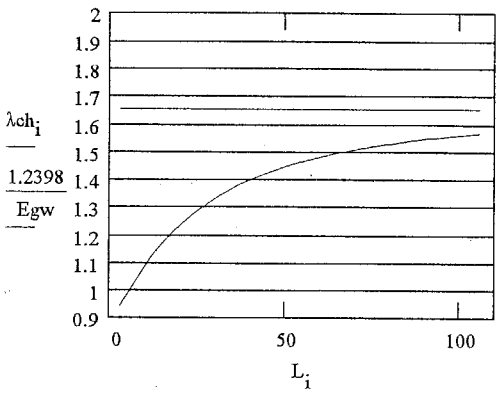

Quantized Energy vs. Well Width

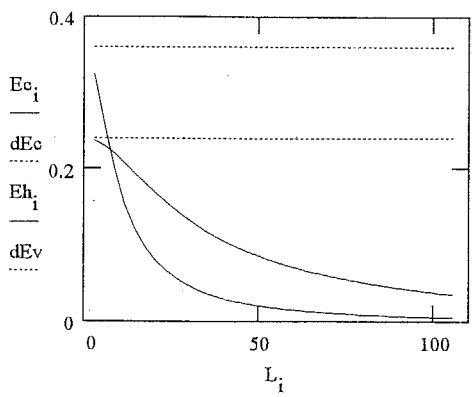

Program D
Optical Confinement Factor of Multilayer Slab Waveguide

Layer Position

$N := rows(n) - 1 \qquad s := 0..N$

Layer Structure

$n_{i-1}\ x_i\ n_i\ x_{i+1}\ n_{i+1}$

$x_0 := 0 \qquad x_{s+1} := x_s + d_s$

$$xc := \frac{1}{2 \cdot \sum act} \cdot \left[\sum_s act_s \cdot \left(x_s + x_{s+1} \right) \right]$$

$x_s := x_s - xc \qquad x_{N+1} := x_{N+1} - xc$

Propagation Coefficient

$$k0 := \frac{2 \cdot \pi}{\lambda} \qquad \beta := k0 \cdot nneq$$

Initial Condition

$$\gamma(\beta, i) := -\sqrt{k0^2 \cdot (n_i)^2 - \beta^2}$$

$\gamma p(\beta, i) := \gamma(\beta, i+1) + \gamma(\beta, i) \qquad \gamma n(\beta, i) := \gamma(\beta, i+1) - \gamma(\beta, i)$

$$M(\beta, i) := \frac{1}{2 \cdot \gamma(\beta, i+1)} \cdot \begin{pmatrix} \gamma p(\beta, i) \cdot \exp\left(j \cdot \gamma n(\beta, i) \cdot x_{i+1}\right) & \gamma n(\beta, i) \cdot \exp\left(j \cdot \gamma p(\beta, i) \cdot x_{i+1}\right) \\ \gamma n(\beta, i) \cdot \exp\left(-j \cdot \gamma p(\beta, i) \cdot x_{i+1}\right) & \gamma p(\beta, i) \cdot \exp\left(-j \cdot \gamma n(\beta, i) \cdot x_{i+1}\right) \end{pmatrix}$$

$$L(\beta) := \left(\prod_{i=1}^{N} M(\beta, N - i) \right)_{(1,1)}$$

$TOL := 10^{-3} \qquad \beta := root(L(\beta), \beta)$

$TOL := 10^{\log(|L(\beta)|)} \qquad \beta := root(L(\beta), \beta)$

$TOL := 10^{\log(|L(\beta)|)} \qquad \beta := root(L(\beta), \beta)$

$TOL := 10^{-5}$

Electric Field Calculation

$p := 1..N$

$$\begin{pmatrix} Eplus_p \\ Eminus_p \end{pmatrix} := \left(\prod_{i=1}^{N} if(p - i \geq 0, M(\beta, p - i), identity(2)) \right)^{\langle 1 \rangle}$$

$Eplus_0 := 0 \qquad Eminus_0 := 1 \qquad Eminus_N := 0$

$E(s, x) := Eplus_s \cdot \exp(-j \cdot \gamma(\beta, s) \cdot x) + Eminus_s \cdot \exp(j \cdot \gamma(\beta, s) \cdot x)$

Confinement Factor Calculation

$$\xi := \frac{\sum_s \int_{x_s}^{x_{s+1}} act_s \cdot E(s,x)^2 \, dx}{\sum_s \int_{x_s}^{x_{s+1}} E(s,x)^2 \, dx}$$

Field Intensity Curve

$q := 0 .. xreso - 1$

$ii := 0 .. N \cdot xreso + xreso - 1$

$xx(s,q) := x_s + q \cdot \frac{x_{s+1} - x_s}{xreso}$

$X_{s \cdot xreso + q} := xx(s,q)$

$EE_{s \cdot xreso + q} := E(s, xx(s,q))^2$

$EA_{s \cdot xreso + q} := act_s \cdot E(s, xx(s,q))^2$

n_{eq} Graph Curve

$k := 0 .. nreso$

$a_k := k0 \cdot \left(maxn - \frac{maxn - minn}{nreso} \cdot k - 0.0001 \right)$

$\overrightarrow{II} := \frac{1}{|L(a)|}$ $\quad \overrightarrow{I} := \frac{II}{max(II)}$ $\quad \overrightarrow{nn} := \frac{a}{k0}$ $\quad neq := \frac{\beta}{k0}$

Conditions and Results

Wavelength (μm)	$\lambda \equiv 1.55$			
Propagation Coefficient	$\beta = 13.18$	Graph Resolution :	$xreso \equiv 50$	$nreso \equiv 100$
Effective Refractive Index	$neq = 3.2514$	Index Range	$minn \equiv 3.17$	$maxn \equiv 3.55$
Confinement Factor	$\xi = 0.0367$	**Initial Effective Index**	$nneq \equiv 3.2$	

Optical Field

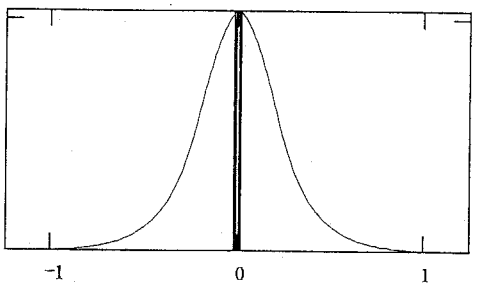

Peak : Eigen Value

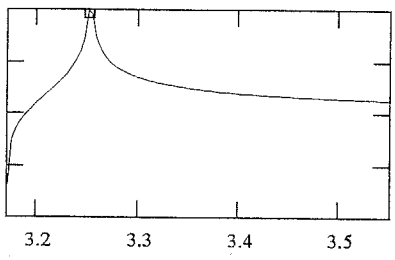

Index	Thickness	Active
3.17	1.0	0
3.34	0.2	0
3.55	0.01	1
$n \equiv$ 3.34	$d \equiv$ 0.02	$act \equiv$ 0
3.55	0.01	1
3.34	0.2	0
3.17	1.0	0

Program E
Hole Tunneling Transmission Current at Heterointerface

Electron Charge	$e := 1.60217733 \cdot 10^{-19}$	[C]
Free Electron Mass	$m0 := 9.1093897 \cdot 10^{-31}$	[kg]
Boltzmann's Constant	$k := 8.617386 \cdot 10^{-5}$	[eV/K]
Planck's Constant	$hbar := 6.582122 \cdot 10^{-16}$	[eVs]
Dielectric Constant	$\varepsilon 0 := 8.854187817 \cdot 10^{-12} \cdot 10^{-2}$	[F/cm]
Temperature	$T := 300$	[K]

Fermi Level Calculation

$i0 := 0 .. 50 \qquad Ef_{i0} := (i0 - 13) \cdot 10 \cdot 10^{-3} \qquad j := 0 .. 15$

$$Nn_{i0} := \left[\frac{1}{2 \cdot \pi^2} \cdot \left(\frac{2 \cdot m0}{hbar^2} \right)^{1.5} \cdot \sum_j \int_{j \cdot 0.1}^{(j+1) \cdot 0.1} \frac{\sqrt{E}}{1 + \exp\left(\frac{E - Ef_{i0}}{k \cdot T} \right)} dE \right] \cdot \sqrt{e} \cdot \frac{e}{e^3} \cdot 10^{-6}$$

$$EF(n, m) := interp\left(pspline(Nn, Ef), Nn, Ef, n \cdot m^{-1.5} \right)$$

$$m1 := \left(m1h^{1.5} + m1l^{1.5} \right)^{\frac{2}{3}} \qquad m2 := \left(m1h^{1.5} + m1l^{1.5} \right)^{\frac{2}{3}}$$

$Ef1 := -EF(N1, m1) \qquad Ef2 := -EF(N2, m2)$

Ef1: Fermi Energy for narrow gap
Ef2: for wide gap

Band Parameters for non-Biased Condition

$$i1 := 0 .. 100 \quad vd1_{i1} := \frac{i1}{100} \cdot 0.15$$

$$vd_{i1} := vd1_{i1} + \frac{\varepsilon 1 \cdot N1}{\varepsilon 2 \cdot N2} \cdot \left[k \cdot T \cdot \left(\exp\left(\frac{vd1_{i1}}{k \cdot T} \right) - 1 \right) - vd1_{i1} \right]$$

$\Delta Ev := 0.6 \cdot (Eg2 - Eg1)$

$VD := \Delta Ev - Ef2 + Ef1$

$VD1 := interp(pspline(vd, vd1), vd, vd1, VD)$

$VD2 := VD - VD1$

$V1 := -interp(pspline(vd, vd1), vd, vd1, VD - V) + VD1$

$V2 := V - V1$

$$L := \sqrt{\frac{2 \cdot \varepsilon 2 \cdot \varepsilon 0 \cdot (VD2 - V2)}{e \cdot N2}} \cdot 10^{-2}$$

ΔEv: Valence band offset
VD: Built in Potential
VD1: Built in Potential for narrow gap
VD2: for wide gap
V: Applied Voltage
V1: Applied Voltage for narrow gap
V2: for wide gap

L: Depletion width [m]

Depletion Region Profile

$Ev1 := VD1 - V1 - \Delta Ev$ $\quad Ev2 := VD - V - \Delta Ev$ Band Edge Energy of wide gap

$$ML := \frac{5.8688}{2} \cdot 10^{-10}$$

$$N := \text{floor}\left(\frac{L}{ML}\right)$$

$s := N, N - 1 .. 0$

$$x_s := \frac{L}{N} \cdot s$$

Potential Profile

$$U_s := -1 \cdot \left[\frac{Ev1 - Ev2}{L^2} \cdot (x_s - L)^2 + Ev2\right]$$

$U_0 := -(VD1 - V1)$

$U_{N+1} := -Ev2$

Effective Mass Profile

$m_s := m2t \cdot m0$

$m_0 := m1t \cdot m0$

$m_{N+1} := m2t \cdot m0$

Tunneling Provability Calculation

$i2 := 0 .. 100$ $\quad Et_{i2} := \left(\frac{i2}{100} \cdot 2 + 10^{-6}\right) - (VD1 - V1)$

$$K_{i2,s} := \frac{\sqrt{2 \cdot m_s \cdot (Et_{i2} - U_s) \cdot e}}{hbar \cdot e}$$

$$K_{i2,N+1} := \frac{\sqrt{2 \cdot m_{N+1} \cdot (Et_{i2} - U_{N+1}) \cdot e}}{hbar \cdot e}$$

$$S_{i2,s} := \frac{m_{s+1}}{m_s} \cdot \frac{K_{i2,s}}{K_{i2,s+1}}$$

$$M(i2) := \prod_s \frac{1}{2} \cdot \begin{bmatrix} (1 + S_{i2,s}) \cdot \exp\left[-i \cdot (K_{i2,s+1} - K_{i2,s}) \cdot x_s\right] & (1 - S_{i2,s}) \cdot \exp\left[-i \cdot (K_{i2,s+1} + K_{i2,s}) \cdot x_s\right] \\ (1 - S_{i2,s}) \cdot \exp\left[i \cdot (K_{i2,s+1} + K_{i2,s}) \cdot x_s\right] & (1 + S_{i2,s}) \cdot \exp\left[i \cdot (K_{i2,s+1} - K_{i2,s}) \cdot x_s\right] \end{bmatrix}$$

$$TP_{i2} := \text{Re}\left[\frac{m_{N+1}}{m_0} \cdot \frac{K_{i2,0}}{K_{i2,N+1}} \cdot \frac{1}{\left[\left|M(i2)_{(1,1)}\right|\right]^2}\right]$$

$D(E) := \text{interp}(\text{pspline}(Et, TP), Et, TP, -E)$

Tunneling Current-Voltage Characteristics

$$mt := \frac{m1t \cdot m2t}{m1t + m2t}$$

$p := 0 .. 40$

$$J := \frac{e \cdot m0 \cdot e^2 \cdot k \cdot T}{2 \cdot \pi^2 \cdot hbar^3 \cdot e^3} \cdot \sum_p \int_{VD1 - V1 - p \cdot 0.05}^{VD1 - V1 - (p+1) \cdot 0.05} D(Ez) \cdot \left[mt \cdot \ln\left[\exp\left[\frac{-(Ef1 - Ez)}{k \cdot T}\right] + 1\right] ... \right.$$
$$\left. + -mt \cdot \ln\left[\exp\left[\frac{-(Ev2 + Ef2 - Ez)}{k \cdot T}\right] + 1\right]\right] dEz$$

Conditions and Results

	Narrow gap	Wide gap		
Bandgap [eV]	$Eg1 \equiv 0.855$	$Eg2 \equiv 1.35$	Band offset	$\Delta Ev = 0.297$
Dielectric Constant	$\varepsilon 1 \equiv 13.6$	$\varepsilon 2 \equiv 12.4$	Depletion Width	$L \cdot 10^{10} = 122.6$
Heavy Hole Mass	$m1h \equiv 0.5$	$m2h \equiv 0.56$		
Light Hole Mass	$m1l \equiv 0.068$	$m2l \equiv 0.12$		
Hole Concentration	$N1 \equiv 2 \cdot 10^{18}$	$N2 \equiv 1 \cdot 10^{18}$		
Fermi Energy	$Ef1 = 0.038$	$Ef2 = 0.057$		

Heavy or Light Hole Current	$m1t \equiv m1l$	$m2t \equiv m2l$
Bias Voltage [V]	$V \equiv 0.13$	
Tunneling Current	$J \cdot 10^{-4} = 3428$	$[A/cm^2]$

$z := 0..10$

Hole Energy vs. Transmitivity

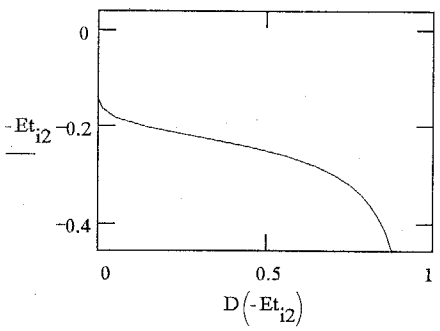

Potential Profile

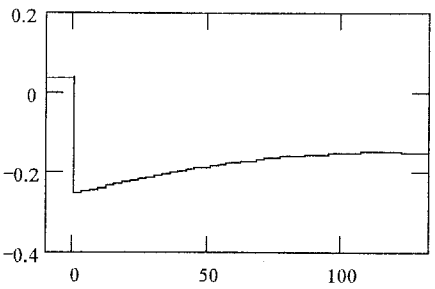

Program F
Current Flow of Ring Electrode Structure

ORIGIN ≡ 1 $\quad e := 1.60217733 \cdot 10^{-19}$

Mobility and Conductivity in p-Cladding Layer

$p_{clad} := 1 \cdot 10^{18} \quad \mu := 80 \quad \sigma_{clad} := \mu \cdot p_{clad} \cdot e$

Generate **Resistance Network**

Division Number of Cladding (r, h), Active, Electrode and Mirror

$$M := \frac{r_{clad}}{dr} \quad N := \frac{h_{clad}}{dh} \quad P := \frac{r_{act}}{dr} \quad Q := \frac{w_{electrode}}{dr} \quad O := \frac{r_{mirror}}{dr}$$

Total Node Number $\quad S := M \cdot N + P + Q$

Active Region Node Position $\quad S1(p) := p$

Cladding Region Node Position $\quad S2(m,n) := M \cdot (n - 1) + m + P$

Electrode Region Node Position $\quad S3(q) := M \cdot N + P + q$

Matrix Element $A_{s,s}$: Conductivity

Connection in Active Layer

$p := 1..P$

$$A_{S1(p),S2(p,1)} := \left[\frac{1}{\pi \cdot (2 \cdot p - 1) \cdot dr^2} \cdot \left(\rho_{hetero_p} + \frac{0.5 \cdot dh}{\sigma_{clad}} \right) \right]^{-1}$$

$$A_{S2(p,1),S1(p)} := A_{S1(p),S2(p,1)}$$

Connection in Radius Direction

$n := 1..N$

$m := 1..M - 1$

$$A_{S2(m,n),S2(m+1,n)} := \frac{2 \cdot \pi \cdot dh}{\ln\left(\frac{m + 0.5}{m - 0.5}\right)} \cdot \sigma_{clad}$$

$$A_{S2(m+1,n),S2(m,n)} := A_{S2(m,n),S2(m+1,n)}$$

Connection in Thickness Direction

$m := 1..M$

$n := 1..N - 1$

$$A_{S2(m,n),S2(m,n+1)} := \frac{\pi \cdot (2 \cdot m - 1) \cdot dr^2}{dh} \cdot \sigma_{clad}$$

$$A_{S2(m,n+1),S2(m,n)} := A_{S2(m,n),S2(m,n+1)}$$

Connection in Electrode

$q := 1..Q$

$$A_{S3(q),S2(O+q,N)} := \left[\frac{1}{\pi \cdot (2 \cdot (O + q) - 1) \cdot dr^2} \cdot \left(\rho_{electrode} + \frac{0.5 \cdot dh}{\sigma_{clad}} \right) \right]^{-1}$$

$$A_{S2(O+q,N),S3(q)} := A_{S3(q),S2(O+q,N)}$$

Diagonal Element

$i := 1..S$

$$A_{i,i} := -\sum_{j=1}^{S} A_{i,j}$$

Voltage Connection List in Active Region

$p := 1..P \qquad U_{p,1} := S1(p) \qquad U_{p,2} := 0$

Voltage Connection List for Electrode

$q := 1..Q \qquad U_{P+q,1} := S3(q) \qquad U_{P+q,2} := V$

$NB := 1..\text{rows}(U) \qquad s := 1..S \qquad B_s := 0$

$A_{U_{NB,1},s} := 0 \qquad A_{U_{NB,1},U_{NB,1}} := 1 \qquad B_{U_{NB,1}} := U_{NB,2}$

$W := A^{-1} \cdot B$

$p := 1..P \qquad I_p := \left(W_{P+p} - W_p\right) \cdot A_{P+p,p} \qquad J_p := \dfrac{I_p}{\pi \cdot (2 \cdot p - 1) \cdot dr^2} \qquad J_{ave} := \dfrac{\sum I}{\pi \cdot r_{act}^2} \qquad R := \dfrac{V}{\sum I}$

$\rho(J) := LSQ^T \cdot \left(J^0 \;\; J^1 \;\; J^2 \;\; J^3 \;\; J^4 \;\; J^5\right)^T \qquad \rho_{new_p} := \rho\left(J_p\right)_{1,1}$

Conditions and Results

$um \equiv 10^{-4}$ (cm)

Element Width	$dr \equiv 0.5 \cdot um$	$dh \equiv 0.2 \cdot um$	
Clad Thickness	$h_{clad} \equiv 1 \cdot um$	Electrode Width	$w_{electrode} \equiv 5 \cdot um$
Clad Radius	$r_{clad} \equiv 10 \cdot um$	Mirror Radius	$r_{mirror} \equiv 5 \cdot um$
Active Radius	$r_{act} \equiv 5 \cdot um$	Specific Resistance	$\rho_{electrode} \equiv 1 \cdot 10^{-5}$

Applied Voltage	$V \equiv 0.33$
Current	$10^3 \cdot \sum I = 4.366$
Current Density	$J_{ave} = 5.56 \cdot 10^3$
Resistance	$R = 75.586$

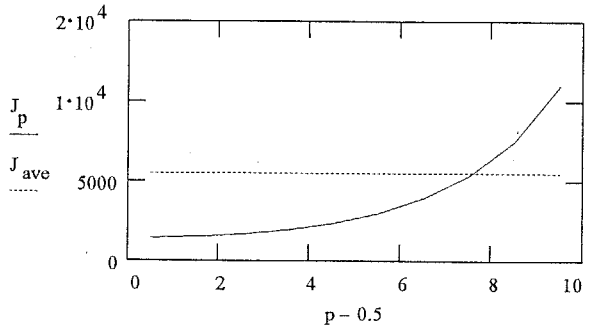

$\rho_{new} =$

	I
1	$3.962 \cdot 10^{-5}$
2	$3.853 \cdot 10^{-5}$
3	$3.651 \cdot 10^{-5}$
4	$3.359 \cdot 10^{-5}$
5	$2.995 \cdot 10^{-5}$
6	$2.586 \cdot 10^{-5}$
7	$2.169 \cdot 10^{-5}$
8	$1.778 \cdot 10^{-5}$
9	$1.436 \cdot 10^{-5}$
10	$1.148 \cdot 10^{-5}$

$\rho_{hetero} \equiv \begin{bmatrix} 3.417 \cdot 10^{-5} \\ 3.323 \cdot 10^{-5} \\ 3.157 \cdot 10^{-5} \\ 2.93 \cdot 10^{-5} \\ 2.663 \cdot 10^{-5} \\ 2.376 \cdot 10^{-5} \\ 2.09 \cdot 10^{-5} \\ 1.82 \cdot 10^{-5} \\ 1.576 \cdot 10^{-5} \\ 1.357 \cdot 10^{-5} \end{bmatrix}$

Coefficients of Least Squares Fit from Results of I-V Characteristics

$LSQ \equiv \begin{bmatrix} 4.714 \cdot 10^{-6} \\ 7.968 \cdot 10^{-2} \\ -5.244 \cdot 10^{1} \\ 1.751 \cdot 10^{4} \\ -2.607 \cdot 10^{6} \\ 1.312 \cdot 10^{8} \end{bmatrix}$

Acknowledgment

I would like to gratefully acknowledge Professor Kenich Iga, the adviser of my thesis at Tokyo Institute of Technology, for his general guidance and support. I also would like to thank Associate Professor Fumio Koyama for his advice and suggestions.

I wish to acknowledge Professor Emeritus Y. Suematsu for his encouragement of this study. I would like to thank Prof. H. Kukimoto, Prof. J. Hanna, Prof. S. Arai, and Associate Prof. H. Munekata for their advice and suggestions to this study. I acknowledge Prof. K. Furuya, Prof. J. Yoshino, Associate Prof. M. Asada, and Associate Prof. Y. Miyamoto of Tokyo Institute of Technology for their technical advice and suggestions.

I wish to acknowledge Prof. H. Kawanishi of Kohgakuin University, Prof. K. Kishino of Sophia University, Prof. M. Yamada of Kanazawa University, Prof. Y. Kokubun of Yokohama National University, Associate Prof. K. Moriki of Musashi Institute of Technology, Associate Prof. K. Shimomura of Sophia University and Associate Prof. T. Baba of Yokohama National University for their helpful discussions.

I wish to thank Dr. A. Kasukawa of Furukawa Electric Co., Dr. S. Uchiyama of Furukawa Electric Co., Dr. T. Tadokoro of NTT Co. and Dr. H. Uenohara of NTT Co. for their fruitful discussions. I thank the member of Kukimoto and Munekata Laboratory, member of Moriki Laboratory and Baba Laboratory for their discussions.

I gratefully appreciate my research colleagues at Tokyo Institute of Technology, Dr. Toshi K. Uchida (presently with Optobahn Corp.), Dr. T. Uchida (presently with the Air Self-Defence Force), Dr. N. Yokouchi (presently with Furukawa Electric Co.), Mr. K. Mise of Anritsu Corp. Mr. S. Kubota (presently with Fujitsu Lab. Ltd.), Mr. Y. Inaba (presently with Matsushita Electric Industrial Co.), Mr. K. Mori (presently with Matsushita Electric Industrial Co.), Mr. T. H. Loh, Mr. S. Mitsugi, Mr. Y. Kurita, Mr. T. Takada, Mr. R. Ubukata, Mr. S. Sekiguchi for their technical support, discussions and warm friendship. I also thank Mr. T. Sakaguchi, Mr. A. Matsutani, Dr. K. Nakamura, and Dr. T. Honda for their discussions and support. I wish to thank Dr. M. Shimizu (presently with Electrotechnical Lab.), Dr. A. Akiba (presently with Nippon Sheet Glass Co.), Dr. M. Oshikiri (presently with National Res. Inst. for Metals), Dr. T. Tamanuki (presently with NEC Co.), Dr. H. Tanobe (presently with NTT Co.), Dr. T. Hamano (presently with Riken) for their helpful discussions. I thank Dr. T. Takagi of KRI International, Mr. Y. Kaneko of Hewlett Packard Labs. Japan, Mr. M. Hirota of Nissan Motorcar Co. for their discussions. I thank Mr. N. Hatori, Mr. T. Kato and the members of Iga and Koyama laboratory. I also thank my colleagues Mr. M. Kato (presently with Canon Co.) and Mr. T. Fukuhisa (presently with Matsushita Electric Industrial Co.) and

Mrs. A. Baba (presently with Matsushita Research Institute Inc.) for their helpful discussions and encouragement. I gratefully appreciate my familiar colleague Dr. T. Mukaihara for his helpful and fruit full discussions, encouragement and warm friendship. I also thank my friends for their encouragement. Finally, I gratefully thank for my parents and brothers for their encouragement and support.

This study was financially supported by Research Fellowships of the Japan Society for the Promotion of Science for Young Scientists.

List of Publications

Papers

[1] N. Yokouchi, T.K. Uchida, T. Uchida, T. Miyamoto, F. Koyama, and K. Iga, "Ultra-thin $Ga_XIn_{1-X}As/InP$ ($0 \leq x \leq 0.47$) layer growth by chemical beam epitaxy," *Journal of Electronic Materials*, vol. 20, pp. 1049-1052, 1991.

[2] N. Yokouchi, T.K. Uchida, T. Uchida, T. Miyamoto, F. Koyama, and K. Iga, "Room-temperature observation of excitonic absorption in $Ga_XIn_{1-X}As/InP$ ($0.2 \leq x \leq 0.47$) quantum wells grown by chemical beam epitaxy," *Jpn. J. Appl. Phys.*, vol. 30, pp. L885-L887, 1991.

[3] T. Uchida, T.K. Uchida, N. Yokouchi, T. Miyamoto, F. Koyama, and K. Iga, "Beryllium doping for $Ga_{0.47}In_{0.53}As/InP$ quantum wells by chemical beam epitaxy (CBE)," *Jpn. J. Appl. Phys.*, vol. 30, pp. L1224-L1226, 1991.

[4] T. Uchida, N. Yokouchi, T. Miyamoto, F. Koyama, and K. Iga, "Chemical beam epitaxy (CBE) growth of GaInAsP/InP and application to surface emitting lasers," IEICE, vol. J75-C-1, pp. 741-747, 1992.

[5] N. Yokouchi, T. Uchida, T. Miyamoto, Y. Inaba, F. Koyama, and K. Iga, "An optical absorption property of highly beryllium-doped GaInAsP grown by chemical beam epitaxy," *Jpn. J. Appl. Phys.*, vol. 31, pp. 1255-1257, 1992.

[6] T. Uchida, N. Yokouchi, T. Miyamoto, Y. Inaba, F. Koyama, and K. Iga, "GaInAsP/InP surface emitting lasers grown by chemical beam epitaxy," *Electron. Lett.*, vol. 28, pp. 550-551, 1992.

[7] T. Uchida, T.K. Uchida, N. Yokouchi, T. Miyamoto, F. Koyama, and K. Iga, "Photoluminescence characterization of $Ga_XIn_{1-X}As(0 \leq x \leq 0.32)$ strained quantum wells grown on InP by chemical beam epitaxy," *Journal of Crystal Growth*, vol. 120, pp. 357-361, 1992.

[8] N. Yokouchi, T. Miyamoto, T. Uchida, Y. Inaba, F. Koyama, and K. Iga, "40Å continuous tuning of a GaInAsP/InP vertical-cavity surface-emitting laser using an external mirror," *IEEE Photonics Technol. Lett.*, vol. 4, pp. 701-703, 1992.

[9] T. Uchida, T. Miyamoto, N. Yokouchi, Y. Inaba, F. Koyama, and K. Iga, "CBE grown 1.5 μm GaInAsP-InP surface emitting lasers," *IEEE J. Quantum Electron.*, vol. 29, pp. 1975-1980, 1993.

[10] N. Yokouchi, T. Miyamoto, T, Uchida, Y. Inaba, F. Koyama, and K. Iga, "GaInAsP/InP surface emitting lasers grown by chemical beam epitaxy and wavelength tuning using an external reflector," *Jpn. J. Appl. Phys.*, vol. 32, pp. 618-621, 1993.

[11] T. Uchida, N. Yokouchi, T. Miyamoto, F. Koyama, and K. Iga, "Some optical characteristics of beryllium-doped InP grown by chemical beam epitaxy (CBE)," *Journal of Crystal Growth*, vol. 129, pp. 275-280, 1993.

[12] Y. Inaba, T. Uchida, N. Yokouchi, T. Miyamoto, F. Koyama, and K. Iga, "GaInAsP/InP multi-quantum barrier (MQB) grown by chemical beam epitaxy (CBE)," *Jpn. J. Appl. Phys.*, vol. 32, pp. 760-761, 1993.

[13] T. Miyamoto, K. Mori, H. Maekawa, Y. Inaba, F. Koyama, and K. Iga, "Carrier transport in *p*-type GaInAsP/InP distributed Bragg reflectors," *Jpn. J. Appl. Phys.*, vol. 33, pp. 4614-4616, 1994.

[14] T. Miyamoto, T. Uchida, N. Yokouchi, and K. Iga, "Surface emitting lasers grown by CBE," *Journal of Crystal Growth*, vol. 136, pp. 210-215, 1994.

[15] Y. Inaba, T. Uchida, N. Yokouchi, T. Miyamoto, K. Mori, F. Koyama, and K. Iga, "Growth of GaInAs(P)/InP multi-quantum barrier (MQB) by chemical beam epitaxy," *Journal of Crystal Growth*, vol. 136, pp. 297-301, 1994.

[16] N. Yokouchi, Y. Inaba, T. Uchida, T. Miyamoto, K. Mori, F. Koyama, and K. Iga, "Composition changes in $Ga_XIn_{1-X}As$/InP super-lattice growth by chemical beam epitaxy," *Journal of Crystal Growth*, vol. 136, pp. 302-305, 1994.

[17] T.H. Loh, T. Miyamoto, F. Koyama, and K. Iga, "Strain-compensated multi-quantum barriers for reduction of electron leakages in long-wavelength semiconductor lasers," *Jpn. J. Appl. Phys.*, vol. 34, pp. 1504-1505, 1995.

[18] Y. Kurita, N. Yokouchi, T. Miyamoto, F. Koyama, and K. Iga, "Refractive index variation in GaInAsP/InP quantum confined structures grown by chemical beam epitaxy," *Jpn. J. Appl. Phys.*, vol. 34, pp. 5626-5627, 1995.

International Conferences

[1] N. Yokouchi*, T.K. Uchida, T. Uchida, T. Miyamoto, F. Koyama, and K. Iga, "Ultra-thin $Ga_XIn_{1-X}As$/InP ($0 \leq x \leq 0.47$) layer growth by chemical beam epitaxy," *3rd Int. Conf. on Indium Phosphide and Related Materials (IPRM'91)*, Cardiff, Wales, UK., paper WK.4, Apr. 8-11, 1991.

[2] T. Miyamoto*, T.K. Uchida, F. Koyama, and K. Iga, "PL study on structure dependence of $Ga_XIn_{1-X}As$/InP strained multi-quantum wells grown by CBE," *The 1991 Int. Conf. on Solid State Devices and Materials (SSDM'91)*, Yokohama, Japan, paper PC2-2, Aug. 27-29, 1991.

[3] T.K. Uchida*, T. Miyamoto, T. Uchida, N. Yokouchi, F. Koyama, and K. Iga, "Photoluminescence characterization of $Ga_XIn_{1-X}As$ ($0<x<0.32$) strained quantum wells grown on InP by chemical beam epitaxy," *3rd Int. Conf. on Chemical Beam Epitaxy and Related Growth Techniques (ICCBE-3)*, Oxford, UK., paper J4, Sep. 1-5, 1991.

[4] T. Uchida*, N. Yokouchi, T. Miyamoto, Y. Inaba, F. Koyama, and K. Iga, "Beryllium doping to InP and GaInAsP by chemical beam epitaxy (CBE)," *4th Int. Conf. on Indium Phosphide and Related Materials (IPRM'92)*, Newport, RI., paper TUP8, Apr. 20-24, 1992.

[5] N. Yokouchi*, T. Uchida, T. Miyamoto, Y. Inaba, F. Koyama, and K. Iga, "Optical absorption measurement for highly beryllium-doped GaInAsP grown by chemical beam epitaxy," *4th Optoelectronics Conf. (OEC'92)*, Chiba, Japan, paper 16D2-20, Jul. 15-17, 1992.

[6] N. Yokouchi*, T. Miyamoto, T. Uchida, Y. Inaba, F. Koyama, and K. Iga, "GaInAsP/InP surface emitting laser grown by CBE and wavelength tuning employing external reflector," *The 1992 Int. Conf. on Solid State Devices and Materials (SSDM'92)*, Tsukuba, Japan, paper B-6-4, Aug. 26-28, 1992.

[7] T. Uchida*, T. Miyamoto, N. Yokouchi, Y. Inaba, F. Koyama, and K. Iga, "CBE grown 1.5μm GaInAsP/InP surface emitting lasers," *13th IEEE Int. Semiconductor Laser Conference*, Takamatsu, Japan, paper L-2, Sep. 21-25, 1992.

[8] T. Miyamoto*, T. Uchida, N. Yokouchi, Y. Inaba, F. Koyama, and K. Iga, "A study on gain-resonance matching of CBE grown λ=1.5μm surface emitting lasers," *IEEE Lasers and Electro-Optics Society 1992 Annual Meeting (LEOS'92)*, Boston, MA, paper DLTA13.2, Nov. 16-19, 1992.

[9] N. Yokouchi*, T. Uchida, T. Miyamoto, Y. Inaba, K. Mori, F. Koyama, and K. Iga, "Loss and index change in GaInAsP/InP multiple quantum well QCSE tuning element for surface emitting lasers," *5th Int. Conf. on Indium Phosphide and Related Materials (IPRM'93)*, Paris, France, paper ThA4, Apr. 18-22, 1993.

[10] T. Miyamoto*, T. Uchida, N. Yokouchi, Y. Inaba, F. Koyama, and K. Iga, "Very low threshold GaInAsP/InP surface emitting laser and its temperature characteristics," *Conference on lasers and Electro-Optics, 1993 (CLEO'93)*, Baltimore, MD, paper CWJ41, May 2-7, 1993.

[11] Y. Inaba*, T. Uchida, N. Yokouchi, T. Miyamoto, K. Mori, F. Koyama, and K. Iga, "Growth of GaInAs(P)/InP multi-quantum barrier (MQB) by chemical beam epitaxy," *4th Int. Conf. on Chemical Beam Epitaxy and Related Growth Techniques (ICCBE-4)*, Nara, Japan, paper VIII-17, Jul. 21-23, 1993.

[12] N. Yokouchi*, Y. Inaba, T. Uchida, T. Miyamoto, K. Mori, F. Koyama, and K. Iga, "Composition changes in $Ga_XIn_{1-X}As$/InP super-lattice growth by chemical beam epitaxy," *4th Int. Conf. on Chemical Beam Epitaxy and Related Growth Techniques (ICCBE-4)*, Nara, Japan, paper VIII-18, Jul. 21-23, 1993.

[13] K. Mori*, T. Miyamoto, N. Yokouchi, Y. Inaba, F. Koyama, and K. Iga, "Band discontinuity reduction of *i*-GaInAsP/*p*-InP for improving 1.55μm GaInAsP/InP surface emitting laser performances," *6th Int. Conf. on Indium Phosphide and Related Materials (IPRM'94)*, Santa Barbara, CA, paper WA2, Mar. 28-31, 1994.

[14] T. Miyamoto*, K. Mori, F. Koyama, and K. Iga, "A study on hole transport in *p*-type GaInAsP/InP multilayer reflectors," *The 1994 Int. Conf. on Solid State Devices and Materials (SSDM'94)*, Yokohama, Japan, paper PB-4-7, Aug. 23-26, 1994.

[15] T.H. Loh*, T. Miyamoto, Y. Kurita, F. Koyama, and K. Iga, "Reduction of inelastic scattering effect by introducing strain-compensated superlattice into GaInAs/GaInP multi-quantum barrier," *7th Int. Conf. on Indium Phosphide and Related Materials (IPRM'95)*, Hokkaido, Japan, paper ThP1, May, 1995.

[16] T. Miyamoto, T. Takada, Y. Kurita, K. Mori, F. Koyama, and K. Iga, "Design of p-cladding layer for low threshold long-wavelength surface-emitting lasers," *The Pacific Rim Conference on Lasers and Electro-Optics (CLEO/Pacific Rim '95)*, Chiba, Japan, paper ThI3, July 11-14, 1995.

Domestic Conferences

[1] N. Yokouchi*, T.K. Uchida, T. Uchida, T. Miyamoto, F. Koyama, and K. Iga, "High rate growth of GaInAs/InP multiple quantum wells by CBE," *The 51th Autumn Meeting of Japan Society of Applied Physics*, 27a-V-7, Morioka, Sep., 1990.

[2] T. Uchida*, T.K. Uchida, N. Yokouchi, T. Miyamoto, F. Koyama, and K. Iga, "GaInAs(P)/InP distributed Bragg reflectors (DBRs) grown by CBE," *The 51th Autumn Meeting of Japan Society of Applied Physics*, 27a-V-8, Morioka, Sep., 1990.

[3] T. Miyamoto*, T.K. Uchida, F. Koyama, and K. Iga, "GaInAs/InP strained super-lattices grown by CBE," *The 38th Spring Meeting of Japan Society of Applied Physics and Related Societies*, 30a-SZK-15, Kanagawa, Mar., 1991.

[4] T. Uchida*, T.K. Uchida, N. Yokouchi, T. Miyamoto, F. Koyama, and K. Iga, "Modulation-doped GaInAs/InP SCH QW laser structure by CBE," *The 38th Spring Meeting of Japan Society of Applied Physics and Related Societies*, 30a-SZK-17, Kanagawa, Mar., 1991.

[5] T. Uchida*, N. Yokouchi, T. Miyamoto, Y. Inaba, F. Koyama, and K. Iga, "Beryllium doping to GaInAsP and InP by CBE," *The 52th Autumn Meeting of Japan Society of Applied Physics*, 11p-W-12, Okayama, Oct., 1991.

[6] T. Miyamoto*, T. Uchida, N. Yokouchi, Y. Inaba, F. Koyama, and K. Iga, "GaInAsP/InP surface emitting laser diode grown by chemical beam epitaxy," *The 39th Spring Meeting of Japan Society of Applied Physics and Related Societies*, 28a-SF-8, Chiba, Mar., 1992.

[7] N. Yokouchi*, T. Uchida, T. Miyamoto, Y. Inaba, F. Koyama, and K. Iga, "CBE growth of GaInAsP/InP surface emitting laser wafers," *The 39th Spring Meeting of Japan Society of Applied Physics and Related Societies*, 31p-ZB-2, Chiba, Mar., 1992.

[8] T. Uchida*, N. Yokouchi, T. Miyamoto, Y. Inaba, F. Koyama, and K. Iga, "CBE growth of GaInAsP/InP distributed Bragg reflector (DBR) II," *The 39th Spring Meeting of Japan Society of Applied Physics and Related Societies*, 31p-ZB-5, Chiba, Mar., 1992.

[9] T. Uchida*, N. Yokouchi, T. Miyamoto, Y. Inaba, F. Koyama, and K. Iga, "GaInAsP/InP surface emitting lasers grown by chemical beam epitaxy (CBE)," *1992 IEICE Spring Conference*, C-164, Chiba, Mar., 1992.

[10] T. Miyamoto*, T. Uchida, N. Yokouchi, Y. Inaba, K. Mori, F. Koyama, and K. Iga, "A study on gain-resonance matching of CBE grown 1.5μm surface emitting lasers," *The 53th Autumn Meeting of Japan Society of Applied Physics*, 16a-V-7, Osaka, Sep., 1992.

[11] N. Yokouchi*, T. Uchida, T. Miyamoto, Y. Inaba, F. Koyama, and K. Iga, "Optical absorption property of CBE grown highly Be-doped GaInAsP," *The 53th Autumn Meeting of Japan Society of Applied Physics*, 17p-ZF-16, Osaka, Sep., 1992.

[12] Y. Inaba*, T. Uchida, N. Yokouchi, T. Miyamoto, F. Koyama, and K. Iga, "GaInAsP/InP multi quantum barrier (MQB) grown by chemical beam epitaxy (CBE)," *The 53th Autumn Meeting of Japan Society of Applied Physics*, 17p-ZF-17, Osaka, Sep., 1992.

[13] N. Yokouchi*, T. Uchida, T. Miyamoto, Y. Inaba, F. Koyama, and K. Iga, "Continuous tuning of a GaInAsP/InP surface emitting laser using an external reflector," *1992 IEICE Fall Conference*, C-157, Tokyo, Sep., 1992.

[14] T. Miyamoto*, T. Uchida, N. Yokouchi, Y. Inaba, F. Koyama, and K. Iga, "GaInAsP/InP surface emitting laser diode grown by chemical beam epitaxy II," *The 40th Spring Meeting of Japan Society of Applied Physics and Related Societies*, 29a-C-11, Tokyo, Mar., 1993.

[15] K. Mori*, T. Miyamoto, N. Yokouchi, Y. Inaba, F. Koyama, and K. Iga, "Effect of a hetero-interface between active layer and p-cladding layer for 1.55μm GaInAsP/InP surface emitting laser," *The 54th Autumn Meeting of Japan Society of Applied Physics*, 27a-H-5, Hokkaido, Sep., 1993.

[16] Y. Inaba*, N. Yokouchi, T. Miyamoto, K. Mori, F. Koyama, and K. Iga, "GaInAs(P)/InP multi quantum barrier grown by chemical beam epitaxy (CBE) II," *The 54th Autumn Meeting of Japan Society of Applied Physics*, 28a-ZS-2, Hokkaido, Sep., 1993.

[17] N. Yokouchi*, T. Miyamoto, Y. Inaba, K. Mori, F. Koyama, and K. Iga, "Composition change in $Ga_XIn_{1-X}As$/InP quantum wells grown by CBE," *The 54th Autumn Meeting of Japan Society of Applied Physics*, 28a-ZS-3, Hokkaido, Sep., 1993.

[18] Y. Inaba, T.H. Loh*, N. Yokouchi, T. Miyamoto, Y. Inaba, F. Koyama, and K. Iga, "Consideration of hole injection in GaInAsP/InP multi-quantum barrier (MQB) laser diodes," *The 41th Spring Meeting of Japan Society of Applied Physics and Related Societies*, 30a-K-6, Kawasaki, Mar., 1994.

[19] S. Mitsugi*, J. Kato, A. Matsutani, T. Miyamoto, T. Mukaihara, F. Koyama, and K. Iga, "Size reduction of micro-arc ring laser," *The 41th Spring Meeting of Japan Society of Applied Physics and Related Societies*, 31a-K-4, Kawasaki, Mar., 1994.

[20] T. Miyamoto*, K. Mori, H. Maekawa, Y. Inaba, N. Yokouchi, F. Koyama, and K. Iga, "Electrical characteristics of p-GaInAsP/InP distributed Bragg reflector," *The 41th Spring Meeting of Japan Society of Applied Physics and Related Societies*, 31a-K-6, Kawasaki, Mar., 1994.

[21] T.H. Loh*, T. Miyamoto, F. Koyama, and K. Iga, "Strain-compensated multi-quantum barriers for hot electron leakage reduction in long-wavelength semiconductor lasers," *The 55th Autumn Meeting of Japan Society of Applied Physics*, 21a-S-7, Nagoya, Sep., 1994.

[22] T. Miyamoto*, T. Takada, K. Mori, Y. Kurita, F. Koyama, and K. Iga, "Effect of p-type doping on lasing characteristics of long-wavelength surface-emitting lasers," *The 42th Spring Meeting of Japan Society of Applied Physics and Related Societies*, 30p-ZG-10, Kanagawa, Mar., 1995.

[23] T. Takada*, T. Miyamoto, K. Suzuki, K. Mori, Y. Kurita, F. Koyama, and K. Iga, "Study on Uniformity of current injection for long-wavelength surface emitting lasers," *The 42th Spring Meeting of Japan Society of Applied Physics and Related Societies*, 30p-ZG-11, Kanagawa, Mar., 1995.

[24] Y. Kurita*, T. Miyamoto, F. Koyama, and K. Iga, "A study on wavelength-tunable vertical-cavity surface-emitting laser using quantum-confined stark effect," *The 42th Spring Meeting of Japan Society of Applied Physics and Related Societies*, 30p-ZG-13, Kanagawa, Mar., 1995.

[25] S. Mitsugi*, A. Matsutani, T. Miyamoto, Y. Kurita, T. Takada, F. Koyama, and K. Iga, "1.55μm GaInAsP/InP Micro-arc ring cavity semiconductor lasers," *The 56th Autumn Meeting of Japan Society of Applied Physics*, 28a-ZA-8, Kanazawa, Aug., 1995.

[26] T.H. Loh*, T. Miyamoto, Y. Kurita, T. Takada, F. Koyama, and K. Iga, "CBE growth of GaInAs/GaInP strain-compensated short-period superlattice to realize strain-compensated multi-quantum barriers," *The 56th Autumn Meeting of Japan Society of Applied Physics*, 29p-ZE-6, Kanazawa, Aug., 1995.

[27] T. Takada*, T. Miyamoto, Y. Kurita, T.H. Loh, S. Mitsugi, F. Koyama, and K. Iga, "PL characteristics of strain-compensated GaInAsP/GaInAsP quantum well grown by CBE," *The 56th Autumn Meeting of Japan Society of Applied Physics*, 29p-ZE-7, Kanazawa, Aug., 1995.

[28] T.H. Loh, T. Miyamoto, T. Takada, F. Koyama, and K. Iga, "Strain-compensated CBE grown InAsP/InP/GaInP short-period superlattice for long-wavelength multi-quantum barriers," submitted to *The 43th Spring Meeting of Japan Society of Applied Physics and Related Societies*.

[29] Y. Kurita, T. Miyamoto, T. Takada, R. Ubukata, S. Sekiguchi, F. Koyama, and K. Iga, "Design and fabrication of wavelength-tunable strained-quantum-well vertical-cavity surface-emitting lasers," submitted to *The 43th Spring Meeting of Japan Society of Applied Physics and Related Societies*.

Symposia

[1] T. Uchida*, T.K. Uchida, N. Yokouchi, T. Miyamoto, K. Mise, F. Koyama, and K. Iga, "GaInAs/InP multiple quantum well and strained-layer superlattice grown by CBE," *IEICE Optical and Quantum Electron. Technical Meeting*, Tokyo, Oct. 15, 1990.

[2] T. Uchida*, T.K. Uchida, N. Yokouchi, T. Miyamoto, F. Koyama, and K. Iga, "Ultra-thin GaInAs/InP quantum wells grown by CBE," *The 8th Semiconductor Laser Symposium*, Yokohama, Mar. 1, 1991.

[3] T. Uchida*, N. Yokouchi, T. Miyamoto, Y. Inaba, F. Koyama, and K. Iga, "GaInAs/InP double-heterostructure laser wafers grown by CBE for surface emitting lasers," *The 9th Semiconductor Laser Symposium*, Yokohama, Mar. 2, 1992.

[4] T. Uchida*, N. Yokouchi, T. Miyamoto, Y. Inaba, F. Koyama, and K. Iga, "Chemical beam epitaxy (CBE) growth of GaInAsP/InP and application to surface emitting lasers," *IEICE Optical and Quantum Electron. Technical Meeting*, Tokyo, Jul. 27, 1992.

[5] T. Uchida*, T. Miyamoto, N. Yokouchi, Y. Inaba, K. Mori, F. Koyama, and K. Iga, "1.5 μm GaInAsP/InP surface emitting lasers grown by chemical beam epitaxy (CBE)," *The 10th Semiconductor Laser Symposium*, Yokohama, Mar. 2, 1993.

[6] T. Miyamoto*, N. Yokouchi, and K. Iga, "Fabrication and characterization of GaInAsP/InP surface emitting lasers grown by CBE," 応用物理学会電子物性分科会定例会, Tokyo, Jul. 27, 1993.

[7] T.H. Loh*, T. Miyamoto, F. Koyama, and K. Iga, "Strain-compensated multi-quantum barriers for reducing hot electron leakage in long-wavelength semiconductor lasers," *13th Symposium on Alloy Semiconductor Physics and Electronics*, F2, Izu-Nagaoka, Jul. 20-22, 1994.